

# Wind turbine wakes: exploring the underexplored -- vertical-axis wind turbines and topography

THÈSE N° 8545 (2018)

PRÉSENTÉE LE 15 AOÛT 2018

À LA FACULTÉ DE L'ENVIRONNEMENT NATUREL, ARCHITECTURAL ET CONSTRUIT  
LABORATOIRE D'INGÉNIERIE ÉOLIENNE ET D'ÉNERGIE RENOUVELABLE  
PROGRAMME DOCTORAL EN MÉCANIQUE

ÉCOLE POLYTECHNIQUE FÉDÉRALE DE LAUSANNE

POUR L'OBTENTION DU GRADE DE DOCTEUR ÈS SCIENCES

PAR

Sina SHAMSODDIN

acceptée sur proposition du jury:

Prof. F. Gallaire, président du jury  
Prof. F. Porté Agel, directeur de thèse  
Prof. C. Meneveau, rapporteur  
Prof. R. J. A. M. Stevens, rapporteur  
Prof. P. Monkewitz, rapporteur  
Prof. M. Parlange, rapporteur



ÉCOLE POLYTECHNIQUE  
FÉDÉRALE DE LAUSANNE

Suisse  
2018



سر ارادت ما و آستان حضرت دوست  
که هر چه بر سرمای رود ارادت اوست  
حافظ

In theory, theory and practice are the same.

In practice, they are not.

— Albert Einstein

To my parents, Sad and Marzieh; and to my brother, Farhang





# Acknowledgements

I have spent around four years to compose this doctoral thesis, but in fact, the number of years required for this accomplishment is much more than this. I am indebted to many who have contributed to both my education and development as a person since my childhood.

In the first place, I would like to express my gratitude to all of my teachers, professors and educational supervisors that I had since my elementary school. All of what I have achieved in this thesis is founded (in many cases directly) on the excellent education I received in the elementary, middle and high schools in the city of Ahvaz, Iran until the age of 18<sup>1</sup>. I definitely owe my mathematical, physics and lingual background to this period of time in Ahvaz. Then comes the university times, where I completed a bachelor's degree in Mechanical engineering in Amirkabir University of Technology (Tehran Polytechnic) in Tehran, Iran. During my time in AUT, I benefited a lot from the knowledge of its professors and their first-class teaching and supervision<sup>2</sup>. It was in this period that I became interested in fluid mechanics, computational fluid dynamics and large-eddy simulation.

Later, I moved to Lausanne, Switzerland to conduct my Master and doctoral studies at EPFL. I have to say I am deeply grateful to EPFL for the high level of education and the remarkable quality and quantity of the resources that it provided in a professional and at the same time friendly academic environment. Of course, I would like to single out Prof. Fernando Porté-Agel, who was my supervisor for both Master and PhD studies. I am sincerely thankful to Fernando for giving me and even showing me the opportunity to study in EPFL. Fernando is, as confirmed also by many other students, one of the best teachers I have ever seen. I appreciate indeed the fact that his office door was always open and he was constantly available for discussions and exchanges about the research. Besides, I would like to thank Fernando, for the freedom that I had in choosing the research topics, in which I was interested. This freedom is a great asset that I enjoyed a lot. In addition, I would be glad to take the opportunity to genuinely thank the jury members of my PhD defense, who graciously devoted their time to reading this dissertation and offered their expertise to the author with their encouraging feedbacks.

---

<sup>1</sup>Just to name a few teachers during this period: Mr. Navarbah, Mr. Massoudnia, Mr. Niamadpour, Mr. Samawati, Mr. Vaezi, Mr. Sarkoohaki, Mr. Kasiri and so on.

<sup>2</sup>Just to name a few professors during this period: Prof. Saffar-Avval, Prof. Lessani and so on.

## Acknowledgements

---

These jury members that I had the honour to have in my defense were: Prof. Charles Meneveau, Prof. Marc Parlange, Prof. Peter Monkewitz, Prof. Richard J.A.M. Stevens and Prof. François Gallaire.

Apart from teachers and supervisors, I benefited much from the unique companionship of many friends and colleagues during these years, without whom walking through this road would not have been so joyful or even possible. I specially want to thank all my present and previous colleagues in the WiRE laboratory for all their individual contributions to maintaining a friendly social atmosphere in the lab and to scientific and academic exchanges. I grab the chance here to mention these great colleagues by name: Majid, Ahmad, Fernando C., Vincent, Ka Ling, Deepu, Mahdi, Jiannong, Corey, Corinne, Carole, Pierre, Farshid, Wai Chi, Ting, Valerio and Hao. Among these, I would like to highlight two persons with whom I had more frequent and regular scientific discussions: Majid and Jiannong. I am really thankful to them for their valuable and enlightening comments and their precious time.

Furthermore, in going along this path, I was lucky for being constantly enriched by the luxury of fabulous friends that I had. Although the list of their names is too long to be fully mentioned here, I cannot resist the temptation of naming at least a few: Maziar, Mohammad, Uzair, Damiano, Ali, Jason, Reza, Elahe, Mehdi, Hassan, Raynald, Michel, Evelyne and many others.

Finally, I would like to reserve the last big expression of gratitude to the most important ones in my life, *i.e.*, my beloved family. The way my parents guided, encouraged and oversaw me in my educational path, from elementary school to the present PhD degree, is exemplary; my scholarly development could not have been fostered better. Beyond this, I feel extremely blessed to be raised in such a family, in which I have been nurtured with the most noble and lofty values. My parents (Sad and Marzieh) and my brother (Farhang) have been the unbounded sources of love and affection, from which I nourished and enriched myself. Unfortunately, as many others have also admitted, the cruel worldly reality is that no one is able to deservedly thank all these blessings – and I am not an exception to this.

*Lausanne, March 2018*

*Sina Shamsoddin*

# Abstract

In this thesis, we aim to contribute to the research on two wind energy topics, namely, vertical-axis wind turbines (VAWTs) and wind turbines on topography. Although these two topics may seem too distant to be reconciled in one thesis, as the title of the thesis suggests, the common feature that they share with each other is that both of them are among the topics that have benefited from relatively little research and development in the wind energy community.

In the VAWT part, first, we adapt and implement two actuator-type VAWT parameterization models (i.e. the actuator swept-surface model and the actuator line model) for use in numerical flow simulations with the purpose of studying the wakes of VAWTs and their performance in the atmospheric boundary layer (ABL) and eventually predicting the flow in sizable wind farms. These models are implemented in a large-eddy simulation (LES) framework, and the results are validated with experimental data. After validating the model, we investigate the energetic performance and wake structure of a megawatt-VAWT which is placed in the ABL. We characterize, in particular, the energetic performance of such a turbine by calculating the power coefficient of the turbine for more than 100 different combinations of tip-speed ratios and blade chord lengths (i.e. different solidities). The optimum combination of solidity (defined as  $Nc/R$ , where  $N$  is the number of blades,  $c$  is the chord length and  $R$  is the rotor radius) and tip-speed ratio is found to be 0.18 and 4.5, respectively. This combination results in a power coefficient of 0.47.

In the topography part, we implement the actuator disk model (to parameterize the effect of wind turbines) together with the coordinate transformation method (to resolve the topography) in our LES framework to simulate a wind farm sited on topography and also to validate our LES framework for turbine-topography systems with wind-tunnel measurements. Next, we consider the effect of pressure gradient (which is an important effect created by topography) on turbulent planar and axisymmetric wakes. For both cases, we develop analytical models to predict the wake evolution in pressure gradient conditions. The models are based on the cross-stream integration of the streamwise momentum equation and use the self-similarity of the mean flow. We also make an experimentally-supported assumption that the ratio of the maximum velocity deficit to the wake width is independent of the imposed pressure gradient. The models are validated with both experimental and LES data.

Furthermore, in the last study of the topography part, we build on all of the previous accomplishments to give a better picture of what happens to a turbine wake when it

## Acknowledgements

---

interacts with a hill. We present an analytical framework to model turbine wakes over two-dimensional hills. The model consists of two steps. In the first step, we deal with the effect of pressure gradient on the wake evolution; and in the second step, we consider the effect of the hill-induced streamline distortion on the wake. This model enables us to obtain the wake recovery rate, the mean velocity and velocity deficit profiles and the wake trajectory in the presence of the hill. Moreover, we perform LES to test our model and also to obtain new complementary insight about such flows. Especially, we take advantage of the LES data to carry out a special treatment for the behaviour of the wake on the leeward side of the hill. It is found that the mainly favourable pressure gradient on the windward side of the hill accelerates the wake recovery and the adverse pressure gradient on the leeward side decelerates it. The wake trajectory for a hill of the same height as the turbine's hub-height is found to be almost following the hill profile in the windward side but it maintains an almost constant elevation (a horizontal line) downstream of the hilltop. The trajectory of the wake on the leeward side is also studied for the limiting case of an escarpment, and it is shown that an internal boundary layer is formed on the plateau which leads to an upward displacement of the wake center. Finally, a parametric study of the position of the turbine with respect to the hill is performed to more elucidate the effect of the hill-induced pressure gradient on the wind turbine wake recovery.

**Key words:** Atmospheric boundary-layer; Large-eddy simulation; Turbine wake; Vertical-axis wind turbine; Actuator line model; Actuator swept-surface model; Topography; Complex terrain; Pressure gradient

# Zusammenfassung

Mit dieser Doktorarbeit beabsichtigen wir, zur Forschung über zwei Themen beizutragen: d.h. Vertikalachswindturbinen (VAWTn) und Windturbinen auf Topografie. Obwohl diese zwei Themen zu unvereinbar scheinen mögen, um zusammen in einer Doktorarbeit behandelt zu werden, ist das gemeinsame Merkmal, (das sie miteinander teilen), (wie der Titel der Doktorarbeit andeutet) dass die beiden zu den Themen gehören, die von Forschung und Entwicklung in Windenergiegemeinschaft relativ wenig profitiert haben.

Im VAWT-Teil bearbeiten und implementieren wir erstens zwei aktuatorartige VAWT-Parametrisierungen (d.h. das Aktuator-überstrichene-Flächen-Modell und Aktuatorlinie-Modell) zur Verwendung in numerischen Strömungssimulationen, mit dem Ziel, die Nachlaufströmung in der atmosphärischen Grenzschicht (AGS) zu erforschen, und schließlich die Strömung in relativ großen Windparks zu simulieren. Diese Modelle werden in einen Grobstruktursimulation (GSS)-Rahmen eingeführt, und die Ergebnisse werden mit Versuchsdaten validiert. Nach Validierung des Modells untersuchen wir die Energieleistung und Nachlaufströmungsstruktur einer Megawatt-VAWT, die in der AGS gestellt wird. Im Besonderen kennzeichnen wir die Energieleistung derartiger Turbine durch die Berechnung des Leistungsbeiwerts der Turbine für mehr als 100 unterschiedliche Kombinationen von Schnelllaufzahlen und Profiltiefen der Rotorblätter (d.h. unterschiedliche Rotor-Flächendichten). Die optimale Kombination der Rotor-Flächendichte (die als  $Nc/R$  definiert wird, wobei  $N$  die Zahl der Rotorblätter,  $c$  die Profiltiefe, und  $R$  der Rotorradius ist) und die Schnelllaufzahl ist, 0,18 beziehungsweise 4,5. Diese Kombination ergibt einen Leistungsbeiwert von 0,47.

Im Topografie-Teil führen wir das verknüpfte Aktuatorscheiben-Modell ein (um die Auswirkung der Turbinen zu parametrisieren) und die Koordinatentransformation-Methode (um mit der Topografie umzugehen) in unserem GSS-Rahmen, um einen Windpark, der auf Topografie liegt, zu simulieren und ebenfalls um unsere GSS-Rahmen für die Turbinen-Topografie-Systeme mit Windkanalmessungen zu validieren. Anschließend berücksichtigen wir die Auswirkung des Druckgradienten (der ein bedeutender Effekt ist und von Topografie erzeugt wird) auf turbulente ebene und runde Nachlaufströmungen. Für beide Fälle entwickeln wir analytische Modelle, um die Nachlaufströmungsevolution in Druckgradientbedingungen vorherzusagen. Die Modelle basieren auf einer querströmungsmäßigen Integration der Impulsgleichung in Strömungsrichtung, und sie verwenden die Selbstähnlichkeit der mittleren Strömung. Wir gehen ebenso von einer experimentell unterstützten Annahme aus, dass das Verhältnis des maximalen Geschwindigkeitsdefizits

zur Breite der Nachlaufströmung unabhängig von dem durchgesetzten Druckgradienten ist. Beide Modelle werden mit Versuchs- als auch GSS-Daten validiert.

Außerdem bauen wir in der letzten Studie dieses Teils auf all die vorherigen Leistungen des Topografie-teils, um besser zu veranschaulichen, was mit einer Turbine-Nachlaufströmung geschieht, wenn sie mit einem Hügel wechselwirkt. Wir legen einen analytischen Rahmen fest, um Turbinen-Nachlaufströmungen über zweidimensionale Hügel zu modellieren. Das Modell besteht aus zwei Schritten. Im ersten Schritt befassen wir uns mit der Auswirkung des Druckgradienten; und im zweiten Schritt betrachten wir die Auswirkung der vom Hügel beeinflussten Stromlinieverzerrung auf die Nachlaufströmung. Dieses Modell ermöglicht uns, die Erholungsrate der Nachlaufströmung, die mittleren Windgeschwindigkeits- und Geschwindigkeitsdefizitprofile und die Nachlaufströmungsflugbahn in Gegenwart des Hügels zu gewinnen. Weiter führen wir GSS aus, um unseres Modell zu überprüfen, und gleichfalls um neue ergänzende Einsichten in derartigen Strömungen zu bekommen. Im Besonderen nützen wir die GSS-Daten, um eine besondere Behandlung für das Verhalten der Nachlaufströmung auf der Leeseite des Hügels auszuführen. Es wird festgestellt, dass der überwiegend günstige (oder negative) Druckgradient auf der Luvseite des Hügels die Nachlaufströmungserholung beschleunigt, und dass der ungünstige (oder positive) Druckgradient auf der Leeseite sie verlangsamt. Wir finden heraus, dass die Nachlaufströmungsflugbahn für einen Hügel, dessen Höhe dieselbe wie die Nabenhöhe der Windturbine ist, auf der Luvseite fast dem Hügelprofil folgt, sie jedoch auf der Leeseite eine konstante Höhe (eine horizontale Linie) behält. Die Nachlaufströmungsflugbahn auf der Leeseite wird ebenso für den Grenzfall einer Schichtstufe untersucht, und es wird aufgezeigt, dass sich eine innere Grenzschicht über das Hochplateau formt, und diese zu einer Aufwärtsverlagerung der Nachlaufströmungsmittelpunkt führt. Schließlich wird eine parametrische Studie über die Stelle der Turbine in Bezug auf den Hügel durchgeführt, um die Wirkung des vom Hügel bewirkten Druckgradienten auf die Windturbinenachlaufströmungserholung weiter aufzuklären.

**Stichwörter:** atmosphärische Grenzschicht; Grobstruktursimulation; Nachlaufströmung; Vertikalachswindturbine; Aktuator-überstrichene-Fläche-Modell; Aktuatorlinie-Modell; Topografie; komplexes Gelände; Druckgradient

# Résumé

Dans cette thèse, nous visons à contribuer à la recherche sur deux sujets : à savoir des éoliennes à axe vertical (ÉAV) et des éoliennes sur topographie. Bien que ces deux sujets puissent sembler trop éloignés pour être conciliés dans une thèse, (comme le titre de la thèse suggère) le trait commun qu'ils partagent est que les deux sont parmi les sujets qui ont bénéficié de relativement peu de recherche et développement dans la communauté de l'énergie éolienne.

Dans la partie d'ÉAV, nous adaptons et implémentons deux modèles de paramétrisation d'ÉAV (c.à.d. le modèle de surface-balayée active et le modèle de ligne active) pour être utilisés dans des simulations numériques d'écoulement dans le but d'étudier le sillage dans la couche limite atmosphérique (CLA) et éventuellement de simuler l'écoulement dans des parcs éoliens d'une taille assez grande. Ces modèles sont implémentés dans un cadre de simulation des grandes structures (SGS), et les résultats sont validés avec des données expérimentales. Après la validation du modèle, nous investiguons la performance énergétique et la structure du sillage pour une ÉAV mégawatt, qui est placée dans la CLA. Nous caractérisons particulièrement la performance énergétique d'une telle éolienne en calculant le coefficient de puissance de l'éolienne pour plus que 100 combinaisons différentes des rapports de vitesse de pointe et des longueurs de corde (c.à.d. la solidité). La combinaison optimale de solidité (définie par  $NC/R$ , où  $N$  est le nombre de pales,  $c$  est la longueur de corde et  $R$  est le rayon du rotor) et de rapport de vitesse de pointe s'est trouvée être 0,18 et 4,5, respectivement. Pour cette combinaison, le coefficient de puissance est de 0,47.

Dans la partie relative à la topographie, nous implémentons la combinaison du modèle de disque actif (pour modéliser l'effet des éoliennes) et de la méthode de transformation des coordonnées (pour traiter la topographie) dans notre cadre de SGS afin de simuler un parc éolien, qui est situé sur une topographie et également afin de valider notre cadre de SGS pour les systèmes d'éolienne-topographie avec des mesures en soufflerie. Ensuite, nous considérons l'effet du gradient de pression (qui est un effet important créé par la topographie) sur des sillages turbulents plats et axisymétriques. Pour les deux cas, nous développons des modèles analytiques afin de prédire l'évolution du sillage dans les conditions de gradient de pression. Les modèles sont basés sur l'intégration dans la direction latérale de l'équation de la quantité de mouvement longitudinale et ils utilisent l'autosimilarité de l'écoulement moyen. Nous faisons aussi l'hypothèse soutenue expérimentalement, que le rapport du déficit de vitesse maximal à la largeur de sillage est

## Acknowledgements

---

indépendant du gradient de pression imposé. Les modèles sont validés avec les données expérimentales ainsi que celles de SGS.

En outre, dans la dernière étude de la partie de topographie, nous nous appuyons sur tous les accomplissements précédents de cette partie afin de donner une meilleure idée de ce qui arrive à un sillage d'éolienne quand il interagit avec une colline. Nous présentons un cadre analytique avec lequel modéliser des sillages d'éolienne au-dessus des collines bidimensionnelles. Le modèle se compose de deux étapes. Dans la première étape, nous nous occupons de l'effet de gradient de pression sur l'évolution du sillage ; et dans la deuxième étape, nous considérons l'effet de la déformation des lignes de courant, qui est causée par la colline, sur le sillage. Le modèle nous permet d'obtenir le taux de récupération du sillage, les profils de vitesse et déficit de vitesse et la trajectoire du sillage en présence de la colline. De plus, nous réalisons la SGS afin de vérifier notre modèle et pour approfondir nos connaissances sur ce genre d'écoulement. Particulièrement, nous profitons des données de la SGS afin d'effectuer un traitement spécial pour le comportement du sillage sur le côté sous le vent de la colline. On trouve que le gradient de pression principalement favorable du côté du vent accélère la récupération du sillage, et le gradient de pression défavorable sur le côté sous le vent la ralentit. On trouve que la trajectoire du sillage pour une colline de même hauteur que la hauteur moyenne de l'éolienne suit le profil de la colline du côté du vent, mais elle maintient une élévation presque constante (une ligne horizontale) en aval du sommet de la colline. La trajectoire du sillage sur le côté sous le vent est étudiée pour le cas limite d'un escarpement, et on montre qu'une couche limite interne se forme sur le plateau, qui à son tour conduit à un déplacement vers le haut du centre du sillage. Finalement, une étude paramétrique de la position de l'éolienne par rapport à la colline est effectuée afin d'élucider l'effet du gradient de pression, qui est causée par la colline, sur la récupération du sillage des éoliennes.

**Mots clefs :** couche limite atmosphérique ; simulation des grandes structures ; sillage d'éolienne ; éolienne à axe vertical ; modèle de surface-balayée active ; modèle de ligne active ; topographie ; terrain complexe ; gradient de pression



# Contents

Acknowledgements	i
Abstract (English/Deutsch/Français)	iii
Contents	xi
List of figures	xiii
List of tables	xix
<b>1 Introduction</b>	<b>1</b>
<b>I Part I: Vertical-axis wind turbines</b>	<b>5</b>
<hr/>	
<b>2 Large-eddy simulation of vertical axis wind turbine wakes</b>	<b>9</b>
2.1 Introduction . . . . .	10
2.2 Large-eddy simulation framework . . . . .	12
2.2.1 Turbulence closure models . . . . .	12
2.2.2 Parameterization of VAWT-induced forces . . . . .	14
2.3 Numerical and experimental setups . . . . .	17
2.3.1 Experimental setup . . . . .	18
2.3.2 Numerical setup . . . . .	19
2.4 Results and discussion . . . . .	21
2.5 Summary . . . . .	28
<b>3 LES of VAWT wakes in the ABL</b>	<b>33</b>
3.1 Introduction . . . . .	34
3.2 Large-eddy simulation framework . . . . .	35
3.3 Numerical setup . . . . .	36
3.4 Results and discussion . . . . .	40
3.4.1 Turbine performance and power extraction . . . . .	40
3.4.2 VAWT wake . . . . .	40
3.5 Summary . . . . .	49

<b>II</b>	<b>Part II: Wind turbines on topography</b>	<b>61</b>
<b>4</b>	<b>LES of ABL flow through a wind farm sited on topography</b>	<b>65</b>
4.1	Introduction . . . . .	66
4.1.1	Flow over complex terrain . . . . .	66
4.1.2	Wind turbines and topography . . . . .	68
4.2	Large-eddy simulation framework . . . . .	70
4.2.1	Coordinate transformation . . . . .	70
4.3	Numerical set-up . . . . .	73
4.4	Results and discussion . . . . .	75
4.5	Summary . . . . .	84
<b>5</b>	<b>Turbulent planar wakes under pressure gradient conditions</b>	<b>85</b>
5.1	Introduction . . . . .	85
5.2	Analytical model for wakes under pressure gradient . . . . .	87
5.2.1	Problem formulation . . . . .	87
5.2.2	Model derivation . . . . .	88
5.2.3	Solving the problem for a given $\delta(x)$ . . . . .	91
5.2.4	Asymptotic solution of the problem . . . . .	92
5.3	Validation of the model . . . . .	93
5.4	Discussion . . . . .	95
5.5	Concluding remarks . . . . .	97
<b>6</b>	<b>A model for the effect of pressure gradient on turbulent axisymmetric wakes</b>	<b>99</b>
6.1	Introduction . . . . .	100
6.2	Analytical model for axisymmetric wakes under pressure gradient . . . . .	101
6.2.1	Problem formulation . . . . .	101
6.2.2	Model derivation . . . . .	101
6.2.3	Asymptotic solution of the problem . . . . .	103
6.2.4	Axisymmetric wakes and planar strain . . . . .	104
6.3	Validation of the model . . . . .	105
6.3.1	The numerical experiment . . . . .	105
6.3.2	Results and comparison . . . . .	106
6.4	Concluding remarks . . . . .	108
<b>7</b>	<b>Wind turbine wakes over hills</b>	<b>111</b>
7.1	Introduction . . . . .	112
7.1.1	Analytical studies of flow over hills . . . . .	112
7.1.2	Wind turbines and topography . . . . .	113
7.2	An analytical modelling framework for wake flows over hills . . . . .	115
7.2.1	Problem formulation . . . . .	115

7.2.2	Effect of the hill-induced pressure gradient on the wake recovery . . . . .	115
7.2.3	Effect of the hill-induced streamline distortion . . . . .	118
7.3	Numerical experiments . . . . .	124
7.3.1	LES set-up . . . . .	124
7.3.2	Qualitative LES results . . . . .	126
7.4	The wake in the leeward side of the hill . . . . .	128
7.4.1	Hills . . . . .	130
7.4.2	Escarpments . . . . .	130
7.5	Validation of the analytical model . . . . .	131
7.6	A closer look into the effect of pressure gradient on the wake recovery over hills . . . . .	132
7.7	Conclusion . . . . .	137
<b>8</b>	<b>Conclusion</b>	<b>139</b>
	Overall summary . . . . .	139
	Future research perspectives . . . . .	141
	<b>Bibliography</b>	<b>157</b>
	<b>Curriculum Vitae</b>	<b>159</b>



# List of Figures

1.1	World slope map ( <a href="#">Fischer et al., 2002</a> ) ( <i>Reproduced with permission from the International Institute for Applied Systems Analysis (IIASA)</i> ). . . . .	2
1.2	Offshore use of vertical-axis wind turbines ( <i>Credits to Sandia National Laboratories, and with permission from Pennwell, <a href="#">Holinka, 2012</a></i> ) ( <i>Illustration by Josh Paquette and Matt Barone</i> ). . . . .	3
2.1	Schematic of a cross-section of a vertical-axis wind turbine (VAWT) blade rotating about the turbine axis ( <a href="#">Paraschivoiu, 2002</a> ). . . . .	15
2.2	Diagram of forces acting on the blade. . . . .	16
2.3	Schematic of a cross-sectional view of the actuator swept-surface in the computational mesh. . . . .	16
2.4	Schematic of a cross-sectional view of the actuator line in the computational mesh. . . . .	18
2.5	Schematic of y-z view (normal to streamwise direction) of the experimental setup. . . . .	19
2.6	Schematic of x-z view of the experimental setup. . . . .	19
2.7	x-y view (normal to the blades) of the computational domain. . . . .	21
2.8	Contours of the normalized mean streamwise velocity, $\bar{u}/U_0$ , in a horizontal plane at the equator height of the rotor for the actuator swept-surface model (ASSM): (a) Smagorinsky model, $Cs = 0.1$ ; (b) modulated gradient model (MGM). . . . .	22
2.9	Contours of the normalized mean streamwise velocity, $\bar{u}/U_0$ , in a horizontal plane at the equator height of the rotor for the actuator line model (ALM): (a) Smagorinsky model, $Cs = 0.2$ ; (b) Smagorinsky model, $Cs = 0.1$ ; (c) MGM. . . . .	23
2.10	(a) A cross-sectional view of the flight path of the blades (black circle) and four azimuthal blade positions (colored circles); (b) the locus of the endpoint of relative velocity vector (dotted circle) and the corresponding velocity triangles. . . . .	24

## List of Figures

---

2.11	Comparison of the spanwise profiles of the normalized mean streamwise velocity, $\bar{u}/U_0$ , at different downstream locations: (a) $x/R = 2.50$ ; (b) $x/R = 3.33$ ; (c) $x/R = 5.0$ ; (d) $x/R = 8.33$ ; (e) $x/R = 11.67$ . Water channel measurements (red circles), ALM-MGM (solid black line), ALM-Smagorinsky $C_S = 0.1$ (dashed black line), ALM-Smagorinsky $C_S = 0.2$ (dashed green line), ASSM-MGM (solid blue line) and ASSM-Smagorinsky $C_S = 0.1$ (dashed blue line). . . . .	25
2.12	Contours of the normalized mean streamwise turbulence intensity (resolved part), $\sigma_u/U_0$ , in a horizontal plane at the equator height of the rotor for the ASSM: (a) Smagorinsky model, $C_s = 0.1$ ; (b) MGM. . . . .	26
2.13	Contours of the normalized mean streamwise turbulence intensity (resolved part), $\sigma_u/U_0$ , in a horizontal plane at the equator height of the rotor for the ALM: (a) Smagorinsky model, $C_s = 0.2$ ; (b) Smagorinsky model, $C_s = 0.1$ ; (c) MGM. . . . .	27
2.14	Contours of the normalized instantaneous streamwise velocity, $u/U_0$ , in a horizontal plane at the equator height of the rotor for the two turbine models: (a) actuator swept surface model; (b) actuator line model. In both contour plots, the MGM is used. . . . .	27
2.15	Comparison of spanwise profiles of the normalized mean streamwise turbulence intensity (resolved part), $\sigma_u/U_0$ , at five downstream locations: (a) $x/R = 2.50$ ; (b) $x/R = 3.33$ ; (c) $x/R = 5.0$ ; (d) $x/R = 8.33$ ; (e) $x/R = 11.67$ . Water channel measurements (red circles), ALM-MGM (solid black line), ALM-Smagorinsky $C_S = 0.1$ (dashed black line), ALM-Smagorinsky $C_S = 0.2$ (dashed green line), ASSM-MGM (solid blue line) and ASSM-Smagorinsky $C_S = 0.1$ (dashed blue line). . . . .	29
2.16	The effect of the grid resolution on the spanwise profiles of the normalized mean streamwise velocity and mean streamwise turbulence intensity (resolved part) for the ASSM ( <b>left</b> ) and the ALM ( <b>right</b> ) simulations at $x/R = 5.0$ . Water channel measurements (red circles), $60 \times 400 \times 80$ (dashed blue line), $30 \times 240 \times 80$ (solid black line) and $15 \times 120 \times 80$ (dash-dotted green line). . . . .	29
3.1	Schematic of the computational domain, including the simulated VAWT. . . . .	38
3.2	Plane views of the geometrical configuration of the simulations: (a) top view of the domain; (b) side view of the domain, seen in the $x$ - $z$ mid-plane of the domain. . . . .	39
3.3	Inflow characteristics: (a) vertical profile of the mean streamwise velocity compared to a log-law profile (horizontal axis in logarithmic scale); (b) vertical profile of the mean streamwise velocity (linear scale); (c) vertical profile of the standard deviation of the streamwise velocity. . . . .	39

3.4	Variation of the power coefficient of a three-bladed VAWT with tip-speed ratio ( $TSR$ ) and chord length: (a) $C_P$ as a function of both $TSR$ and chord length; (b) $C_P$ as a function of $TSR$ for four different chord lengths; (c) $C_P$ as a function of chord length for four different $TSR$ values. . . . .	41
3.5	Contour plots of the instantaneous normalized streamwise velocity ( $u/U_{eq}$ ) in three different planes: (a) the $x-y$ plane at the equator height of the turbine; (b) the $x-z$ plane going through the center of the turbine; (c) the $y-z$ plane which is 2D downstream of the center of the turbine. . . . .	42
3.6	Contours of the normalized mean streamwise velocity ( $\bar{u}/U_{eq}$ ) in the $x-y$ plane at the equator height of the turbine. . . . .	43
3.7	Contours of the normalized mean streamwise velocity ( $\bar{u}/U_{eq}$ ) in the $x-z$ plane going through the center of the turbine. . . . .	43
3.8	Contour plots of the normalized mean streamwise velocity ( $\bar{u}/U_{eq}$ ) in six different $y-z$ planes at different distances downstream of the center of the turbine. . . . .	44
3.9	Horizontal-spanwise profiles of the normalized mean streamwise velocity ( $\bar{u}/U_{eq}$ ) in the $x-y$ plane at the equator height of the turbine at different downstream positions. The blue horizontal dashed lines show the extent of the turbine. . . . .	45
3.10	Vertical profiles of the normalized mean streamwise velocity ( $\bar{u}/U_{eq}$ ) in the $x-z$ plane going through the center of the turbine at different downstream positions. The black dashed line represents the inflow profile, and the blue horizontal dashed lines show the extent of the turbine. . . . .	46
3.11	Contour plots of the streamwise turbulence intensity, $\sigma_u/U_{eq}$ : (a) in the $x-y$ plane at the equator height of the turbine; (b) in the $x-z$ plane going through the center of the turbine. . . . .	47
3.12	Contour plots of the streamwise turbulence intensity, $\sigma_u/U_{eq}$ , in six different $y-z$ planes at different distances downstream of the center of the turbine. . . . .	47
3.13	Horizontal profiles of the streamwise turbulence intensity in the $x-y$ plane at the equator height of the turbine at different downstream positions. The black dashed line represents the inflow profile, and the blue horizontal dashed lines show the extent of the turbine. . . . .	48
3.14	Vertical profiles of the streamwise turbulence intensity in the $x-z$ plane going through the center of the turbine at different downstream positions. The black dashed line represents the inflow profile, and the blue horizontal dashed lines show the extent of the turbine. . . . .	50
3.15	Contour plot of the normalized lateral turbulent flux, $\overline{u'v'}/U_{eq}^2$ , in the $x-y$ plane at the equator height of the turbine. . . . .	51
3.16	Contour plots of the normalized lateral turbulent flux, $\overline{u'v'}/U_{eq}^2$ , in six different $y-z$ planes at different distances downstream of the center of the turbine. . . . .	51

## List of Figures

---

3.17	Horizontal profiles of the normalized lateral turbulent flux $(\overline{u'v'}/U_{eq}^2)$ in the $x$ - $y$ plane at the equator height of the turbine at different downstream positions. The black dashed line represents the inflow profile, and the blue horizontal dashed lines show the extent of the turbine. . . . .	52
3.18	Contour plots of the normalized vertical turbulent flux, $\overline{u'w'}/U_{eq}^2$ , in the $x - z$ plane going through the center of the turbine. . . . .	52
3.19	Contour plots of the normalized vertical turbulent flux, $\overline{u'w'}/U_{eq}^2$ , in six different $y$ - $z$ planes at different distances downstream of the center of the turbine. . . . .	53
3.20	Vertical profiles of the normalized vertical turbulent flux $(\overline{u'w'}/U_{eq}^2)$ in the $x$ - $z$ plane going through the center of the turbine at different downstream positions. The black dashed line represents the inflow profile, and the blue horizontal dashed lines show the extent of the turbine. . . . .	53
3.21	The time-averaged (black circles) and curve-fitted (red line) behavior of the variation of angle of attack as a function of azimuthal angle in one revolution of a blade element . . . . .	56
3.22	Lift coefficient curve under the dynamic stall model (black line) as compared to the static lift coefficient curve (red line). The four states in the dynamic stall model are indicated in the graph. . . . .	59
3.23	Flowchart to implement the modified MIT dynamic stall model for a VAWT in turbulent flow. . . . .	60
4.1	Coordinate transformation . . . . .	71
4.2	Schematic of the computational set-up, seen in the $xz$ midplane of the domain . . . . .	75
4.3	Contours of the instantaneous streamwise velocity component in the vertical midplane of the domain in the case without the turbines . . . . .	76
4.4	Contours of the mean streamwise velocity component in the vertical midplane of the domain in the case without the turbines . . . . .	76
4.5	Vertical profiles of the mean streamwise velocity component in five different streamwise positions in the vertical midplane of the domain in the case without the turbines (wind-tunnel data from <a href="#">Tian et al., 2013</a> ) . . . . .	77
4.6	Contours of the streamwise turbulence intensity in the vertical midplane of the domain in the case without the turbines . . . . .	77
4.7	Vertical profiles of the streamwise turbulence intensity in five different streamwise positions in the vertical midplane of the domain in the case without the turbines (wind-tunnel data from <a href="#">Tian et al., 2013</a> ) . . . . .	78
4.8	Contours of the mean streamwise velocity component in the vertical midplane of the domain in the case with the turbines . . . . .	79
4.9	Vertical profiles of the mean streamwise velocity component in five different streamwise positions in the vertical midplane of the domain in the case with the turbines (wind-tunnel data from <a href="#">Tian et al., 2013</a> ) . . . . .	80

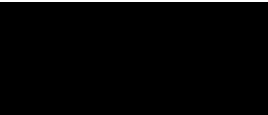


4.10	Contours of the streamwise turbulence intensity in the vertical midplane of the domain in the case with the turbines . . . . .	80
4.11	Vertical profiles of the streamwise turbulence intensity in five different streamwise positions in the vertical midplane of the domain in the case with the turbines (wind-tunnel data from <a href="#">Tian et al., 2013</a> ) . . . . .	81
4.12	Contours of the instantaneous streamwise velocity component in the vertical midplane of the domain in the case where the thrust coefficients of the turbines are increased . . . . .	82
4.13	Contours of the mean streamwise velocity component in the vertical midplane of the domain in the case where the thrust coefficients of the turbines are increased . . . . .	83
4.14	Vertical profiles of the mean streamwise velocity in five different streamwise positions in the vertical midplane of the domain in the case where the thrust coefficients of the turbines are increased . . . . .	83
4.15	Contours of the streamwise turbulence intensity in the vertical midplane of the domain in the case where the thrust coefficients of the turbines are increased . . . . .	84
5.1	Schematic of the velocity profile of a typical turbulent planar wake. . . . .	88
5.2	Normalized maximum velocity deficit as a function of the streamwise distance for ZPG (black), FPG (red) and APG (green) cases. The circles indicate measurements of <a href="#">Liu et al. (2002)</a> , the solid lines are the full solution obtained from Equation (5.13), and the dashed lines are the asymptotic solution of Equation (5.21). . . . .	94
5.3	Normalized wake half-width as a function of the streamwise distance. For the legend, refer to the caption of Figure 5.2. . . . .	95
5.4	Normalized maximum velocity deficit as a function of the streamwise distance for different pressure gradient cases. The value of $\alpha$ is written on each curve with the unit of $[m^{-1}]$ . The red line indicates the ZPG case. The curves are the solution of Equation (5.13). . . . .	96
5.5	Normalized wake half-width as a function of the streamwise distance for different pressure gradient cases. For the legend, refer to the caption of Figure 5.4. . . . .	96
6.1	Domain of the simulations. . . . .	107
6.2	Contours of the normalized velocity deficit in FPG, ZPG and APG cases. . . . .	107
6.3	Left: evolution of $\lambda(x)$ as a function of streamwise distance. Right: base flow velocity $U_b(x)$ for FPG (red), ZPG (black) and APG (green) cases. . . . .	108
6.4	Normalized maximum velocity deficit (left) and wake width (right) as a function of the streamwise distance for ZPG (black), FPG (red) and APG (green) cases. The circles indicate LES results, the solid lines are the full solution obtained from Equation (6.8), and the dashed lines are the asymptotic solution of Equation (6.13). . . . .	109

## List of Figures

---

6.5	Normalized velocity deficit profiles at different streamwise positions. The circles show LES results and the red lines show the model predictions. . .	109
7.1	Schematic of the problem and the modeling framework. . . . .	116
7.2	Schematic of the second step of the model. . . . .	119
7.3	Domain of the simulations. . . . .	124
7.4	Contours of the normalized mean streamwise velocity ( $\bar{u}/U_h$ ) in the $xz$ -plane going through the center of the turbine. Top: no wake case. Down: turbine case. . . . .	126
7.5	Contours of the normalized mean streamwise velocity deficit ( $\bar{u}_{def}/U_h$ ) in the $xz$ -plane going through the center of the turbine. Wake center trajectory (solid line) and streamlines going through the center of the rotor for the no-wake (dashed line) and wake (dash-dotted line) cases are also shown. . . . .	127
7.6	Contours of the normalized mean streamwise velocity deficit ( $\bar{u}_{def}/U_h$ ) in several $yz$ planes at different streamwise positions . . . . .	129
7.7	Trajectory of the turbine wake over 6 hills of different leeward shapes. The blue lines show the wake center trajectory for hills of different leeward profile. Each black line shows a leeward hill profile corresponding to a blue line with the same line marker. The half-length of the leeward hill profile ( $L_2$ ) for each case (or line marker) is specified in the legend. . . .	130
7.8	The inputs of the model. Left: the wake width over flat terrain. Right: $U_b(x)$ as obtained from equation (7.13) (i.e. $U_b(x) = \bar{u}_{nw}^U$ ) for the hill (red line) and flat terrain (black line) . . . . .	132
7.9	Normalized maximum velocity deficit as a function of the streamwise distance over flat terrain (black) and over the hill (red). The circles indicate LES results, the solid lines are the solution obtained from equation (7.2), and the dashed lines are the asymptotic solution of equation (7.7). .	133
7.10	Normalized velocity deficit profiles at different streamwise positions obtained from LES (black circles) and the analytical model (blue line) . . .	134
7.11	Normalized mean streamwise velocity profiles at different streamwise positions obtained from LES (black circles) and the analytical model (blue line) . . . . .	135
7.12	Contours of velocity deficit in the $xz$ plane predicted by the model . . . .	135
7.13	Trajectory of the wake obtained from LES (blue lines) and the analytical model (red lines) . . . . .	136
7.14	Schematic of different turbine placements with respect to the hill. The distance of the turbine to the hilltop is shown on top of the turbine for each placement case. . . . .	136
7.15	Wake center velocity recovery for different turbine positions with respect to the hill. The legend is related to Figure 7.14. . . . .	136



# List of Tables

4.1 Thrust coefficient of the turbines . . . . .	75
--	----



# 1 Introduction

At the end of 2016, the total worldwide wind power capacity was 486.8 GW. Of this amount, 14.4 GW is the share of offshore wind farms and the rest is attributed to onshore wind turbines ([GWEC, 2016](#)). Therefore, the lion's share of the current wind power is generated by onshore wind turbines. Moreover, a quick look at the world slope map (Figure 1.1) shows that there is a high chance that an onshore wind turbine is situated on non-flat and complex terrain, where wind resource potential is high. This chance especially keeps increasing with the current expansion of wind power capacity. For example, the United States has the target to cover 20% of its electricity demand with wind energy by 2030. In other words, its wind power capacity should reach 300 GW by that time (250 GW of which is envisaged to be onshore and 50 GW to be offshore) ([Lindenberg et al., 2008](#)). This means that the US has to add around 220 GW of wind power to its current capacity (82.18 GW at the end of 2016, of which only 30 MW is offshore) in the next 13 years; this is equivalent to 110 000 wind turbines (by assuming an average 2 MW nominal power capacity for each turbine). The same applies to Europe, where the European Wind Energy Association (EWEA) has projected that its current (at the end of 2016) capacity of 161.3 GW (of which 12.6 GW is offshore) will grow to 320 GW (66 GW offshore) by 2030 ([EWEA, 2015](#); [GWEC, 2016](#)). This would mean the addition of around 80 000 wind turbines. Regardless of whether the US or Europe can reach their targets or not, only looking at the numbers shows that it is quite likely that many turbines are deemed to be installed on *complex terrain*.

Moreover, in a future sustainable energy vision, in which diversified conversion of renewable energies is essential, vertical axis wind turbines (VAWTs) exhibit some potential as a reliable means of wind energy extraction alongside conventional horizontal axis wind turbines (HAWTs). VAWTs have shown significant favourable features especially for offshore applications, such as lower turbine center of gravity, reduced machine complexity, insensitivity to wind direction and placement of the drive-train on the ground (see Figure 1.2). Offshore wind farms, with their installation costs decreasing, are gaining more potential to grow in the coming years. Based on the above-mentioned statistics, Europe

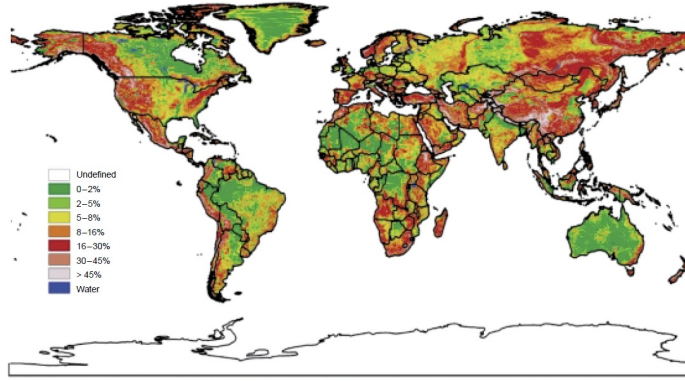


Plate C. Median of terrain slopes derived from GTOPO30.

Figure 1.1 – World slope map (Fischer et al., 2002) (*Reproduced with permission from the International Institute for Applied Systems Analysis (IIASA)*).

and the US are planning to install a total of 100 GW offshore wind power capacity by 2030 (from the end of 2016). This means around 50 000 offshore wind turbines. In this regard, the prospects of VAWTs as alternative wind energy generators to their conventional counterparts, HAWTs, is particularly important in a sustainable energy future vision, which is likely to be marked by *diversity*.

Having the motivations from the above two paragraphs in mind, in this thesis we aim to contribute to the research on two topics, namely, VAWTs and wind turbines on topography. Although these two topics may seem too distant to be reconciled in one thesis, as the title of the thesis suggests, the common feature that they share with each other is that both of them are among the topics that have benefited from relatively little research and development in the wind energy community up to the completion of this thesis. That is why we want to “*explore the underexplored*” in these two realms, in order to acquire a better understanding about the energetic performance and wake structure of a VAWT and its modeling in large-eddy simulation (LES) of the atmospheric boundary layer (ABL); and in order to obtain a clearer view on what happens to a wind turbine wake when it meets a typical hill. More detailed introduction on each of these two topics and the corresponding literature review will be presented accordingly in the beginning of each chapter.

This thesis is structured in the following manner. It is divided into two parts. Part I includes the VAWT studies, and Part II covers the turbine-topography interaction. Part I consists of two chapters (i.e. Chapters 2 and 3). In Chapter 2, two VAWT parameterization models are introduced and implemented in LES, and the results are validated against experimental data. After validating the model, in Chapter 3, we investigate the energetic performance and wake structure of a megawatt-VAWT which is placed in the ABL. Part II comprises four chapters (i.e. Chapters 4, 5, 6 and 7). In

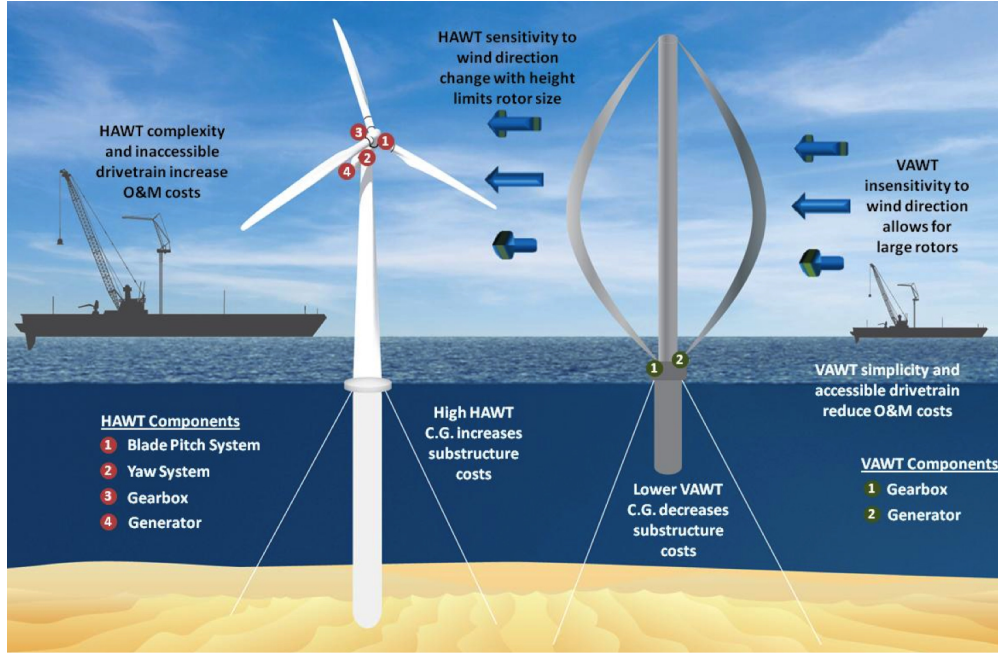


Figure 1.2 – Offshore use of vertical-axis wind turbines (*Credits to Sandia National Laboratories, and with permission from Pennwell, Holinka, 2012*) (*Illustration by Josh Paquette and Matt Barone*).

Chapter 4, we implement the actuator disk model (to parameterize the effect of turbines) together with the coordinate transformation method (to resolve the topography) in our LES framework to simulate a wind farm sited on topography and also to validate our LES framework for turbine-topography systems against wind-tunnel measurements. In Chapters 5 and 6, we consider the effect of pressure gradient, an important effect created by topography, on turbulent planar and axisymmetric wakes, respectively. For both cases, we develop analytical models to predict the wake evolution in pressure gradient conditions. The last chapter in this part, i.e. Chapter 7, is a venue where we build on all of the accomplishments of the previous chapters of this part to give a better picture on what happens to a turbine wake when it interacts with a hill. Finally, in Chapter 8, we provide a summary of what has been performed in this thesis, and also we cast a glance at what can or should be done in these contexts in the future.





# Vertical-axis wind turbines **Part I**







## 2 Large-eddy simulation of vertical axis wind turbine wakes<sup>1</sup>

### Abstract

In this study, large-eddy simulation (LES) is combined with a turbine model to investigate the wake behind a vertical-axis wind turbine (VAWT) in a three-dimensional turbulent flow. Two methods are used to model the subgrid-scale (SGS) stresses: (a) the Smagorinsky model; and (b) the modulated gradient model. To parameterize the effects of the VAWT on the flow, two VAWT models are developed: (a) the actuator swept-surface model (ASSM), in which the time-averaged turbine-induced forces are distributed on a surface swept by the turbine blades, *i.e.*, the actuator swept surface; and (b) the actuator line model (ALM), in which the instantaneous blade forces are only spatially distributed on lines representing the blades, *i.e.*, the actuator lines. This is the first time that LES has been applied and validated for the simulation of VAWT wakes by using either the ASSM or the ALM techniques. In both models, blade-element theory is used to calculate the lift and drag forces on the blades. The results are compared with flow measurements in the wake of a model straight-bladed VAWT, carried out in the Institut de Mécanique et Statistique de la Turbulence (IMST) water channel. Different combinations of SGS models with VAWT models are studied, and a fairly good overall agreement between simulation results and measurement data is observed. In general, the ALM is found to better capture the unsteady-periodic nature of the wake and shows a better agreement with the experimental data compared with the ASSM. The modulated gradient model is also found to be a more reliable SGS stress modeling technique, compared with the Smagorinsky model, and it yields reasonable predictions of the mean flow and turbulence characteristics of a VAWT wake using its theoretically-determined model coefficient.

---

<sup>1</sup>The contents of this chapter are published in: Shamsoddin, S. and Porté-Agel, F. Large eddy simulation of vertical axis wind turbine wakes. *Energies*, 7(2):890–912, 2014.

### 2.1 Introduction

Revived attention towards vertical axis wind turbines (VAWTs) has been observed in recent years. VAWTs are claimed to have several advantages over the conventional horizontal axis wind turbines (HAWTs), such as: insensitivity to the wind direction and, consequently, the absence of any yaw equipment; lower noise, due to the lower tip-speed of the blades; and placement of the drive train system on the ground ([Paraschivoiu, 2002](#)). Recently, [Dabiri \(2011\)](#) has claimed that the power density of wind farms consisting of counter-rotating VAWTs can be potentially greater than HAWT wind farms by an order of magnitude. To understand the performance of VAWTs better, detailed knowledge of the flow through them and the wakes behind them is necessary. Furthermore, to optimize the efficiency of a single VAWT or an array of VAWTs in a wind farm, an accurate and reliable prediction of the flow field behind the turbines is essential. For this purpose, numerical simulations can provide valuable quantitative understanding of VAWT wakes in a relatively fast and cheap way.

Almost 40 years after Darrieus' patent was registered (in 1931), researchers, mainly from some North American institutes (such as the National Research Council of Canada, NASA Langley Research Center and the Sandia National Laboratories), started to study VAWTs extensively. Rigorous and exhaustive experimental data from both wind tunnel and field measurements for different sizes of VAWTs were collected by these institutes in the 1970s and 1980s ([Blackwell et al., 1976](#); [Sheldahl and Blackwell, 1977](#); [Sheldahl et al., 1980](#); [Johnston, 1980](#); [Worstell, 1981](#); [McNerney, 1981](#)). These experiments and other wind tunnel and field measurements, which were done during those years ([South and Rangi, 1975](#); [Nguyen et al., 1981](#); [Vittecoq and Laneville, 1982](#); [Penna and Kuzina, 1984](#); [Schienbein, 1979](#); [Richards, 1987](#)), mainly focused on overall rotor performance (e.g., power and torque) and loading on the blades. The first attempts to experimentally study the wake behind a VAWT date back to the late 1970s, when [Muraca and Guillotte \(1976\)](#) performed velocity measurements in the near wake of a VAWT in a wind tunnel, and [Vermeulen et al. \(1979\)](#) carried out flow measurements in the wake of a full-scale VAWT in the natural wind environment. None of them reported wake turbulence data. Later, in the 1980s, [Strickland et al. \(1981\)](#) and [Brochier et al. \(1986\)](#) carried out water channel experiments to quantify the flow field downstream of a model straight-bladed VAWT. [Bergeles et al. \(1991\)](#) performed hot-wire measurements in the near wake of a Troposkein-shaped VAWT in a wind tunnel and reported the profiles of mean velocity and turbulence intensity for different tip-speed ratios and two downstream positions. More recently, [Battisti et al. \(2011\)](#) carried out wind tunnel measurements on the wake of a VAWT and provided data on time-averaged and phase-resolved velocity and turbulence intensity in a vertical plane located 1.5 rotor diameters downstream of the turbine axis. They showed that large-scale aerodynamic unsteadiness is greater in the tip region than in the central region. With the emergence of particle image velocimetry (PIV) techniques, some flow visualizations and measurements have been done to study the dynamic stall

phenomenon and vortex evolution inside and behind a VAWT (Fujisawa and Shibuya, 2001; Simao Ferreira et al., 2007; Hofemann et al., 2008; Tescione et al., 2013). Tescione et al. (2013) has reported contours of average velocity and vorticity up to about 1.5 rotor diameters downstream of the turbine in a wind tunnel.

Besides experimental investigations, analytical and numerical studies have also been employed with the aim of VAWT performance prediction. The aerodynamic models that have been proposed for VAWTs can be classified in two main groups: streamtube models (Paraschivoiu, 2002) (e.g., single streamtube model, multiple streamtube model, double multiple streamtube model) and vortex models (e.g., fixed-wake vortex model (Wilson and Walker, 1981) and free-wake vortex model (Strickland et al., 1981)). In streamtube models, the time-averaged forces on the blades are equated to the change in the streamwise momentum of the wind. Although, in principle, with vortex models, one can obtain the flow field downstream of a VAWT, the main focus of both models has been on the prediction of forces on the blades and overall rotor performance.

Simulation of VAWTs by solving the Navier–Stokes equations with numerical techniques was pioneered by Rajagopalan and Fanucci (1985), who introduced the actuator swept-surface method in a two-dimensional space as a cylindrical porous shell on which the time-averaged blade forces act continuously on the fluid. This method was extended to a three-dimensional actuator swept-surface model for a curved-bladed VAWT in Rajagopalan et al. (1995). In both studies, the flow was considered laminar. Fortunato et al. (1995) applied the same turbine modeling and solved the 2D compressible laminar Euler equation with a finite difference method. Shen et al. (2009) used a 2D Navier–Stokes solver, using the  $k - \omega$  shear stress transport turbulence model, to obtain the flow field past a VAWT. They modeled the turbine blades as two rotating actuator surfaces, on which the body forces are distributed. In the above works, mainly power coefficients and forces acting on the blades are quantitatively compared with experimental data, while the wake flow field is only demonstrated qualitatively. Moreover, considering the highly turbulent wake of a VAWT, the application of a numerical turbulence-resolving technique can potentially improve the quality of the wake prediction.

The present work aims at simulating the turbulent wake of a VAWT in a large-eddy simulation (LES) framework by solving the full filtered Navier–Stokes equations in three dimensions, using an actuator swept-surface and an actuator line method to model the turbine effects on the flow and two turbulence modeling techniques to parameterize the subgrid-scale (SGS) stresses. It is worth mentioning that it is the first time that LES has been applied and validated for the simulation of VAWT wakes by using either the actuator swept-surface model (ASSM) or the actuator line model (ALM) techniques. The LES framework and model formulations are presented in Section 2.2. Next, we simulate the wake behind a straight-bladed VAWT for one special case and compare the results with corresponding experimental data. The numerical and experimental setups are described in Section 2.3, and the results are presented in Section 2.4. A summary of

the study is given in Section 2.5.

## 2.2 Large-eddy simulation framework

LES solves the filtered incompressible Navier–Stokes equations, which can be written in rotational form as:

$$\frac{\partial \tilde{u}_i}{\partial x_i} = 0 \quad (2.1)$$

$$\frac{\partial \tilde{u}_i}{\partial t} + \tilde{u}_j \left( \frac{\partial \tilde{u}_i}{\partial x_j} - \frac{\partial \tilde{u}_j}{\partial x_i} \right) = -\frac{\partial \tilde{p}^*}{\partial x_i} + \nu \frac{\partial}{\partial x_j} \frac{\partial \tilde{u}_i}{\partial x_j} - \frac{\partial \tau_{ij}}{\partial x_j} - \frac{f_i}{\rho} + F_p \delta_{i1} \quad (2.2)$$

where the tilde represents a three-dimensional spatial filtering operation at scale  $\tilde{\Delta}$ ,  $\tilde{u}_i$  is the filtered velocity in the  $i$ -direction (with  $i = 1, 2, 3$  corresponding to streamwise ( $x$ ), spanwise ( $y$ ) and vertical ( $z$ ) directions, respectively),  $\tilde{p}^* = \frac{\tilde{p}}{\rho} + \frac{1}{2} \tilde{u}_i \tilde{u}_i$  is the modified kinematic pressure where  $\tilde{p}$  is the filtered pressure,  $\tau_{ij} = \widehat{u_i u_j} - \tilde{u}_i \tilde{u}_j$  is the kinematic SGS stress,  $\nu$  is the fluid kinematic viscosity,  $f_i$  is a body force (per unit volume) used to model the effects of the turbine on the flow,  $F_p$  is an imposed pressure gradient and  $\rho$  is the constant fluid density (following the Boussinesq approximation). For pointwise conservation of kinetic energy, the rotational form of the convective term is used (using the incompressible flow identity) (Orszag and Pao, 1975; Ferziger and Perć, 1996; Albertson and Parlange, 1999). In the next subsections, we discuss the parameterization of SGS stresses ( $\tau_{ij}$ ) and the turbine-induced forces ( $f_i$ ).

### 2.2.1 Turbulence closure models

Two closure models for parameterizing the SGS stresses are considered: the traditional Smagorinsky model and the modulated gradient model.

#### The Smagorinsky model

The traditional Smagorinsky model (Smagorinsky, 1963) for the deviatoric part of the SGS stress is:

$$\tau_{ij} - \frac{1}{3} \delta_{ij} \tau_{kk} = -2(C_S \tilde{\Delta})^2 |\tilde{S}| \tilde{S}_{ij} \quad (2.3)$$

where  $\tilde{S}_{ij} = \frac{1}{2} \left( \frac{\partial \tilde{u}_i}{\partial x_j} + \frac{\partial \tilde{u}_j}{\partial x_i} \right)$  is the resolved strain-rate tensor, whose magnitude is  $|\tilde{S}|$ ;  $\tilde{\Delta}$  is the filter width and  $C_S$  is the Smagorinsky coefficient. As common practice in the application of the Smagorinsky model in the LES of wall-bounded flows, we use the *ad hoc* wall damping function proposed by Mason and Thomson (1992) and commonly used



for the calculation of the Smagorinsky coefficient near walls. Further details regarding the application of the Smagorinsky model in the present code (including the near-wall treatment) can be found, for instance, in [Porté-Agel et al. \(2000\)](#) and [Wan et al. \(2007\)](#).

### The modulated gradient model

The modulated gradient model (MGM), which was proposed by [Lu and Porté-Agel \(2010\)](#), is an alternative to standard eddy-viscosity closure models. In the MGM, the SGS stress tensor is modeled as:

$$\tau_{ij} = 2k_{sgs} \left( \frac{\tilde{G}_{ij}}{\tilde{G}_{kk}} \right) \quad (2.4)$$

If  $\tilde{\Delta}_x$ ,  $\tilde{\Delta}_y$  and  $\tilde{\Delta}_z$  are taken to be filter sizes in the  $x$ -,  $y$ - and  $z$ -directions, then  $\tilde{G}_{ij}$  is defined as:

$$\tilde{G}_{ij} = \frac{\tilde{\Delta}_x^2}{12} \frac{\partial \tilde{u}_i}{\partial x} \frac{\partial \tilde{u}_j}{\partial x} + \frac{\tilde{\Delta}_y^2}{12} \frac{\partial \tilde{u}_i}{\partial y} \frac{\partial \tilde{u}_j}{\partial y} + \frac{\tilde{\Delta}_z^2}{12} \frac{\partial \tilde{u}_i}{\partial z} \frac{\partial \tilde{u}_j}{\partial z} \quad (2.5)$$

To evaluate the SGS kinetic energy,  $k_{sgs}$ , the local equilibrium hypothesis is used, which assumes there is a local balance between SGS energy production,  $P$ , and dissipation,  $\varepsilon$ . These two terms are calculated as:

$$P = -\tau_{ij} \left( \frac{\partial \tilde{u}_i}{\partial x_j} \right) = -\tau_{ij} \tilde{S}_{ij} \quad (2.6)$$

and:

$$\varepsilon = C_\varepsilon \left( \frac{k_{sgs}^{3/2}}{\tilde{\Delta}} \right) \quad (2.7)$$

where the coefficient,  $C_\varepsilon$ , is assumed to have the theoretical value of 1.0 ([Yoshizawa and Horiuti, 1985](#); [Kim and Menon, 1995](#)). Replacing  $\tau_{ij}$  with the expression of Equation (2.4) in Equation (2.6) and equating Equations (2.6) and (2.7), one can solve for  $k_{sgs}$ :

$$k_{sgs} = \left( \frac{4\tilde{\Delta}^2}{C_\varepsilon^2} \right) \left[ - \left( \frac{\tilde{G}_{ij}}{\tilde{G}_{kk}} \right) \tilde{S}_{ij} \right]^2 \quad (2.8)$$

Replacing the above expression for  $k_{sgs}$  in Equation (2.7) gives the following equation for the SGS dissipation,  $\varepsilon$ :

$$\varepsilon = \left( \frac{8\tilde{\Delta}^2}{C_\varepsilon^2} \right) \left[ - \left( \frac{\tilde{G}_{ij}}{\tilde{G}_{kk}} \right) \tilde{S}_{ij} \right]^3 \quad (2.9)$$

To ensure numerical stability and that energy does not transfer locally from unresolved to resolved scales, we use the following clipping procedure:

$$k_{sgs} = \begin{cases} \left( \frac{4\tilde{\Delta}^2}{C_\varepsilon^2} \right) \left[ - \left( \frac{\tilde{G}_{ij}}{\tilde{G}_{kk}} \right) \tilde{S}_{ij} \right]^2 & \text{if } \tilde{G}_{ij}\tilde{S}_{ij} < 0 \\ 0 & \text{otherwise} \end{cases} \quad (2.10)$$

With Equation (2.10), the set of equations for the MGM model is closed, and  $\tau_{ij}$  is fully expressed in terms of resolved variables. The model has been successfully validated in the simulation of a neutral atmospheric boundary layer (Lu and Porté-Agel, 2010, 2013, 2014) and a boundary layer over a 2D block using the immersed boundary method (Cheng and Porté-Agel, 2013).

### 2.2.2 Parameterization of VAWT-induced forces

In this study, two methods are used to model the turbine-induced forces: (a) the actuator swept-surface model (ASSM); and (b) the actuator line model (ALM). Both models are based on blade-element theory, and therefore, they do not require resolving the boundary-layer flow around the turbine blade surfaces, which greatly reduces the computational cost requirements. In the blade-element theory, the turbine blades are divided into  $N$  blade elements that are assumed to behave aerodynamically as two-dimensional airfoils. The aerodynamic forces are determined using the lift and drag characteristics of the airfoil type, as well as the local flow conditions.

Figure 2.1 shows a horizontal cross-section of a blade in Darrieus motion in an arbitrary angular position,  $\theta$ . In this figure,  $\Omega_b$  is the rotor angular velocity,  $R$  is the radius of the rotor,  $u_\infty$  is the unperturbed wind velocity magnitude and  $\mathbf{V}_{local}$  is the local wind velocity vector at the position of the blade. Denoting the radial and tangential components of the local wind velocity in the inertial frame of reference as  $V_{local,n}$  and  $V_{local,s}$ , respectively, the local relative wind velocity vector with respect to the rotating blade can be written as  $\mathbf{V}_{rel} = V_{local,n}\mathbf{e}_n + (V_{local,s} - \Omega_b R)\mathbf{e}_s$ , where  $\mathbf{e}_n$  and  $\mathbf{e}_s$  are unit vectors in the radial and tangential directions, respectively. As is common for VAWTs, the airfoil is considered to be symmetrical, and the chord-line is assumed to be normal to the rotor radius; thus the angle of attack can be written as:

$$\alpha = \arctan\left(\frac{V_{local,n}}{V_{local,s} - \Omega_b R}\right) \quad (2.11)$$

The lift and drag forces (see Figure 2.2) are calculated as:

$$L\mathbf{e}_L + D\mathbf{e}_D = \frac{\rho V_{rel}^2}{2} c \Delta l (C_L \mathbf{e}_L + C_D \mathbf{e}_D) \quad (2.12)$$

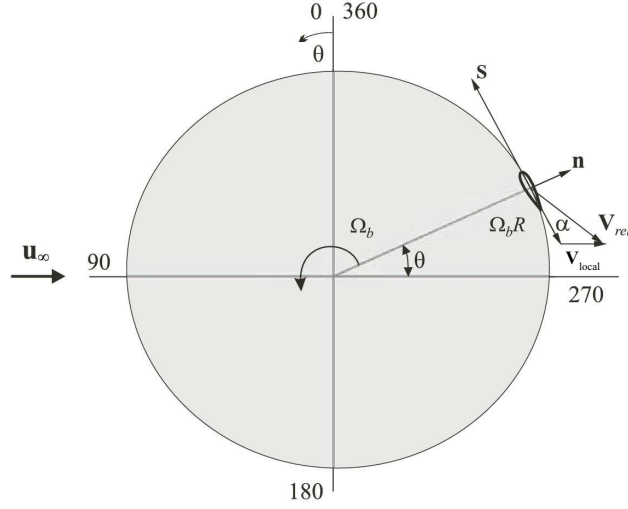


Figure 2.1 – Schematic of a cross-section of a vertical-axis wind turbine (VAWT) blade rotating about the turbine axis (Paraschivoiu, 2002).

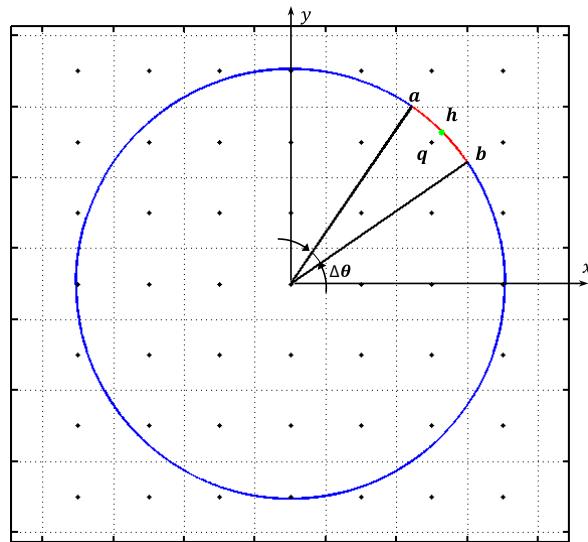
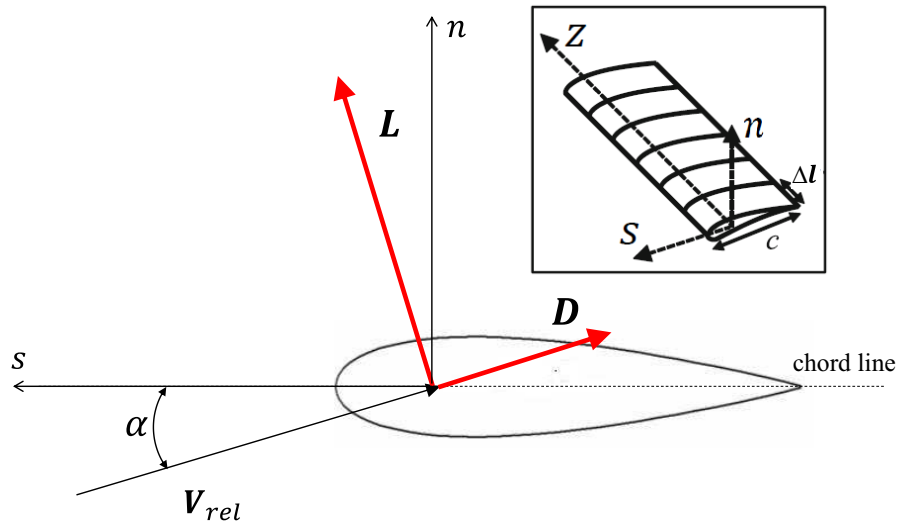
where  $C_L = C_L(\alpha, Re_c)$  and  $C_D = C_D(\alpha, Re_c)$  are the lift and drag coefficients obtained from tabulated airfoil data, respectively,  $Re_c$  is the Reynolds number based on relative velocity and chord length,  $\mathbf{e}_L$  and  $\mathbf{e}_D$  are unit vectors in the lift and drag directions,  $\Delta l$  is the vertical length of the two-dimensional airfoil element and  $c$  is the chord length.

### Actuator swept-surface model

In the ASSM approach, the actuator swept surface is defined as the surface swept by the blades. For example, in the case of a straight-bladed VAWT, this actuator swept surface is an actuator cylinder. We distribute the time-averaged turbine-induced forces on this surface and integrate them over time and space. Figure 2.3 shows a horizontal cross-section of the actuator swept surface in the computational mesh, where the black points are grid points and the dashed lines show the control volumes surrounding them.

For illustration reasons and for the sake of clarity, the size of the grid cells with respect to the diameter of the rotor is shown as being much bigger than in the simulations. The turbine forces are distributed among grid points, whose corresponding control volumes intersect the actuator swept surface. For instance, arc  $\widehat{ab}$  with an angle of  $\Delta\theta$  is located inside the control volume of grid point  $q$  in Figure 2.3. We take the midpoint,  $h$ , as a representative point of this arc and calculate  $\mathbf{V}_{rel}$ ,  $C_L$  and  $C_D$  on this point. The time fraction that each blade spends in arc  $\widehat{ab}$  is  $(\Delta\theta/\Omega_b) \times (\Omega_b/2\pi)$ , and considering the number of blades,  $B$ , the time-averaging weight for the calculated force on this point is  $B\Delta\theta/2\pi$ . Finally, the term,  $f_i/\rho$ , in the Navier–Stokes equations [Equation (2.2)] for a given grid point,  $q$ , is calculated as:

$$\frac{f_1}{\rho}\mathbf{i} + \frac{f_2}{\rho}\mathbf{j} = \left(\frac{V_{rel}^2}{2}\right)(c\Delta l)(B\Delta\theta/2\pi)(\Delta x\Delta y\Delta z)^{-1}(C_L\mathbf{e}_L + C_D\mathbf{e}_D) \quad (2.13)$$



where  $\mathbf{i}$  and  $\mathbf{j}$  are unit vectors in the streamwise and spanwise directions, respectively; and  $\Delta x$ ,  $\Delta y$  and  $\Delta z$  are grid sizes in the  $x$ -,  $y$ - and  $z$ -directions, respectively. At each time-step, this calculation is done for all grid points whose control volumes intersect the actuator swept-surface, and the obtained forces are applied for each of them. It is worth mentioning that if one applies the ASSM approach to HAWTs, it would simply reduce to the conventional actuator disk model.

### Actuator line model

In the ALM, the turbine forces are distributed vertically along lines that represent the blades of the wind turbine. In this model, which was introduced by [Shen and Sørensen \(2002\)](#) and has already been implemented for horizontal-axis wind turbines ([Shen and Sørensen, 2002](#); [Troldborg et al., 2007](#); [Ivanell et al., 2009](#); [Lu and Porté-Agel, 2011](#); [Porté-Agel et al., 2011](#)), there is no need to time-average the forces, because the blades are tracked in each time-step, and the forces are applied only at the physical position of the blades.

First, each grid point whose corresponding control volume encompasses the blade line is identified, and then, the airfoil data and subsequent loading are determined by computing local angles of attack from the movement of the blades and the local flow field. For instance, in [Figure 2.4](#), it can be seen that the blade is located at point  $h$ , which is within the control volume of grid point  $q$ ; hence, theoretically, the term,  $f_i/\rho$ , in the Navier–Stokes equations [[Equation \(2.2\)](#)] should only be assigned to this grid point with the following formula:

$$\frac{f_1}{\rho}\mathbf{i} + \frac{f_2}{\rho}\mathbf{j} = \left(\frac{V_{rel}^2}{2}\right)(c\Delta l)(\Delta x\Delta y\Delta z)^{-1}(C_L\mathbf{e}_L + C_D\mathbf{e}_D) \quad (2.14)$$

By explicitly representing the individual blade motions, the ALM enables us to capture in more detail the complex and unsteady vortical structure of the near-wake flow. Consequently, it is likely to improve the near-wake predictions with respect to the ASSM. The application of the ALM seems particularly crucial for VAWTs, since, in contrast to HAWTs, a blade of a VAWT passes through the wakes generated by other blades, as well as its own wake; this fact makes the ALM approach attractive, because it allows us to study the blade-wake interaction phenomenon more realistically.

## 2.3 Numerical and experimental setups

In this section, the details of the numerical simulations, as well as the experimental setup, with which our results are compared, are presented. We have chosen the experimental study by [Brochier et al. \(1986\)](#) to compare our simulation results with, because it contains

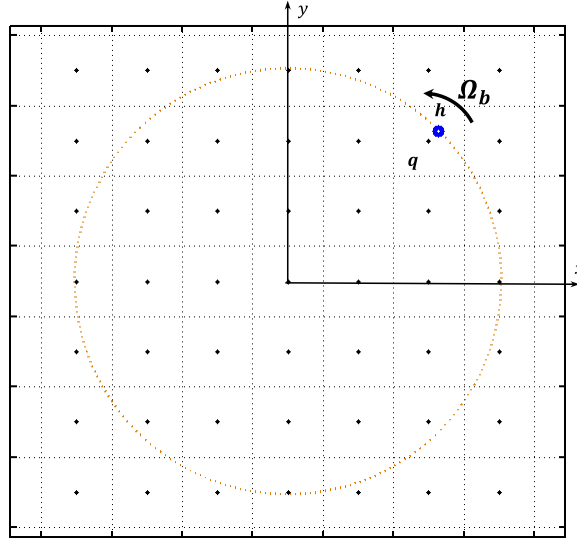


Figure 2.4 – Schematic of a cross-sectional view of the actuator line in the computational mesh.

data on mean velocity and turbulence intensity at several downstream positions in the wake of a model VAWT, even though it was conducted under uniform flow conditions. In fact, in previous VAWT wind tunnel experiments, the turbine has never been placed in a turbulent boundary layer flow, which is the regular flow regime, where full-scale turbines are located. It should be mentioned that more systematic and rigorous experimental studies on VAWT wakes, especially in a turbulent boundary layer flow, are still needed to deepen our understanding of the flow structure and behavior.

### 2.3.1 Experimental setup

In 1986, [Brochier et al. \(1986\)](#) conducted a water channel experiment with a straight-bladed Darrieus wind turbine under controlled-rotation conditions in the Institut de Mécanique et Statistique de la Turbulence (IMST) water channel. Velocity measurements were made using a laser-Doppler velocimeter (LDV), and quantitative profiles of mean velocity and turbulence intensity were provided.

The water channel was vertical, and the driving force of the flow was gravity. The length of the channel in the streamwise direction (vertical direction in the experiment) was 1.5 m, and the cross-section of the channel (normal to the streamwise direction) was a square of a side length of 20 cm (see Figures 2.5 and 2.6). The walls of the channel were transparent (made of plexiglass) to allow for LDV measurements and flow visualization. The model rotor was made up of two straight blades with a chord length of 2 cm. The blades are composed of a NACA 0018 airfoil. The length of the blades was 20 cm, and the diameter of the rotor was 12 cm. The center column of the turbine had a diameter

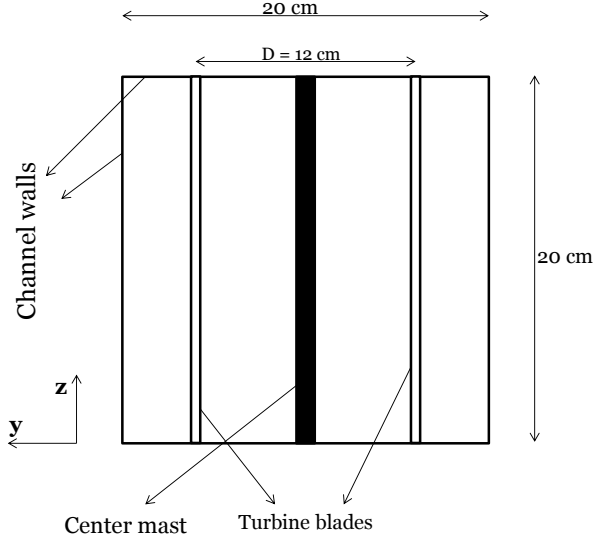


Figure 2.5 – Schematic of y-z view (normal to streamwise direction) of the experimental setup.

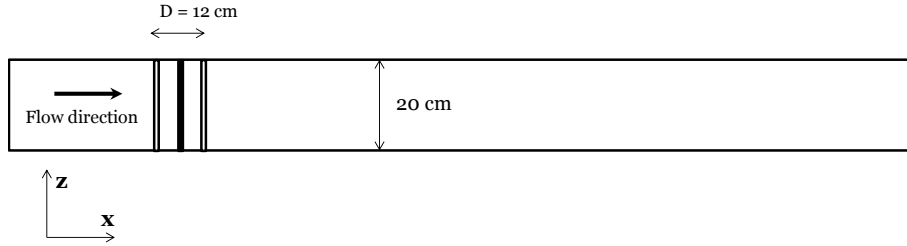


Figure 2.6 – Schematic of x-z view of the experimental setup.

of 1 cm. The measurements were obtained for two tip speed ratios of 2.14 and 3.85. The flow speed in the water channel was 15 cm/s, and the center of the turbine was located 13 chord lengths downstream of the nozzle plane through which the inflow enters the test section.

### 2.3.2 Numerical setup

The LES code is a modified version of the code described by [Albertson and Parlange \(1999\)](#), [Porté-Agel et al. \(2000\)](#) and [Porté-Agel et al. \(2011\)](#). A 3D structured mesh is employed, which has  $N_x$  and  $N_y$  nodes in the  $x$ - and  $y$ -directions, respectively, and  $N_z$  nodes in the  $z$ -direction. The mesh is staggered in the  $z$ -direction; this means the layers in which the vertical component of velocity ( $w$ ) is stored are located halfway between the layers in which all the other main flow variables ( $u, v, p$ ) are stored. The first  $w$ -nodes are located on the  $z = 0$  plane, while the first  $u, v, p$ -nodes are located on the  $z = \frac{\Delta z}{2}$

plane.

To compute the spatial derivatives, a Fourier-based pseudospectral scheme is used in the horizontal directions, and a second-order finite difference method is used in the vertical direction. The governing equations for conservation of momentum are integrated in time with the second-order Adams–Bashforth scheme.

The boundary conditions in the horizontal directions are mathematically periodic. For the bottom and top boundary conditions, the instantaneous surface shear stress is calculated using the Monin–Obukhov similarity theory (Monin and Obukhov, 1954) as a function of the local horizontal velocities at the nearest (to the wall) vertical grid points ( $z = \frac{\Delta z}{2}$  for the bottom wall and  $z = L_z - \frac{\Delta z}{2}$  for the top wall) (see, for instance, (Moeng, 1984; Stoll and Porté-Agel, 2006a; Abkar and Porté-Agel, 2012)).

In the simulations for this case, the same dimensions as in the experiment are used in the  $y$ - and  $z$ -directions, while in the streamwise direction, the domain is taken longer than the channel length, because of the presence of a buffer zone (which will be described later). Thus, the domain dimensions are  $L_x = 200$  cm,  $L_y = 20$  cm (not including the width of the buffer zone for side-walls) and  $L_z = 20$  cm in the streamwise, spanwise and vertical directions, respectively. Regarding the computational mesh, the number of grid points in each of the three directions is  $N_x = 240$ ,  $N_y = 30$  (not including the 4 auxiliary grid points within the buffer zone for side-walls), and  $N_z = 80$ .

Because of the periodic boundary conditions in the  $x$ - and  $y$ -directions, it is implicitly assumed that there are similar turbines upstream, downstream and on both sides of the VAWT under consideration. To eliminate the effects of the upstream turbine wake on the flow and to ensure that we have a uniform inflow (as in the experiment), a buffer zone upstream of the turbine is employed to adjust the flow to an undisturbed uniform inflow condition. The use of this technique, *i.e.*, using an inflow boundary condition in a direction in which the flow variables are discretized using Fourier series, has been shown to be successful in the works of Tseng et al. (2006), Wan and Porté-Agel (2011) and Wu and Porté-Agel (2011).

In the  $y$ -direction, to account for the effect of the side walls, an immersed boundary technique is used. We have set the wall-normal velocity component ( $v$ ) to zero at the location of the walls and have also modified the  $\tau_{xy}$  component of the stress tensor for the grid points, which are located on the side walls, to a value obtained from assuming a logarithmic velocity profile near the side walls. The computational domain is shown in Figure 2.7. In this figure, the location of *Side-wall 2* can be assumed to be at the other end of the  $y$ -direction axis (because of the periodic boundary condition in  $y$ -direction), so that *Side-wall 1* and *Side-wall 2* represent the two side walls of the experiment, which are 20 cm apart.

As discussed in Subsection 2.2.2, for both VAWT models (ASSM and ALM), we need



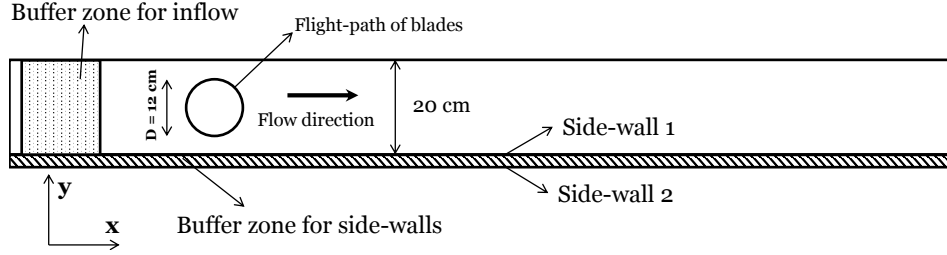


Figure 2.7 – x-y view (normal to the blades) of the computational domain.

tabulated data for lift and drag coefficients. The conventional source for aerodynamic characteristics of symmetrical airfoils, used in VAWTs, is the tabulated data of [Sheldahl and Klimas \(1981\)](#); however, for low Reynolds numbers (which is the case for this experiment), these data show some anomalies for low angles of attack (*i.e.*, the lift coefficient tends to be negative). This data anomaly has been reported by [Shen et al. \(2009\)](#), [Kumar et al. \(2010\)](#) and [Hara et al. \(2011\)](#). As a solution, for low angles of attack, the data of [Kumar et al. \(2010\)](#) is used, and for high angles of attack, the data of [Sheldahl and Klimas \(1981\)](#) is used (for NACA 0018 airfoil). This approach to obtain the lift and drag coefficients has been employed by [Hara et al. \(2011\)](#), as well. To account for the dynamic stall phenomenon and to consider its effect on  $C_L$  and  $C_D$  curves, the modified MIT dynamic stall model is employed ([Noll and Ham, 1983](#)). It is worth mentioning that the dynamic stall phenomenon has a significant effect on the values of the airfoil lift and drag coefficients and, hence, on the turbine performance ([Scheurich and Brown, 2011](#); [Shen et al., 2009](#); [Paraschivoiu, 2002](#)).

The turbine center mast is also modeled as a cylindrical body, which applies a drag force on the fluid. The drag coefficient for the mast is considered to be equal to 1.0. In our simulations, the tip speed ratio (defined as the ratio between the velocity of the blades and the incoming flow velocity) of the turbine is taken to be 3.85 to match that of the experiment. The inflow of the simulation is a uniform flow with a velocity of 15 cm/s and a turbulent intensity of 2.5%, as in the experiment.

## 2.4 Results and discussion

In this section, the results of our simulations for the above-described case are presented for five different combinations of the turbine and SGS models. Three simulations are performed for the ALM (with the MGM and the traditional Smagorinsky model with  $C_S = 0.1$  and  $0.2$ ), and two are done for the ASSM (with the MGM and the traditional Smagorinsky model with  $C_S = 0.1$ ).

Figures [2.8](#) and [2.9](#) show time-averaged streamwise velocity contours on a horizontal plane (top view) at the equator height of the turbine for the actuator swept-surface

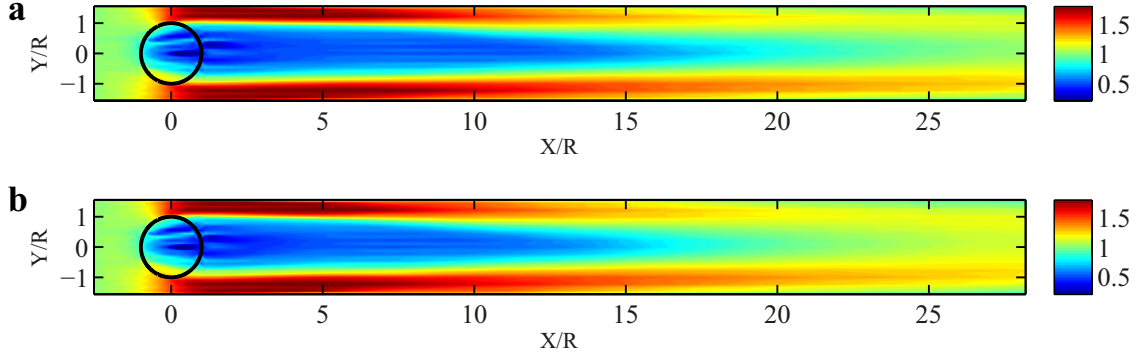


Figure 2.8 – Contours of the normalized mean streamwise velocity,  $\bar{u}/U_0$ , in a horizontal plane at the equator height of the rotor for the actuator swept-surface model (ASSM): (a) Smagorinsky model,  $C_s = 0.1$ ; (b) modulated gradient model (MGM).

and actuator line models, respectively. The black circle in each figure represents the flight path of the turbine blades, which rotate in the counter clockwise direction. It is obvious from the figures that the turbine extracts momentum from the flow, resulting in a low velocity region in its wake. As can be seen in the contours, when we go further downstream of the turbine, the wake recovers by entraining the neighboring high velocity fluid. In these figures, the blockage effect is evident near the channel side-walls (two ends of the  $y$ -axis), where the streamwise velocity magnitude is substantially larger than the incoming flow velocity. This is due to the narrow channel in which the experiment was performed. It should be noted that the presence of the blockage effect affects the recovery rate of the wake, due to the higher velocity gradients at the edge of the wake with respect to unconfined VAWTs. In these velocity maps, the effect of the turbine wake can be seen at downstream distances as large as 20 rotor radii. In all the following figures the streamwise ( $X$ ) and spanwise ( $Y$ ) distances are non-dimensionalized by the rotor radius,  $R$ , and the velocities are normalized by the incoming uniform flow velocity,  $U_0$ .

As can be observed in the figures, the wake of a VAWT is not symmetric in the spanwise direction ( $y$ -direction). This lack of symmetry, which is a typical behavior of VAWT wakes, was also reported by Battisti et al. (2011), Simao Ferreira et al. (2006) and Brochier et al. (1986). We can see that in the region where the streamwise component of the blade velocity is in the opposite direction of the inflow velocity, *i.e.*, upcoming blade region, (positive  $y$  in the figure), the wake is stronger than in the region where these two velocities are in the same direction, *i.e.*, retreating blade region, (negative  $y$  in the figure). The primary reason behind this observation can be found by inspecting the velocity triangles at two typical blade positions in these two regions, as shown in Figure 2.10. In Figure 2.10a, the black circle is the flight path of the blades, on which four typical blade positions are highlighted. From the point of view of an observer who sits on the blades, the blade velocity is a constant vector (with a magnitude of  $R\Omega_b$ ) and the induced flow velocity at the point of the blade is a vector that rotates with the same average frequency as  $\Omega_b$ . The dotted circle in Figure 2.10b is the locus of the endpoint

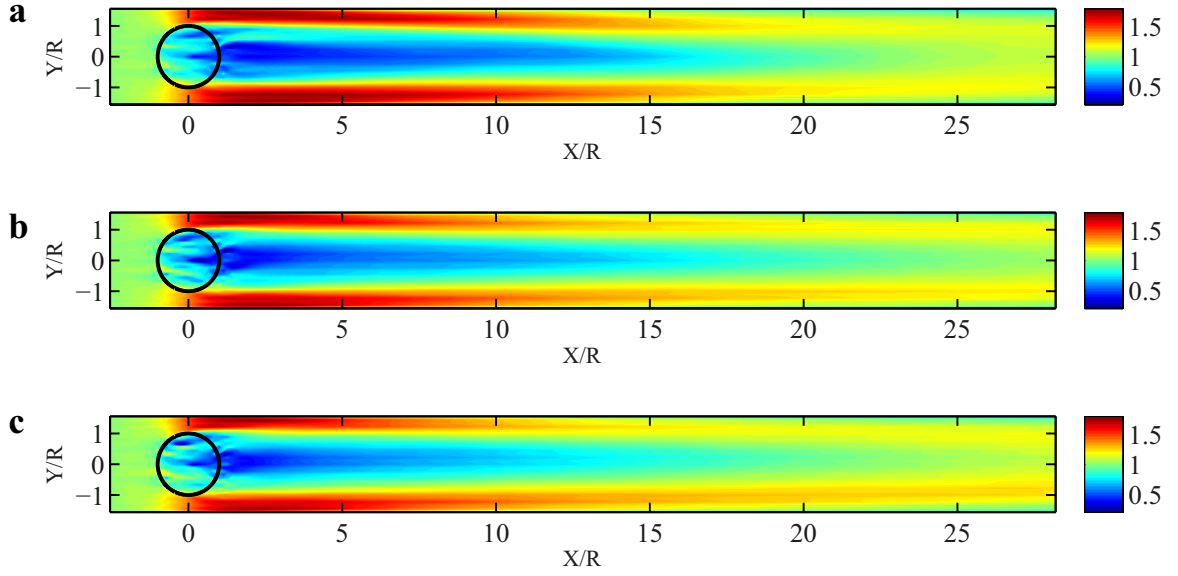


Figure 2.9 – Contours of the normalized mean streamwise velocity,  $\bar{u}/U_0$ , in a horizontal plane at the equator height of the rotor for the actuator line model (ALM): (a) Smagorinsky model,  $C_s = 0.2$ ; (b) Smagorinsky model,  $C_s = 0.1$ ; (c) MGM.

of the induced velocity vector, and the four points that correspond to the highlighted blade positions in Figure 2.10a are illustrated on this circle, as well. It is clear from the velocity triangles of points *a* and *b* that the relative velocity at point *a* is larger than the one at point *b*. As the blade forces are proportional to the square of the relative velocity at the blades, this explains why the velocity deficit is stronger at points *a* and *d* as compared to points *b* and *c*. It is noteworthy that in this analysis, for the sake of simplicity, the induced velocities at all blade positions are considered to be the same; however, it is evident that the induced velocities at points *d* and *c* are smaller than the ones at points *a* and *b*. This is because the downwind half of the rotor is located in the wake of the upwind half.

To obtain a more quantitative understanding of the turbine wake, mean velocity profiles in the spanwise direction and at the equator height of the rotor are plotted in Figure 2.11 for five downstream locations:  $x/R = 2.50, 3.33, 5.0, 8.33, 11.67$ . In these plots, the five combinations of SGS and VAWT models are compared together and also with experimental data. As can be seen in the figure, although both turbine models are able to predict the evolution of the wake in a fairly acceptable manner, the agreement between the ALM results and the experimental data is slightly superior to that of the ASSM results. One important feature that can be observed in this figure (and also in Figures 2.8 and 2.9) is the different ability of each model in predicting the wake recovery rate. Clearly, the wake recovers more slowly in the simulations run with the ASSM than in the ones with the ALM. This relatively slow wake recovery is also observed for the Smagorinsky model with  $C_s = 0.2$ . Since the wake recovery rate is closely

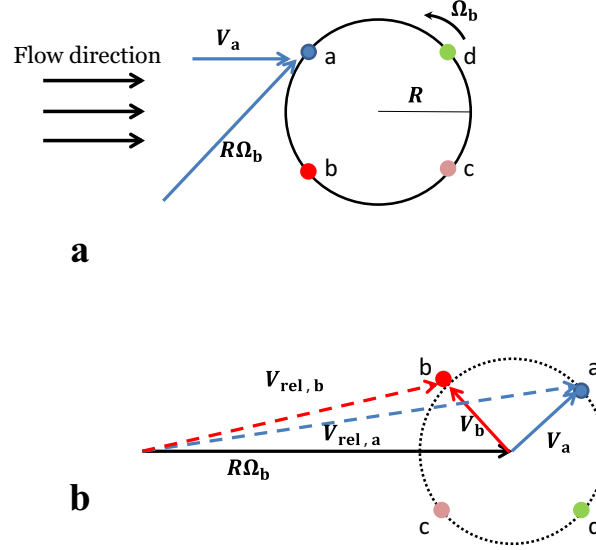


Figure 2.10 – (a) A cross-sectional view of the flight path of the blades (black circle) and four azimuthal blade positions (colored circles); (b) the locus of the endpoint of relative velocity vector (dotted circle) and the corresponding velocity triangles.

correlated to the turbulence intensity level in the flow (e.g., [Wu and Porté-Agel \(2012\)](#) for horizontal-axis wind turbines), it would be insightful to look at how the VAWT generates turbulence in the flow.

Figures 2.12 and 2.13 show contours of the mean streamwise turbulence intensity (TI) in a horizontal plane at the equator height of the rotor for the ASSM and the ALM, respectively. As can be understood readily from these contours, the difference between the ASSM and the ALM is even more pronounced considering the distribution of turbulence intensity. In these figures, one should pay attention to the trends in turbulence intensity distribution in the spanwise and streamwise directions. In the spanwise direction, all of the models qualitatively predict two regions of relatively high turbulence intensity in the vicinity of the wake edges. More details on the spanwise variation of TI will be discussed later. While in the spanwise direction, the same trends exist, in the streamwise direction, the differences between different models are more obvious. As can be seen in the contours, for the ASSM model, we have very low levels of TI in the turbine region and also in the near wake; then, TI gradually increases, until a point where it reaches a maximum ( $x/R$  around 10), and then, it starts to decrease. However, for the ALM, we observe a very high TI in the turbine region and in the near wake, and it decreases as we go downstream. Of these two trends, the one obtained by the ALM is qualitatively in better agreement with the experiments of [Brochier et al. \(1986\)](#). Looking at instantaneous velocity fields (Figure 2.14) can shed more light on the dissimilar effects of the two turbine models on the near wake flow. In Figure 2.14b (the ALM simulation), the wavy and wiggling edges of the wake near the turbine are clearly distinguishable from the rather straight and

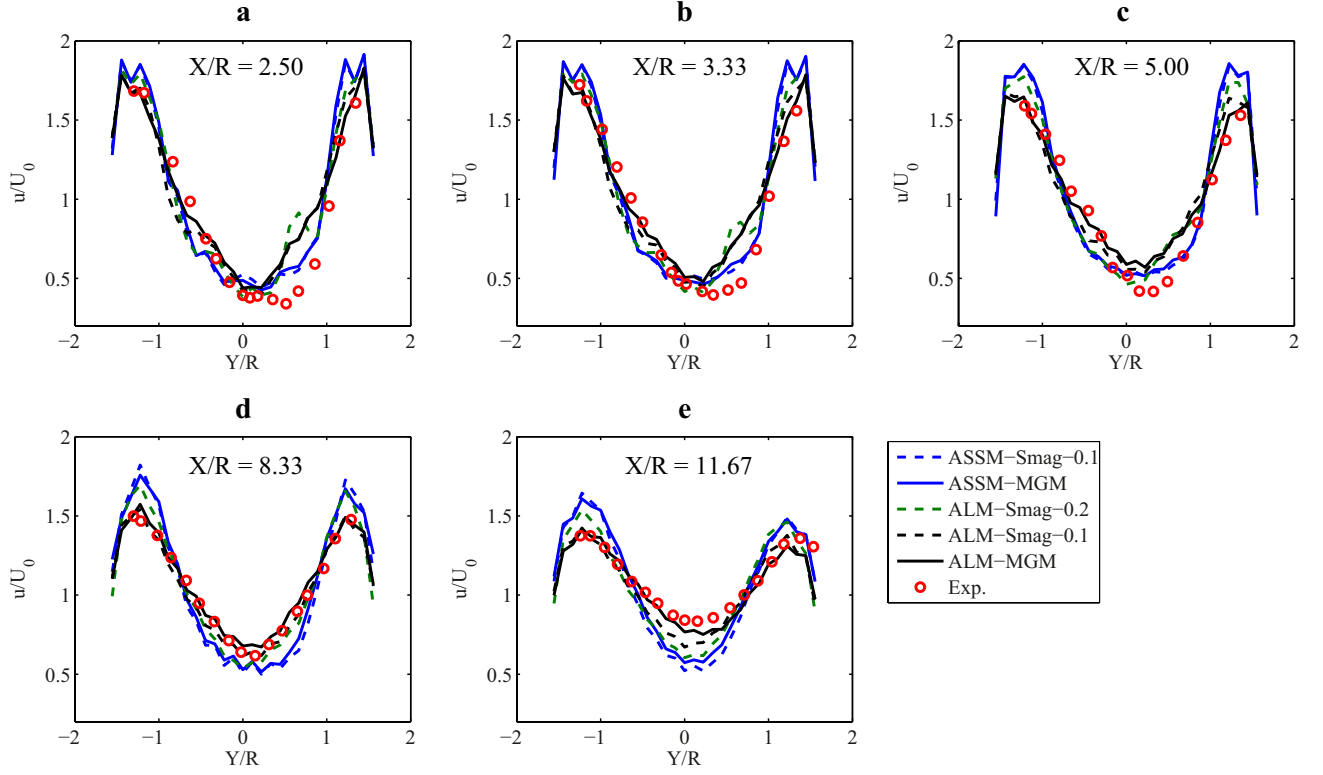


Figure 2.11 – Comparison of the spanwise profiles of the normalized mean streamwise velocity,  $\bar{u}/U_0$ , at different downstream locations: (a)  $x/R = 2.50$ ; (b)  $x/R = 3.33$ ; (c)  $x/R = 5.0$ ; (d)  $x/R = 8.33$ ; (e)  $x/R = 11.67$ . Water channel measurements (red circles), ALM-MGM (solid black line), ALM-Smagorinsky  $C_S = 0.1$  (dashed black line), ALM-Smagorinsky  $C_S = 0.2$  (dashed green line), ASSM-MGM (solid blue line) and ASSM-Smagorinsky  $C_S = 0.1$  (dashed blue line).

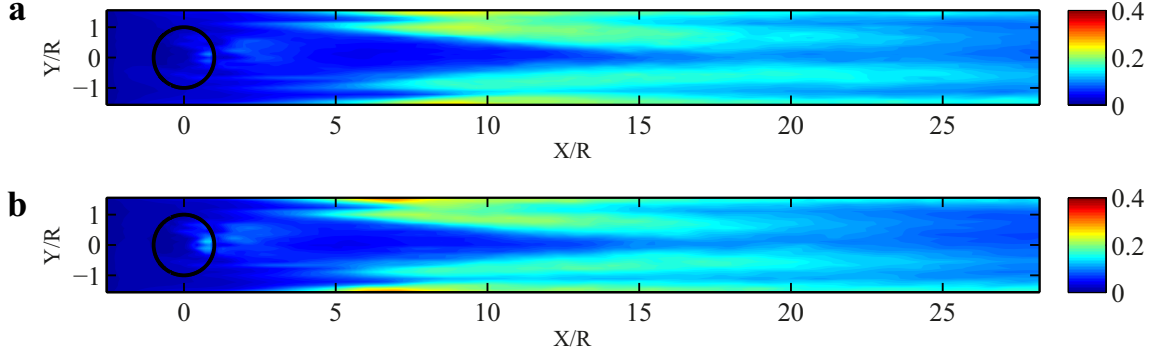


Figure 2.12 – Contours of the normalized mean streamwise turbulence intensity (resolved part),  $\sigma_u/U_0$ , in a horizontal plane at the equator height of the rotor for the ASSM: (a) Smagorinsky model,  $C_s = 0.1$ ; (b) MGM.

smooth wake edges in the same region in the ASSM simulation (Figure 2.14a). One can attribute this difference to the fact that the ALM can better capture the vorticity shed from the blades in the near wake by resolving the motion of individual blades. Another interesting observation that can be made in Figure 2.13 is the existence of four locations on the flight path of the blades around which the TI is maximum. This is likely due to the fact that, in those locations, the magnitude of the forces induced by the flow on the blades is locally maximum.

In Figure 2.15, where the spanwise variation of TI is shown for five downstream locations ( $x/R = 2.50, 3.33, 5.0, 8.33, 11.67$ ), the above-discussed streamwise trends can be seen more clearly for the ASSM (blue lines) and the ALM (black lines). Also seen in this figure is the fact that in the spanwise direction the TI profile has two maxima, which are located on the edges of the wake. This is due to the unsteady shed vorticity from the blades and is reported in the works of Fujisawa and Shibuya (2001), Battisti et al. (2011) and Brochier et al. (1986). Moreover, we see different behavior of the flow turbulence in the spanwise direction for different turbine models. The ASSM overestimates the difference of TI between the retreating-blade half of the domain (negative  $y$ ) and the upcoming-blade half of the domain (positive  $y$ ); in contrast, the TI profiles obtained from the ALM show a better agreement with the measurements. This can be attributed in part to the inability of the ASSM to capture the unsteady-periodic nature of the flow, especially in the near wake region. This is, in contrast to the ALM, that, by resolving the unsteadiness of the blade forces, which improves the prediction of the turbulent behavior of the flow, particularly in the retreating-blade half of the domain.

At this point, we are able to draw conclusions regarding the links between the mean velocity field and the turbulence predictions of different models. First of all, as discussed earlier, the fact that the ASSM predicts lower levels of TI in the near wake leads to slower wake recovery. This can be seen clearly in Figure 2.11e, where the ASSM simulations (blue lines) overestimate the velocity deficit at  $x/R = 11.67$  with respect to the ALM simulations (black lines) and also the measurements. Regarding the SGS models, we can

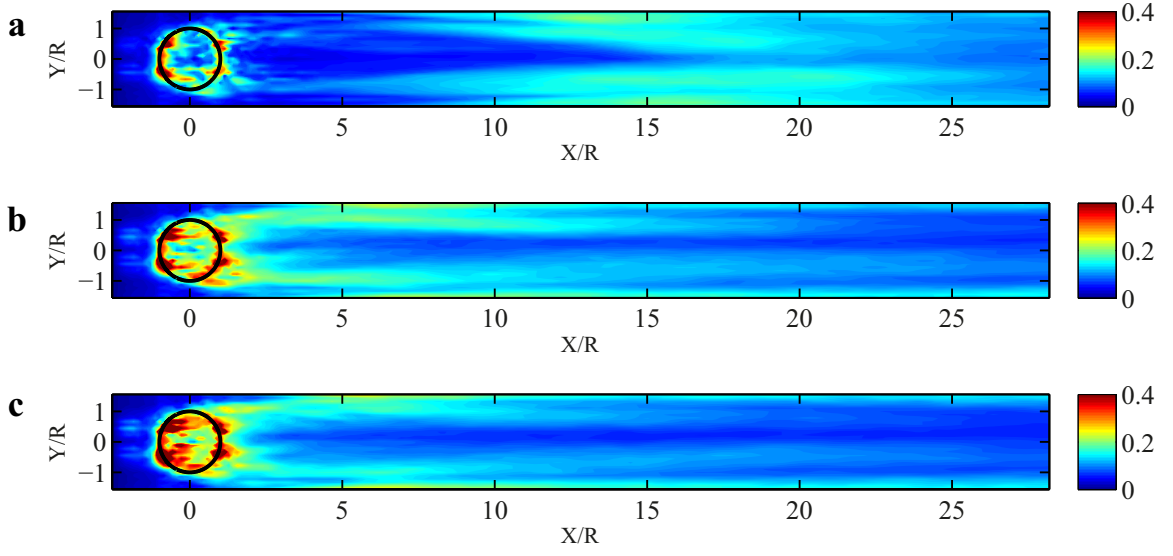


Figure 2.13 – Contours of the normalized mean streamwise turbulence intensity (resolved part),  $\sigma_u/U_0$ , in a horizontal plane at the equator height of the rotor for the ALM: (a) Smagorinsky model,  $Cs = 0.2$ ; (b) Smagorinsky model,  $Cs = 0.1$ ; (c) MGM.

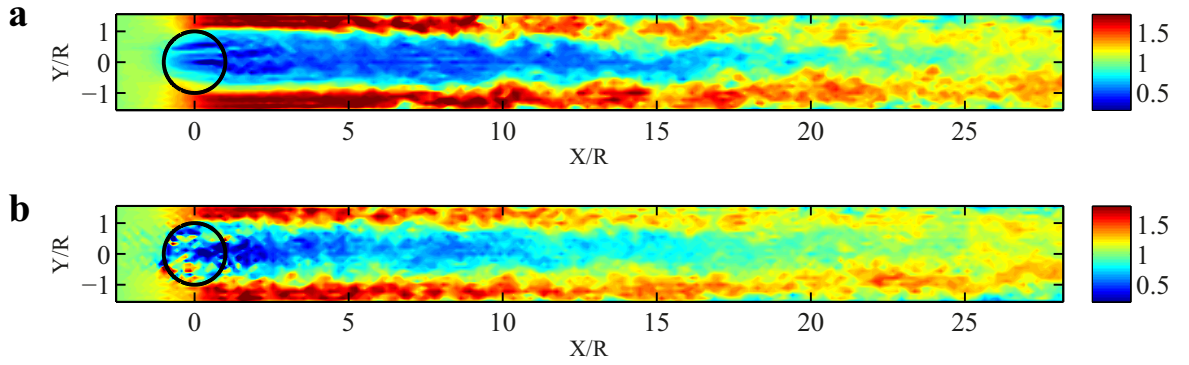


Figure 2.14 – Contours of the normalized instantaneous streamwise velocity,  $u/U_0$ , in a horizontal plane at the equator height of the rotor for the two turbine models: (a) actuator swept surface model; (b) actuator line model. In both contour plots, the MGM is used.



see that, as expected, the high SGS dissipation rate forced by the Smagorinsky model with  $C_S = 0.2$  leads to lower resolved turbulence intensity predictions (Figure 2.15, green line) and, consequently, to a slower wake recovery (Figure 2.11e, green line).

By observing the presented results, one can conclude that the ALM, coupled with the MGM or the Smagorinsky model with  $C_S = 0.1$ , gives the best agreement with the measurements. However, it should be noted that the MGM has a clear advantage over the Smagorinsky model in that it does not need tuning for its model coefficient [Lu and Porté-Agel \(2014\)](#). In contrast, even though the value of  $C_S = 0.1$  gives the best agreement of the Smagorinsky model results with experimental data for this specific problem, the optimum value could be different for other experimental or field conditions. Specifically, this advantage of the MGM is expected to be even more decisive in the case of VAWTs placed in turbulent boundary layer flows, for which the MGM has been shown to provide better predictions (without turbines) than the standard Smagorinsky model ([Lu and Porté-Agel, 2010, 2013, 2014](#)). Another advantage of the MGM over the Smagorinsky model (in fact, all Smagorinsky-based models) is the ability of the MGM to calculate the unresolved part of the TI in addition to its resolved part. This is due to the fact that in the MGM, the complete SGS stress tensor is modeled, which is in contrast to Smagorinsky-based models for which only the deviatoric part of the SGS stress tensor is parameterized. In our case, the unresolved part of the TI was about 5% of the total TI throughout the domain.

To show the grid resolution sensitivity of the computational results, we performed simulations for the ALM-MGM and ASSM-MGM model combinations with three different grid resolutions (the resolution is varied in the horizontal directions, which is critical in capturing the blade motions). It was observed that, for the range of resolutions considered here, resolution had only a small effect on the results. Figure 2.16 shows spanwise plots of mean streamwise velocity and turbulence intensity in the middle downstream position ( $x/R = 5.0$ ) for the three grid resolutions.

## 2.5 Summary

In this study, large-eddy simulation (LES), coupled with a turbine model, is used to investigate the 3D unsteady turbulent wake flow behind a vertical-axis wind turbine (VAWT). To model the SGS momentum fluxes, two SGS models are used, namely, the traditional Smagorinsky model and the modulated gradient model (MGM) ([Lu and Porté-Agel, 2010](#)). To parameterize the effects of a VAWT on the flow, two VAWT models are developed: (a) the actuator swept-surface model (ASSM), in which the time-averaged turbine-induced forces are distributed on a surface swept by the turbine blades, *i.e.*, the actuator swept-surface; and (b) the actuator line model (ALM), in which the instantaneous blade forces are only spatially distributed on lines representing the blades, *i.e.*, the actuator lines. In both models, blade-element theory is used to calculate



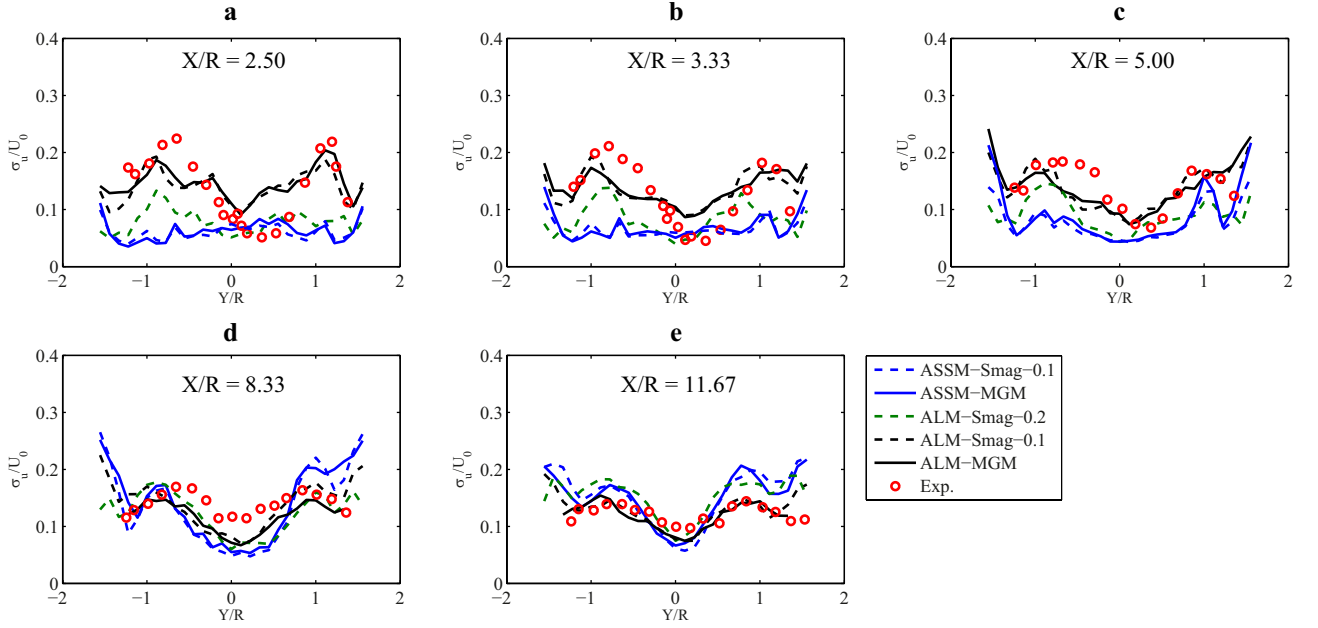


Figure 2.15 – Comparison of spanwise profiles of the normalized mean streamwise turbulence intensity (resolved part),  $\sigma_u/U_0$ , at five downstream locations: (a)  $x/R = 2.50$ ; (b)  $x/R = 3.33$ ; (c)  $x/R = 5.0$ ; (d)  $x/R = 8.33$ ; (e)  $x/R = 11.67$ . Water channel measurements (red circles), ALM-MGM (solid black line), ALM-Smagorinsky  $C_S = 0.1$  (dashed black line), ALM-Smagorinsky  $C_S = 0.2$  (dashed green line), ASSM-MGM (solid blue line) and ASSM-Smagorinsky  $C_S = 0.1$  (dashed blue line).

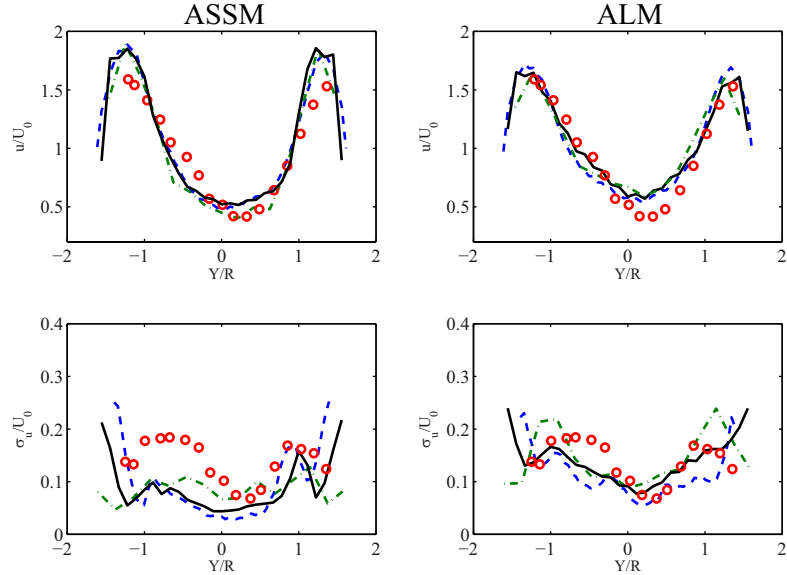


Figure 2.16 – The effect of the grid resolution on the spanwise profiles of the normalized mean streamwise velocity and mean streamwise turbulence intensity (resolved part) for the ASSM (left) and the ALM (right) simulations at  $x/R = 5.0$ . Water channel measurements (red circles), 60 × 400 × 80 (dashed blue line), 30 × 240 × 80 (solid black line) and 15 × 120 × 80 (dash-dotted green line).

the lift and drag forces acting on the blades. This is the first time that LES has been applied and validated for the simulation of VAWT wakes by using either the ASSM or the ALM technique. The results are compared with flow field measurements in the wake of a model straight-bladed VAWT, carried out in the Institute de Mécanique et Statistique de la Turbulence (IMST) water channel.

Different combinations of VAWT and SGS models are tested and compared against each other, and a fairly good agreement with the experimental data is observed. It is found out that, in general, the results obtained with the ALM agree better with the measurements and also with the physics of the flow than the ones from the ASSM. The inherent advantage of the ALM in resolving the periodic location of the blade forces allows one to capture the unsteady-periodic nature of the wake and, thus, the blade-wake interaction, which is a characteristic of the aerodynamics of a VAWT rotor. The slight superiority of the ALM over the ASSM was shown quantitatively in the better prediction of the turbulence intensity and, consequently, of the wake recovery, which is very important in designing and optimizing potential VAWT arrays. However, it is worth bearing in mind that the ASSM could potentially be the preferable turbine model in simulations of VAWT wind farms, due to its lower grid resolution requirement. Regarding the SGS models, although both tested models showed reasonable turbulence modeling capabilities, it should be noted that the traditional Smagorinsky model needs its model coefficient to be optimized, depending on the local flow characteristics, while the MGM proved that it can, with its theoretically-determined model coefficient, capture the mean flow and turbulent characteristics of a VAWT wake. This advantage of the MGM is expected to be even more decisive in the case of VAWTs placed in turbulent boundary layer flows, where the MGM has previously been shown to have a superior prediction ability (without turbines) compared with the standard Smagorinsky model (Lu and Porté-Agel, 2010, 2013, 2014).

Potential sources of the observed discrepancies between simulation results and measurement data can be summarized as: (a) inherent limitations of the proposed numerical model; (b) inherent measurement errors in the experiment; and (c) inaccuracies in the tabulated airfoil data. It is worth noting that, in effect, the final results are considerably dependent on the lift and drag coefficient curves as a function of the angle of attack.

As mentioned by Paraschivoiu (2002), the most important shortcoming that VAWTs are suffering from, at present, is that they have not benefited from research and development as much as HAWTs. Therefore, more rigorous and systematic studies on different technical aspects of VAWTs are still needed. For the aerodynamic aspect, high-resolution wind tunnel measurements of the flow field in the wake of VAWTs placed in a boundary layer flow would be highly valuable. Furthermore, for the numerical simulation of the wake, the authors believe that, if one lesson has to be learned from the development of HAWTs, it is that the most feasible and practical way of taking into account the effects of the turbine on the flow is through using immersed-body-force approaches, such as an actuator

swept surface, actuator line or rotating actuator surface. With these techniques, the simulation, optimization and design of VAWT wind farms will be an attainable and realizable objective in the near future.



# 3 A large-eddy simulation study of vertical axis wind turbine wakes in the atmospheric boundary layer<sup>1</sup>

## Abstract

In a future sustainable energy vision, in which diversified conversion of renewable energies is essential, vertical axis wind turbines (VAWTs) exhibit some potential as a reliable means of wind energy extraction alongside conventional horizontal axis wind turbines (HAWTs). Nevertheless, there is currently a relative shortage of scientific, academic and technical investigations of VAWTs as compared to HAWTs. Having this in mind, in this work, we aim to, for the first time, study the wake of a single VAWT placed in the atmospheric boundary layer using large-eddy simulation (LES). To do this, we use a previously-validated LES framework in which an actuator line model (ALM) is incorporated. First, for a typical three- and straight-bladed 1-MW VAWT design, the variation of the power coefficient with both the chord length of the blades and the tip-speed ratio is analyzed by performing 117 simulations using LES-ALM. The optimum combination of solidity (defined as  $Nc/R$ , where  $N$  is the number of blades,  $c$  is the chord length and  $R$  is the rotor radius) and tip-speed ratio is found to be 0.18 and 4.5, respectively. Subsequently, the wake of a VAWT with these optimum specifications is thoroughly examined by showing different relevant mean and turbulence wake flow statistics. It is found that for this case, the maximum velocity deficit at the equator height of the turbine occurs 2.7 rotor diameters downstream of the center of the turbine, and only after that point, the wake starts to recover. Moreover, it is observed that the maximum turbulence intensity (TI) at the equator height of the turbine occurs at a distance of about 3.8 rotor diameters downstream of the turbine. As we move towards

---

<sup>1</sup>The contents of this chapter are published in: Shamsoddin, S. and Porté-Agel, F. A Large-Eddy Simulation Study of Vertical Axis Wind Turbine Wakes in the Atmospheric Boundary Layer. *Energies*, 9(5):366, 2016.

the upper and lower edges of the turbine, the maximum TI (at a certain height) increases, and its location moves relatively closer to the turbine. Furthermore, whereas both TI and turbulent momentum flux fields show clear vertical asymmetries (with larger magnitudes at the upper wake edge compared to the ones at the lower edge), only slight lateral asymmetries were observed at the optimum tip-speed ratio for which the simulations were performed.

### 3.1 Introduction

Vertical axis wind turbines (VAWTs) offer some advantages over their horizontal axis counterparts and are being considered as a viable alternative to horizontal axis wind turbines (HAWTs). The research on VAWT technology started in the 1970s, and while the main focus of the performed studies has been on the overall turbine performance (quantities such as power and torque) and on the mechanical loading on the blades, relatively few studies have attempted to analyze the wake of a VAWT (for a comprehensive and chronological review of the studies on VAWTs before 2000, see [Paraschivoiu \(2002\)](#) (Chapters 4–7)). Having a thorough understanding of VAWT wakes is especially crucial in designing VAWT wind farms, where downstream turbines can potentially be located in the wake of upstream ones, and consequently, the performance of the whole wind farm could be significantly affected by the wake flow characteristics. Among the experimental works investigating VAWT wakes, one can find a relatively larger number of studies that have focused only on the near wake region (e.g., ([Tescione et al., 2013](#); [Battisti et al., 2011](#); [Bachant and Wosnik, 2015](#); [Araya and Dabiri, 2015](#))), compared to those that have considered also the far wake region (e.g., ([Brochier et al., 1986](#); [Rolin and Porté-Agel, 2015](#); [Ryan et al., 2016](#))). Nevertheless, from a wind farm design point of view, it is the far wake behavior of the flow that has more relevance and importance.

In the numerical flow simulation domain, the studies performed on the flow through VAWTs can be divided into two main categories: (1) the simulations in which the blades of the turbine (and consequently, the boundary layer around them) are resolved; and (2) the simulations in which the blades are modeled by an actuator-type technique, which uses immersed-body forces to take into account the effects of the blades on the flow. While the first approach (for instance, the work of [Castelli et al. \(2011\)](#)) can be highly valuable to calculate the loading on the blades and the flow characteristics inside the rotor and in the near wake, to simulate the far wake of VAWTs and especially VAWT wind farms, the second approach is deemed to be more feasible and attainable ([Pierce et al., 2013](#); [Shamsoddin and Porté-Agel, 2014](#)). The use of actuator-type techniques for VAWTs dates back to the 1980s, when [Rajagopalan and Fanucci \(1985\)](#) for the first time modeled the VAWT rotor by a porous surface, swept by the blades, on which time-averaged blade forces are distributed and continuously act on the flow (which has also been called the actuator swept-surface model ([Shamsoddin and Porté-Agel, 2014](#))). An extension of this work to three dimensions was made by [Rajagopalan et al. \(1995\)](#). Later on, [Shen et al.](#)

(2009) introduced the actuator surface model and employed it to obtain the flow field past a VAWT in two dimensions. More recently, Shamsoddin and Porté-Agel (2014) used large-eddy simulation (LES) coupled with both the actuator-swept surface model (ASSM) and the actuator line model (ALM) to simulate the flow through a VAWT placed in a water channel and compared the resulting wake profiles with experimental data.

Acknowledging the fact that any given real VAWT is likely to be working in the atmospheric boundary layer (ABL) and benefiting from the helpful experience gained from the extensive research on HAWT wakes, it is imperative to study in detail the characteristics of the wake of VAWTs placed in boundary layer flows, especially if VAWT farms are to be envisaged as a viable source of power in future energy outlooks. Having this in mind, the present study is a step in this direction and attempts to use a previously-validated LES framework, in which an actuator line model is incorporated, to analyze the wake of a typical straight-bladed VAWT in a relatively long downstream range. Moreover, before the wake study, using the same framework, the power production performance of the VAWT for different combinations of blade chord lengths and tip-speed ratios is studied to find the optimum combination for the aforementioned wake analysis. To the best knowledge of the authors, this study is the first attempt to characterize the wake of a VAWT in ABL using LES.

The LES framework is presented in Section 3.2, and the numerical setups and techniques are described in Section 3.3. Next, the results for both the power production parametric study and the wake analysis are presented and discussed in Section 3.4. Finally, a summary of the study is given in Section 3.5.

## 3.2 Large-eddy simulation framework

In the LES framework used for the simulations of this paper, the filtered incompressible Navier–Stokes equations (for a neutrally-stratified ABL) are solved. These equations can be written in rotational form as:

$$\frac{\partial \tilde{u}_i}{\partial x_i} = 0 \quad (3.1)$$

$$\frac{\partial \tilde{u}_i}{\partial t} + \tilde{u}_j \left( \frac{\partial \tilde{u}_i}{\partial x_j} - \frac{\partial \tilde{u}_j}{\partial x_i} \right) = -\frac{\partial \tilde{p}^*}{\partial x_i} - \frac{\partial \tau_{ij}}{\partial x_j} - \frac{f_i}{\rho} + F_p \delta_{i1} \quad (3.2)$$

where the tilde represents a three-dimensional spatial filtering operation at scale  $\tilde{\Delta}$ ,  $\tilde{u}_i$  is the filtered velocity in the  $i$ -th direction (with  $i = 1, 2, 3$  corresponding to the streamwise ( $x$ ), spanwise ( $y$ ) and vertical ( $z$ ) directions, respectively),  $\tilde{p}^* = \frac{\tilde{p}}{\rho} + \frac{1}{2} \tilde{u}_i \tilde{u}_i$  is the modified kinematic pressure where  $\tilde{p}$  is the filtered pressure,  $\tau_{ij} = \widetilde{u_i u_j} - \tilde{u}_i \tilde{u}_j$  is the kinematic

subgrid-scale (SGS) stress,  $f_i$  is a body force (per unit volume) representing the force exerted by the flow on the turbine blades (observe the minus sign),  $F_p$  is an imposed pressure gradient and  $\rho$  is the constant fluid density. In this paper,  $u$ ,  $v$  and  $w$  notations are also used for the  $u_1$ ,  $u_2$  and  $u_3$  velocity components, respectively. Regarding the parametrization of the SGS stresses, in these simulations, the Lagrangian scale-dependent dynamic model (Stoll and Porté-Agel, 2006b) is used.

To parameterize the VAWT-induced forces on the flow (*i.e.*, to model the term  $f_i/\rho$  in Equation (3.2)), an actuator line model is used. According to the ALM, each blade of the turbine is represented by an actuator line on which the turbine forces, calculated based on the blade-element theory, are distributed. This method has the advantage of being capable of tracking the rotation of the blades at each time step. For a detailed explanation of the application of the ALM for VAWTs, the reader can refer to Shamsoddin and Porté-Agel (2014) (Section 2.2).

### 3.3 Numerical setup

In this section, the techniques used to numerically solve Equations (3.1) and (3.2), as well as the configuration of the performed numerical experiments are presented.

The LES code, which is used to realize the simulations in this study, is a modified version of the code described by Albertson and Parlange (1999), Porté-Agel et al. (2000) and Porté-Agel et al. (2011). The computational mesh is a 3D structured one, which has  $N_x$ ,  $N_y$  and  $N_z$  nodes in the  $x$ ,  $y$  and  $z$  directions, respectively. The mesh is staggered in the  $z$  direction in a way that the layers in which the vertical component of velocity ( $w$ ) is stored are located halfway between the layers in which all of the other main flow variables ( $u, v, p$ ) are stored. The first  $w$ -nodes are located on the  $z = 0$  plane, while the first  $uvp$ -nodes are located on the  $z = \Delta z/2$  plane.

To compute the spatial derivatives, a Fourier-based pseudospectral scheme is used in the horizontal directions, and a second-order finite difference method is used in the vertical direction. The governing equations for conservation of momentum are integrated in time with the second-order Adams–Bashforth scheme.

The pressure term in Equation (3.2) is not a thermodynamic quantity, and it only serves to have a divergence-free (*i.e.*, incompressible) velocity field. Therefore, by taking the divergence of the momentum Equation (3.2) and using the continuity Equation (3.1), we can solve the arising Poisson equation for the modified pressure,  $\tilde{p}^*$ , using the spectral method in the horizontal directions and finite differences in the vertical direction.

The boundary conditions (BCs) in the horizontal directions are mathematically (and implicitly through using the spectral method) periodic. For the bottom BC, the instantaneous surface shear stress is calculated using the Monin–Obukhov similarity theory



(Monin and Obukhov, 1954) as a function of the local horizontal velocities at the nearest (to the surface) vertical grid points ( $z = \Delta z/2$ ) (see, for instance, Moeng (1984); Stoll and Porté-Agel (2006a)). For the upper boundary, an impermeable stress-free BC is applied, *i.e.*,  $\partial \tilde{u}_1 / \partial z = \partial \tilde{u}_2 / \partial z = \tilde{u}_3 = 0$ .

Since the study of the flow through a single turbine is desired, we need to numerically enforce an inflow BC to practically override the implicitly-imposed periodic BC in the  $x$  direction. For this purpose, a buffer zone upstream of the VAWT is employed to adjust the flow to an undisturbed ABL inflow condition. The inflow field is obtained by saving the instantaneous velocity components in a specific  $y$ - $z$  plane in a similar precursory simulation of ABL over a flat terrain (with the same surface roughness) with no turbine on it. The use of this technique, *i.e.*, using an inflow boundary condition in a direction in which the flow variables are discretized using Fourier series, has been shown to be successful in the works of Tseng et al. (2006), Wu and Porté-Agel (2011) and Porté-Agel et al. (2013).

To implement the ALM, values of the airfoil's lift and drag coefficients ( $C_L$  and  $C_D$ , respectively) as a function of Reynolds number ( $Re$ ) and angle of attack ( $\alpha$ ) (*i.e.*,  $C_{L(D)} = f(Re, \alpha)$ ) are needed. This information was obtained from the tabulated data provided by Sheldahl and Klimas (1981). Moreover, the dynamic stall phenomenon, which is known to have a considerable effect on the performance of VAWTs (Shen et al., 2009; Scheurich and Brown, 2011), is accounted for using the modified MIT model (Noll and Ham, 1983). A detailed explanation of the implementation of the dynamic stall model is provided in Appendix A.

Figures 3.1 and 3.2 show the geometrical specifications of the VAWT and the computational domain in which it is placed. The turbine rotor is made of three straight blades and has a diameter ( $D$ ) of 50 m and a height of 100 m. The blades' airfoil is selected to be the symmetrical NACA 0018 airfoil, which is widely used for VAWTs. It is attempted that these chosen turbine specifications are representative of those of real VAWTs with a nominal capacity of 1 MW (this fact will be reaffirmed by the results of the simulations). For example, a curve-bladed (or  $\Phi$ -rotor) VAWT of similar size and capacity (96 m high and an equatorial diameter of 64 m) with two NACA 0018 blades of a 2.4-m chord length was operational as part of Project Éole in Cap Chat, Quebec, Canada, between 1987 and 1993 (Templin and Rangi, 1983). This turbine was designed to deliver a maximum power of about 4 MW (at high winds and high rotational speeds), and its maximum measured power of about 1.3 MW is hitherto one of the greatest measured power outputs for a VAWT ((Paraschivoiu, 2002) Section 7.3.4).

The buffer zone occupies about 12% of the domain length. The domain dimensions are  $L_x = 1200$  m ( $=24D$ ),  $L_y = 600$  m ( $=12D$ ) and  $L_z = 400$  m ( $=8D$ ) in the streamwise, spanwise and vertical directions, respectively. The blockage ratio of the turbine in the computational domain is 2.08%, which is well below the value of 10%, which is reported

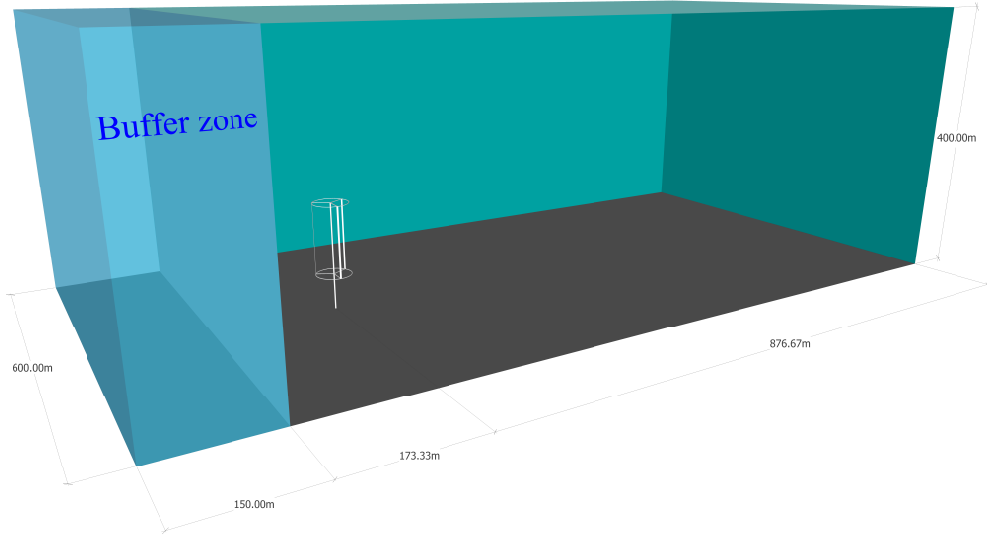


Figure 3.1 – Schematic of the computational domain, including the simulated VAWT.

by [Chen and Liou \(2011\)](#) as the threshold below which it is acceptable to neglect the blockage effect. Regarding the computational mesh, the number of grid points in each of the three directions is  $N_x = 360$ ,  $N_y = 180$  and  $N_z = 240$ . The code has been shown to yield grid-independent results provided that a minimum number of grid points is used to resolve the rotor ([Shamsoddin and Porté-Agel, 2014](#)). In this study, we chose a resolution (15 points in each horizontal direction covering the rotor area) that falls within the grid-independent range. The time resolution for all of the simulations is 0.0155 s. For the wake study simulation, the total physical time of the simulation is 90.4 min, and for mean velocity and turbulence statistics results, we have time-averaged the quantities in question over the final 77.5-min time span.

Figure 3.3 shows mean and standard deviation profiles of the inflow streamwise velocity. As mentioned earlier, the inflow field is generated by using the flow field of a precursory simulation of the neutrally-stratified ABL on a flat terrain. The surface roughness,  $z_o$ , and the friction velocity,  $u_*$ , used in this precursory simulation are 0.1 m and 0.52 m/s, respectively. In Figure 3.3a, it can be seen that the mean streamwise velocity profile approximately follows the log law in the surface layer. The mean inflow streamwise velocity at the equator height of the turbine (*i.e.*,  $z = 100$  m in this case),  $U_{eq}$ , and the turbulence intensity of the inflow at the same height ( $\sigma_u/U_{eq}$ ) are 9.6 m/s and 8.3%, respectively. It should be noted that the above-mentioned inflow field is used for all of the simulations of this paper (*i.e.*, both Subsections 3.4.1 and 3.4.2).

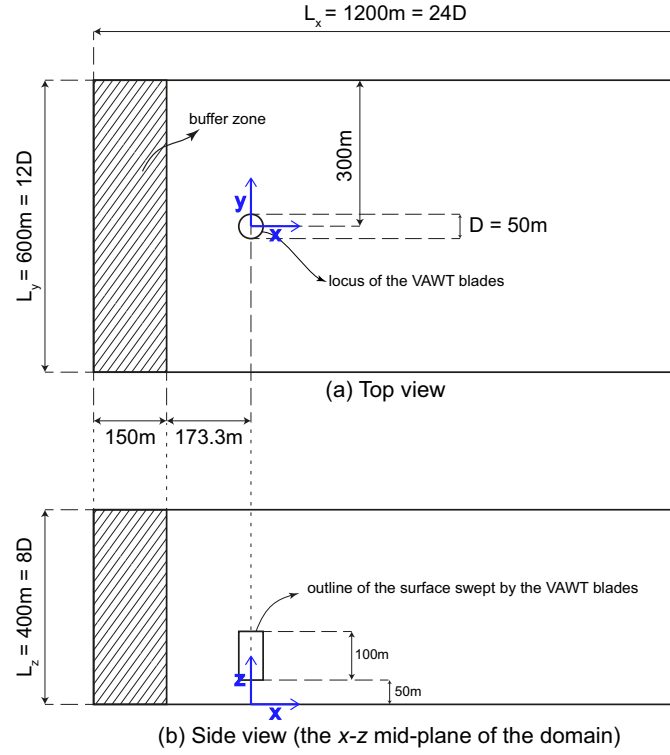


Figure 3.2 – Plane views of the geometrical configuration of the simulations: (a) top view of the domain; (b) side view of the domain, seen in the  $x$ - $z$  mid-plane of the domain.

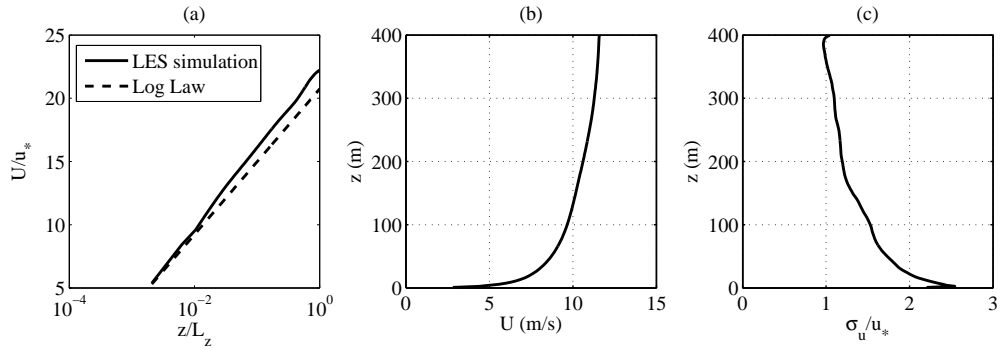


Figure 3.3 – Inflow characteristics: (a) vertical profile of the mean streamwise velocity compared to a log-law profile (horizontal axis in logarithmic scale); (b) vertical profile of the mean streamwise velocity (linear scale); (c) vertical profile of the standard deviation of the streamwise velocity.

## 3.4 Results and discussion

In this section, the results of the simulations are presented and discussed. First, we examine the turbine’s energy-extraction performance, and next, we study the wake flow of a VAWT placed in the ABL.

### 3.4.1 Turbine performance and power extraction

In this subsection, we are interested in how the power production of the turbine is affected by different combinations of tip-speed ratio,  $TSR$ , and chord length,  $c$ . For this purpose, 117 simulations have been performed to obtain the power coefficient,  $C_P$ , of the turbine as a function of both  $TSR$  and  $c$ , *i.e.*,  $C_P(TSR, c)$ . Figure 3.4 shows how  $C_P$  varies with different values of  $TSR$  and  $c$ . Figure 3.4a is generated with a resolution of 0.5 m for chord length and 0.5 for  $TSR$ . It can be seen that, as we increase the chord length, the useful  $TSR$  range (a range in which  $C_P$  is higher than a certain value) decreases. Moreover, the figure shows that the maximum power coefficient of the turbine occurs for a  $TSR$  of 4.5 and a chord length of 1.5 m (which corresponds to a solidity of  $Nc/R = 0.18$ , where  $N$  is the number of blades and  $R$  is the rotor radius). This combination results in a power extraction,  $P$ , of 1.3 MW and a  $C_P$  of 0.47 ( $C_P$  is defined as  $C_P = P/(0.5\rho DHU_{eq}^3)$ , where  $\rho$  is the fluid density and considered equal to 1.225 kg/m<sup>3</sup>,  $D$  is the rotor diameter and  $H$  is the rotor height).

### 3.4.2 VAWT wake

In this subsection, we have picked the optimum combination of  $TSR$  and chord length ( $TSR = 4.5$  and  $c = 1.5$  m) for the VAWT rotor and studied the wake flow behind it. Figure 3.5 shows the instantaneous streamwise velocity field of the flow in three different orthogonal planes. In all of the following figures in this section containing contour plots, the black circles and rectangles represent the outline of the locus of the blades. The sense of the rotation of the turbine blades is counterclockwise when seen from above. The wake of the VAWT and the highly turbulent nature of the flow are obvious in this figure and in the Videos S1 and S2 included in the Supplementary Material. It should be noted that the average thrust coefficient of the turbine (defined as  $C_T = T/(0.5\rho DHU_{eq}^2)$ , where  $T$  is the total thrust force of the turbine in the  $x$  direction) in this case is found to be 0.8.

Figures 3.6 and 3.7 show contour plots of the mean streamwise velocity in the  $x$ - $y$  plane at the equator height of the turbine and in the  $x$ - $z$  mid-plane of the turbine. It can be seen in these figures that it takes a long distance for the wake to recover; at a downwind distance as large as 14 rotor diameters, the wake center velocity reaches only 85% of the incoming velocity. Moreover, Figure 3.8 shows the mean velocity contours in six  $y$ - $z$  planes downstream of the turbine. In all of these figures (Figures 3.6–3.8), one can observe how the wake recovers in the streamwise direction (after a certain distance) and

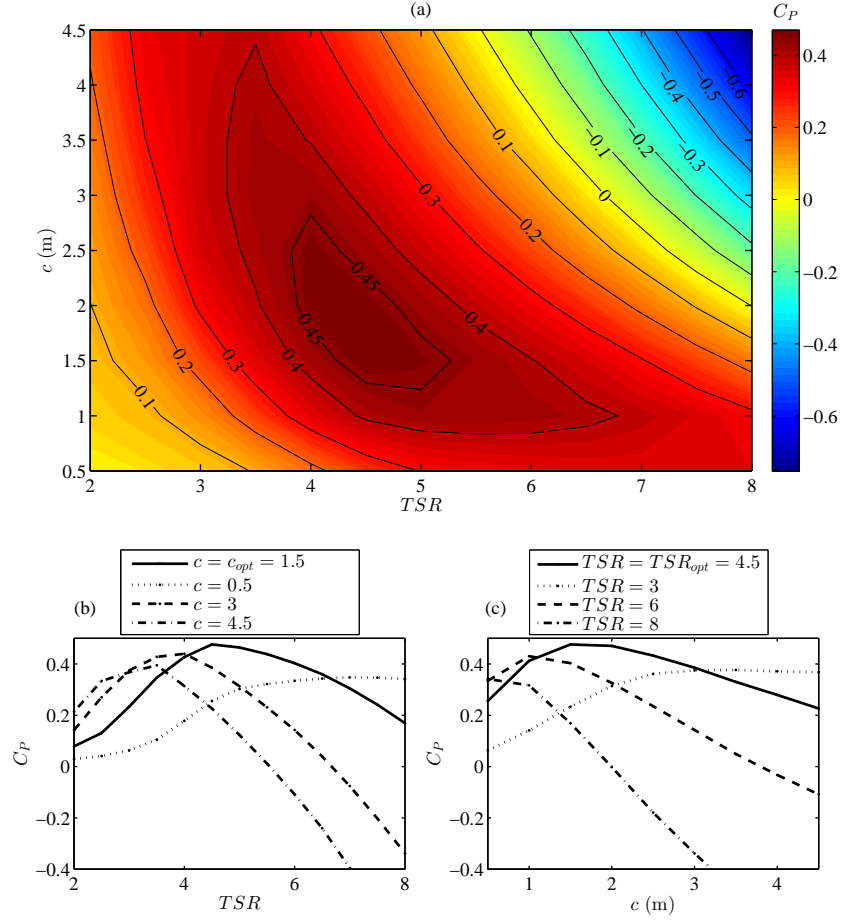


Figure 3.4 – Variation of the power coefficient of a three-bladed VAWT with tip-speed ratio ( $TSR$ ) and chord length: (a)  $C_P$  as a function of both  $TSR$  and chord length; (b)  $C_P$  as a function of  $TSR$  for four different chord lengths; (c)  $C_P$  as a function of chord length for four different  $TSR$  values.

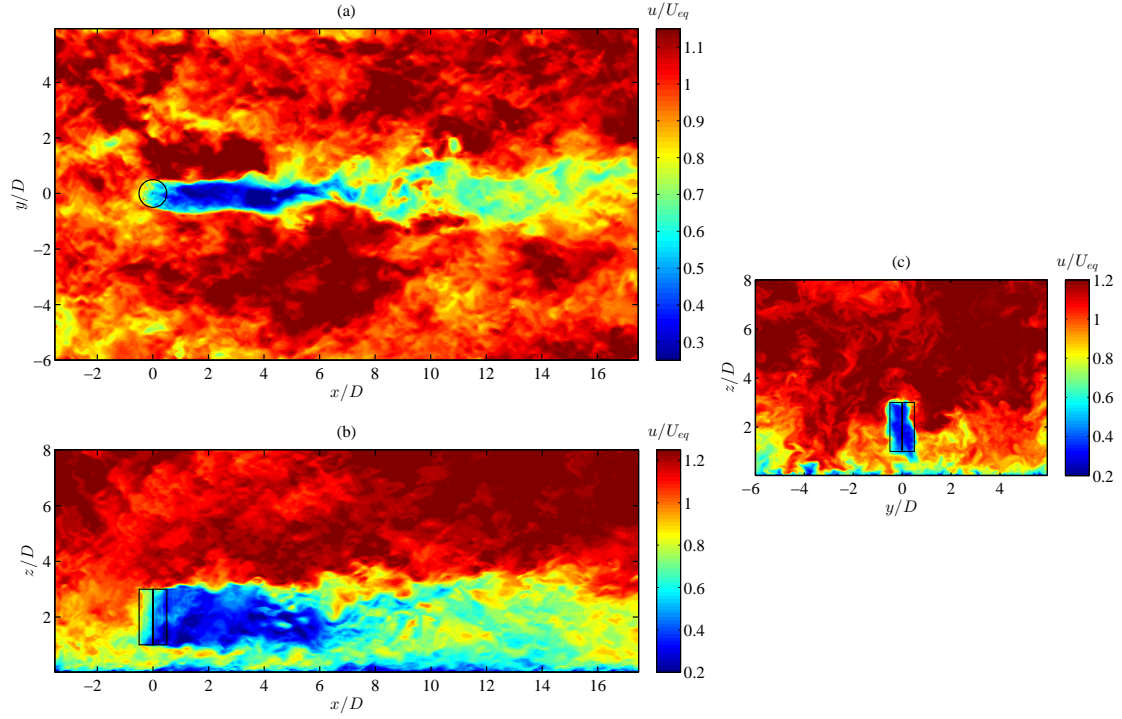


Figure 3.5 – Contour plots of the instantaneous normalized streamwise velocity ( $u/U_{eq}$ ) in three different planes: (a) the  $x-y$  plane at the equator height of the turbine; (b) the  $x-z$  plane going through the center of the turbine; (c) the  $y-z$  plane which is 2D downstream of the center of the turbine.

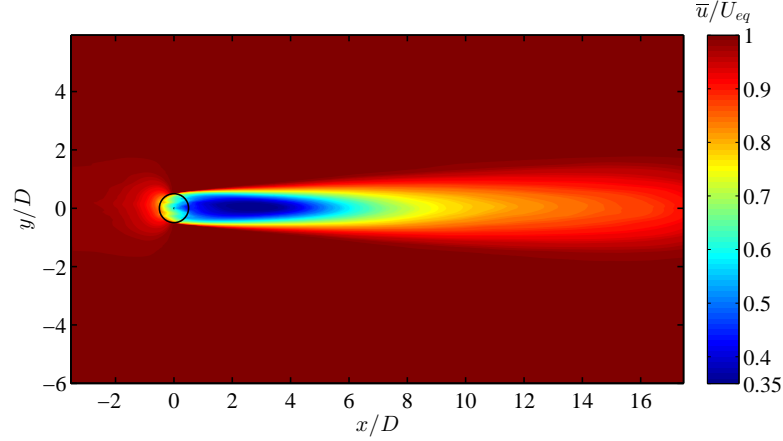


Figure 3.6 – Contours of the normalized mean streamwise velocity ( $\bar{u}/U_{eq}$ ) in the  $x$ - $y$  plane at the equator height of the turbine.

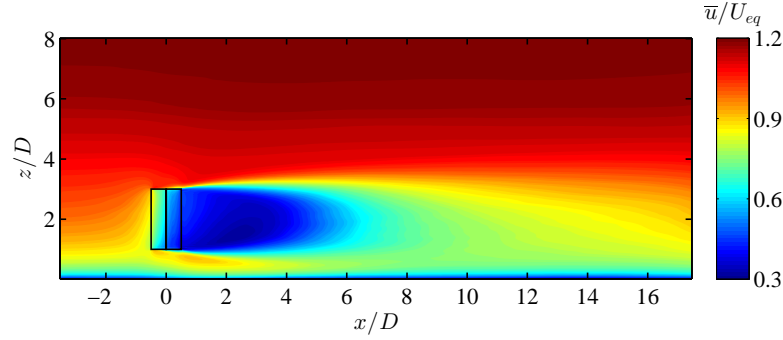


Figure 3.7 – Contours of the normalized mean streamwise velocity ( $\bar{u}/U_{eq}$ ) in the  $x$ - $z$  plane going through the center of the turbine.

how it expands in the spanwise direction as it advances farther downstream.

To have a more quantitative and precise insight about the VAWT wake, Figures 3.9 and 3.10 can be consulted. Figure 3.9 shows spanwise profiles of the mean streamwise velocity in a horizontal plane at the equator height of the turbine in eight downstream positions. Besides, Figure 3.10 presents vertical profiles of the mean streamwise velocity in the  $x$ - $z$  mid-plane of the turbine at different downstream positions. An interesting observation that can be made from Figures 3.6, 3.9 and 3.10 is that the maximum velocity deficit occurs at a downstream distance of about 2.7 rotor diameters; this distance is significantly larger than the equivalent one for the case of HAWT wakes (Wu and Porté-Agel, 2011). After the point where the maximum velocity deficit (more than 65% of  $U_{eq}$  in this case) occurs has been reached, the wake starts to recover with a relatively high recovery rate (defined here as the magnitude of the rate of change of the maximum velocity deficit with streamwise distance). As we go farther downstream, the rate of the wake recovery decreases considerably; so that in the distances as large as 17 rotor diameters, where the

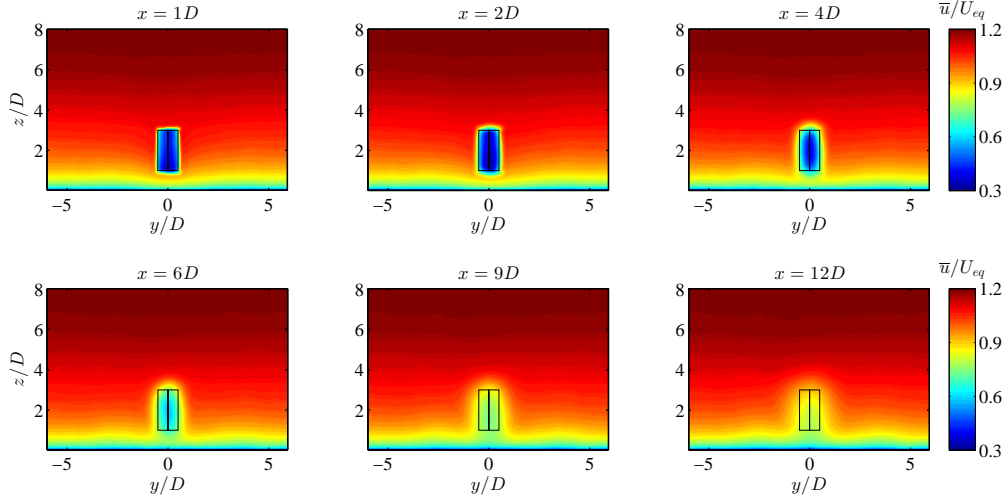


Figure 3.8 – Contour plots of the normalized mean streamwise velocity ( $\bar{u}/U_{eq}$ ) in six different  $y$ - $z$  planes at different distances downstream of the center of the turbine.

velocity deficit reaches values of about 90%, the recovery rate is comparably very small.

Another group of crucial quantities that has a significant importance in characterizing turbine wakes is the turbulence-related statistics, such as turbulence intensity and turbulent fluxes. These quantities are especially important for the design of wind farms, due to their role in both wake recovery and mechanical loads on turbine blades. Figure 3.11 shows contours of turbulence intensity (TI) in two different orthogonal planes ( $x$ - $y$  and  $x$ - $z$ ) in the wake of the turbine. Here, the turbulence intensity is defined as  $TI = \sigma_u/U_{eq}$ . In addition, Figure 3.12 shows the distribution of TI in  $y$ - $z$  planes at different downstream locations. In Figure 3.11a, it can be seen that two branches of high TI regions start to develop from the two spanwise extremities of the rotor swept surface (the black circle in the figure). These two branches grow in spanwise width as we go further downstream, until the point where they meet each other (for this case, in about 3.5 rotor diameters downstream of the turbine in the horizontal mid-plane of the turbine). Starting from the turbine area, the TI in each of these branches increases, until a point where the maximum TI occurs (about 3.8 rotor diameters downstream in this case); after this maximum point, the TI starts to decrease as the flow advances downstream, while the width of the branches continues to expand. Figure 3.13 examines the previous figure quantitatively, by showing the spanwise profiles of the TI in the equator height of the turbine. One can readily see that at each downstream position, the horizontal TI profiles have two maxima at two spanwise positions, which correspond to the two aforementioned TI branches. Although slight asymmetries can still be seen in the TI values of the two branches, the lateral asymmetry is not significantly pronounced. It should be noted that the degree to which the VAWT wake is laterally asymmetric is influenced by parameters, such as  $TSR$ , airfoil type and the Reynolds number in which the turbine is working.



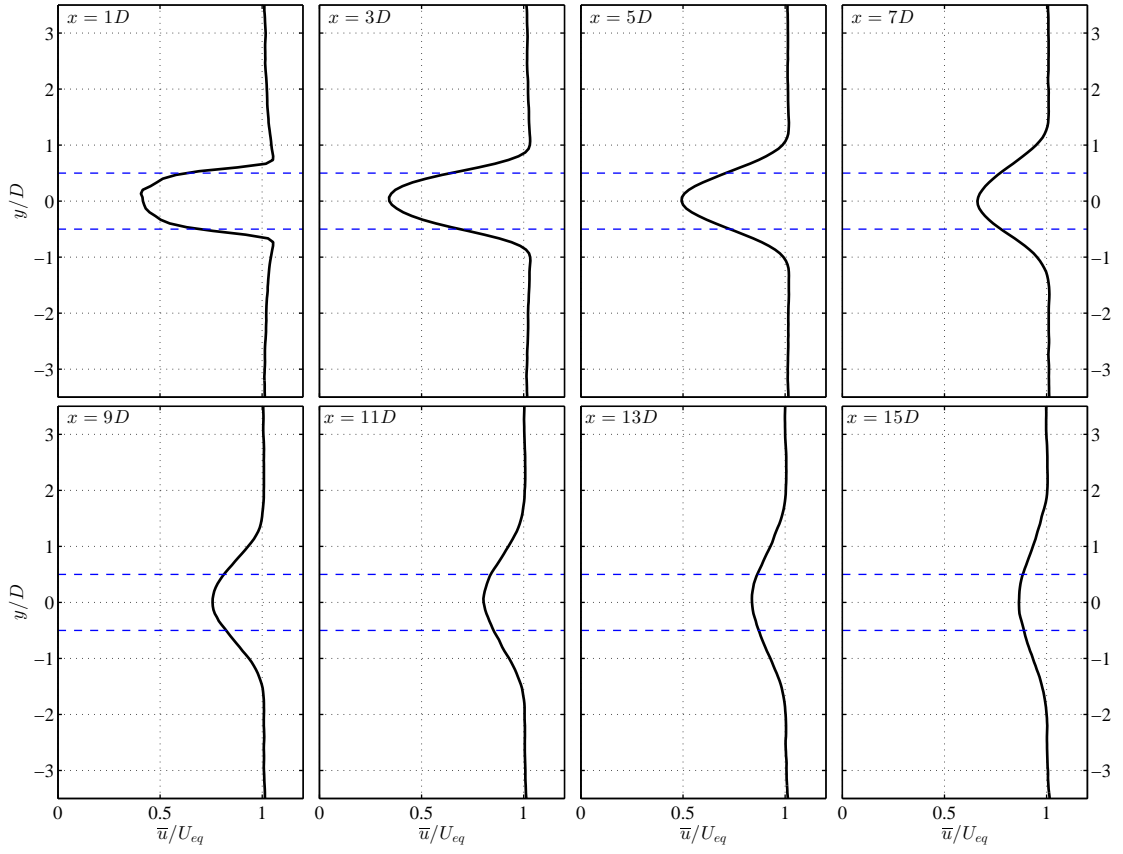


Figure 3.9 – Horizontal-spanwise profiles of the normalized mean streamwise velocity ( $\bar{u}/U_{eq}$ ) in the  $x$ - $y$  plane at the equator height of the turbine at different downstream positions. The blue horizontal dashed lines show the extent of the turbine.

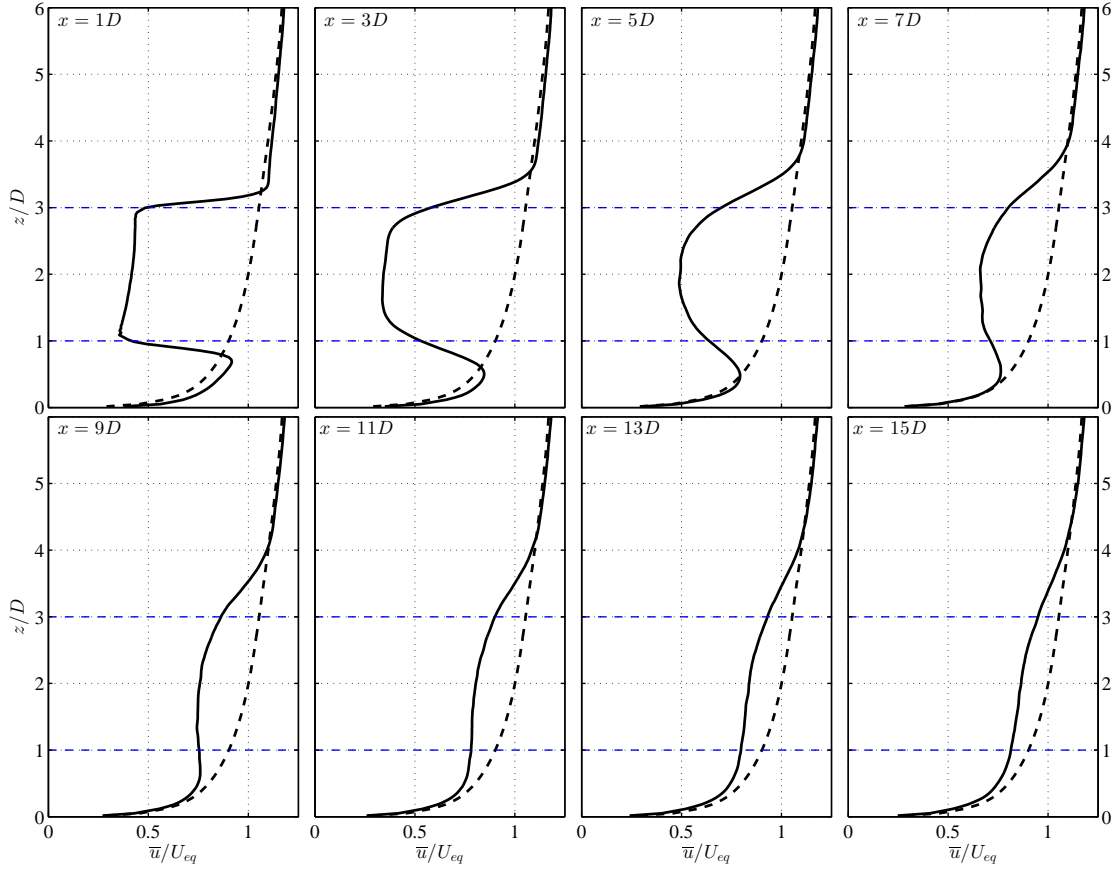


Figure 3.10 – Vertical profiles of the normalized mean streamwise velocity ( $\bar{u}/U_{eq}$ ) in the  $x$ - $z$  plane going through the center of the turbine at different downstream positions. The black dashed line represents the inflow profile, and the blue horizontal dashed lines show the extent of the turbine.

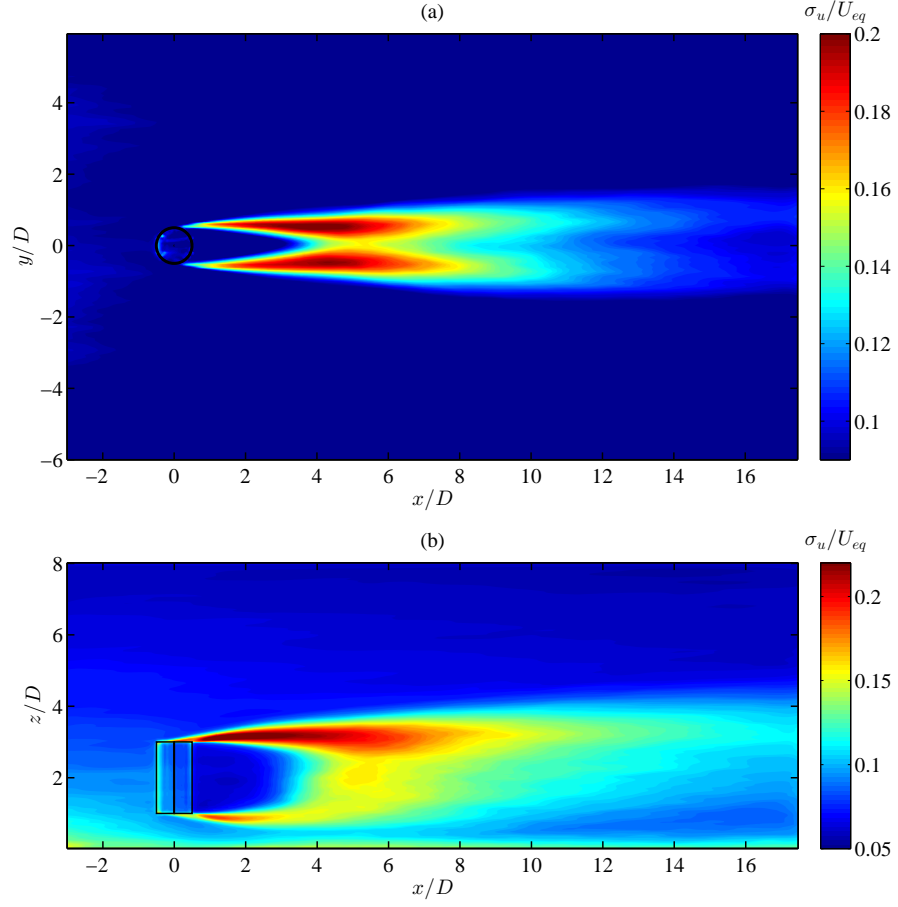


Figure 3.11 – Contour plots of the streamwise turbulence intensity,  $\sigma_u/U_{eq}$ : (a) in the  $x-y$  plane at the equator height of the turbine; (b) in the  $x-z$  plane going through the center of the turbine.

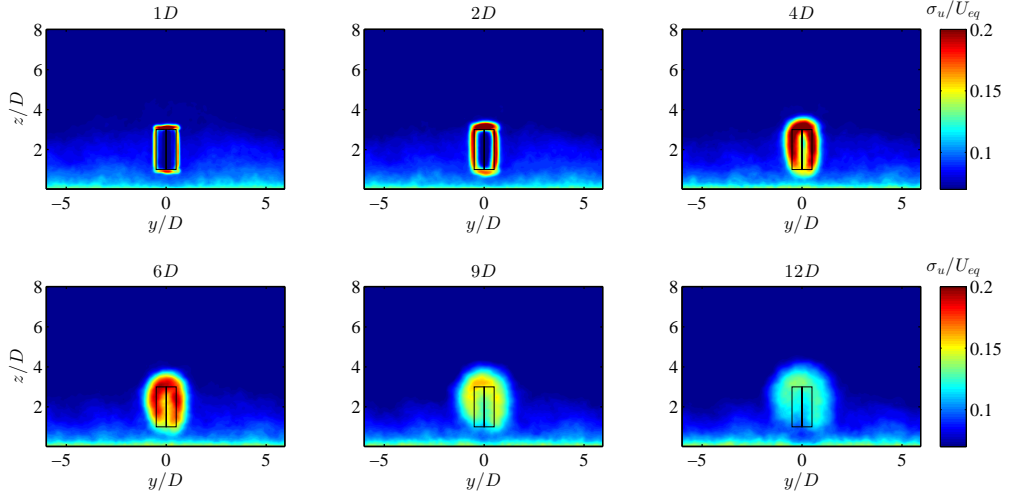


Figure 3.12 – Contour plots of the streamwise turbulence intensity,  $\sigma_u/U_{eq}$ , in six different  $y-z$  planes at different distances downstream of the center of the turbine.

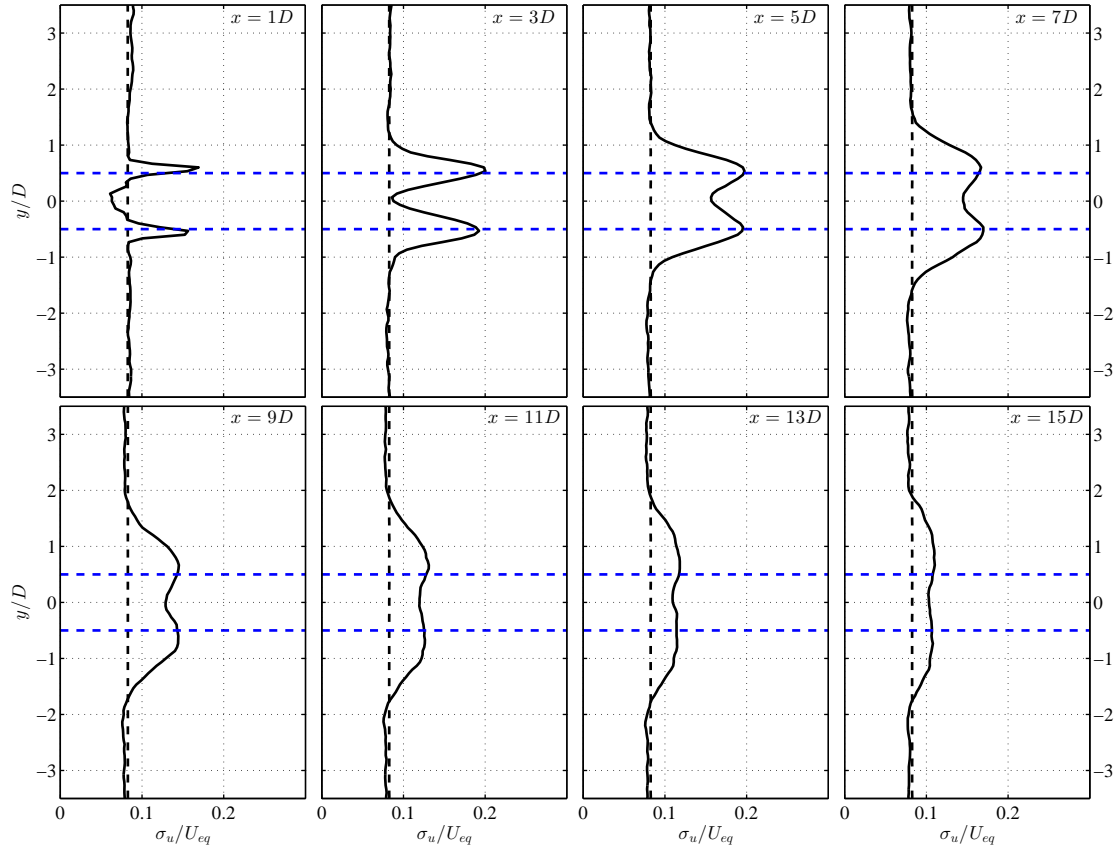


Figure 3.13 – Horizontal profiles of the streamwise turbulence intensity in the  $x$ - $y$  plane at the equator height of the turbine at different downstream positions. The black dashed line represents the inflow profile, and the blue horizontal dashed lines show the extent of the turbine.

In Figure 3.11b, one can observe a similar behavior by noticing the two high TI regions originating from the upper and lower extremities of the turbine; however, in this case, the TI originating from the upper edge of the blades is clearly larger than the one originating from the lower edge. To further quantify this, and to have a better understanding of the vertical variation of the TI in a VAWT wake, one can study Figure 3.14, in which vertical profiles of TI are shown at different downstream positions. In this figure, it can also be seen that in the region below the turbine blades' lower edge, the turbulence intensity has even decreased to values lower than the inflow TI; this behavior has also been observed in HAWT wakes, as well (e.g., (Wu and Porté-Agel, 2011)).

Furthermore, turbulent momentum fluxes in the VAWT wake are believed to be worthy of inspection, as they quantify the rate of flow entrainment into the wake, which is responsible for the recovery and lateral expansion of the wake. Figure 3.15 shows the normalized lateral turbulent flux ( $\overline{u'v'}$ ) at the horizontal mid-plane of the turbine. The positive and negative regions of  $\overline{u'v'}$ , which are located on the two lateral edges of the wake, show an inward entrainment of momentum into the wake region. This lateral entrainment can also be seen in the  $y$ - $z$  planes in Figure 3.16. Figure 3.17 shows the spanwise profiles of  $\overline{u'v'}$  at the equator height of the turbine at different downstream distances from the turbine. We notice that for this case, the maximum absolute value of  $\overline{u'v'}$  at the equator height of the turbine occurs between  $4.5D$  and  $5D$  ( $4.9D$  for positive values and  $4.7D$  for negative values) downstream of the turbine, which is about  $1D$  farther downwind compared to the maximum TI point. It should be noted that, again in this figure, only a slight lateral asymmetry (in terms of  $|\overline{u'v'}|$ ) can be observed.

Figures 3.18 and 3.19 show the normalized vertical turbulent flux ( $\overline{u'w'}$ ) in the wake flow. The vertical inward entrainment from both above and below the wake region is clear in these figures. Figure 3.20 displays the vertical profiles of  $\overline{u'w'}$  in the  $x$ - $z$  plane going through the center of the turbine. It can be seen in this figure that the values of the vertical turbulent flux are higher in upper edge of the wake with respect to the lower edge. Here, we can observe that the magnitude of  $\overline{u'w'}$  (in the aforesaid vertical plane) peaks relatively close to the turbine ( $1.9D$  for positive values and  $0.5D$  for negative values) at heights near to the ones of the upper and lower edges of the blades.

### 3.5 Summary

Acknowledging the prospects of VAWTs as alternative wind energy extractors along with HAWTs in a future clean-energy outlook, which is likely to be marked by diversity, targeted research on VAWTs' performance is deemed to be highly useful and necessary. One of the research targets, which is especially crucial in designing potential VAWT farms, is to characterize VAWT wakes; a target which is still considerably underachieved for VAWTs, particularly with respect to HAWTs. In this view, one of the approaches that can greatly contribute to the cause is to use turbulence-resolving numerical simulation techniques,

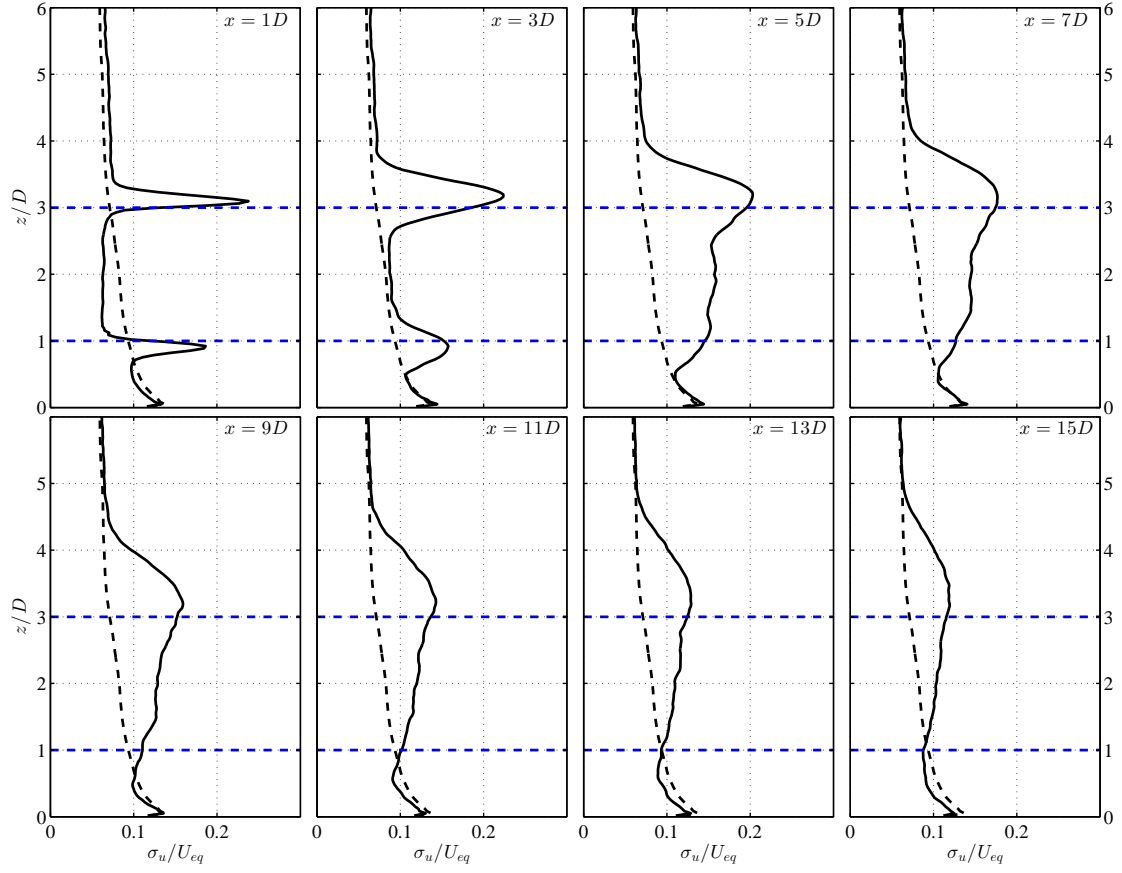


Figure 3.14 – Vertical profiles of the streamwise turbulence intensity in the  $x$ - $z$  plane going through the center of the turbine at different downstream positions. The black dashed line represents the inflow profile, and the blue horizontal dashed lines show the extent of the turbine.

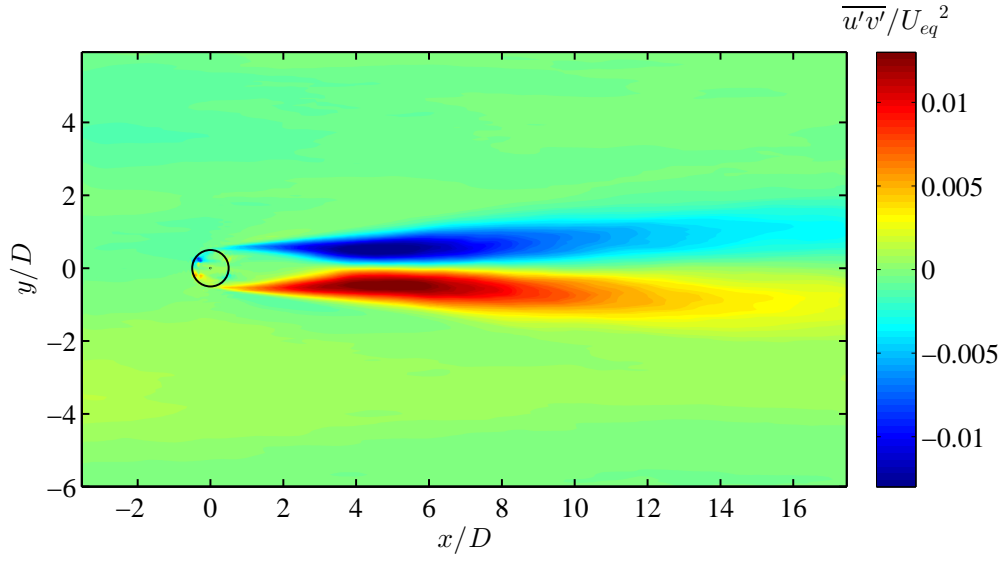


Figure 3.15 – Contour plot of the normalized lateral turbulent flux,  $\overline{u'v'}/U_{eq}^2$ , in the  $x$ - $y$  plane at the equator height of the turbine.

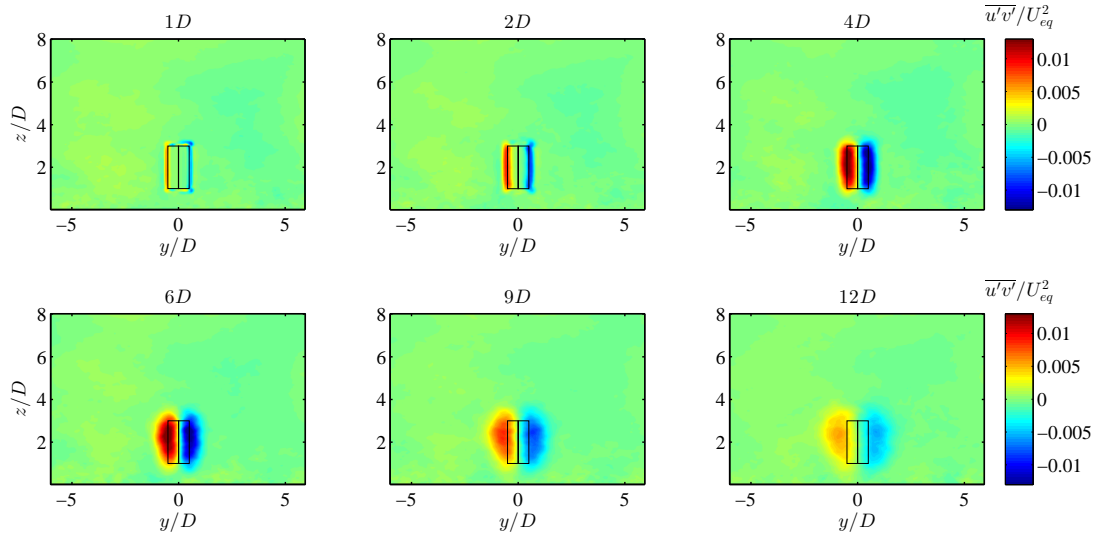


Figure 3.16 – Contour plots of the normalized lateral turbulent flux,  $\overline{u'v'}/U_{eq}^2$ , in six different  $y$ - $z$  planes at different distances downstream of the center of the turbine.

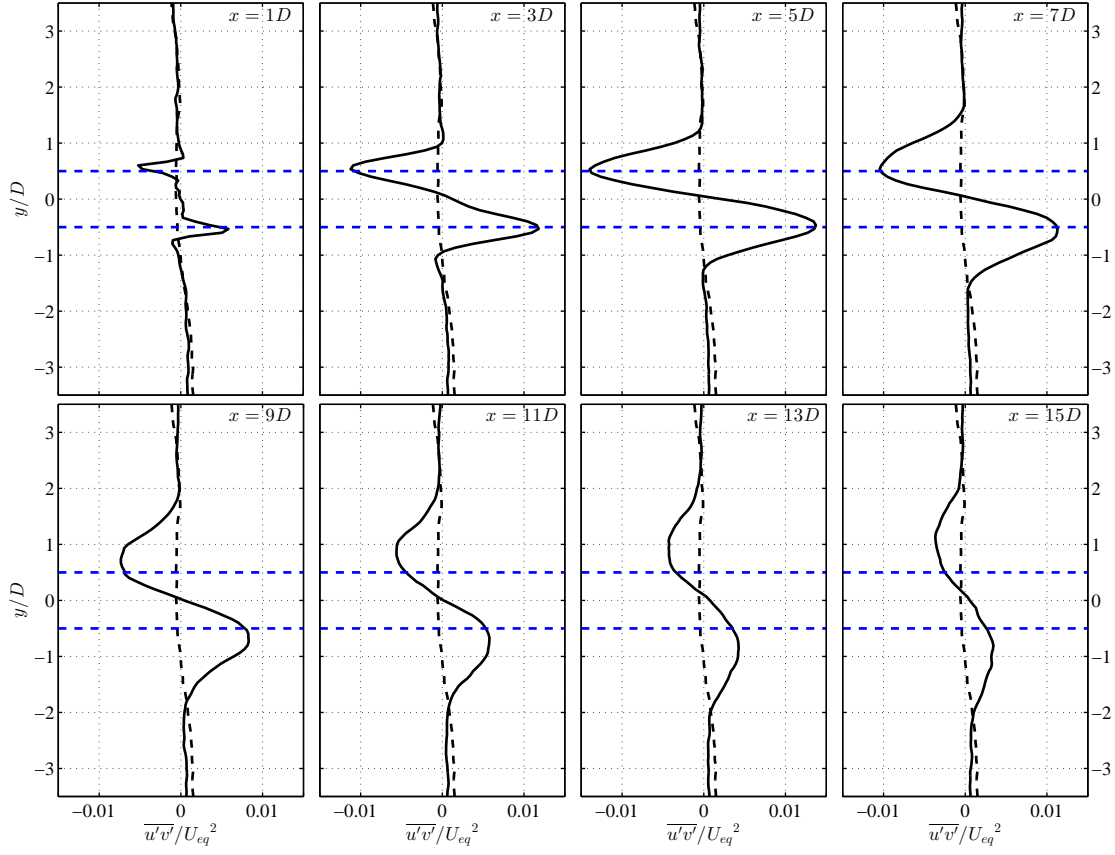


Figure 3.17 – Horizontal profiles of the normalized lateral turbulent flux ( $\overline{u'v'}/U_{eq}^2$ ) in the  $x$ - $y$  plane at the equator height of the turbine at different downstream positions. The black dashed line represents the inflow profile, and the blue horizontal dashed lines show the extent of the turbine.

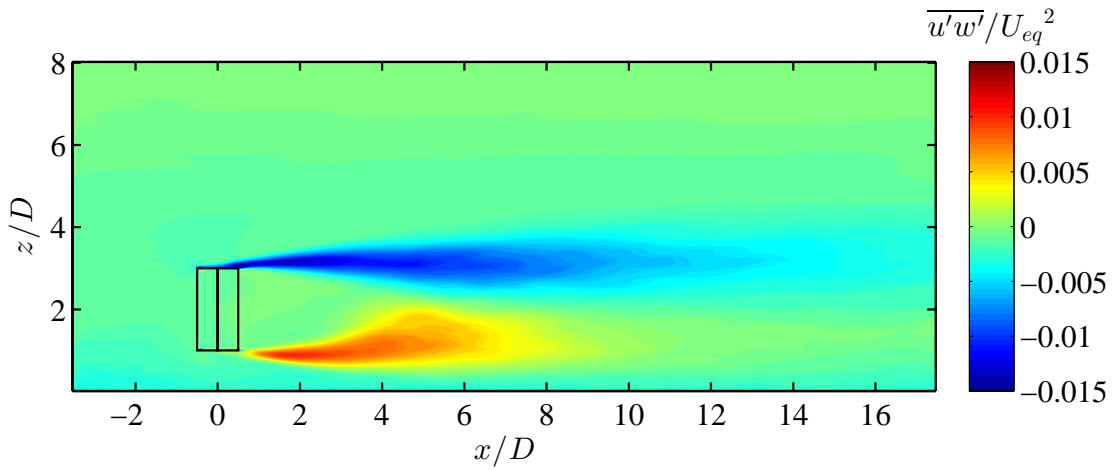


Figure 3.18 – Contour plots of the normalized vertical turbulent flux,  $\overline{u'w'}/U_{eq}^2$ , in the  $x$  -  $z$  plane going through the center of the turbine.



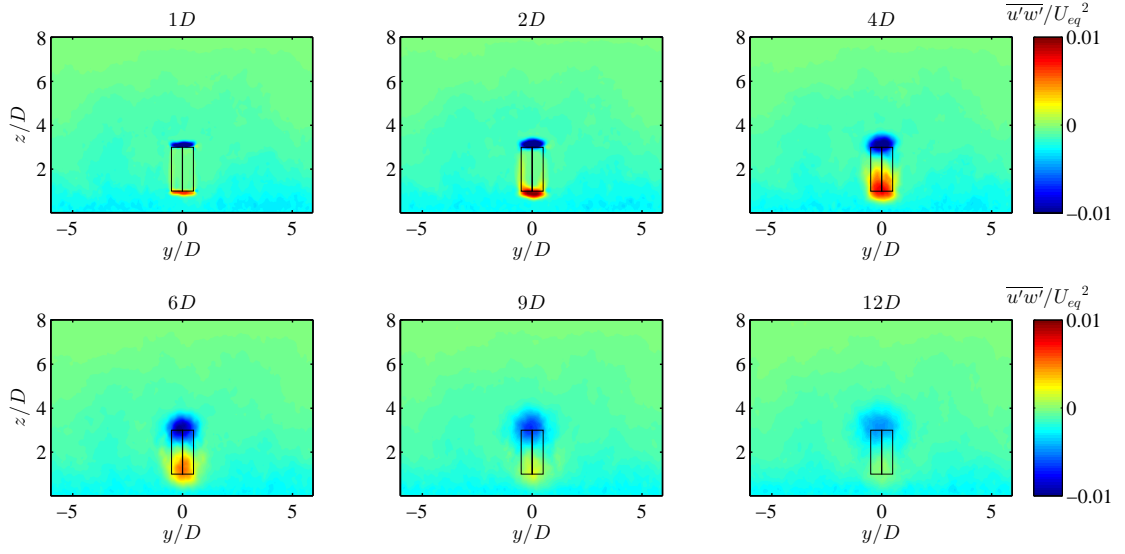


Figure 3.19 – Contour plots of the normalized vertical turbulent flux,  $\overline{u'w'}/U_{eq}^2$ , in six different  $y$ - $z$  planes at different distances downstream of the center of the turbine.

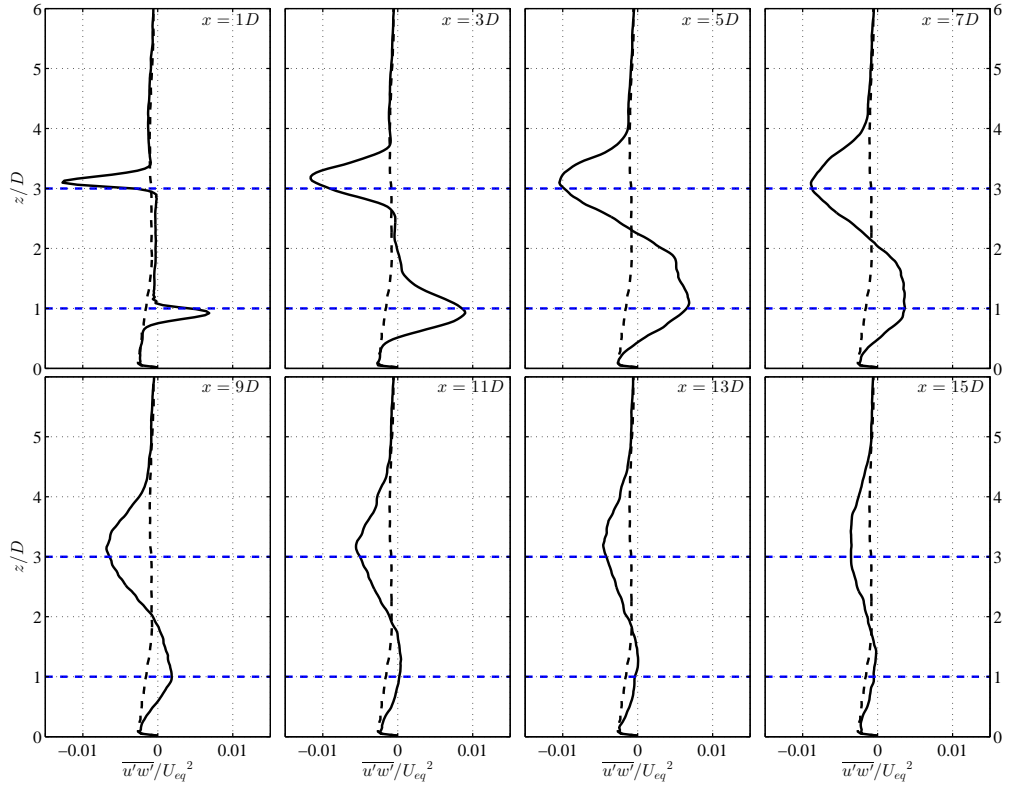


Figure 3.20 – Vertical profiles of the normalized vertical turbulent flux ( $\overline{u'w'}/U_{eq}^2$ ) in the  $x$ - $z$  plane going through the center of the turbine at different downstream positions. The black dashed line represents the inflow profile, and the blue horizontal dashed lines show the extent of the turbine.

which can provide plenitude of high-resolution spatial and temporal information about the flow field and lead to valuable insight into the behavior of the turbine wake.

In this study, we used a previously-validated large-eddy simulation framework, in which an actuator line model is employed to parameterize the blade forces on the flow, to simulate the atmospheric boundary layer flow through stand-alone VAWTs placed on a flat terrain. For a typical straight-bladed 1-MW VAWT rotor design, first, the variation of the power coefficient with the tip-speed ratio and the chord length of the blades was studied. In doing so, the optimum combination of  $TSR$  and solidity ( $Nc/R$ ), which yielded the maximum power coefficient of 0.47, was found to be 4.5 and 0.18, respectively. Second, for a VAWT with this optimum combination, a detailed study on the characteristics of its wake was performed, in which different mean and turbulence statistics were inspected. The mean velocity in the wake was found to need a long distance to recover; for example, the wake requires a distance of 14 rotor diameters to recover its center velocity to 85% of the incoming velocity. It was also seen that for this case, the point with the maximum velocity deficit is located 2.7 rotor diameters downstream of the center of the turbine (at the equator height of the turbine), and only after this point, the wake recovery starts with a rate (based on the change of the maximum velocity deficit) that is decreasing with streamwise distance. The turbulence intensity was observed to reach its maximum value (at the equator height of the turbine) 3.8 rotor diameters downstream of the VAWT. As we go towards the upper and lower extremities of the rotor, the height-specific maximum of the TI moves closer to the turbine and its value also increases. Turbulent momentum fluxes, which are a gauge for flow entrainment and, as a consequence, are responsible for the recovery of the wake, were also quantified, and it was shown that in the equator height of the turbine, the magnitude of the lateral flux peaks about  $1D$  farther downwind of the maximum TI point. The above-mentioned mean and turbulence statistics corresponding to the optimum tip-speed ratio show only slight lateral asymmetries in the wake. However, significant vertical asymmetries were observed in terms of both the TI and magnitude of momentum fluxes, with higher values at the upper edge of the blades compared to the ones at the lower edge.

This study paves the way to further explore VAWT wakes and to discover the effects of different relevant parameters on the wake behavior. Moreover, it can serve as a solid foundation for future studies on performance, characteristics and optimization of VAWT farms.

## Appendix A

In this Appendix, the procedure of the method with which the dynamic stall phenomenon is modeled is described in detail. The dynamic stall model is based on the modified MIT model developed by [Noll and Ham \(1983\)](#), which is a practical modification of

the original MIT model (Ham, 1968). This model has the advantage of being simple and easy to use and also has been found to work better for VAWTs compared to other available models (Paraschivoiu, 2002). It is noteworthy that the following procedure can be implemented for both VAWTs and HAWTs.

Dynamic stall is a phenomenon that occurs for an airfoil when the angle of attack of the incident flow keeps changing with time and its rate of change (*i.e.*,  $\dot{\alpha} = \frac{d\alpha}{dt}$ ) is sufficiently large. For a blade element of a turbine (either VAWT or HAWT) (placed in a turbulent flow), the change of  $\alpha$  with time can be originated by three main sources: (1) the turbulent fluctuations of the incident flow; (2) the changes (spatial or temporal) in the mean incident flow; and (3) the rotation of the blades. Of these three reasons, the second one is normally specific to HAWTs, since an HAWT blade element experiences the variation of the boundary layer mean velocity profile at different heights; which is not the case for a VAWT blade element, as it moves at a constant height. However, the third reason is specific to VAWTs, because the geometry of a VAWT rotor is such that  $\alpha$  (for a given blade element) oscillates between a maximum positive value and a minimum negative value in each revolution (even with a uniform inflow); however, for an HAWT blade element, assuming a uniform mean inflow,  $\alpha$  remains constant during one revolution. Since the MIT model (and other similar practical models) is (are) only appropriate for the large-scale behavior of  $\alpha$  in time, in our implementation of this model, the dynamic stall effects arising from the above-mentioned second and third sources, as well as the relatively large-scale turbulent fluctuations (from the first source) are modeled, while the changes of  $\alpha$  arising from the relatively small-scale turbulent fluctuations of the incident flow are filtered out.

In order to implement the above-mentioned procedure,  $\dot{\alpha}$  is calculated from a time-averaged and smoothed curve of  $\alpha_f = \alpha_{fit}(\theta)$  during one revolution. For this purpose, the angle of attack at each azimuthal angle is time-averaged during each  $N_{rev}$  revolutions of the blades, and then, a polynomial curve,  $\alpha_{fit}(\theta)$ , is fitted on the time-averaged curve,  $\alpha_{avg}(\theta)$ . For the rest of the dynamic stall calculations, it is the  $\alpha_{fit}(\theta)$  curve that is used. Figure 3.21 shows an example for this procedure for  $TSR = 2$  and  $c = 2$  m. The azimuthal angle,  $\theta$ , is considered to increase counterclockwise (when seen from above) from  $-90^\circ$  to  $270^\circ$ , in a way that  $\theta = 0^\circ$  and  $\theta = 180^\circ$  correspond to the most downstream and the most upstream points of the rotor, respectively. It is also noteworthy to mention again that the sense of the rotation of the turbine blades is counterclockwise when seen from above. Here, for the curve fitting, an eighth order polynomial is used to detect the two extrema accurately.

Subsequently, we implement the modified MIT model on the  $\alpha_{fit}(\theta)$  curve and construct  $C_{L,DS}(\alpha)$  and  $C_{D,DS}(\alpha)$  curves, which are lift and drag coefficients as a function of the angle of attack considering dynamic stall. In the modified MIT model, we use the tabulated airfoil data for lift and drag coefficients, and based on that,  $C_{L,DS}(\alpha)$  and  $C_{D,DS}(\alpha)$  are constructed. Based on the tabulated airfoil data, we can determine the

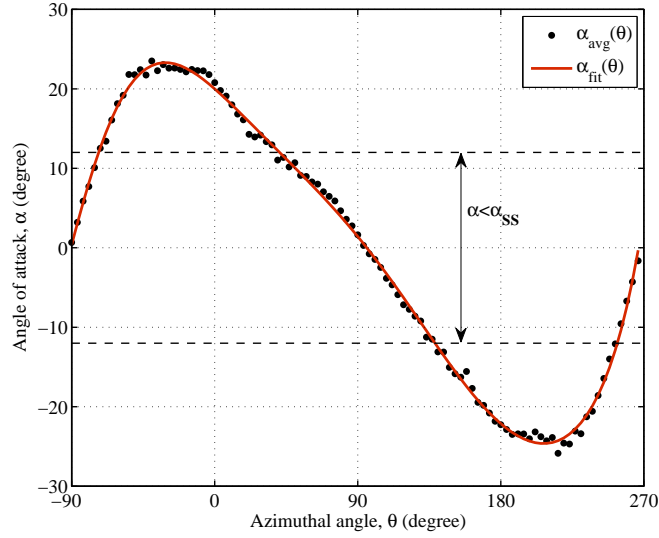


Figure 3.21 – The time-averaged (black circles) and curve-fitted (red line) behavior of the variation of angle of attack as a function of azimuthal angle in one revolution of a blade element

static stall angle,  $\alpha_{SS} > 0$ , and the lift coefficient at static stall,  $C_{L,SS} > 0$ . The static lift and drag coefficient functions derived from the tabulated airfoil data are designated as  $C_{L,table}(\alpha)$  and  $C_{D,table}(\alpha)$  hereafter. Moreover, the slope of the  $C_{L,table}(\alpha)$  curve before the static stall can be calculated as  $a_s = C_{L,SS}/\alpha_{SS}$ , considering that in this region, normally,  $C_{L,table}(\alpha)$  is linear.

As can be seen in Figure 3.21, the global (*i.e.*, the curve-fitted) behavior of  $|\alpha|$  in one revolution of a blade element is such that  $|\alpha|$  twice (once for positive  $\alpha$  values and once for negative  $\alpha$  values) increases from zero to a maximum value and then decreases to zero again. In each of these increase-decrease cycles of  $|\alpha|$ , the MIT dynamic stall model casts the flow in one of the four below dynamic stall states:

**State 1** occurs when  $|\alpha| \leq \alpha_{SS}$ . In this state, both lift and drag coefficients are extracted directly from the static tabulated airfoil data:

$$C_{L,DS}(\alpha) = C_{L,table}(|\alpha|) \quad (3.3)$$

$$C_{D,DS}(\alpha) = C_{D,table}(|\alpha|) \quad (3.4)$$

**State 2** occurs when  $\alpha_{SS} < |\alpha| < \alpha_{DS}$  and  $\alpha_f \dot{\alpha} > 0$  (*i.e.*,  $|\alpha|$  is increasing in

time).  $\alpha_{DS}$  is calculated with the following formula:

$$\alpha_{DS} = \alpha_{SS} + \gamma \sqrt{\left(\frac{|\dot{\alpha}|c}{2V_{rel}}\right)} \quad (3.5)$$

where  $c$  is the blade chord length,  $V_{rel}$  is the magnitude of the relative velocity (which is also a function of the azimuthal angle),  $\dot{\alpha} = \Omega d\alpha_{fit}/d\theta$ ,  $\Omega$  is the angular velocity of the blade and  $\gamma$  is a constant that has a dimension of an angle and is weakly a function of the airfoil type and is determined experimentally (Noll and Ham, 1983). If an experimental value for  $\gamma$  is not available, a value of one radian is recommended (Hibbs, 1986). We keep calculating  $\alpha_{DS}$  in this state, until the point at which  $|\alpha|$  is on the verge of becoming larger than  $\alpha_{DS}$  (*i.e.*, the point at which the model goes to State 3). We designate this last value of  $\alpha_{DS}$  as  $\alpha_{DS,final}$ , and with this value, we calculate the maximum value of  $C_{L,DS}$  (*i.e.*,  $C_{L,max}$ ):

$$C_{L,max} = C_{L,SS} + 40\left(\frac{|\dot{\alpha}|c}{V_{rel}}\right) \quad (3.6)$$

and we apply the following clipping conditions on  $C_{L,max}$ :

$$\begin{aligned} \text{If } C_{L,max} > 3.0 \quad \text{then } C_{L,max} &= 3.0 \\ \text{If } C_{L,max} < a_s \sin(\alpha_{DS,final}) \quad \text{then } C_{L,max} &= a_s \sin(\alpha_{DS,final}) \end{aligned} \quad (3.7)$$

Throughout this state, the lift coefficient is extrapolated from static values, and the drag coefficient is still directly extracted from the static tabulated data:

$$C_{L,DS}(\alpha) = a_s \sin(|\alpha|) \quad (3.8)$$

$$C_{D,DS}(\alpha) = C_{D,table}(|\alpha|) \quad (3.9)$$

where (as in Noll and Ham (1983)) a sine function is used for extrapolation (noting that in the range of angles of attack, on which we normally apply the model,  $|\alpha|$  is small, and we have  $\sin(|\alpha|) \approx |\alpha|$ ).

**State 3** occurs when  $\alpha_{DS,final} < |\alpha|$  and  $\alpha_f \dot{\alpha} > 0$  (*i.e.*,  $|\alpha|$  is still increasing in time). As soon as the model enters State 3, we start to calculate the elapsed time from the moment in which State 3 is triggered; in other words, we start to calculate the time elapsed after the  $\alpha_{DS,final}$  value has been reached; we call this time  $t_{DS}$ .

In this state, the lift and drag coefficients are calculated as:

$$C_{L,DS}(\alpha) = a_s \sin(|\alpha|) \quad (3.10)$$

$$C_{D,DS}(\alpha) = C_{L,DS} \tan(|\alpha|) \quad (3.11)$$

However, in this state, we only keep using Equations (3.10) and (3.11) as long as these conditions are both satisfied:  $C_{L,DS} \leq C_{L,max}$  and  $t_{DS}V_{rel}/c < 1$ ; otherwise, we set the lift coefficient to the  $C_{L,max}$  value and calculate the drag coefficient accordingly (as shown below). We designate the value of  $|\alpha|$  of the moment in which either of the aforesaid conditions is on the verge of being violated as  $\alpha_{C_{L,max}}$ .

$$\begin{aligned} \text{If } C_{L,DS} > C_{L,max} \quad \text{Or} \quad t_{DS} \frac{V_{rel}}{c} \geq 1 : \\ C_{L,DS} &= C_{L,max} \\ C_{D,DS} &= C_{L,max} \tan(\alpha_{C_{L,max}}) \end{aligned} \quad (3.12)$$

**State 4** occurs when  $|\alpha| > \alpha_{SS}$  and  $\alpha_f \dot{\alpha} \leq 0$  (*i.e.*, when  $|\alpha|$  starts to decrease with time). We designate the azimuthal angle of the moment in which  $|\alpha|$  starts to decrease as  $\theta_{\alpha_{max}}$ . At this stage,  $C_{L,DS}$  is lowered exponentially (in time) from  $C_{L,max}$  to  $C_{L,SS}$ .

$$C_{L,DS} = (C_{L,max} - C_{L,SS}) \exp\left(-(\theta - \theta_{\alpha_{max}}) \frac{2R}{c}\right) + C_{L,SS} \quad (3.13)$$

$$C_{D,DS}(\alpha) = C_{L,DS} \tan(|\alpha|) \quad (3.14)$$

where  $R$  is the radius of the blade element about the axis of rotation (in the case of a VAWT,  $R$  is simply the radius of the VAWT rotor).

As can be noticed in the above procedure,  $\alpha(t)$  (*i.e.*,  $\alpha(\theta)$ ) needs to be a smooth function for the above model to work. Because of this, we use  $\alpha_f = \alpha_{fit}(\theta)$  (*i.e.*, the time-averaged and curve-fitted value of  $\alpha$ ) in the above procedure instead of  $\alpha$ . Thus, at the end of each  $N_{rev}$  revolution and after getting the  $\alpha_{fit}(\theta)$  function, we apply the MIT model on this curve, and we construct the  $C_{L,DS}(\alpha)$  and  $C_{D,DS}(\alpha)$  functions, which will be used in the next  $N_{rev}$  revolutions. For the first  $N_{rev}$  revolutions (for which we still do not have  $\alpha_{fit}(\theta)$ ), one can preliminarily just use the static tabulated airfoil data.

Figure 3.22 shows an example of a constructed  $C_{L,DS}(\alpha)$  curve under dynamic stall,

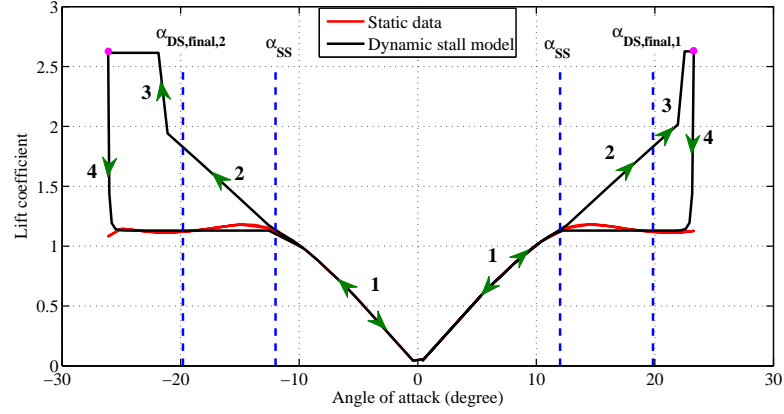


Figure 3.22 – Lift coefficient curve under the dynamic stall model (black line) as compared to the static lift coefficient curve (red line). The four states in the dynamic stall model are indicated in the graph.

which corresponds to the  $\alpha_{fit}(\theta)$  shown in Figure 3.21. The aforesaid states of the model are shown in the figure. As can be seen in this figure, to construct this curve, we need both the tabulated airfoil data and some parameters, which we should obtain from the MIT model. As a summary, all of the necessary data and parameters required to construct the  $C_{L,DS}(\alpha)$  and  $C_{D,DS}(\alpha)$  curves are listed below:

- (1) Tabulated airfoil data:  $C_{L,table}(\alpha)$  and  $C_{D,table}(\alpha)$ ; (2)  $\alpha_{SS}$ ; (3)  $C_{L,SS}$ ; (4)  $a_s$ ;
- (5)  $\gamma$ ; (6)  $\alpha_{DS,final}$ ; (7)  $\alpha_{C_{L,max}}$ ; (8)  $C_{L,max}$ ; (9)  $\theta_{\alpha_{max}}$

It should be noted that for the last four items, two values are obtained for each revolution: one for the  $\alpha \geq 0$  cycle and one for the  $\alpha < 0$  cycle. In our simulations, we have used  $\gamma = 1$  radian and  $N_{rev} = 15$ .

A comprehensive and step-by-step procedure to implement the MIT dynamic stall model is given in the flowchart of Figure 3.23; the flowchart is deliberately given in a way that can be followed for coding purposes in any common programming language.

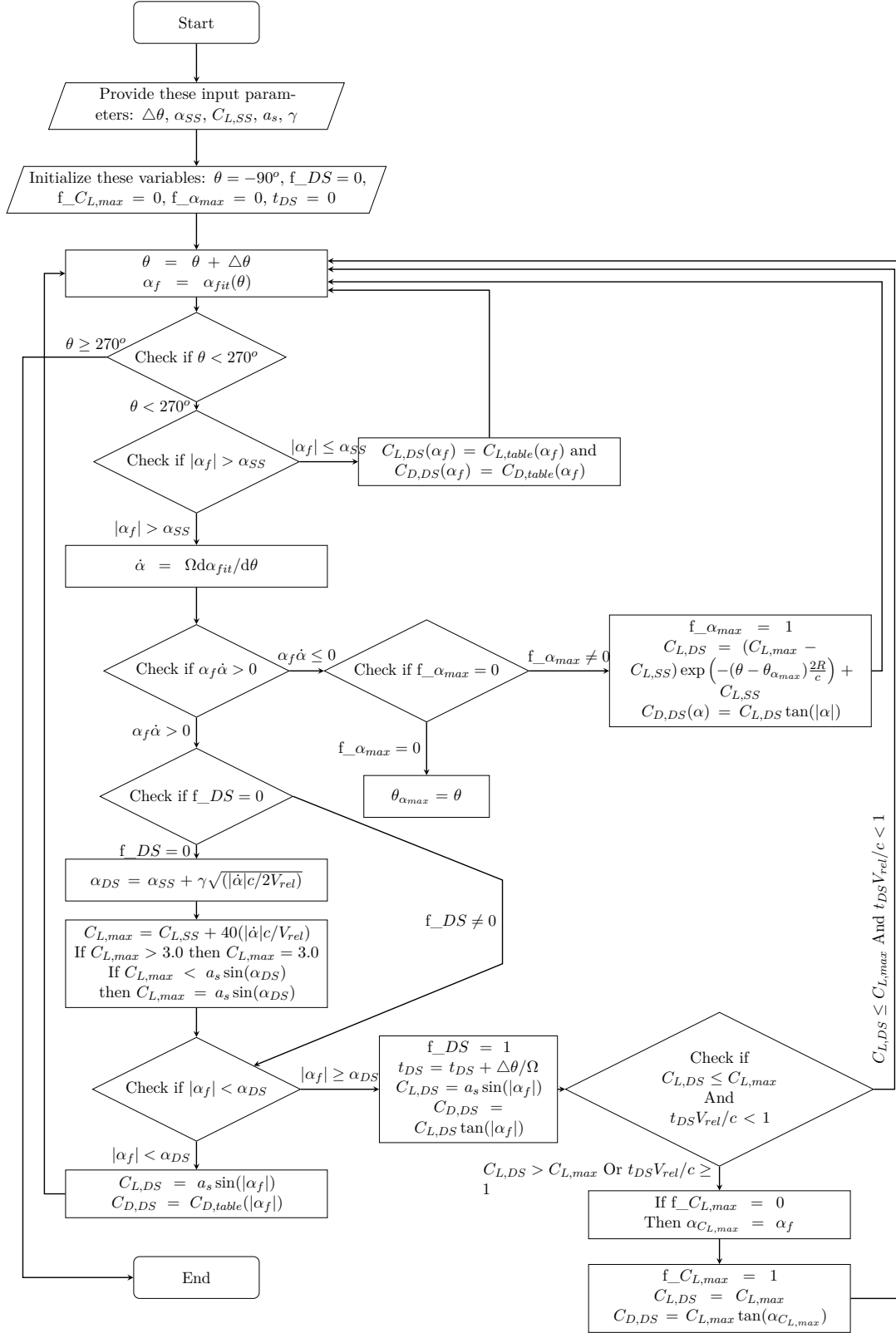


Figure 3.23 – Flowchart to implement the modified MIT dynamic stall model for a VAWT in turbulent flow.



# Wind turbines on topography **Part II**







## 4 Large-eddy simulation of atmospheric boundary-layer flow through a wind farm sited on topography<sup>1</sup>

### Abstract

Large-eddy simulation (LES) has recently been well validated and applied in the context of wind turbines over flat terrain; however, to date its accuracy has not been tested systematically in the case of turbine wake flows over topography. In this work, the wake flow in a wind farm situated on hilly terrain is studied using LES for a case where wind-tunnel experimental data are available. To this end, first boundary-layer flow is simulated over a two-dimensional hill in order to characterize the spatial distribution of the mean velocity and the turbulence statistics. A flow simulation is then performed through a wind farm consisting of five horizontal-axis wind turbines sited over the same hill in an aligned layout. The resulting flow characteristics are compared with the former case, i.e., without wind turbines. To assess the validity of the simulations, the results are compared with the wind-tunnel measurements. It is found that LES can reproduce the flow field effectively, and, specifically, the speed-up over the hilltop and the velocity deficit and turbulence intensity enhancement induced by the turbines are well captured by the simulations. Besides, the vertical profiles of the mean velocity and turbulence intensity at different streamwise positions match well the ones of the experiment. In addition, another numerical experiment is carried out to show how higher (and more realistic) thrust coefficients of the turbines can lead to stronger wakes and, at the same time, higher turbulence intensities.

---

<sup>1</sup>The contents of this chapter are published in: Shamsoddin, S. and Porté-Agel, F. Large-Eddy Simulation of Atmospheric Boundary-Layer Flow Through a Wind Farm Sited on Topography. *Boundary-Layer Meteorology*, 163(1):1-17, 2017.

### 4.1 Introduction

A brief summary is given of previous research on turbulent boundary-layer flow over complex terrain and the effect of topography on wind-turbine wakes. The first part presents a review on the experimental, analytical and numerical studies of flow over complex terrain carried out during the last 50 years. In the second part, the rather new topic of wake-topography interaction is traced back.

#### 4.1.1 Flow over complex terrain

##### Experimental studies

Field measurements of the wind-velocity distribution over hills have been particularly valuable to both the scientific and engineering communities. The first of this category of measurements (to the best knowledge of the authors) is the surface wind observations of [Mason and Sykes \(1979\)](#) over Brent Knoll, a nearly circular isolated hill located in Somerset, England. In their study, they extended the Jackson–Hunt theory (see Section 4.1.1) to three dimensions and compared their experimental data with the results of their model. Subsequently, the British Meteorological Office (Met Office) and the Commonwealth Scientific and Industrial Research Organisation (CSIRO) made observations of flow over Black Mountain ([Bradley, 1980](#)), Ailsa Craig ([Jenkins et al., 1981](#)), Bungendore Ridge ([Bradley, 1983](#)), Blashaval ([Mason and King, 1985](#)) and Nyland hill ([Mason, 1986](#)).

Probably the Askervein project is the most detailed and comprehensive of all measurement campaigns in the twentieth century, which was comprised of two field experiments in 1982 and 1983 on and around Askervein, a 116 m high hill on the west coast of the island of South Uist in the Outer Hebrides of Scotland (for an overview, see [Taylor and Teunissen, 1987](#)). With over 50 towers whose heights ranged from 10 m to 50 m, three-component turbulence measurements were performed and nearly 150 h of data obtained. Later on, wind-tunnel simulations and numerical studies, which aimed to reproduce the flow field over the Askervein hill, were carried out by [Teunissen et al. \(1987\)](#) and [Raithby et al. \(1987\)](#), respectively. To date, the Askervein project has been a benchmark case against which numerical and analytical models of flow over topography have been tested ([Bechmann et al., 2011](#)).

Recently, [Berg et al. \(2011\)](#) performed an experimental campaign in 2007-2008 to obtain wind and turbulence data over the Bolund hill, an isolated steep hill located in the Bolund peninsula in Denmark. They reported dramatic turbulence intensity enhancements over the hill with respect to the incoming flow (a 300% increase) and a significant reverse flow near the surface. Therefore, they argued that to numerically simulate the flow successfully, models capable of resolving at least the most important spatial and temporal

structures of the turbulent flow are necessary and, accordingly, suggested that large-eddy simulation (LES) models would be the most appropriate tools for this purpose. The Bolund project, for neutral thermal conditions, has emerged as a new benchmark to validate numerical flow models (Bechmann et al., 2011); however, it should be noted that, because of the steep slopes of the hill, this project cannot be envisaged as a proper case to test the traditional linear models.

Apart from field measurements, laboratory experiments of flow over hills and ridges have also been performed substantially during the past few decades primarily using wind tunnels. Extensive wind-tunnel studies of flow over topography began in the early 1980s, when Britter et al. (1981) conducted flow measurements over a rough, relatively steep, bell-shaped, two-dimensional hill placed in a neutrally-stratified boundary layer. They reported a good agreement between their results and the previously developed analytical and numerical models (Jackson and Hunt, 1975; Taylor, 1977) for the upstream of and above the hill, but not for the wake. They also studied the flow over a smooth hill placed on a rough surface, and elaborated on the differences between the turbulent flow structures found close to the surface and those observed well above the surface. Pearse et al. (1981) and Arya and Shipman (1981) performed boundary-layer flow measurements over and past two-dimensional conical (triangular) ridges, and reported the spatial distribution of the mean velocity and turbulence statistics. Latterly, other groups carried out similar experiments on mainly simple two-dimensional hills (e.g., Finnigan et al., 1990; Snyder et al., 1991; Gong et al., 1996). More recently, flow measurements over three-dimensional hills have been performed in neutral stratification conditions by Ishihara et al. (1999), and in different stability conditions (neutral, stable and unstable) by Takahashi et al. (2005).

### Analytical and numerical studies

Analytical studies of turbulent flows over topography commenced with the groundbreaking analysis of Jackson and Hunt (1975) who developed a linear solution for two-dimensional turbulent flow over low hills with arbitrary shapes. They influenced and inspired numerous analytical studies in the following years (e.g., Mason and Sykes, 1979; Sykes, 1980; Hunt et al., 1988).

While the above-mentioned attempts to analytically characterize the flow over low hills were remarkably successful in developing a deeper understanding of the linear response of the flow to topography, the non-linear nature of the problem has been essentially elusive for such analyses. Non-linear effects, amongst which flow separation is the most notable, are more likely to occur for relatively steep topography that induces greater perturbations to the flow than do the low hills suited for analytical analysis. Therefore, being able to predict the non-linear reactions of the flow to complex terrain is highly important both from an engineering and a weather prediction standpoint (Wood, 2000).

For this purpose, numerical solutions of the non-linear governing equations of the flow have been attempted since the mid 1970s, when [Taylor and Gent \(1974\)](#) developed a numerical model for two-dimensional turbulent boundary-layer flow above gentle topography. They used conformal mapping for the geometrical transformation of the domain along with mixing length and turbulent energy equation models for the turbulence closure. In 1977, [Clark \(1977\)](#) employed a terrain-following curvilinear coordinate system in his three-dimensional flow model over topography, and presented the derivation of the governing equations in a meticulous way. Later, other numerical simulations of flow over hills were performed, reporting comparisons with experimental data, and contributing to a better understanding of the physics of the flow (e.g., [Deaves, 1976, 1980](#); [Zeman and Jensen, 1987](#); [Uchida and Ohya, 1999](#)).

In the 1990s, the LES technique proved to be a useful tool for numerical simulation of the atmospheric boundary layer (ABL) ([Mason, 1994](#)). The first application of LES for simulation of the neutral ABL over hills was achieved by [Gong et al. \(1996\)](#) (as mentioned by [Wood, 2000](#)), who used a modified code that was previously developed by [Krettenauer and Schumann \(1992\)](#) and [Dörnbrack and Schumann \(1993\)](#). They represented the topography with the same coordinate-transformation technique as [Clark \(1977\)](#) and, for turbulence parametrization, used an eddy diffusivity model that is a function of the grid scale and the subgrid-scale (SGS) kinetic energy. [Iizuka and Kondo \(2004\)](#), [Wan et al. \(2007\)](#) and [Wan and Porté-Agel \(2011\)](#) performed LES of ABL flow over two-dimensional hills and by comparing their results with wind-tunnel data, evaluated the performance of different SGS models. They all suggested that the inaccuracy of the scale-invariance assumption in standard dynamic models can lead to considerable errors in prediction of flow statistics. It is noteworthy to mention that in most of the numerical simulations of the flow over complex terrain, the terrain-following coordinate system has been implemented; however, considering the limitations of this technique, particularly for steep hills, the immersed-boundary method (IBM) (proposed by [Peskin, 1972](#)) can be a reliable alternative (for a comparison between these two methods see [Uchida and Ohya, 1999](#)). Recently, [Diebold et al. \(2013\)](#) coupled the IBM with LES to simulate flow over topography and compared their results with the field data of [Berg et al. \(2011\)](#) (the Bolund project) and the wind-tunnel measurements of [Ishihara et al. \(1999\)](#).

### 4.1.2 Wind turbines and topography

Investigation of the effect of complex terrain on wind-turbine wakes began in the early 1990s. In 1991, [Taylor and Smith \(1991\)](#) performed the first (to our knowledge) wind-tunnel measurements to study the influence of topography on wake flows. They placed a static turbine simulator in several positions over a flat-topped two-dimensional hill exposed to boundary-layer flow. They discussed in detail about the degree of significance of the influence of the topography on the wake and the fact that the presence of turbines on hills can delay the flow separation. [Helmis et al. \(1995\)](#) presented field measurements



of the near-wake of a single wind turbine situated on complex terrain. More recently, [Tian et al. \(2013\)](#) carried out a wind-tunnel experiment of an array of five turbines over a two-dimensional Gaussian low-slope hill. By comparing the power output and fatigue loads between wind farms on flat terrain and hilly terrain, they assessed the influence of topography on the wake flow.

The early stages of the numerical and analytical studies of wake flows over topography included [Voutsinas et al. \(1990\)](#) and [Hemon et al. \(1991\)](#). In their numerical model, [Voutsinas et al. \(1990\)](#) introduced a correction velocity term to take into account the streamline curvatures in the undisturbed flow that arise under the influence of the topography. [Hemon et al. \(1991\)](#), in their numerical code that uses a vortex method to compute the vorticity generated from the turbine blades, and a finite difference method to solve for the flow field in the turbulent wake of the turbine, accounted for the effect of the hill with an induced velocity caused by a straight vortex filament. More recently, [Politis et al. \(2012\)](#) simulated flow through wind turbines over complex terrain by solving the Navier–Stokes equations, using two Navier–Stokes solvers with  $k - \epsilon$  and  $k - \omega$  turbulence models and an actuator-disk model for the turbines. They simulated a real wind farm in Spain and compared the power outputs with field measurements. Moreover, they simulated the flow over a Gaussian hill with a turbine on the hilltop and compared its wake flow with the wake over a flat terrain. Later on, [Yang et al. \(2014\)](#) performed LES of the flow through a hypothetical wind farm situated downwind of complex terrain. They used an immersed-boundary method to represent the topography, a standard dynamic model for modelling the SGS stresses, and an actuator-line model to parametrize the wind-turbine forces.

Surveying the literature, a point comes to one’s attention, namely, even though study of the flow through wind farms sited on flat terrain by using numerical simulation techniques (especially LES) has been already rather well developed and even validated with measurements (e.g., [Wu and Porté-Agel, 2013](#)), relatively few works have focused on wind farms on topography. In view of this shortage of research activity in this area, we aim to address the subject of wind farms on topography. To our knowledge, this presents the first study in which LES of flow through a wind farm sited on topography is validated with experimental data.

Herein, we perform simulations of neutrally-stratified boundary-layer flow through a wind farm sited on an isolated hill within an LES framework. The LES framework and the coordinate-transformation technique are presented in Section 4.2. Next, the boundary-layer flow is simulated over a hill both with and without the presence of the wind turbines, and the results are compared with experimental data. The numerical and experimental setups are described in Section 4.3, and the results are presented in Section 4.4. A summary is given in Section 4.5.

## 4.2 Large-eddy simulation framework

LES solves the filtered incompressible Navier–Stokes equations (for a neutrally-stratified ABL), which can be written in rotational form as,

$$\frac{\partial \tilde{u}_i}{\partial x_i} = 0, \quad (4.1)$$

$$\frac{\partial \tilde{u}_i}{\partial t} + \tilde{u}_j \left( \frac{\partial \tilde{u}_i}{\partial x_j} - \frac{\partial \tilde{u}_j}{\partial x_i} \right) = -\frac{\partial \tilde{p}^*}{\partial x_i} - \frac{\partial \tau_{ij}}{\partial x_j} - \frac{f_i}{\rho} + F_p \delta_{i1}, \quad (4.2)$$

where the tilde represents a three-dimensional spatial filtering operation at scale  $\tilde{\Delta}$ ,  $\tilde{u}_i$  is the filtered velocity in the  $i$ -direction (with  $i = 1, 2, 3$  corresponding to the streamwise ( $x$ ), spanwise ( $y$ ) and vertical ( $z$ ) directions, respectively),  $\tilde{p}^* = \tilde{p}/\rho + \frac{1}{2}\tilde{u}_i\tilde{u}_i$  is the modified kinematic pressure where  $\tilde{p}$  is the filtered pressure,  $\tau_{ij} = \tilde{u}_i\tilde{u}_j - \tilde{u}_i\tilde{u}_j$  is the kinematic SGS stress,  $f_i$  is a body force (per unit volume) used to model the effects of the turbine on the flow,  $F_p$  is an imposed pressure gradient (acting as the driving force of the flow), and  $\rho$  is the constant fluid density. Herein,  $u$ ,  $v$  and  $w$  notations are also used for the  $u_1$ ,  $u_2$  and  $u_3$  velocity components, respectively. Regarding the parametrization of the SGS stresses, the Lagrangian scale-dependent dynamic model (Stoll and Porté-Agel, 2006b) is used.

### 4.2.1 Coordinate transformation

Coordinate transformation is one way of representing complex geometries in numerical flow simulations. In this method, a curvilinear grid that exactly follows the boundaries of the physical domain is created and, then, this body-conformal grid is transformed to a simple Cartesian grid (Figure 4.1). Since the spatial derivatives in the transformed and curvilinear grids are not equal, we need to establish relationships between them. Here, a brief presentation of the derivation process, which was first done by Clark (1977), is presented.

As can be seen in Figure 4.1, the physical domain has a terrain following coordinate system,  $(x, y, z)$ , over a hill whose surface equation can be described by the function  $Z_s(x, y)$ ; in other words,  $Z_s$  is the elevation of the ground surface with respect to a given fixed origin. This domain is transformed to a computational domain with coordinates

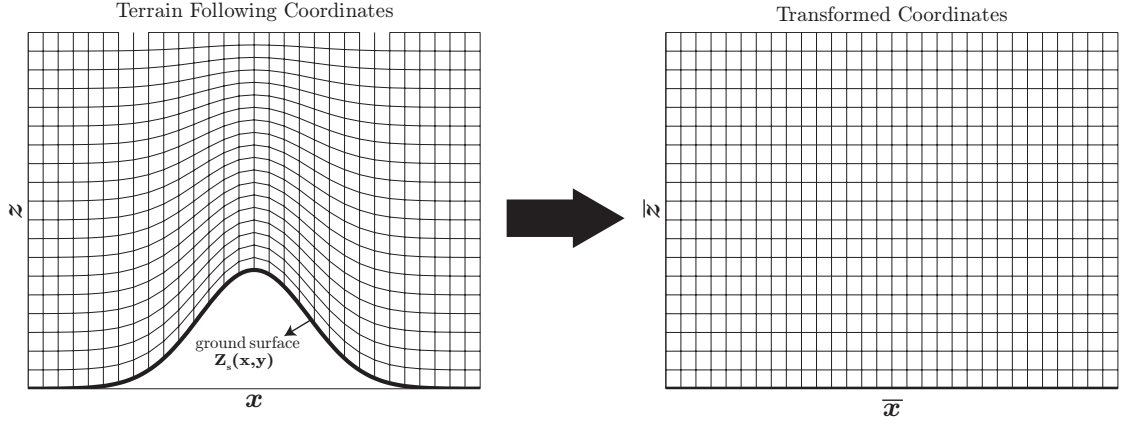


Figure 4.1 – Coordinate transformation

$(\bar{x}, \bar{y}, \bar{z})$ . The relations between these two coordinate systems are as follows,

$$\bar{x} = x, \quad (4.3a)$$

$$\bar{y} = y, \quad (4.3b)$$

$$\bar{z} = H \frac{z - Z_s}{H - Z_s}, \quad (4.3c)$$

where  $H$  is the maximum height of the domain.

All of the spatial derivatives in the governing equations (Equations 4.1 and 4.2) are in terms of the physical coordinates, and we need to write them in terms of the derivatives in the transformed coordinates, which can be calculated using common numerical schemes. In other words, if  $\phi$  is an arbitrary flow variable, we aim to write  $\partial\phi/\partial x_i$  as a function of  $\partial\phi/\partial\bar{x}_i$ . To do this, we construct the Jacobian matrix of the transformation,

$$J = \begin{bmatrix} \frac{\partial x}{\partial \bar{x}} & \frac{\partial y}{\partial \bar{x}} & \frac{\partial z}{\partial \bar{x}} \\ \frac{\partial x}{\partial \bar{y}} & \frac{\partial y}{\partial \bar{y}} & \frac{\partial z}{\partial \bar{y}} \\ \frac{\partial x}{\partial \bar{z}} & \frac{\partial y}{\partial \bar{z}} & \frac{\partial z}{\partial \bar{z}} \end{bmatrix} = \begin{bmatrix} 1 & 0 & (1 - \frac{\bar{z}}{H}) \frac{\partial Z_s}{\partial x} \\ 0 & 1 & (1 - \frac{\bar{z}}{H}) \frac{\partial Z_s}{\partial y} \\ 0 & 0 & (1 - \frac{Z_s}{H}) \end{bmatrix}. \quad (4.4)$$

We define  $G$  as the determinant of this matrix,

$$G \equiv \det(J) = 1 - \frac{Z_s}{H}. \quad (4.5)$$

In fact, the Jacobian matrix, by definition, is a matrix that enables us to express the transformed derivatives  $(\partial\phi/\partial\bar{x}_i)$  in terms of the original derivatives  $(\partial\phi/\partial x_i)$ ,

$$\begin{bmatrix} \frac{\partial\phi}{\partial\bar{x}} \\ \frac{\partial\phi}{\partial\bar{y}} \\ \frac{\partial\phi}{\partial\bar{z}} \end{bmatrix} = J \begin{bmatrix} \frac{\partial\phi}{\partial x} \\ \frac{\partial\phi}{\partial y} \\ \frac{\partial\phi}{\partial z} \end{bmatrix}. \quad (4.6)$$

However, we need exactly the opposite, namely, to express the original derivatives in terms of the transformed derivatives. Thus, the inverse of the Jacobian matrix should be used,

$$\begin{bmatrix} \frac{\partial\phi}{\partial x} \\ \frac{\partial\phi}{\partial y} \\ \frac{\partial\phi}{\partial z} \end{bmatrix} = J^{-1} \begin{bmatrix} \frac{\partial\phi}{\partial\bar{x}} \\ \frac{\partial\phi}{\partial\bar{y}} \\ \frac{\partial\phi}{\partial\bar{z}} \end{bmatrix}. \quad (4.7)$$

The inverse of the Jacobian matrix can be calculated as follows,

$$J^{-1} = \frac{1}{G} \begin{bmatrix} G & 0 & (\frac{\bar{z}}{H} - 1) \frac{\partial Z_s}{\partial x} \\ 0 & G & (\frac{\bar{z}}{H} - 1) \frac{\partial Z_s}{\partial y} \\ 0 & 0 & 1 \end{bmatrix} = \frac{1}{G} \begin{bmatrix} G & 0 & G_x \\ 0 & G & G_y \\ 0 & 0 & 1 \end{bmatrix}, \quad (4.8)$$

where  $G_x$  and  $G_y$  are defined such that,

$$G_x = (\frac{\bar{z}}{H} - 1) \frac{\partial Z_s}{\partial x}, \quad (4.9a)$$

$$G_y = (\frac{\bar{z}}{H} - 1) \frac{\partial Z_s}{\partial y}. \quad (4.9b)$$

We are now in a position to fully express the original derivatives in terms of the transformed derivatives. In order to retain the equations in conservative form, a small mathematical manipulation (the chain rule) is applied and the derivatives of an arbitrary variable,  $\phi$ , in the three directions, can be expressed in the transformed coordinates as follows,

$$G \frac{\partial \phi}{\partial x} = \frac{\partial}{\partial \bar{x}} (G\phi) + \frac{\partial}{\partial \bar{z}} (G_x \phi), \quad (4.10a)$$

$$G \frac{\partial \phi}{\partial y} = \frac{\partial}{\partial \bar{y}} (G\phi) + \frac{\partial}{\partial \bar{z}} (G_y \phi), \quad (4.10b)$$

$$G \frac{\partial \phi}{\partial z} = \frac{\partial \phi}{\partial \bar{z}}. \quad (4.10c)$$

Thus, in this fashion, we implement the above derivative transformations for all spatial derivatives present in the governing equations of the flow.

### 4.3 Numerical set-up

In this section, the details of the numerical techniques used and the set-up configuration are presented. We have attempted to reproduce in our simulations the experimental set-up used by [Tian et al. \(2013\)](#) in order to compare and validate our results with their measurements.

The LES code is a modified version of that described by [Albertson and Parlange \(1999\)](#), [Porté-Agel et al. \(2000\)](#), [Wan et al. \(2007\)](#) and [Porté-Agel et al. \(2011\)](#). A three-dimensional structured mesh is employed, which has  $N_x$  and  $N_y$  nodes in the  $x$  and  $y$  directions, respectively, and  $N_z$  nodes in the  $z$  direction. The mesh is staggered in the  $z$  direction; this means the layers in which the vertical component of velocity ( $w$ ) is stored are located halfway between the layers in which all the other main flow variables ( $u, v, p$ ) are stored. The first  $w$  nodes are located on the  $z = 0$  plane, while the first ( $u, v, p$ )-nodes are located on the  $z = \Delta z/2$  plane.

To compute the spatial derivatives, a Fourier-based pseudospectral scheme is used in the horizontal directions, and a second-order finite difference method is used in the vertical direction. The governing equations for conservation of momentum are integrated in time with the second-order Adams–Bashforth scheme.

The boundary conditions in the horizontal directions are mathematically periodic. For the bottom boundary condition, the instantaneous surface shear stress is calculated using the Monin–Obukhov similarity theory ([Monin and Obukhov, 1954](#)) as a function of the local horizontal velocities at the nearest (to the wall) vertical grid points ( $z = \Delta z/2$ ) (see, for instance, [Moeng, 1984](#); [Stoll and Porté-Agel, 2006a](#); [Abkar and Porté-Agel, 2012](#)). Implementation of the surface boundary condition on the hill is done in the same way as described in [Wan et al. \(2007\)](#). For the upper boundary, an impermeable free-stress boundary condition is assigned, i.e.,  $\partial \tilde{u}_1 / \partial z = \partial \tilde{u}_2 / \partial z = \tilde{u}_3 = 0$

To eliminate the effects of the periodicity of the flow in the  $x$  direction and to ensure that we have an undisturbed inflow (as in the experiment), a buffer zone upstream of the hill is employed to adjust the flow to an undisturbed inflow condition which matches that of the experiment both in terms of the mean velocity and the turbulence intensity (for comparison see Section 4.4). The use of this technique, i.e., using an inflow boundary condition in a direction in which the flow variables are discretized using Fourier series, has been shown to be successful in the works of [Tseng et al. \(2006\)](#), [Wan and Porté-Agel \(2011\)](#) and [Wu and Porté-Agel \(2011\)](#). To generate the inflow field, a precursory simulation of the boundary-layer flow over a flat terrain (with a surface roughness length to boundary-layer height ratio of  $5.6 \times 10^{-5}$ ) is performed, and instantaneous 3D velocity components in a specific  $yz$  plane are saved. These stored planes of velocity vectors from the precursory simulation are later fed into the simulation of the flow over the hilly terrain, at the most downwind  $yz$  plane of the buffer zone.

Figure 4.2 shows a schematic of the geometrical configuration of the computational domain. The hill is two-dimensional with the following surface relation,

$$Z_s(x) = h \exp \left[ -0.5 \left( \frac{x}{\sigma} \right)^2 \right], \quad (4.11)$$

where  $h = 285$  mm is the hill height,  $L = 570$  mm is the hill half-length (the distance from the hilltop to a point whose height is half the hill height), and  $\sigma = L/1.1774$ . The buffer zone takes up about 12% of the domain length. The domain dimensions are  $L_x = 12$  m,  $L_y = 2$  m and  $L_z = 2.3$  m in the streamwise, spanwise and vertical directions, respectively. Regarding the computational mesh, the number of grid points in each of the three directions is  $N_x = 128$ ,  $N_y = 50$ , and  $N_z = 80$ . The chosen resolution of the grid is well within the range that has been previously shown to result in grid-independent results for the cases of flow over a hilly terrain (see [Wan et al. \(2007\)](#), Section 3) and flow through wind turbines (see [Wu and Porté-Agel \(2011\)](#), Section 4, and [Wu and Porté-Agel \(2013\)](#), Section 4.1). The positions of the five model horizontal-axis wind turbines are indicated in the figure, with the middle turbine (T3) exactly located on the hilltop. The centres of all five turbine rotors are located in the vertical midplane of the domain. The hub height,  $Z_h$ , of the model wind turbines is 225 mm, and their rotor diameter,  $D$ , is 254 mm. The turbine forces on the flow are modelled with the standard actuator-disk model, for which the value of the thrust coefficients ( $C_T$ ) of the turbines is needed. Therefore, for each turbine the  $C_T$  values reported by [Tian et al. \(2013\)](#) (see Table 4.1) are used. The reference wind velocity for all  $C_T$  values is the velocity of the undisturbed inflow at a height equal to the hub height of the turbines (this velocity is designated as  $U_h$ ).

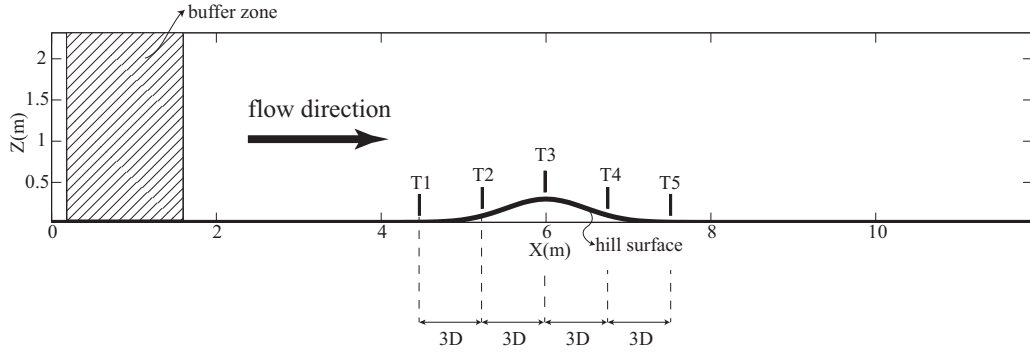


Figure 4.2 – Schematic of the computational set-up, seen in the  $xz$  midplane of the domain

Table 4.1 – Thrust coefficient of the turbines

	T1	T2	T3	T4	T5
Thrust coefficient, $C_T$	0.14	0.132	0.287	0.129	0.091

## 4.4 Results and discussion

Figures 4.3-4.7 show the results of the simulation of the flow over the hill when the turbines are not present. Figures 4.3 and 4.4 show contour plots of the instantaneous and mean streamwise velocity component (for all the mean quantities reported herein, the averaging time is 38.2 s) in the vertical midplane of the domain. The speed-up of the flow over the hilltop and the creation of a low-speed region immediately downstream

of the hill, which are among the most well-known effects of the hills on the flow, can be easily seen in these figures. Since the hill cannot be considered as a steep one (its mean slope ( $s = h/2L = 0.25$ ) is less than 0.3, which is a limit proposed by [Mason and King, 1985](#)), a reverse flow is not observed in the wake of the hill. The vertical profiles of the mean streamwise velocity component in five different positions can be seen in Figure 4.5. Each position mentioned in this figure refers to the position of the corresponding turbine indicated in Figure 4.2. The results show a fairly good agreement with the wind-tunnel measurements of [Tian et al. \(2013\)](#). Figure 4.6 shows a contour plot of the streamwise turbulence intensity (TI) in the vertical midplane of the domain, and the vertical profiles of the TI at the five above-mentioned positions can be seen in Figure 4.7. It should be noted that TI is calculated as the standard deviation of the streamwise velocity component at a given point divided by the local mean streamwise velocity component at the same point. One can observe the drop of TI above the hilltop and the creation of a high-TI region in the lee-side of the hill. In Figure 4.7, likewise, a good agreement between the simulation results and the measurements can be seen. An animation of the simulated flow in this case is available in Online Resource 1.

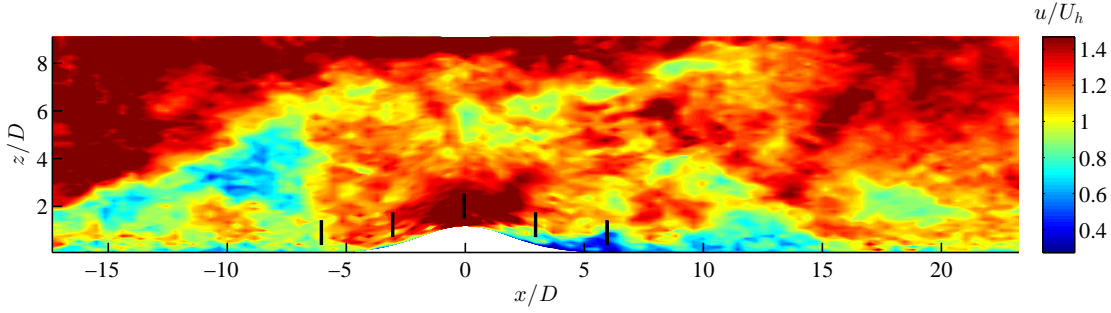


Figure 4.3 – Contours of the instantaneous streamwise velocity component in the vertical midplane of the domain in the case without the turbines

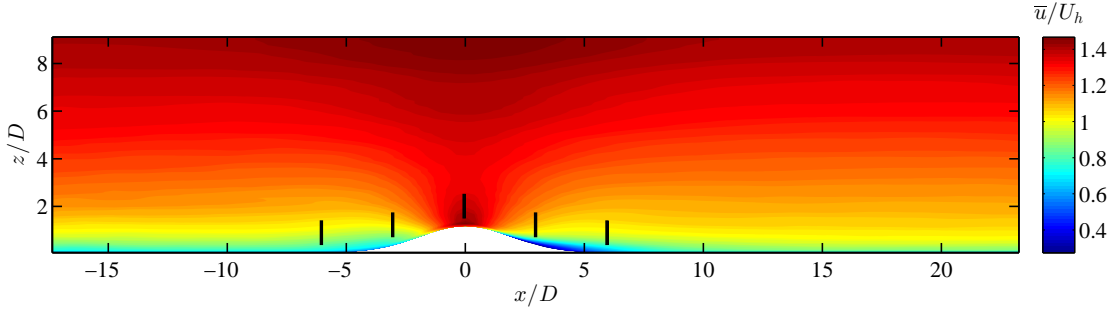


Figure 4.4 – Contours of the mean streamwise velocity component in the vertical midplane of the domain in the case without the turbines



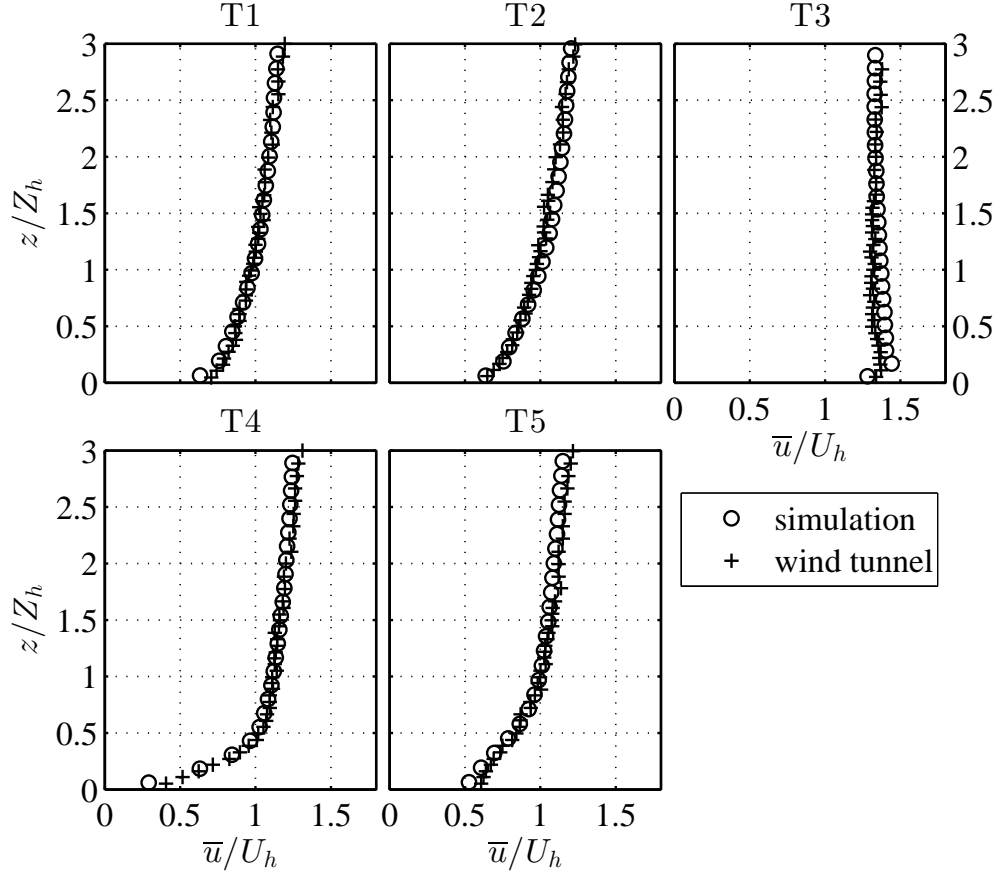


Figure 4.5 – Vertical profiles of the mean streamwise velocity component in five different streamwise positions in the vertical midplane of the domain in the case without the turbines (wind-tunnel data from [Tian et al., 2013](#))

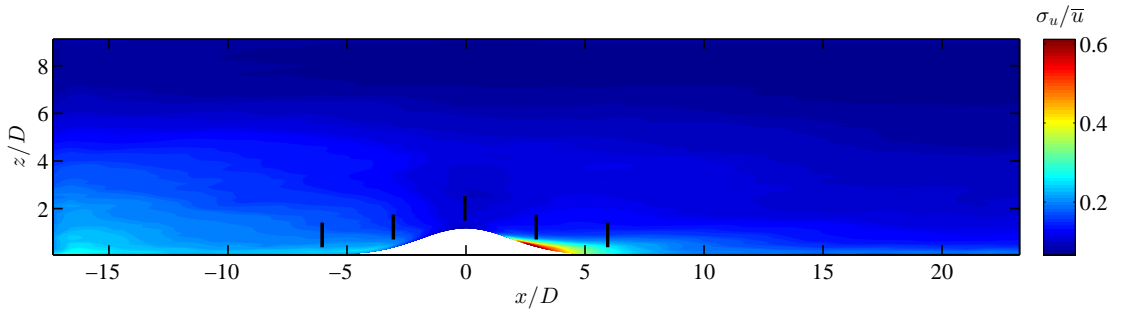


Figure 4.6 – Contours of the streamwise turbulence intensity in the vertical midplane of the domain in the case without the turbines

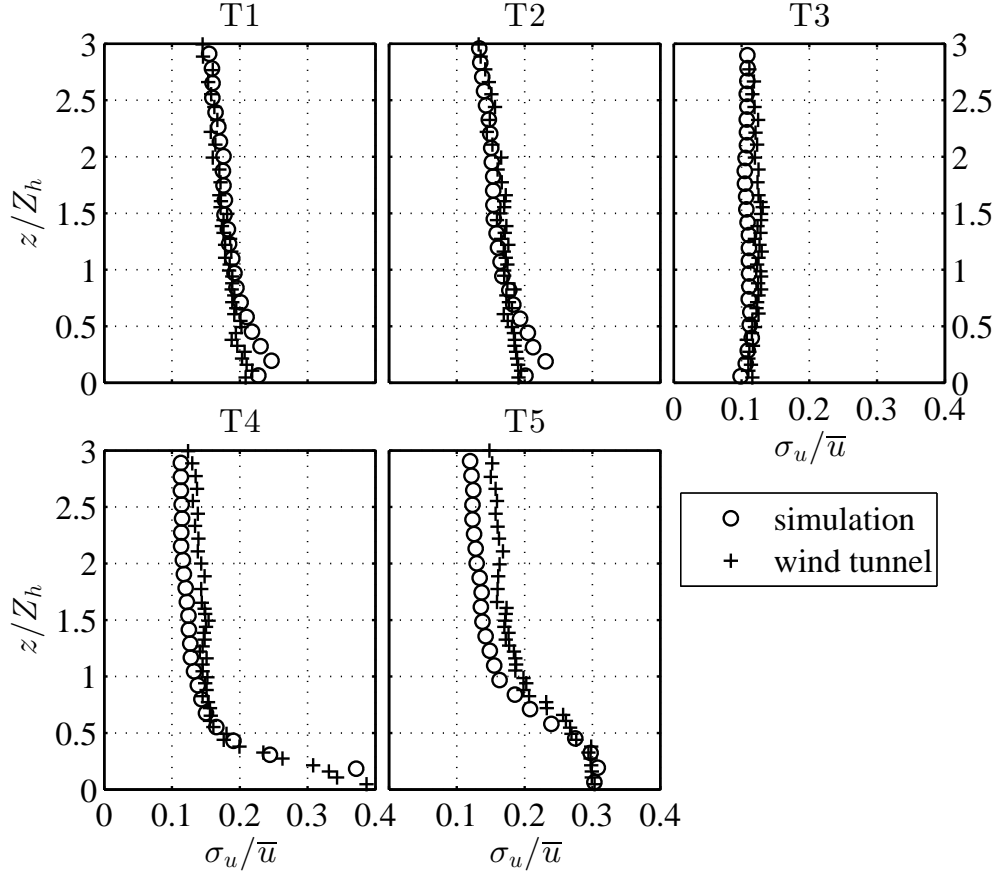


Figure 4.7 – Vertical profiles of the streamwise turbulence intensity in five different streamwise positions in the vertical midplane of the domain in the case without the turbines (wind-tunnel data from [Tian et al., 2013](#))

Figures 4.8-4.11 show the flow field in the presence of the turbines. It should be noted that the figures containing the contour plots (Figures 4.8 and 4.10) show the case with all five turbines working, while in Figures 4.9 and 4.11, at each streamwise position, the corresponding profile shows the distribution of the quantity in question (mean velocity or turbulence intensity) in the case when the turbine at that position is removed and only the remaining four turbines are working. This is because the measurements were done in this way and we wanted our simulated profiles to be comparable to the experimental data. In Figure 4.8, the effect of the turbine wakes can be seen by observing the deformation of the contour lines with respect to the case without the turbines (see Figure 4.4). In Figure 4.9, a comparison between the simulation results and wind-tunnel measurements can be seen for the vertical profiles of the mean streamwise velocity component at five different positions in the vertical midplane of the domain. Figure 4.10 displays the contours of the streamwise TI. The added TI from each turbine can be noticed in this figure. Finally, Figure 4.11 shows the vertical distribution of the streamwise TI by displaying both the simulation and wind-tunnel data. It can be said that the overall agreement between these two sets of data is satisfactory. An interesting observation that can be made in this figure is the fact that the value of TI in the immediate wake of the hill and near the ground ( $z/Z_h < 0.5$ ) is less than the one for the case without the turbines (see Figures 4.7 and 4.11 for comparison). This is likely due to the fact that the deceleration of the flow by the turbines decreases the vertical gradients of the streamwise velocity component in the lee-side of the hill (compare Figures 4.5 and 4.9 in position 4).

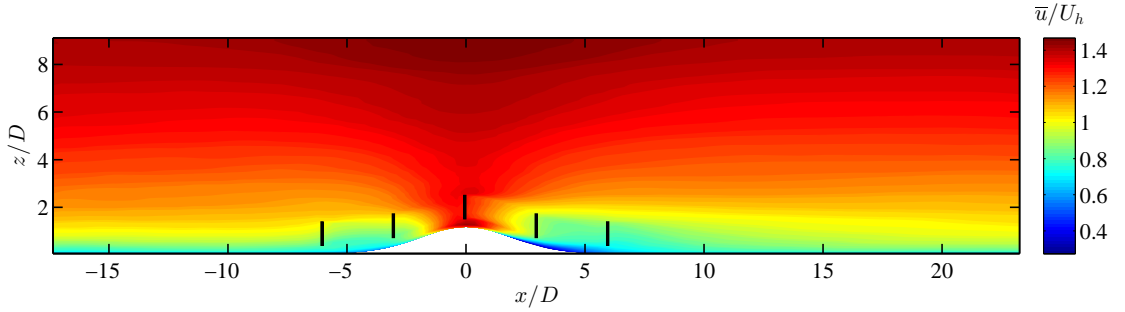


Figure 4.8 – Contours of the mean streamwise velocity component in the vertical midplane of the domain in the case with the turbines

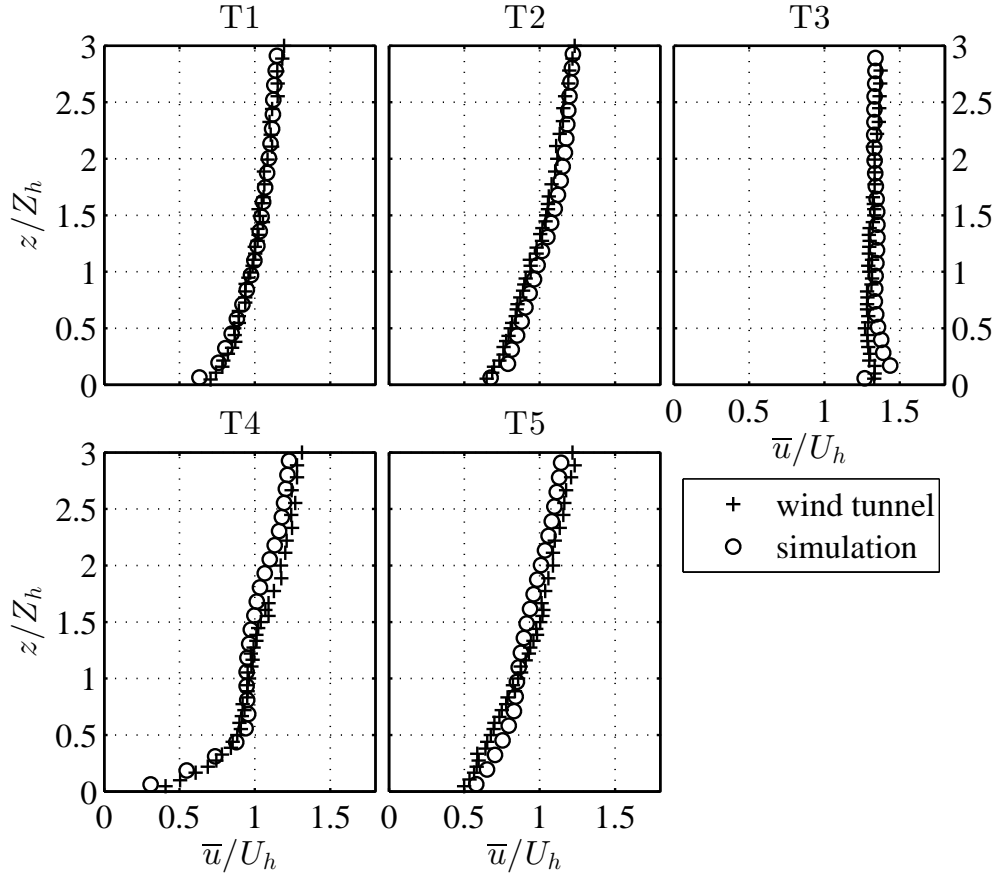


Figure 4.9 – Vertical profiles of the mean streamwise velocity component in five different streamwise positions in the vertical midplane of the domain in the case with the turbines (wind-tunnel data from [Tian et al., 2013](#))

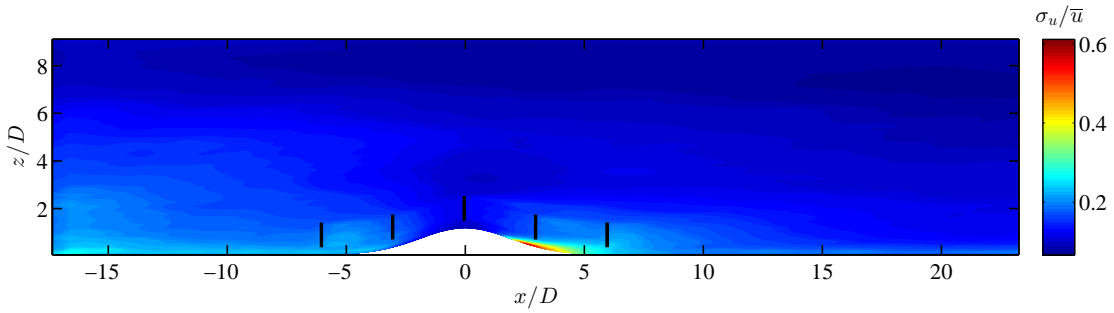


Figure 4.10 – Contours of the streamwise turbulence intensity in the vertical midplane of the domain in the case with the turbines

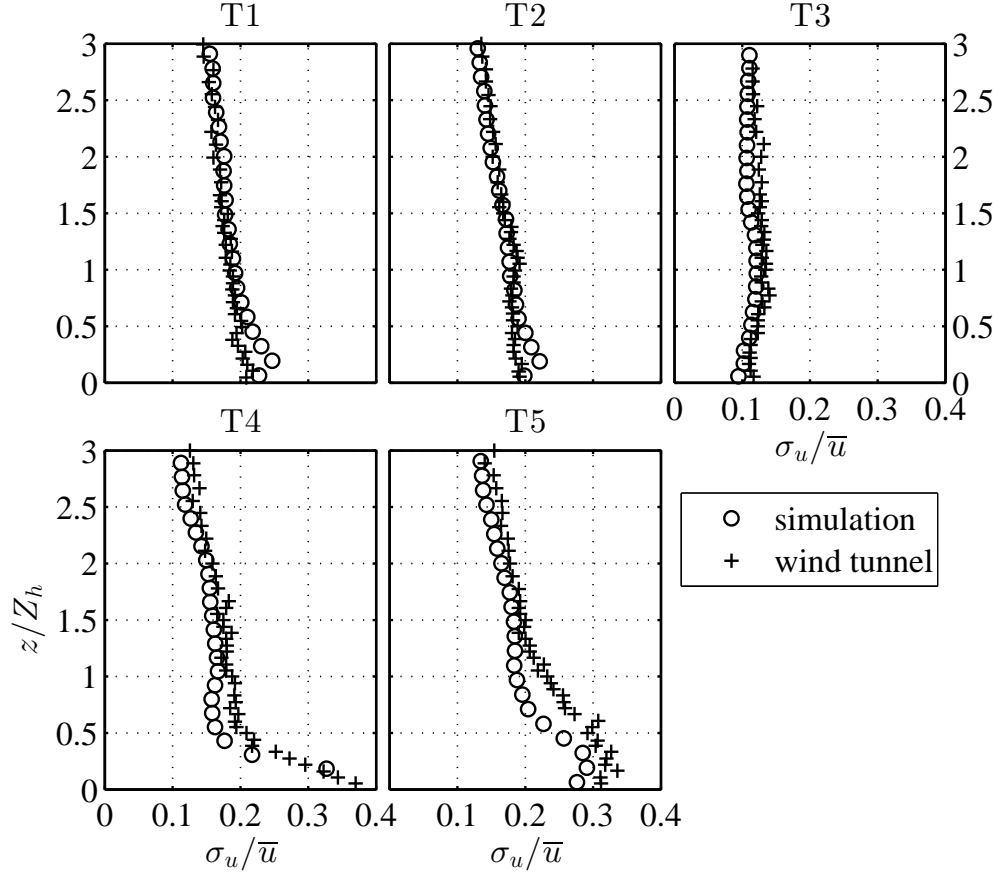


Figure 4.11 – Vertical profiles of the streamwise turbulence intensity in five different streamwise positions in the vertical midplane of the domain in the case with the turbines (wind-tunnel data from [Tian et al., 2013](#))

It should be noted that the measured thrust coefficients of the turbines in the experiment are relatively low with respect to large-scale wind turbines operating in the field (for instance, see Hansen et al., 2012). If we consider higher (and consequently more realistic) thrust coefficients for the turbines in the same setup, the wake effects would be more obvious. To illustrate this, a simulation is performed in a set-up whose only difference with the above-mentioned one is that the thrust coefficients of the turbines are increased to higher values: the  $C_T$ s of the three upstream turbines are tripled, and the ones of the other two are doubled. These new values of  $C_T$  (which are used here only to show a representative case of turbines with more realistic  $C_T$ ) are chosen such that the turbine at the hilltop acquires a thrust coefficient (based on the *local* upstream velocity) of around 0.7. Also note that since  $C_T$  is defined here based on the undisturbed flow velocity, and the last two turbines are operating in a strongly waked condition, their values of  $C_T$  are increased with a lower factor than the upstream turbines. Figure 4.12 shows an instantaneous representation of the flow field in the vertical midplane of the domain where the wakes of the turbines are more clear and pronounced. Furthermore, Figure 4.13 shows the contours of the mean streamwise velocity component in which the wake flow of the wind farm on the hill can be seen clearly. The figure shows as well that the wake region generated by the turbines almost conforms geometrically with the hill shape. Besides, in Figure 4.14, one can observe the new vertical velocity profiles in this case, and compare them with the original case where the thrust coefficients are relatively low. Finally, in Figure 4.15, it is seen that higher  $C_T$ s can dramatically increase the TI in the lee-side of the hill; here, the TI has increased to more than 120% (For comparison reasons, the same colourbar as the previous cases has been used in this figure as well). This could be due to the higher shear and, consequently, increased mixing that is caused by higher  $C_T$ s in this case. An animation of the simulated flow in this case is available in Online Resource 2, where we can see the accumulation of the velocity deficit near the position of T4 (also seen in Figure 4.13). One can also note that the location of the region of maximum velocity deficit (i.e., minimum velocity) is approximately the same as the one of the maximum TI.

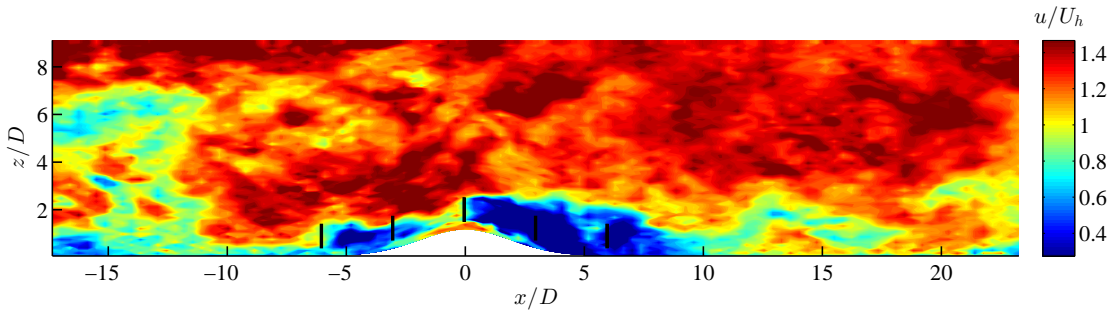


Figure 4.12 – Contours of the instantaneous streamwise velocity component in the vertical midplane of the domain in the case where the thrust coefficients of the turbines are increased

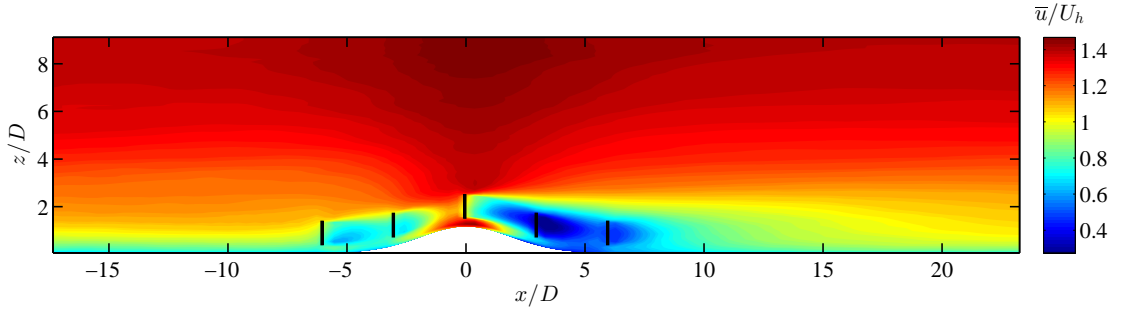


Figure 4.13 – Contours of the mean streamwise velocity component in the vertical midplane of the domain in the case where the thrust coefficients of the turbines are increased

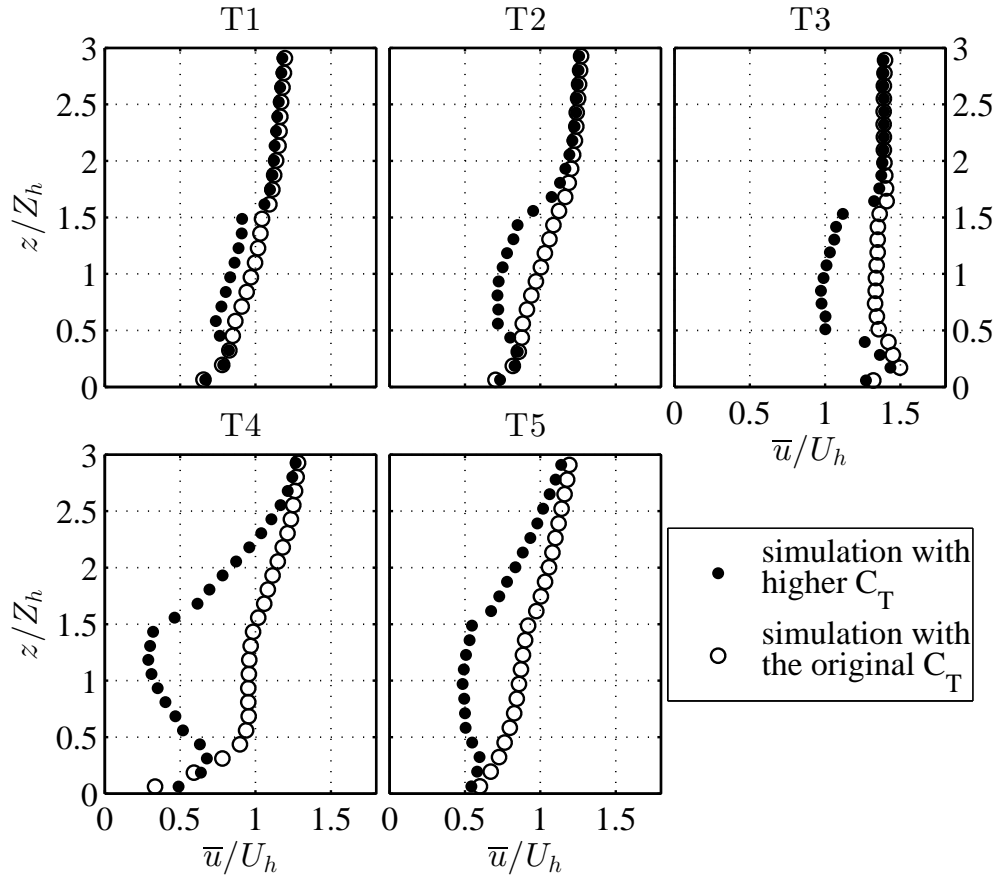


Figure 4.14 – Vertical profiles of the mean streamwise velocity in five different streamwise positions in the vertical midplane of the domain in the case where the thrust coefficients of the turbines are increased

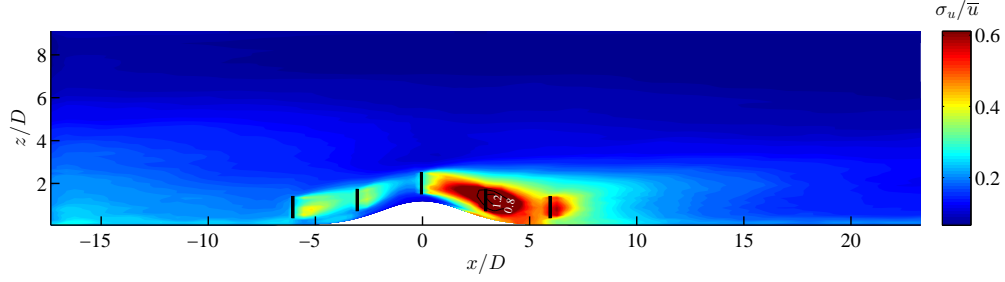


Figure 4.15 – Contours of the streamwise turbulence intensity in the vertical midplane of the domain in the case where the thrust coefficients of the turbines are increased

## 4.5 Summary

Noting that onshore wind turbines (and wind farms) are often installed in complex terrain, it is of great importance, both from a practical and scientific point of view, to be able to accurately predict turbine wake flows over topography. Before using and implementing a given modelling framework for a real wind farm in realistic complex terrain, one would envisage that the first step to assess the accuracy of that modelling framework for such a complex flow (in which many different factors play a role) is to apply the model to an idealized case and compare the model results with the data from an experiment carried out on the same idealized case.

In the present study, seeking to realize the above-mentioned goal, we used large-eddy simulation, in which a coordinate transformation technique is employed to resolve the topography, to simulate boundary-layer flow through and above a wind farm sited on a hill. The simulations were performed for two cases: (1) the case in which no turbine is located on the hill, and (2) the case in which turbines are sited on the hill. For both cases, the simulation results were compared with the experimental data obtained from a wind-tunnel study of [Tian et al. \(2013\)](#). The agreement between the LES results and the measurements was observed to be fairly good. To the best knowledge of the authors, this is the first study in which a large-eddy simulation of flow in a wind farm sited on hilly terrain has been validated with experimental data. In addition, another numerical experiment was carried out to show how higher thrust coefficients of the turbines can lead to stronger wakes and at the same time higher turbulence intensities.

Future research should focus on extending the validation of the LES technique to the simulation of a wider and more realistic range of flow and turbine operation conditions over complex terrain. Considering the current shortage of experimental datasets available, achieving that goal requires designing and carrying out new experiments (in the wind tunnel and in the field) that include a broader range of topographies (e.g., different terrain shapes and slopes), thermal stratification (neutral, stable and unstable), and turbine operating conditions (e.g., turbine thrust and power coefficients).



# 5 Turbulent planar wakes under pressure gradient conditions<sup>1</sup>

## Abstract

Accurate prediction of the spatial evolution of turbulent wake flows under pressure gradient conditions is required in some engineering applications such as the design of high-lift devices and wind farms over topography. In this paper, we aim to develop an analytical model to predict the evolution of a turbulent planar wake under an arbitrary pressure gradient condition. The model is based on the cross-stream integration of the streamwise momentum equation and uses the self-similarity of the mean flow. We have also made an experimentally-supported assumption that the ratio of the maximum velocity deficit to the wake width is independent of the imposed pressure gradient. The asymptotic response of the wake to the pressure gradient is also investigated. After its derivation, the model is successfully validated against experimental data by comparing the evolution of the wake width and maximum velocity deficit. The inputs of the model are the imposed pressure gradient and the wake width under zero pressure gradient. The model does not require any parameter tuning and is deemed to be practical, computationally fast, accurate enough, and therefore useful for the scientific and engineering communities.

## 5.1 Introduction

A better understanding of turbulent wakes under different pressure gradient scenarios is beneficial from both an engineering and a pure fluid mechanics points of view. As examples of engineering domains in which this phenomenon is involved, one can mention

---

<sup>1</sup>The contents of this chapter are published in: Shamsoddin, S. and Porté-Agel, F. Turbulent planar wakes under pressure gradient conditions. *Journal of Fluid Mechanics*, 830:R4, 2017.

the aerodynamics of high-lift devices and also the wake structure and recovery in wind farms over hilly terrain. In high-lift devices, which are used in modern airliners, the wing is composed of several components, around which the air flows. The wake of the upstream components (e.g. the leading edge slat) has a crucial effect on the performance of the downstream components (e.g. the main wing and the flap(s)). These wakes are typically under strong (mainly adverse) pressure gradient conditions (Smith, 1975; Rumsey and Ying, 2002). Therefore, accounting for the pressure gradient effects for such wakes is decisive in the design of such systems. Wind-turbine wakes over hilly terrain (unlike flat terrain) also undergo nonzero pressure gradients and this affects their recovery rate and, consequently, the optimum design of modern wind farms over topography.

Several interesting studies have been performed on the subject at hand. Nakayama (1987) studied the effects of both pressure gradient and streamline curvature on mean flow and turbulence statistics of turbulent planar small-defect wakes. Liu et al. (2002) performed a systematic and rigorous experimental investigation on the effect of pressure gradient on turbulent planar wakes. They observed that the wake velocity deficit recovers faster in the favorable pressure gradient case, and slower in the adverse pressure gradient case. They also conducted a detailed analysis on how and why the pressure gradient affects the wake flow in such a manner. The same group carried out a similar experimental investigation, but this time for asymmetric wakes in Thomas and Liu (2004). An interesting finding in both experiments is the fact that the ratio of the maximum velocity deficit to the wake width was “virtually identical for each pressure gradient case”, i.e. this ratio was invariant under different pressure gradient values. Rogers (2002) performed direct numerical simulations (DNS) of temporally strained planar wakes and did a thorough analysis of the self-similarity behaviour of the wake flow in strained conditions. He concluded that classical self-similarity leads to results which do not match those of DNS, and he developed a modified similarity formulation for strained wakes, which is mainly based on the fact that the growth of the wake width is determined by the straining. In that study, different rates and geometries (planar and axisymmetric) of strain are studied. One conclusion of his work was that the shape of the velocity deficit profile is universal in all strain geometries and values, and this shape is the same as that of an unstrained wake.

The objective that we pursue in this paper is to develop an analytical model to predict the evolution of a turbulent planar wake under an arbitrary pressure gradient condition. Specifically, we aim to predict how a turbulent planar wake in zero pressure gradient, which has a well-established behaviour, is perturbed by imposing a nonzero pressure gradient. The model is based on the cross-stream integration of the streamwise momentum equation and uses the self-similarity of the mean flow. The model proves to be computationally fast and easy to use for engineering and scientific purposes.

This article is structured as follows: the proposed model, with all its variants, is derived in Section 5.2. The model is then validated against experimental data in Section 5.3. A

discussion about the effect of pressure gradient on turbulent planar wakes in a broader perspective is given in Section 5.4, and the paper is concluded with Section 5.5.

## 5.2 Analytical model for wakes under pressure gradient

### 5.2.1 Problem formulation

It is accepted that turbulent far wakes behave in a self-similar manner under zero pressure gradient condition (Tennekes and Lumley, 1972; Pope, 2000; Wygnanski et al., 1986). It has also been shown that turbulent wakes preserve their self-similar behaviour in the mean streamwise velocity under nonzero pressure gradient (or strained) conditions (Rogers, 2002; Liu et al., 2002; Thomas and Liu, 2004). A schematic of key variables in a turbulent planar wake is shown in Figure 5.1. As it can be seen,  $x$  is the streamwise direction,  $y$  is the lateral direction, the  $x$ -axis is coincident with the centerline of the wake,  $\bar{u}(x, y)$  is the velocity (hereafter, by velocity, we imply the mean streamwise velocity, unless otherwise stated) of the wake flow,  $U_b(x)$  is the velocity of the base flow, i.e. the velocity of the flow assuming there is no wake (in other words,  $U_b(x) = \lim_{|y| \rightarrow \infty} \bar{u}(x, y)$ ). We can express the velocity self-similarity of the wake as:

$$\frac{U_b - \bar{u}}{U_b} = C(x)f(y/\delta), \quad (5.1)$$

where  $C(x)$  is a function determining the maximum velocity deficit at each  $x$ -position,  $\delta(x)$  is a length scale in the  $y$ -direction and  $f(y/\delta)$  is a shape function that describes the shape of the velocity profile. It is also already shown that the shape function for turbulent wakes under zero (Wygnanski et al., 1986; Pope, 2000) and nonzero (Liu et al., 2002; Rogers, 2002) pressure gradients can be expressed by a Gaussian function. Thus, for a planar wake we have:

$$\frac{U_b - \bar{u}}{U_b} \equiv C(x)e^{-\frac{y^2}{2\delta^2}}. \quad (5.2)$$

In fact, the profile proposed by Wygnanski et al. (1986) has also a term involving  $\exp(y^4)$ , which can be, to a good accuracy, neglected (Rogers, 2002).

With this representation of the wake velocity,  $\delta(x)$  can be regarded as the wake width. The wake width for the zero pressure gradient case  $\delta_0(x)$  is determined by the geometry of the wake-generating object and the incoming turbulence level of the flow. For example, it is known that for a planar wake and a laminar inflow  $\delta_0(x) \sim x^{1/2}$ . Depending on the turbulence level of the inflow and the geometry of the object, this relation is subject to change.

We now state the problem that we want to solve. The problem is: assuming the wake width for the zero pressure gradient case is given, it is desired to find the maximum

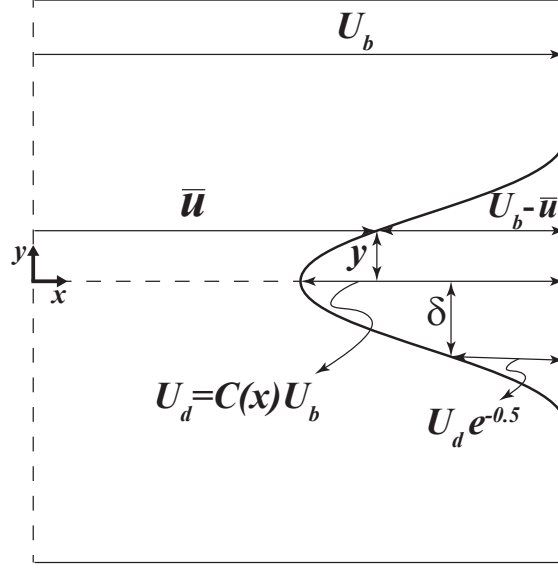


Figure 5.1 – Schematic of the velocity profile of a typical turbulent planar wake.

deficit function  $C(x)$  (including  $C_0$ ) and  $\delta(x)$  under any given pressure gradient. In other words, we want to be able to analytically predict how the wake flow changes, with respect to the zero pressure gradient one, for different pressure gradient conditions.

In the above formulation, the pressure gradient ( $d\bar{p}/dx$ ) shows itself in the way the base flow velocity  $U_b$  varies with  $x$ , i.e. if we have a base flow acceleration ( $dU_b/dx > 0$ ) then  $d\bar{p}/dx < 0$ , and we have the so-called favorable pressure gradient (FPG) condition; alternatively, if we have a base flow deceleration ( $dU_b/dx < 0$ ) then  $d\bar{p}/dx > 0$ , and we have the so-called adverse pressure gradient (APG) condition. For the zero pressure gradient (ZPG) case, we have  $U_b(x) = U_{b0} = \text{constant}$ .

### 5.2.2 Model derivation

We start with the mean momentum conservation equation in the  $x$ -direction for a 2D planar turbulent flow:

$$\bar{u} \frac{\partial \bar{u}}{\partial x} + \bar{v} \frac{\partial \bar{u}}{\partial y} = -\frac{1}{\rho} \frac{\partial \bar{p}}{\partial x} - \frac{\partial \overline{u'v'}}{\partial y} - \frac{\partial \overline{u'^2}}{\partial x}, \quad (5.3)$$

where  $u$  and  $v$  are the streamwise and lateral components of velocity,  $p$  is the pressure,  $\rho$  is the fluid density, the overbar indicates a mean quantity and the prime shows the fluctuation quantities (e.g.  $u' = u - \bar{u}$ ). Here, we have already neglected viscous effects as the Reynolds number is taken to be sufficiently high. As the variation of the turbulent fluxes in the streamwise direction is negligible, the last term on the right-hand side of

## 5.2. Analytical model for wakes under pressure gradient

the above equation can also be neglected. The pressure gradient term can be written as  $U_b(dU_b/dx)$ . With these considerations and adding the term  $-\bar{u}dU_b/dx$  to both sides of (5.3), we can rewrite this equation in the following form:

$$\bar{u}\frac{\partial(U_b - \bar{u})}{\partial x} + \bar{v}\frac{\partial(U_b - \bar{u})}{\partial y} = \frac{\partial\bar{u}'v'}{\partial y} - U_b\frac{dU_b}{dx} + \bar{u}\frac{dU_b}{dx}. \quad (5.4)$$

Using continuity, we obtain:

$$\frac{\partial\bar{u}(U_b - \bar{u})}{\partial x} + \frac{\partial\bar{v}(U_b - \bar{u})}{\partial y} = \frac{\partial\bar{u}'v'}{\partial y} - \frac{dU_b}{dx}(U_b - \bar{u}). \quad (5.5)$$

Now, we integrate the above equation in the  $y$ -direction. As both  $(U_b - \bar{u})$  and  $\bar{u}'v'$  vanish far from the wake center, the following equation is yielded:

$$\frac{d}{dx} \int_{-\infty}^{\infty} \bar{u}(U_b - \bar{u})dy + \int_{-\infty}^{\infty} \frac{dU_b}{dx}(U_b - \bar{u})dy = 0. \quad (5.6)$$

As can be noticed, the second term on the left-hand side of the equation is responsible for the pressure gradient effect. In the special case of the zero pressure gradient case, the second term will be equal to zero, and the above equation is reduced to the well-known momentum defect equation for turbulent wakes (Tennekes and Lumley, 1972). Plugging Equation (5.2) into Equation (5.6), and using  $\int_{-\infty}^{\infty} \exp[-y^2/(2\delta^2)]dy = \sqrt{2\pi}\delta$ , we obtain the following:

$$\frac{d}{dx} \left[ \sqrt{\pi}U_b^2(x)\delta(x) \left( \sqrt{2}C(x) - C^2(x) \right) \right] + \frac{1}{2}\sqrt{2\pi}\frac{dU_b^2}{dx}\delta(x)C(x) = 0. \quad (5.7)$$

As can be seen, in a zero pressure gradient case, the second term vanishes and we are left with an algebraic equation for  $C(x)$  (the same as Bastankhah and Porté-Agel (2014) for an axisymmetric wake). However, in the case of non-zero pressure gradient we encounter a nonlinear ordinary differential equation (ODE). We first solve the above equation for the ZPG case, as its solution will be useful later in our derivation. In the ZPG case, Equation (5.7) reduces to:

$$\left[ \sqrt{\pi}U_{b0}^2\delta_0(x) \left( \sqrt{2}C_0(x) - C_0^2(x) \right) \right] = M, \quad (5.8)$$

where the 0 subscript indicates the ZPG case. The term on the left-hand side of the above equation is the net momentum deficit flux per unit density per unit spanwise (normal to

the  $xy$ -plane) depth, and is equal to a constant (Tennekes and Lumley, 1972). The value of this constant is related to the momentum flux removal by the wake-generating object, and it is equal to  $M = \frac{1}{2}C_D D U_{b0}^2$ , where  $C_D$  is the drag coefficient of the wake-generating object and  $D$  is its width. Therefore,  $C_0(x)$  is found to be:

$$C_0(x) = \frac{\sqrt{2}}{2} - \sqrt{\frac{1}{2} - \frac{C_D}{2\sqrt{\pi}\delta_0(x)D}} \quad , \quad (x \geq x_i). \quad (5.9)$$

Note that  $\delta_0(x)$  is treated as a known function, so with the above equation,  $C_0(x)$  is fully determined. The condition  $x \geq x_i$  is only to ensure that the expression under the square root is non-negative. Thus,  $x_i$  is equal to the minimum non-negative value of  $x$ , for which the expression under the square root remains non-negative.

We now turn back to Equation (5.7), in which we have one equation and two unknowns (i.e.  $C(x)$  and  $\delta(x)$ ). Therefore, to be able to solve the problem we need another equation that relates  $C(x)$  and  $\delta(x)$ . For this purpose we define  $\lambda(x)$  as:

$$\lambda(x) \equiv \frac{U_d}{\delta}, \quad (5.10)$$

where  $U_d(x) \equiv C(x)U_b(x)$  is the maximum velocity deficit at a given streamwise position. Although both  $U_d(x)$  and  $\delta(x)$  vary with pressure gradient, it has been experimentally shown by Liu et al. (2002) and Thomas and Liu (2004) that  $\lambda(x)$  is virtually invariant under pressure gradient changes. To explain this finding, they have argued that  $\lambda(x)$  is proportional to the maximum of  $\partial\bar{u}/\partial y$  and, hence, to the maximum of the mean normal-to-plane vorticity  $\bar{\omega}_z$ . As in the vorticity equation for  $\bar{\omega}_z$ , the imposed pressure gradient does not appear ( $\nabla \times \nabla\bar{p} = 0$ ), the imposed pressure gradient does not have a direct effect on the evolution of the maximum of  $\bar{\omega}_z$ . We take advantage of this, and further our derivation, by equating  $\lambda$  for any pressure gradient to the value of  $\lambda$  for the ZPG case, i.e.  $\lambda_0$ :

$$\lambda(x) = \lambda_0(x) = \frac{U_{b0}C_0(x)}{\delta_0(x)}, \quad (5.11)$$

which, considering Equation (5.9), is regarded as a known function.  $\delta(x)$  can then be expressed as:

$$\delta(x) = \frac{U_b(x)}{\lambda_0(x)}C(x). \quad (5.12)$$

## 5.2. Analytical model for wakes under pressure gradient

Plugging Equation (5.12) into Equation (5.7), the following ODE is obtained for  $C(x)$ :

$$\frac{dC(x)}{dx} = \frac{-1}{\left(\frac{U_b^3}{\lambda_0}\right) (2\sqrt{2}C - 3C^2)} \left[ \frac{\sqrt{2}}{3} \frac{dU_b^3}{dx} \frac{C^2}{\lambda_0} + (\sqrt{2}C^2 - C^3) \frac{d}{dx} \left( \frac{U_b^3}{\lambda_0} \right) \right]. \quad (5.13)$$

The boundary condition for the above ODE is:

$$C(x_i) = C_0(x_i). \quad (5.14)$$

In fact, by (5.14), we have assumed that  $C(x)$  has the same initial value for both the ZPG and nonzero pressure gradient cases. In other words, in the immediate vicinity of the wake-generating object, the effect of pressure gradient on  $C(x)$  is assumed to be negligible. This notion is fully accurate in cases where the imposed pressure gradient starts to be nonzero after some distance from the object (e.g. see the validation case of Section 5.3).

Equation (5.13), which is nonlinear in  $C(x)$ , enables us to explicitly express  $dC(x)/dx$  as a function of  $U_b$ ,  $\lambda_0$  and  $C(x)$ , i.e.  $dC(x)/dx = f(U_b, \lambda_0, C)$ . This form of the ODE is suitable for common numerical ODE solvers, and it can be solved very easily and fast. Hence, with Equations (5.13) and (5.14), the solution of the initially stated problem (Section 5.2.1) is fully achieved. In the remainder of this section, we approach the problem from two other different angles, which we believe can shed more light on the problem at hand.

### 5.2.3 Solving the problem for a given $\delta(x)$

Herein, we consider the problem as such:  $\delta(x)$  is given for a desired pressure gradient, and the objective is to find  $C(x)$ . This approach is beneficial because it disentangles Equation (5.7) from Equation (5.11), and we can isolate the behaviour of these two equations, and consequently assess them individually. This may be particularly useful for the insight it provides.

For this purpose, we proceed by defining a dummy variable  $h(x)$  such that  $h(x) \equiv \delta(x) (\sqrt{2}C(x) - C^2(x))$ . Then, Equation (5.7) becomes:

$$\frac{dh(x)}{dx} = -h(x) \frac{1}{U_b^2} \frac{dU_b^2}{dx} - \frac{\sqrt{2}}{2} \frac{1}{U_b^2} \frac{dU_b^2}{dx} \delta \left( \frac{\sqrt{2}}{2} - \sqrt{\frac{1}{2} - \frac{h}{\delta}} \right), \quad (5.15)$$

with the boundary condition being:

$$h(0) = h_0(x) = \frac{1}{2\sqrt{\pi}}DC_D. \quad (5.16)$$

The above ODE is nonlinear in  $h(x)$  and has the explicit form  $dh(x)/dx = f(U_b, \delta, h)$ . Equation (5.15) can again be easily solved in a fast way by numerical techniques, which are available in common commercial softwares. Finally,  $C(x)$  is recovered as:

$$C(x) = \frac{\sqrt{2}}{2} - \sqrt{\frac{1}{2} - \frac{h}{\delta}}, \quad (x \geq x_i). \quad (5.17)$$

Note that  $h(x)$  becomes independent of  $x$  in the ZPG case (Equation 5.16). Notice also that in the derivations of this section, wherever one of the two roots of a quadratic equation was needed (5.9, 5.15 and 5.17), the physically acceptable one was chosen, and the unacceptable one was ignored. The unacceptable root leads to negative flow velocity and an amplifying deficit in the  $x$ -direction instead of an attenuating one for the ZPG case.

#### 5.2.4 Asymptotic solution of the problem

Here, we try to find an asymptotic solution for the problem at hand for sufficiently large  $x$ . To this end, we consider that  $0 < C(x) < 1$ , and thus  $C^2(x) < C(x)$ . We know that  $C(x) \rightarrow 0$  as  $x \rightarrow \infty$  (at least for ZPG and FPG cases, as we will see in Section 5.3, this assumption does not necessarily hold for the APG case). Hence, in the far wake, where  $x$  is sufficiently large, we have  $C^2(x) \ll C(x)$ . Therefore, here we can consider the term involving  $C^2(x)$  as negligible with respect to the term involving  $C(x)$ . Neglecting the  $C^2(x)$ , amounts to an important change in Equation (5.7), that is to say, converting the nonlinear ODE to a linear one:

$$\frac{d}{dx} \left[ \sqrt{2\pi} U_b^2(x) \delta \tilde{C}(x) \right] + \frac{\sqrt{2\pi}}{2} \frac{dU_b^2}{dx} \delta \tilde{C}(x) = 0, \quad (5.18)$$

where  $\tilde{C}$  is the asymptotic solution of  $C$ . After some manipulation, we obtain the following equation:

$$\sqrt{2\pi} \frac{1}{U_b} \frac{d}{dx} \left[ \delta(x) \tilde{C}(x) U_b^3 \right] = 0, \quad (5.19)$$

The coefficient  $\sqrt{2\pi}$  is maintained deliberately, so that the constant of integration for the above equation for the ZPG case will be equal to  $M$  in Equation (5.8). The solution to the above equation can be obtained with the proper determination of the constant of



integration. Thus,  $\tilde{C}(x)$  can be written as:

$$\tilde{C}(x) = \frac{1}{2\sqrt{2\pi}} \frac{C_D}{\left(\frac{\delta}{D}\right)} \left(\frac{U_{b0}}{U_b(x)}\right)^3. \quad (5.20)$$

It is noteworthy to mention that the above expression in the case of ZPG (i.e.  $\tilde{C}_0(x) = 1/(2\sqrt{2\pi})DC_D/\delta_0$ ) is, in fact, equal to the first-order Taylor expansion of the full solution of  $C_0(x)$ , i.e. Equation (5.9).

Now, using Equation (5.11), we can find the final asymptotic solution for  $C(x)$  as:

$$\tilde{C}(x) = \tilde{C}_0(x) \left(\frac{U_{b0}}{U_b(x)}\right)^2. \quad (5.21)$$

### 5.3 Validation of the model

In this section, we aim to validate the above-derived model by comparing its predictions with experimental measurements. The experiment that we choose is the one performed by Liu et al. (2002), in which the wake generated by a flat splitter plate under different constant pressure gradient conditions is measured. The pressure gradient along the streamwise direction has the following distribution:

$$\frac{dC_p}{dx} \equiv \frac{1}{\frac{1}{2}\rho U_{b0}^2} \frac{d\bar{p}}{dx} = -\frac{d}{dx} \left(\frac{U_b}{U_{b0}}\right)^2 = \begin{cases} 0, & x \leq x_p \\ \alpha, & x > x_p, \end{cases} \quad (5.22)$$

where  $C_p$  is the pressure coefficient. It is clear from the above distribution that the wake is initially under zero pressure gradient and, after a certain position  $x_p$  ( $x_p/\theta_0 = 40$ ), it undergoes a constant pressure gradient which is dictated by the parameter  $\alpha$ .  $\theta_0$  is the initial momentum thickness of the wake, which is equal to 7.2 mm for all the cases considered here. Three cases of ZPG, FPG and APG are considered, such that:

$$\alpha = \begin{cases} -0.6 \text{ m}^{-1}, & \text{FPG} \\ 0, & \text{ZPG} \\ +0.338 \text{ m}^{-1}, & \text{APG.} \end{cases} \quad (5.23)$$

We here apply the model described in Section 5.2 to these three cases. Note that in the model one can use the wake half-width  $\delta_h = \sqrt{2\ln(2)}\delta$  instead of  $\delta$ , as Equation (5.7) is linear in  $\delta$ . The lengths are normalized by  $\theta_0$ . Using the curve of  $C_0(x)$  in the experiment, the value of the  $DC_D$  in Equation (5.9) can be obtained, and this equation

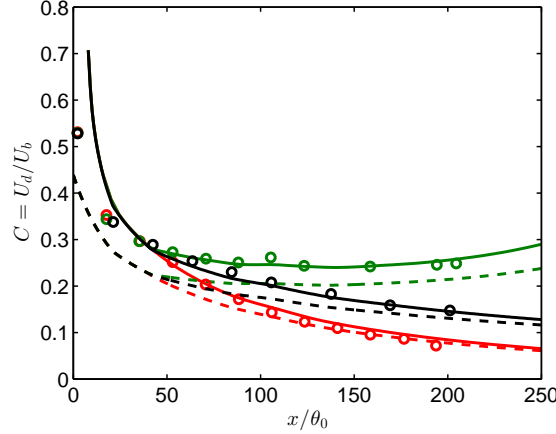


Figure 5.2 – Normalized maximum velocity deficit as a function of the streamwise distance for ZPG (black), FPG (red) and APG (green) cases. The circles indicate measurements of Liu et al. (2002), the solid lines are the full solution obtained from Equation (5.13), and the dashed lines are the asymptotic solution of Equation (5.21).

eventually takes the following form:

$$C_0(x) = \frac{\sqrt{2}}{2} - \sqrt{\frac{1}{2} - \frac{2.2}{2\sqrt{\pi} \left( \frac{\delta_{h,0}(x)}{\theta_0} \right)}}, \quad (5.24)$$

where  $\delta_{h,0}$  is the wake half-width for the ZPG case.

Figure 5.2 shows  $C(x) = U_d(x)/U_b(x)$  for the different pressure gradient cases both from the measurements and from the model. Note that, along with the full solution<sup>2</sup> of the model (i.e. Equation 5.13), the asymptotic solution is also shown. The agreement between the model and the experimental data is remarkable. It is also clear how the asymptotic solution converges to the full solution for the ZPG and FPG cases. For the APG case, as the condition  $\lim_{x \rightarrow \infty} C(x) = 0$  does not hold, we see that no convergence to the full solution is achieved. It is also worth mentioning that the asymptotic solution performs best for the FPG case, and this is because the value of  $C(x)$  is the smallest for this case, and consequently, the error caused by neglecting  $C^2(x)$  is also the smallest. It can be observed that the recovery of the maximum velocity deficit is fastest for the FPG case and slowest for the APG case. In fact, for the APG case, after a certain  $x$ ,  $C(x)$  even starts to increase. This is also reported by Liu et al. (2002), and it is well predicted by our model. Moreover, Figure 5.3 shows the modelled and experimental  $\delta_h(x)$  functions. Again, it can be seen that the agreement between the model and measurements is good. Note that the black line in this figure is the input of the model. This curve, as also reported by Liu et al. (2002), grows proportional to  $x^{1/2}$ .

<sup>2</sup>All ODEs in this paper are solved with “ode45” routine of MATLAB, which uses an explicit Runge-Kutta (4,5) algorithm, namely, the Dormand-Prince method.

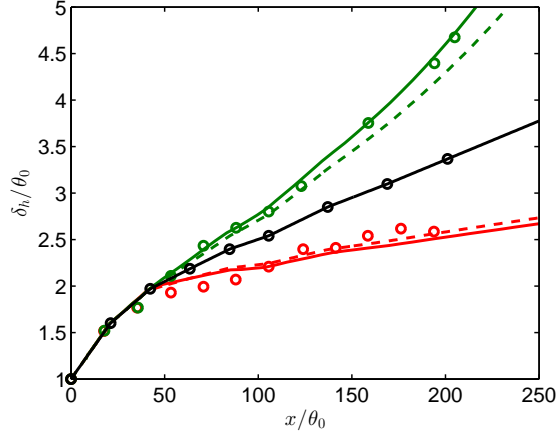


Figure 5.3 – Normalized wake half-width as a function of the streamwise distance. For the legend, refer to the caption of Figure 5.2.

## 5.4 Discussion

After validation of the model, we aim to employ the model to give us more insight about the response of planar wakes to pressure gradient conditions. To this end, we use the setup presented in the previous section, and examine the behaviour of the wake with varying pressure gradients. To do this, we vary the parameter  $\alpha$  and obtain the solutions of  $C(x)$  and  $\delta_h(x)$ , as can be seen in Figures 5.4 and 5.5, respectively. First of all, we see in these figures that, for the APG cases, there is a certain value of  $x/\theta_0$  beyond which the solution becomes unstable. We hypothesize that one possible reason for this behaviour can be the separation of the flow, which is reported broadly in literature as a characteristic of APG wakes. It is worth noting that Liu et al. (2002) have mentioned for  $\alpha = 0.468m^{-1}$  the flow undergoes separation “near the aft portion of the diffuser wall”, i.e.  $x/\theta_0 \approx 250$ ; interestingly, we observe in Figures 5.4 and 5.5 that this agrees well with the point where the model becomes unstable. Moreover, for the case of constant adverse pressure gradient ( $\alpha > 0$ ), the existence of a certain  $x$  at which the model becomes unstable does not depend on the magnitude of  $\alpha$ . In the above figures, also for  $\alpha = 0.1m^{-1}$  the model becomes unstable, but at  $x/\theta_0 \approx 1000$ , which is not within the range of the shown plots. We emphasize that linking the instability of the model to flow separation is only a hypothesis, and investigation of the separation is not within the scope of this study. Another interesting point about this figure is the fact that wakes under APG are more sensitive to pressure gradient than wakes under FPG; in contrast to FPG cases, the wake responds to a small APG relatively strongly. Finally, we see that when the magnitude of the favorable pressure gradient is larger than a certain value (i.e.  $\alpha < \alpha_{cr} < 0$ ),  $\delta$  varies only slightly with  $x$ , i.e.  $\delta \approx \text{constant}$ . This means that the flow becomes close to a parallel flow. This behaviour is also mentioned by Liu et al. (2002) and Rogers (2002).

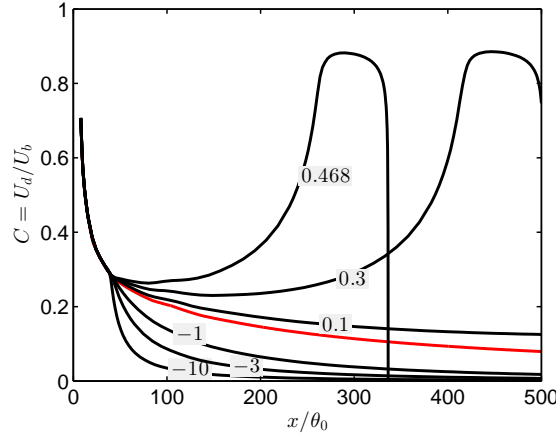


Figure 5.4 – Normalized maximum velocity deficit as a function of the streamwise distance for different pressure gradient cases. The value of  $\alpha$  is written on each curve with the unit of  $[m^{-1}]$ . The red line indicates the ZPG case. The curves are the solution of Equation (5.13).

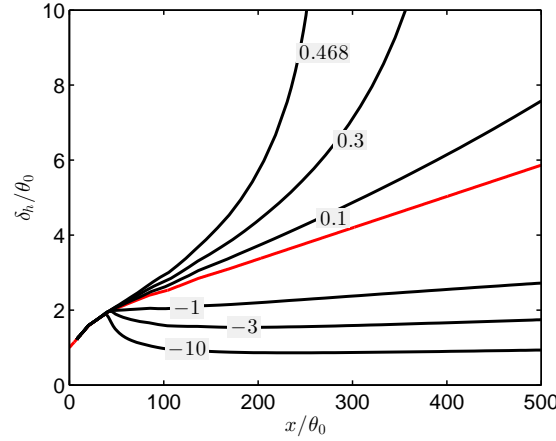


Figure 5.5 – Normalized wake half-width as a function of the streamwise distance for different pressure gradient cases. For the legend, refer to the caption of Figure 5.4.

## 5.5 Concluding remarks

In this paper, we pursue the objective of developing an analytical model to predict the evolution of a turbulent planar wake under an arbitrary pressure gradient condition. Specifically, we aim to predict how a turbulent planar wake in zero pressure gradient, which has a well-established behaviour, is perturbed by imposing a nonzero pressure gradient. The model is based on the cross-stream integration of the streamwise momentum equation and uses the self-similarity of the mean flow.

The inputs of the model are: (1) the ZPG wake width evolution function  $\delta_0(x)$ , and (2) the imposed pressure gradient, or equivalently, the streamwise distribution of the base flow velocity  $U_b(x)$ . Both input functions can be data-driven or analytical. The outputs of the model are the maximum deficit function  $C(x)$  and the wake width function  $\delta(x)$ . The model amounts to solving a nonlinear ODE for  $C(x)$ , which can be easily solved in a fast way with common commercial ODE solvers. An asymptotic variant of the model (mainly applicable for APG and FPG cases) is also developed which leads to an algebraic equation for  $C(x)$ . The asymptotic method was found to have no computational advantage over the exact method, but it can help to give a clearer insight about the problem. The model is successfully validated against experimental data by comparing the evolution of the wake width and maximum velocity deficit for both FPG and APG cases. The model is shown to be useful to predict a broad range of pressure gradients.

Finally, as mentioned in Section 5.1, apart from high-lift devices, wind-turbine wakes can also involve pressure gradient effects. The main characteristic difference between these two cases is that the wake in high-lift devices is planar, but the wake of wind turbines is axisymmetric. The approach described here for planar wakes can easily be extended to axisymmetric wakes. Although this can be accomplished using a similar general approach, the results will be different and, therefore, a proper separate investigation of axisymmetric wakes under pressure gradient conditions is required. We are planning to undertake this challenge in our future research.



# 6 A model for the effect of pressure gradient on turbulent axisymmetric wakes<sup>1</sup>

## Abstract

Turbulent axisymmetric wakes under pressure gradient have received little attention in the literature, in spite of their fundamental and practical importance, for example, in the case of wind turbine wakes over topography. In this paper, we develop an analytical framework to analyse turbulent axisymmetric wakes under different pressure gradient conditions. Specifically, we develop a model to predict how an arbitrary imposed pressure gradient perturbs the evolution of the zero-pressure-gradient wake. The starting point of the model is the basic mean conservation of the streamwise momentum equation. We take advantage of the self-similarity of the wake velocity deficit and the assumption that the ratio of the maximum velocity deficit to the wake width is independent of the pressure gradient; such an assumption is supported experimentally for planar wakes, and numerically for axisymmetric wakes in this study. Furthermore, an asymptotic solution for the problem is also derived. The problem is considered both for an axisymmetric strain and a planar strain. The inputs to the model are the imposed pressure gradient and the wake width in the zero-pressure-gradient case. To validate the model results, a set of large-eddy simulations (LES) are performed. Comparing the evolution of the maximum velocity deficit and the wake width, the model results and the LES data show good agreement. Similar to planar wakes, it is observed that the axisymmetric wake recovers faster in the favourable pressure gradient compared to the adverse one.

---

<sup>1</sup>The contents of this chapter are published in: Shamsoddin, S. and Porté-Agel, F. A model for the effect of pressure gradient on turbulent axisymmetric wakes. *Journal of Fluid Mechanics*, 837:R3, 2018.

### 6.1 Introduction

The problem of turbulent axisymmetric wakes under pressure gradient is interesting, and its study is useful; firstly because it can be regarded as a classical fundamental fluid mechanics problem, and secondly because such a phenomenon can have engineering implications. One example that is worthy of attention is the design of wind farms sited on topography. The axisymmetric wind turbine wakes are subjected to non-zero pressure gradients, which are caused by variations in the underlying terrain elevation. This changes the wind turbines' wake recovery characteristics with respect to the flat terrain case, and, in turn, can affect the design of the optimum layout of the wind farm.

In spite of its importance, few studies have been done on this subject. In their analytical study on wakes in complex flows, [Hunt and Eames \(2002\)](#), among other things, derived the solution for the mean velocity for a laminar axisymmetric wake under a specific strain caused by an external flow. [Magnaudet et al. \(1995\)](#) and [Bagchi and Balachandar \(2002\)](#) performed numerical simulations of flow past a sphere (rigid and bubble-like) which is subjected to strain (planar and axisymmetric). The focus of their studies are more on the direct impact of the flow on the sphere (e.g. forces, separation, etc) rather than the evolution of the wake itself. In contrast to turbulent axisymmetric wakes, some interesting research has already been performed for the planar case using numerical ([Rogers, 2002](#)) and experimental ([Liu et al., 2002](#); [Thomas and Liu, 2004](#)) approaches, supported also by concurrent analytical ([Shamsoddin and Porté-Agel, 2017a](#)) developments. Based on these studies, it is known that favourable pressure gradients (accelerating base flows) lead to a faster recovery of the wake.

As mentioned in the conclusion of [Shamsoddin and Porté-Agel \(2017a\)](#), turbulent axisymmetric wakes ought to be studied under the influence of imposed pressure gradients, especially because of the arising of such scenarios in the case of wind turbine wakes over topography. In the current paper, we aim to accomplish this objective by proposing an analytical framework to analyse such wakes and eventually by developing a model to predict how an arbitrary imposed non-zero pressure gradient alters the evolution of a turbulent axisymmetric wake under zero pressure gradient. In addition, we provide large-eddy simulation (LES) results related to such wakes, against which we can test our model. To the best knowledge of the authors, no study (neither experimental nor numerical nor analytical) on this topic (turbulent axisymmetric wakes under different imposed pressure gradients) is available in the literature. Therefore, this paper can provide useful insight (by presenting both a theoretical framework and an LES dataset) related to this subject.

This article is ordered in this manner: In Section [6.2](#), the problem is defined, and the model is derived with all its variants. In Section [6.3](#), the numerical experiments, which are performed for the purpose of the validation of the model, are described, and their results are compared with the predictions of the model. Finally, Section [6.4](#) concludes



the paper.

## 6.2 Analytical model for axisymmetric wakes under pressure gradient

### 6.2.1 Problem formulation

The mean velocity deficit profiles of turbulent axisymmetric wakes are known to be self-similar and to have a Gaussian shape function (Pope, 2000):

$$\frac{U_b(x) - \bar{u}(x, r)}{U_b(x)} \equiv C(x) e^{-\frac{r^2}{2\delta^2}}, \quad (6.1)$$

where  $x$  is the streamwise direction,  $r$  is the radial direction from the wake centre,  $\bar{u}(x, r)$  is the velocity (hereafter, by velocity, we imply the mean streamwise velocity, unless otherwise stated) of the wake flow,  $U_b(x)$  is the velocity of the base flow,  $C(x)$  is a function determining the maximum velocity deficit at each  $x$ -position and  $\delta(x)$  is the wake width.

Here, we assume the axisymmetric wake retains its Gaussian shape under non-zero pressure gradients. This assumption will be verified further in the paper (Section 6.3). It is noteworthy to mention that it is already shown that for a turbulent planar wake, this assumption is valid (Rogers, 2002; Liu et al., 2002; Shamsoddin and Porté-Agel, 2017a).

The imposed pressure gradient shows itself in the above formulation in the function  $U_b(x)$ . For an accelerating base flow ( $dU_b/dx > 0$ ) we have the so-called favourable pressure gradient (FPG) and for a decelerating base flow ( $dU_b/dx < 0$ ) we have the so-called adverse pressure gradient (APG). Obviously, for the zero pressure gradient (ZPG) case,  $U_b(x) = U_{b0} = \text{const.}$

Our objective in this section is to solve the following problem: for a given ZPG wake (for which we know the wake width evolution), how is the mean velocity field of the wake (i.e.  $C(x)$  and  $\delta(x)$ ) changed after imposing an arbitrary pressure gradient?

### 6.2.2 Model derivation

The mean conservation of momentum equation in the  $x$ -direction for a turbulent axisymmetric wake can be written as:

$$\frac{\partial \bar{u}(U_b - \bar{u})}{\partial x} + \frac{\partial \bar{v}(U_b - \bar{u})}{\partial y} + \frac{\partial \bar{w}(U_b - \bar{u})}{\partial z} = -\frac{dU_b}{dx}(U_b - \bar{u}) + \frac{\partial \overline{u'v'}}{\partial y} + \frac{\partial \overline{u'w'}}{\partial z}, \quad (6.2)$$

where  $u$ ,  $v$  and  $w$  are the streamwise ( $x$ ), lateral ( $y$ ), and vertical ( $z$ ) components of the velocity, the overbar indicates a mean quantity and the prime shows the fluctuation quantities (e.g.  $u' = u - \bar{u}$ ). In deriving this equation, the continuity equation is used, the viscous and  $\partial \bar{u'^2}/\partial x$  terms are neglected, and the mean pressure gradient term,  $-(1/\rho)\partial \bar{p}/\partial x$ , is replaced by  $U_b(dU_b/dx)$ . For intermediate steps, through which this equation is obtained, the interested reader is referred to [Shamsoddin and Porté-Agel \(2017a\)](#).

After integrating in the  $x$ -normal plane, we obtain the integral form of the  $x$ -momentum equation:

$$\frac{d}{dx} \int_0^\infty \bar{u}(U_b - \bar{u})(2\pi r dr) + \int_0^\infty \frac{dU_b}{dx} (U_b - \bar{u})(2\pi r dr) = 0. \quad (6.3)$$

It should be noted, as  $(U_b - \bar{u})$ ,  $\overline{u'v'}$  and  $\overline{u'w'}$  all vanish far from the wake centre (in a given  $x$ -normal plane), the integrals of the last two terms on both sides of (6.2) are zero. Here, we assume that the strain which causes the pressure gradient is also axisymmetric, and therefore the wake retains its axisymmetry after imposing the pressure gradient (for the case of a planar strain see Section 6.2.4). Thus, we can directly substitute (6.1) into (6.3), and use  $\int_0^\infty \exp[-r^2/(2\delta^2)](2\pi r dr) = 2\pi\delta^2$ , to obtain:

$$\frac{d}{dx} \left[ 2\pi U_b^2(x) \delta^2(x) \left( C(x) - \frac{C^2(x)}{2} \right) \right] + \pi \frac{dU_b^2}{dx} \delta^2(x) C(x) = 0. \quad (6.4)$$

As it can be seen, we are left with a nonlinear ordinary differential equation (ODE). We first show the solution of the equation for the ZPG case, because it proves to be helpful later. In fact, in the ZPG case, (6.4) reduces to an algebraic equation (the second term vanishes), whose solution has already been obtained by [Bastankhah and Porté-Agel \(2014\)](#):

$$C_0(x) = 1 - \sqrt{1 - \frac{C_D}{8 \left( \frac{\delta_0(x)}{D} \right)^2}} \quad , \quad (x \geq x_i), \quad (6.5)$$

where the subscript 0 indicates a quantity in ZPG case,  $D$  is the diameter of the wake-generating object and  $C_D$  is the drag coefficient of the object (or in the case of a power-generating device, the thrust coefficient). The condition  $(x \geq x_i)$  is only to make sure that the expression under the square root always remains non-negative.

Now, we focus on the ODE of (6.4). In this ODE, we have one equation and two unknowns ( $C$  and  $\delta$ ). Therefore, we need another equation to close the problem. For this purpose, following [Shamsoddin and Porté-Agel \(2017a\)](#), we use the invariance of the ratio  $\lambda(x) \equiv U_d(x)/\delta(x)$  under pressure gradient changes, where  $U_d(x) \equiv C(x)U_b(x)$  is

## 6.2. Analytical model for axisymmetric wakes under pressure gradient

the maximum velocity deficit at a given streamwise position. This invariance is shown experimentally (Liu et al., 2002; Thomas and Liu, 2004) and is used to develop a model for the case of planar wakes by Shamsoddin and Porté-Agel (2017a). For the case of axisymmetric wakes, we will reaffirm the validity of this assumption based on LES data in Section 6.3. Hence, because  $\lambda$  is insensitive to pressure gradient and thus  $U_b$ , we have:

$$\lambda(x) = \lambda_0(x) = \frac{U_{b0}C_0(x)}{\delta_0(x)}. \quad (6.6)$$

Consequently,  $\delta$  can be expressed as

$$\delta(x) = \frac{U_b(x)}{\lambda_0(x)}C(x). \quad (6.7)$$

Now, substituting (6.7) into (6.4), the final ODE for  $C(x)$  is obtained:

$$\frac{dC(x)}{dx} = \frac{-1}{\left(\frac{U_b^4}{\lambda_0^2}\right)(3C^2 - 2C^3)} \left[ \frac{1}{4} \frac{dU_b^4}{dx} \frac{C^3}{\lambda_0^2} + \left( C^3 - \frac{C^4}{2} \right) \frac{d}{dx} \left( \frac{U_b^4}{\lambda_0^2} \right) \right], \quad (6.8)$$

with the boundary condition

$$C(x_i) = C_0(x_i). \quad (6.9)$$

Equation (6.8) is a nonlinear ODE in the explicit form of  $dC(x)/dx = f(U_b, \lambda_0, C(x))$ . This ODE can be solved easily and fast with common commercial ODE solvers. Thus, with (6.8) and (6.9), our objective, which was the solution of the problem defined in Section 6.2.1, is accomplished.

### 6.2.3 Asymptotic solution of the problem

Since  $\bar{u} \rightarrow U_b$  far downstream of the wake-generating object, we have  $C^2(x) \ll C(x)$  for sufficiently large  $x$  (at least for the FPG and ZPG cases)(Shamsoddin and Porté-Agel, 2017a). Therefore, neglecting the term involving  $C^2(x)$  in (6.4) leads to the following linear ODE:

$$\frac{d}{dx} \left[ 2\pi U_b^2(x) \delta^2(x) \tilde{C}(x) \right] + \pi \frac{dU_b^2}{dx} \delta^2(x) \tilde{C}(x) = 0, \quad (6.10)$$

where  $\tilde{C}$  is the asymptotic solution of  $C$ . The above equation is exactly equivalent to the following:

$$2\pi \frac{1}{U_b} \frac{d}{dx} \left[ \delta^2(x) \tilde{C}(x) U_b^3 \right] = 0, \quad (6.11)$$

Using the readily obtainable asymptotic ZPG solution for  $\tilde{C}_0$  from (6.4) (i.e.  $\tilde{C}_0 = D^2 C_D / (16\delta_0^2)$ ) to find the correct constant of integration, the solution to (6.11) can be found as:

$$\tilde{C}(x) = \frac{1}{16} \frac{C_D}{\left(\frac{\delta(x)}{D}\right)^2} \left(\frac{U_{b0}}{U_b(x)}\right)^3, \quad (6.12)$$

which by employing (6.6–6.7) can be further simplified as:

$$\tilde{C}(x) = \tilde{C}_0 \left(\frac{U_{b0}}{U_b(x)}\right)^{\frac{5}{3}}. \quad (6.13)$$

It is worth to note that for the planar case the exponent of  $(U_{b0}/U_b)$  was found to be 2 (Shamsoddin and Porté-Agel, 2017a), whereas for the axisymmetric case this exponent is  $\frac{5}{3}$ . Furthermore,  $\tilde{C}_0(x)$  can be shown to be the second-order Taylor expansion of the full solution of  $C_0(x)$ , i.e. (6.5), in terms of  $\delta_0^{-1}$ .

### 6.2.4 Axisymmetric wakes and planar strain

In the above derivations, we had assumed an axisymmetric strain and, consequently, that the wake retains its axisymmetry (e.g. when a wake passes through a circular nozzle/diffuser). This assumption provides a perfect analogy to the case of a planar wake under a planar strain (e.g. Liu et al., 2002; Thomas and Liu, 2004; Shamsoddin and Porté-Agel, 2017a). In this subsection, we are interested to study the case of an axisymmetric wake which undergoes an imposed pressure gradient which is a result of a planar strain (e.g. when passing through a planar nozzle/diffuser). This case is interesting because of its practical use, in particular, for the case of wind turbine wakes flowing over topography: in this case the topography generates a planar strain on the axisymmetric wake of a wind turbine rotor.

Without losing generality, we consider the planar strain to be in the  $z$ -direction. In this case (unlike the axisymmetric strain case), the wake width in  $y$ - and  $z$ - directions are not necessarily equal. Therefore, following Bastankhah and Porté-Agel (2016), we assume the velocity deficit profile of the wake to have the following general shape:

$$\frac{U_b(x) - \bar{u}(x, y, z)}{U_b(x)} \equiv C(x) \exp \left[ - \left( \frac{y^2}{2\delta_y^2} + \frac{z^2}{2\delta_z^2} \right) \right], \quad (6.14)$$

where  $\delta_y$  and  $\delta_z$  are the wake widths in the  $y$ - and  $z$ -directions. In the case of  $\delta_y = \delta_z$ , the above equation reduces to (6.1) (as in Vermeulen et al., 1979; Jensen, 1983; Bastankhah and Porté-Agel, 2014). We have  $\int_{-\infty}^{\infty} \int_{-\infty}^{\infty} \exp[-(y^2/(2\delta_y^2) + z^2/(2\delta_z^2))] dy dz = 2\pi\delta_y\delta_z$ , and this paves the way to define an equivalent wake width  $\delta_{eq}$  as the geometric mean of

$\delta_y$  and  $\delta_z$ :

$$\delta_{eq} = \sqrt{\delta_y \delta_z}. \quad (6.15)$$

Now, if we substitute (6.14) into (6.3), and follow the same procedure as in Section 6.2.2 and Section 6.2.3, we obtain exactly the same equations with the only difference that  $\delta_{eq}$  replaces  $\delta$  in all those equations.

In fact, in the case of planar strain, we solve our problem for  $C(x)$  and  $\delta_{eq}(x)$ . To further obtain  $\delta_y$  and  $\delta_z$  individually requires more information about the geometry and history of the flow and strain, which is beyond the scope of the framework of the current model. However, being able to predict  $C(x)$  and  $\delta_{eq}$  still enables us to obtain a great deal of information about the flow which can be useful in many practical applications.

## 6.3 Validation of the model

### 6.3.1 The numerical experiment

To validate the model, we compare its results with results from the LES of axisymmetric wakes in three specific FPG, ZPG and APG cases. The numerical experiments are performed in an ideal spanwise-periodic channel with rectangular cross-section. To create the desired non-zero pressure gradient, the walls of the channel are curved so that its cross-sectional area varies in the streamwise direction. The wake itself is generated with an actuator disk of diameter  $D$  and drag (or thrust) coefficient  $C_D = 0.8$ . As can be seen in Figure 6.1, three different geometries of the channel wall are used respectively for FPG, ZPG and APG cases: (i) convex walls, which create a contraction and consequently flow acceleration ( $dU_b/dx > 0$ ) up to the channel throat, (ii) straight walls, which create neither acceleration nor deceleration ( $dU_b/dx = 0$ ) along the channel, and (iii) concave walls, which create an expansion and consequently flow deceleration ( $dU_b/dx < 0$ ) up to the channel throat. The upper and lower walls are symmetric with respect to the centre plane of the channel, and the surface equation of the lower wall has the following general cosine form:

$$Z_s(x) = \begin{cases} \frac{1}{2}h \left[ 1 + \cos \left[ \frac{\pi}{2L_1}(x - x_{th}) \right] \right], & -2L_1 \leq x - x_{th} < 0 \\ \frac{1}{2}h \left[ 1 + \cos \left[ \frac{\pi}{2L_2}(x - x_{th}) \right] \right], & 0 \leq x - x_{th} < 2L_2 \\ 0, & \text{otherwise,} \end{cases} \quad (6.16)$$

where  $Z_s$  is the height of the wall with respect to the straight wall of the ZPG case, the origin of  $x$  (as shown in Figure 6.1) is the position of the wake-generating disk,  $x_{th} = 17D$  is the position of the channel throat,  $h$  is the maximum height of the wall (occurring at the throat) which has the values of  $1.25D$ ,  $0$  and  $-1.25D$  for FPG, ZPG and APG

cases, respectively, and  $L_1 = 6D$  and  $L_2 = 5D$  are the half-length of the cosine functions for the sections upstream and downstream of the throat, respectively. In each case, the region in which we are interested for our study is the region downstream of the disk up until the throat of the channel. This region is shown by the shaded area in Figure 6.1.

For the sake of conciseness and without affecting the purpose of the paper, we do not bring the details of the LES framework here, to avoid repetition of what is already available in the literature. The governing equations (the momentum and continuity equations), general numerics and the subgrid-scale model (the Lagrangian scale-dependent dynamic model) are described in [Porté-Agel et al. \(2000\)](#) and [Stoll and Porté-Agel \(2006b\)](#). For modelling the wake-generating disk, we have used the standard actuator disk model ([Wu and Porté-Agel, 2011](#)). To resolve the curved wall of the channel, a coordinate transformation technique is employed, whose details can be found in [Shamsoddin and Porté-Agel \(2017b\)](#) (with the slight difference that in that study the domain comprised the half-channel). The boundary conditions in the horizontal directions are mathematically periodic. For the upper and lower channel walls, the instantaneous surface shear stress is calculated using the Monin-Obukhov similarity theory (which for the neutral case of this study simply reduces to the log law). To overcome the streamwise periodicity and to have a prescribed inflow to the domain, a buffer zone technique is used to feed an inflow field which is generated offline with performing a precursory simulation in a periodic straight channel ([Shamsoddin and Porté-Agel, 2017b](#)). It should be noted that the turbulence intensity of the incoming flow at the centre of the channel (defined as the standard deviation of the streamwise velocity divided by  $U_{b0}$ ) is 0.03 for all cases.

The streamwise ( $x$ ), spanwise ( $y$ ) and vertical ( $z$ ) lengths of the computational domain are  $52.5D$ ,  $8.75D$  and  $10D$ , respectively. The number of grid points in the  $x$ ,  $y$  and  $z$  directions are 210, 60 and 122. Regarding the accuracy and validations of the framework, it should be noted that the validation of the actuator disk model was done in [Wu and Porté-Agel \(2011\)](#) and the validation of the coordinate transformation technique was carried out in [Wan et al. \(2007\)](#). On top of these, the combined application of the actuator disk and coordinate transformation methods was validated in [Shamsoddin and Porté-Agel \(2017b\)](#). The chosen resolution of the grid is well within the range that has been previously shown to result in grid-independent results for the cases of application of the coordinate transformation (see [Wan et al. \(2007\)](#), Sect. 3) and flow through actuator disks (see [Wu and Porté-Agel \(2011\)](#), Sect. 4, and [Wu and Porté-Agel \(2013\)](#), Sect. 4.1), and the case of the combined application of the the coordinate transformation and the actuator disks ([Shamsoddin and Porté-Agel, 2017b](#)).

### 6.3.2 Results and comparison

For each case, we perform two simulations: one without the presence of the disk, which serves as the base flow field, and one with the presence of the disk. To isolate the turbine

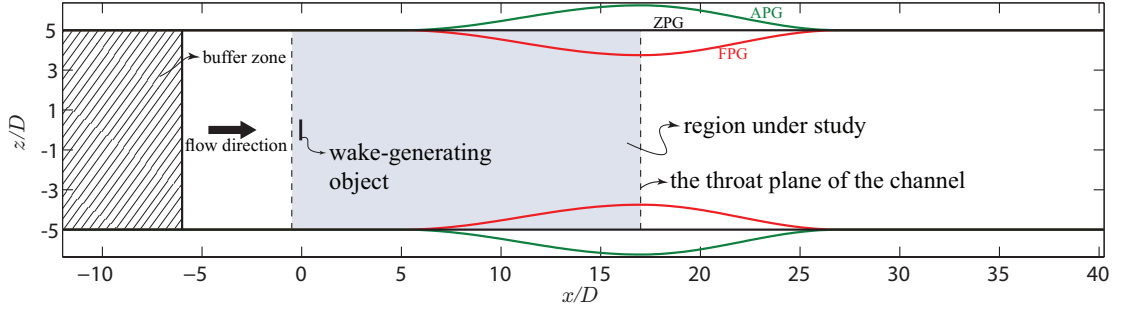


Figure 6.1 – Domain of the simulations.

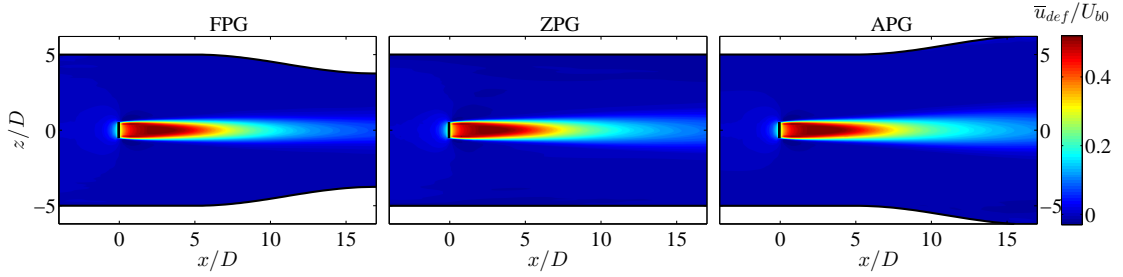


Figure 6.2 – Contours of the normalized velocity deficit in FPG, ZPG and APG cases.

wake and in accordance with Section 6.2.1, we define the velocity deficit as follows:

$$\bar{u}_{def}(x, y, z) = \bar{u}_{nw}(x, y, z) - \bar{u}_w(x, y, z), \quad (6.17)$$

where the subscripts  $w$  and  $nw$  indicate wake and no-wake cases, respectively. In other words, to obtain the velocity deficit at a given point, we subtract the velocity of that point in the wake case from the velocity of the same point in the no-wake case. Figure 6.2 shows the contours of the  $\bar{u}_{def}$  in all three cases. The larger width and slower recovery of the APG wake compared to the FPG one is clear in this figure. Before applying the developed model of Section 6.2, we need to extract  $U_b(x) = \bar{u}_{nw}(x, 0, 0)$  which is an input to the model, and also to verify the assumption of Equation (6.6). Figure 6.3 shows these two pieces of information. As can be seen,  $\lambda(x) = U_d(x)/\delta(x)$  is almost independent of pressure gradient for these three cases. It is also noteworthy that the blockage ratio of the turbine in the channel is 0.009, which can safely be considered as negligible (Segalini and Inghels, 2014).

Now we are fit to implement our proposed model to the aforementioned cases, to see how it predicts the effect of pressure gradient on the wake. Figure 6.4 shows the comparison of the results of the LES and the model for the streamwise evolution of  $C(x)$  and  $\delta_{eq}$ . It can be observed that the model predictions agree well with LES results. In the figure, in addition to the full solution of the ODE (6.8), the asymptotic solutions, resulting from (6.13), are also shown. Note that, all ODEs in this paper are solved with “ode45” routine of MATLAB, which uses an explicit Runge-Kutta (4,5) algorithm, namely, the

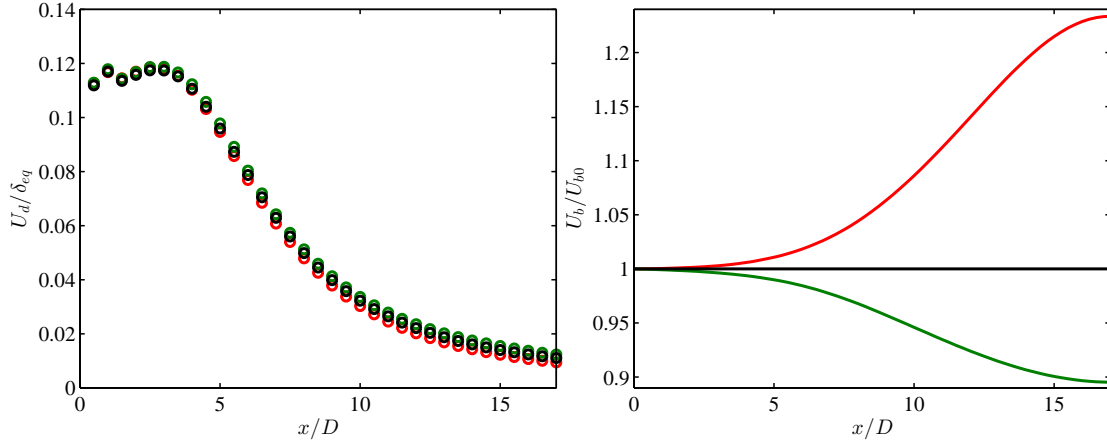


Figure 6.3 – Left: evolution of  $\lambda(x)$  as a function of streamwise distance. Right: base flow velocity  $U_b(x)$  for FPG (red), ZPG (black) and APG (green) cases.

Dormand-Prince method. The black curve in Figure 6.4(right), i.e.  $\delta_0(x)$ , is the input of the model, together with the  $U_b(x)$  which is shown in Figure 6.3(right). Thus, the model results shown here are independently reproducible by the interested reader simply by using the information provided in the paper. Moreover, Figure 6.5 shows a comparison of the normalized velocity deficit profiles in the  $z$ - and  $y$ -directions obtained from the LES and the model for both FPG and APG cases. It can be observed that the model can reproduce the profiles with a good accuracy.

## 6.4 Concluding remarks

We have developed an analytical model which enables us to predict the effect of an imposed pressure gradient on the evolution of turbulent axisymmetric wakes. In particular, the model predicts how the evolution of the wake's maximum velocity deficit and width is altered with respect to the ZPG case by the imposed pressure gradient. The model uses the cross-stream integration of the basic mean momentum conservation equation and uses the self-similarity of the wake and the assumption that the ratio of the maximum velocity deficit to the wake width is invariant under pressure gradient changes. The validity of this assumption has been shown experimentally for planar wakes (Liu et al., 2002) and we have reaffirmed it here for axisymmetric wakes with our large-eddy simulations. An asymptotic solution of the problem is also provided. The problem is considered for both an axisymmetric strain and a planar one. The inputs to the model are the imposed pressure gradient and the wake width in the zero-pressure-gradient case. For the purpose of the validation of the model, a set of numerical experiments, using LES, has been performed. After comparing the maximum velocity deficit and wake width predicted by the model to those of LES, a good agreement was observed.



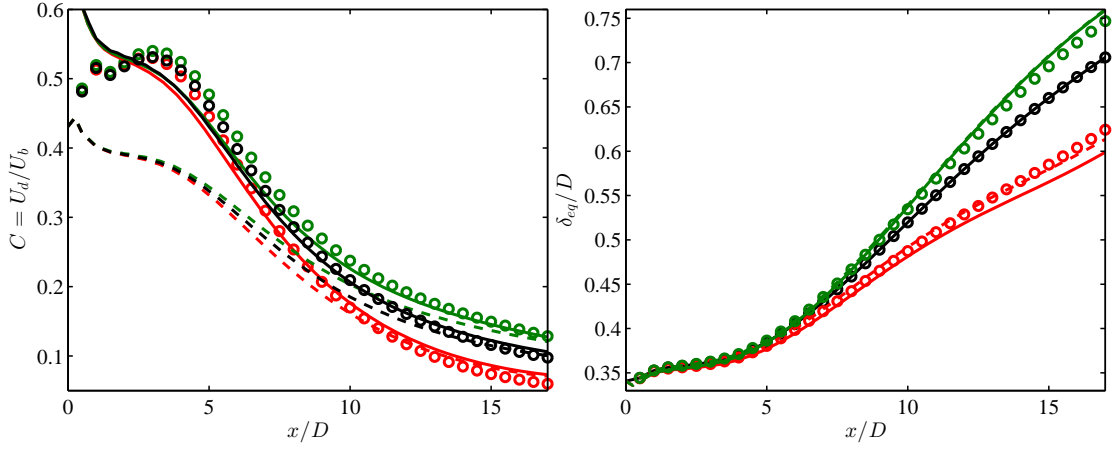


Figure 6.4 – Normalized maximum velocity deficit (left) and wake width (right) as a function of the streamwise distance for ZPG (black), FPG (red) and APG (green) cases. The circles indicate LES results, the solid lines are the full solution obtained from Equation (6.8), and the dashed lines are the asymptotic solution of Equation (6.13).

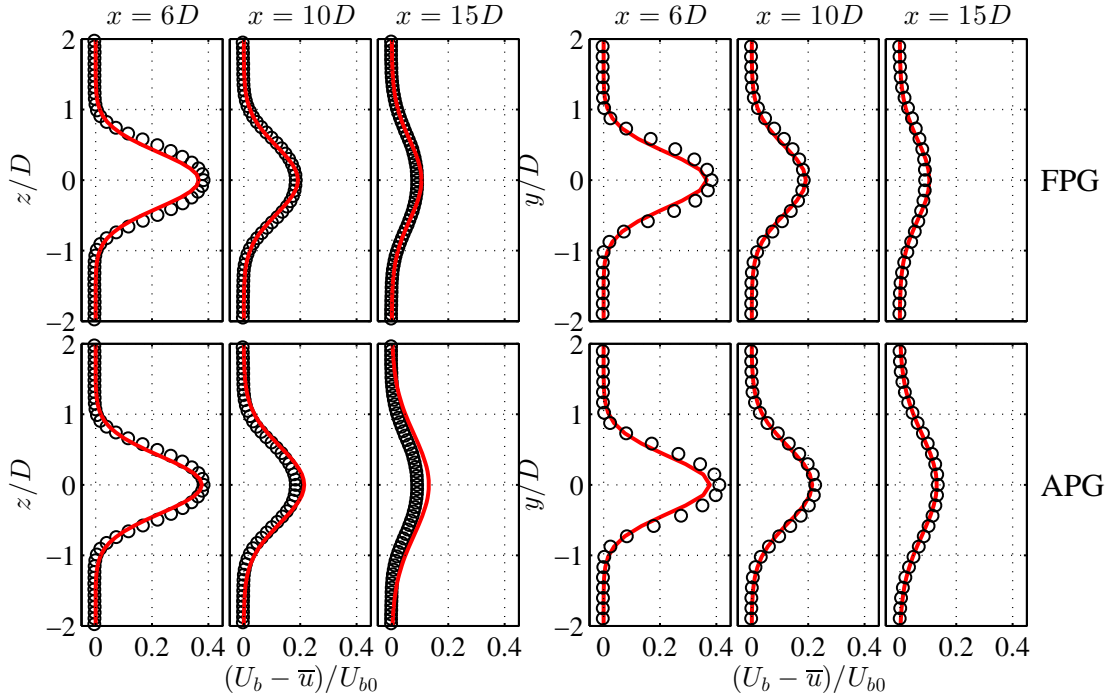


Figure 6.5 – Normalized velocity deficit profiles at different streamwise positions. The circles show LES results and the red lines show the model predictions.

As mentioned in the introduction, one pertinent practical situation where turbulent axisymmetric wakes under pressure gradient conditions emerge in the real world is the case of wind turbine wakes over topography. However, it is important to note that for such cases, in addition to the pressure gradient effects, there is also the effect of streamline curvature. One particular value of the present work is that it isolates the effect of pressure gradient, as it considers a wake, whose centreline is straight (no streamline curvature). In other words, we have decoupled the effect of pressure gradient from that of streamline curvature. That being said, the effect of streamline curvature has also to be taken into account for a proper understanding of the problem of wakes over topography; this issue will be addressed in our future research.

# 7 Wind turbine wakes over hills<sup>1</sup>

## Abstract

Understanding and predicting the behaviour of wind turbine wake flows over hills are important for optimal design of wind farm configurations on topography. In this study, we present an analytical modelling framework together with large-eddy simulation (LES) results to investigate turbine wakes over two-dimensional hills. The analytical model consists of two steps. In the first step, we deal with the effect of pressure gradient on the wake evolution; and in the second step, we consider the effect of the hill-induced streamline distortion on the wake. This model enables us to obtain the wake recovery rate, the mean velocity and velocity deficit profiles, and the wake trajectory in the presence of the hill. Moreover, we perform LES to test our model and also to obtain new complementary insight about such flows. Especially, we take advantage of the LES data to perform a special analysis of the behaviour of the wake on the leeward side of the hill. It is found that the mainly favourable pressure gradient on the windward side of the hill accelerates the wake recovery and the adverse pressure gradient on the leeward side decelerates it. The wake trajectory for a hill of the same height as the turbine's hub-height is found to closely follow the hill profile in the windward side, but it maintains an almost constant elevation (a horizontal line) downstream of the hilltop. The trajectory of the wake on the leeward side is also studied for a limiting case of an escarpment, and it is shown that an internal boundary layer forms on the plateau which leads to an upward displacement of the wake center. Finally, a parametric study of the position of the turbine with respect to the hill is performed to further elucidate the effect of the hill-induced pressure gradient on the wind turbine wake recovery.

---

<sup>1</sup>The contents of this chapter are under review in *Journal of Fluid Mechanics*.

### 7.1 Introduction

For onshore wind farms, unlike the offshore ones, there is a high chance that they are located on non-flat and complex terrain, where wind resource potential is high. This chance keeps increasing with the current expansion of wind power capacity. On the other hand, most of the studies on wind turbine wakes have been carried out assuming a flat underlying terrain, and relatively little attention has been devoted to wakes over topography. Therefore, more careful and refined investigation of wind turbine wakes over topography is much needed and it can highly contribute to better wind-farm site selections and configuration designs.

Although the problem of wakes on topography has received little attention, there is a rich literature on the subject of atmospheric boundary layer flows over topography. There are numerous experimental, numerical and analytical investigations on this subject, for a review of which [Wood \(2000\)](#) and [Belcher and Hunt \(1998\)](#) can be consulted. Before addressing the issue of wind turbine wakes over topography, we cast a brief retrospective look at the key analytical developments of flow over hills (without the presence of turbines), as they play a significant role in the contents of the present paper. A same kind of review but for experimental and numerical studies is also available in [Shamsoddin and Porté-Agel \(2017b\)](#). Subsequently, we consider the interaction of wind turbines and topography in the following subsection.

#### 7.1.1 Analytical studies of flow over hills

From the 1940s to the 1980s, a substantial effort and a significant progress was made in theoretical study and characterization of different features of the flow over topography. This nearly half a century of extensive investigation can be essentially divided into two periods ([Wood, 2000](#)); in the first period, which extends from the 1940s to the 1960s, most of the theoretical work was focused on the inviscid response of stably stratified flows to hills (for detailed reviews about the research in this period see: [Corby, 1954](#); [Wurtele et al., 1996](#)).

The second period commenced with the groundbreaking analysis of [Jackson and Hunt \(1975\)](#) who developed a linear solution for two-dimensional turbulent flows over low hills with arbitrary shapes. After using perturbation methods and performing an order of magnitude analysis on the Navier-Stokes equations (continuity and two equations of motion in the horizontal and vertical directions), they argued that the flow can be considered to be divided into two layers: a thin *inner* layer in which the perturbation turbulent shear stresses are significant and modeled by a simple mixing-length model; and an *outer* layer in which the perturbation stresses are shown to be negligible and the disturbance to be almost irrotational. By asymptotic expansion of the perturbation variables (pressure and two components of velocity), the linearized, Fourier-transformed

equations were solved, and analytical solutions (to the leading order) were obtained in wavenumber space.

The paper of Jackson and Hunt influenced and inspired numerous researches in the forthcoming years. [Mason and Sykes \(1979\)](#) extended the model to three dimensions and compared the results with their field data. Next, [Sykes \(1980\)](#) presented his own asymptotic analysis of a turbulent boundary-layer flow encountering a small two-dimensional hump. While his analysis was, in many ways, similar to the one of Jackson and Hunt, it had major distinctions and contributions. First, instead of two layers, he considered three layers by adding a very thin wall layer to impose the surface boundary condition more consistently. He also used a second-order closure model to model the Reynolds stress perturbations and was able to calculate the net force perturbation (pressure drag) on the obstacle. Further modifications to the linear theory were realized by [Hunt et al. \(1988\)](#), who developed an analysis for turbulent shear flows over two- and three-dimensional hills, which is capable of dealing with different upwind velocity profiles. By keeping the wall layer, which was proposed by [Sykes \(1980\)](#), and subdividing the inviscid outer layer of Jackson and Hunt theory to two sublayers, they considered four different layers in their analysis, among which, the middle layer was newly introduced to allow for significant shear in the upstream flow. Other advancements of the theory was achieved by [Taylor et al. \(1983\)](#) who employed a wavenumber-dependent strategy to assign a specific horizontal length-scale to each wavenumber in Fourier space. In the 1990s, attempts for analytically including non-linear effects in the solution of the flow over low-slope hills are found in the works of [Xu and Taylor \(1992\)](#) and [Xu et al. \(1994\)](#).

### 7.1.2 Wind turbines and topography

Experimental (both wind tunnel and field) measurements of wind turbine wakes over hilly terrain started from the early 1990s (e.g. [Taylor and Smith, 1991](#); [Stefanatos et al., 1994](#); [Helmis et al., 1995](#); [Stefanatos et al., 1996](#)). More recently, some various cases of wind turbines siting on topography have been studied. [Tian et al. \(2013\)](#) considered an array of five turbines distributed on a single hill, and compared the wind farm performance with the flat terrain case. [Yang et al. \(2015\)](#), on the other hand, placed a turbine downstream of a single hill, and observed that the turbine wake recovery rate increases due to the turbulence generated by the hill. Moreover, [Hyvärinen and Segalini \(2017a\)](#) performed measurements of the flow around two tandem wind turbines which were sited on a terrain consisted of a series of sinusoidal hills. They also observed a faster wake recovery, and as they have put it, ‘a positive impact on the wind-turbine performance’ due to the presence of the hills.

Furthermore, numerical models have also been developed for this problem (e.g., [Voutsinas et al., 1990](#); [Hemon et al., 1991](#); [Günther et al., 1993](#); [Ansorge et al., 1994](#); [Chaviaropoulos and Douvikas, 1999](#); [Ivanova and Nadyozhina, 2000](#); [Migoya et al., 2007](#)). More recently,

[Politis et al. \(2012\)](#) have performed RANS (Reynolds-averaged Navier–Stokes) simulations of both a real wind farm on complex terrain and a single turbine sited on top of a single hill. They have observed that the wake recovery is slower with respect to the flat-terrain case. Moreover, using terrain-following coordinates, [Shamsoddin and Porté-Agel \(2017b\)](#) performed large-eddy simulation (LES) of flow through a wind farm sited on a single hill and validated the results using the dataset of [Tian et al. \(2013\)](#). Employing a different approach, [Segalini \(2017\)](#) used the linearized continuity and momentum equations to solve for the flow field around turbines located on low-slope topography. This method has the advantage of incurring significantly less computational cost. In addition to these, there have also been other numerical studies on this subject both for real complex terrain (e.g. [Schulz et al., 2014](#); [Yang et al., 2014](#); [Castellani et al., 2015, 2017](#); [Berg et al., 2017](#)) and idealized hills (e.g. [Yang et al., 2015](#); [Zheng et al., 2017](#)).

The common simple method in industry to model the effect of topography on turbine wakes is the idea of superposition, in which the turbine velocity deficit over flat terrain is superposed on the flow over the topography (without the turbines). This method has been used by several researchers (e.g., [Crespo and Hernandez, 1986](#); [Crespo et al., 1993](#); [Hyvärinen and Segalini, 2017b](#)) and in some cases (e.g. [Crespo et al., 1993](#); [Hyvärinen and Segalini, 2017b](#)) has resulted in acceptable results. However, its general applicability, even for hills of moderate slope, has been called into question ([Politis et al., 2012](#); [Segalini, 2017](#)).

In this paper, we aim to investigate how a single hill affects the wake of a wind turbine sited upstream of it. We are going to answer questions such as: why have [Politis et al. \(2012\)](#) observed a slower wake recovery when the turbine is located on the hilltop (compared with flat-terrain case), whereas others ([Hyvärinen and Segalini, 2017a](#); [Yang et al., 2015](#)) mostly have reported a faster wake recovery on hilly terrain? We will see that the reasons for each of these two trends have completely different natures. We also present an analytical modeling framework which enables us to predict how a hill affects a turbine wake flow. In doing so, we use the substantial and valuable analytical developments of flow over hills (e.g. [Hunt et al., 1988](#)), and we also take advantage of some wake-specific studies of pressure-gradient effect on wake flows (e.g. [Liu et al., 2002](#); [Shamsoddin and Porté-Agel, 2017a, 2018](#)). Moreover, we perform LES of such flows in order to test our model and also to acquire more detailed insight about these flows.

This article is structured in the following manner. In Section 7.2, the analytical framework is derived and illustrated. The LES set-up and some key LES qualitative results are described in Section 7.3. A special attention is paid to the wake on the leeward side of the hill in Section 7.4. At this stage, we will be ready to test the developed analytical framework against LES data in Section 7.5. In Section 7.6, the effect of pressure gradient on wake recovery is inspected more thoroughly, and finally Section 7.7 concludes the paper.

## 7.2 An analytical modelling framework for wake flows over hills

### 7.2.1 Problem formulation

The objective of this section is to develop an analytical model which enables us to predict the evolution of a turbine wake flow over a two-dimensional (2D) hill of moderate slope. More specifically, we are interested to solve the following problem: for a given wake over flat terrain, how does the introduction of a 2D hill downwind of the turbine perturb the wake flow field? In particular, we are interested in the wake recovery rate, the mean velocity and velocity deficit profiles, and the wake trajectory in the presence of the hill. The starting and end points of the problem are shown in the schematic of Figure 7.1.

In general, the topography is considered to produce two major effects on the flow passing above it: (1) the non-zero pressure gradient up- and downwind of the hilltop, and (2) the streamline curvature that it causes (for instance, see Nakayama, 1987; Baskaran et al., 1991). The pressure gradient effect is specially important for wake flows above hills, because it considerably affects the wake recovery, i.e., depending on the sign of the pressure gradient, the wake recovers faster or slower with respect to a wake in zero pressure gradient. In our approach to model a wake flow over a hill we decouple the analysis of these two effects on the wake. In accordance with these two major effects, the modelling framework that we will present comprises two steps. In the first step, we predict how the induced pressure gradient by the hill alters the wake recovery evolution. In the second step, we calculate how the wake (which is now already modified by the effect of the pressure gradient) flows over the hill by taking into account the distortion of the streamlines caused by the hill. By doing so, we model these two effects separately. This two-step approach is also shown in Figure 7.1. Each of these two steps will be described in the next two subsections (Section 7.2.2 and Section 7.2.3).

### 7.2.2 Effect of the hill-induced pressure gradient on the wake recovery

It is known that hills produce non-zero pressure gradients in the flow above them. Particularly, hills induce mainly a favourable pressure gradient (FPG) on their windward side and an adverse pressure gradient (APG) on their leeward side (normally a slight APG precedes the FPG in the windward side, but its magnitude is much smaller). This is equivalent with the fact that the flow undergoes mainly an acceleration upwind of the hilltop and a deceleration downwind of it. On the other hand, pressure gradient affects the wake recovery characteristics. The wake centre velocity recovers faster in FPG conditions and slower in APG conditions (with respect to the zero-pressure-gradient (ZPG) case). The wake width, however, grows more rapidly under APG and more slowly under FPG compared with the ZPG case. These trends have been shown for planar wakes in the works of Rogers (2002) (numerically), Liu et al. (2002) and Thomas

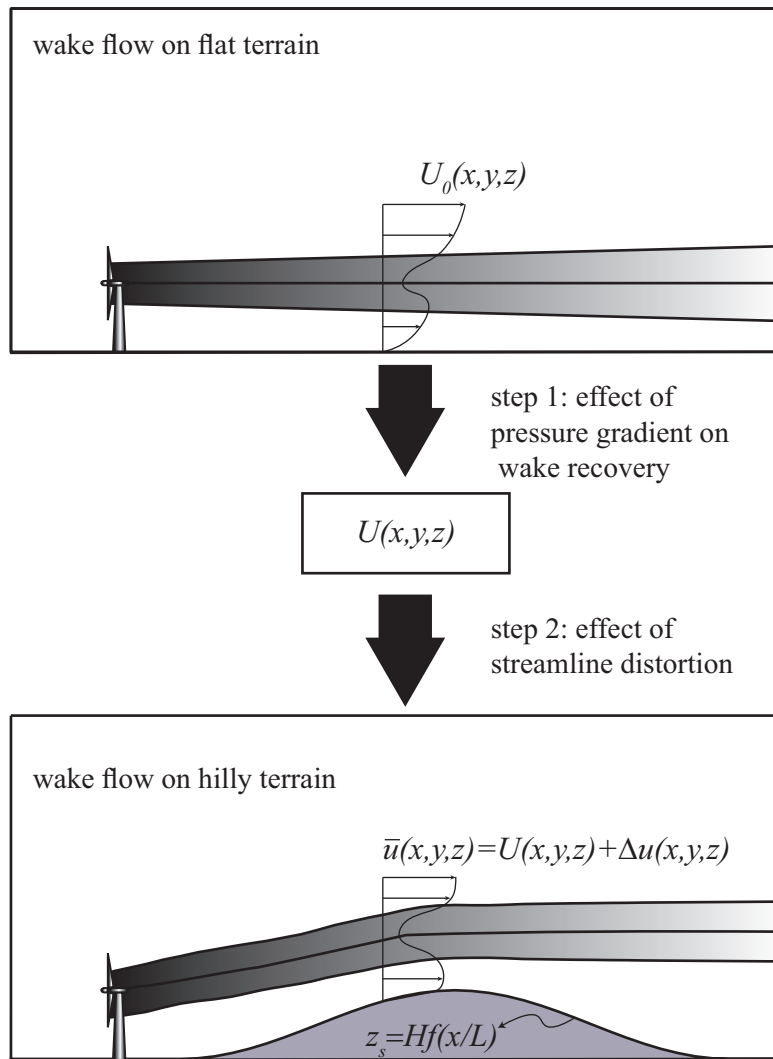


Figure 7.1 – Schematic of the problem and the modeling framework.



## 7.2. An analytical modelling framework for wake flows over hills

and Liu (2004) (experimentally) and recently in Shamsoddin and Porté-Agel (2017a) (analytically). Moreover, Shamsoddin and Porté-Agel (2018) have recently shown that the above trends also apply to axisymmetric wakes (which is the case for a wind turbine wake) by using both an analytical approach and LES data.

Herein, we use the model developed by Shamsoddin and Porté-Agel (2018) to model the effect of the hill-induced pressure gradient on the axisymmetric wake of a wind turbine. The model needs two inputs. First, the mean velocity evolution in the absence of the turbine which is indicative of the imposed pressure gradient. Second, the wake width of the corresponding ZPG case, which, in this case, would be the wake over flat terrain.

The mean velocity deficit profiles of a turbulent axisymmetric wake is taken to have a self-similar Gaussian shape:

$$\frac{U_b(x) - \bar{u}(x, r)}{U_b(x)} \equiv C(x) e^{-\frac{r^2}{2\delta^2}}, \quad (7.1)$$

where  $x$  is the streamwise direction,  $r$  is the radial direction from the wake centre,  $\bar{u}(x, r)$  is the velocity (hereafter, by velocity, we imply the mean streamwise velocity, unless otherwise stated) of the wake flow,  $U_b(x)$  is the velocity of the flow under pressure gradient but without the wake,  $C(x)$  is a function determining the maximum velocity deficit at each  $x$ -position and  $\delta(x)$  is the wake width. For the problem at hand, we consider  $U_b(x)$  to be equal to the velocity at a distance equal to the hub-height of the turbine over the hill, i.e.  $U_{nw}^h(x)$ .

For  $C(x)$  the following ODE can be obtained:

$$\frac{dC(x)}{dx} = \frac{-1}{\left(\frac{U_b^4}{\lambda_0^2}\right) (3C^2 - 2C^3)} \left[ \frac{1}{4} \frac{dU_b^4}{dx} \frac{C^3}{\lambda_0^2} + \left( C^3 - \frac{C^4}{2} \right) \frac{d}{dx} \left( \frac{U_b^4}{\lambda_0^2} \right) \right], \quad (7.2)$$

with the boundary condition

$$C(x_i) = C_0(x_i), \quad (7.3)$$

where  $C_0(x)$  and  $\lambda_0(x)$  are:

$$C_0(x) = 1 - \sqrt{1 - \frac{C_T}{8 \left( \frac{\delta_0(x)}{D} \right)^2}} \quad , \quad (x \geq x_i), \quad (7.4)$$

and

$$\lambda_0(x) = \frac{U_{b0}C_0(x)}{\delta_0(x)}, \quad (7.5)$$

where the subscript 0 indicates a quantity in the ZPG case,  $D$  is the diameter of the wake-generating object and  $C_T$  is the thrust coefficient of the turbine. The condition ( $x \geq x_i$ ) is only to make sure that the expression under the square root always remains non-negative. Finally,  $\delta$  can be expressed as

$$\delta(x) = \frac{U_b(x)}{\lambda_0(x)}C(x). \quad (7.6)$$

It can be shown that the following asymptotic solution (designated as  $\tilde{C}(x)$ ) for the ODE of (7.2) can be obtained for sufficiently large  $x$  (Shamsoddin and Porté-Agel, 2018):

$$\tilde{C}(x) = \tilde{C}_0 \left( \frac{U_{b0}}{U_b(x)} \right)^{\frac{5}{3}}, \quad (7.7)$$

where  $\tilde{C}_0 = D^2C_D/(16\delta_0^2)$  is the asymptotic ZPG solution for  $\tilde{C}_0$ , which is equal to the second-order Taylor expansion of the full solution of  $C_0(x)$ , i.e. (7.4), in terms of  $\delta_0^{-1}$ .

$U_{nw}^h$  can be obtained by linearized models such as the one proposed by Jackson and Hunt (1975). We will elaborate more on this in the next subsection. Up to this stage, with (7.2) and (7.6), one can obtain the wake evolution under the pressure gradient caused by the hill.

### 7.2.3 Effect of the hill-induced streamline distortion

In this subsection, we employ a linearized perturbation approach to calculate how the wake moves over the hill. One important assumption of this method is that the flow remains attached to the hill, and there is no flow separation. For a hill of moderate slope, this assumption holds for the windward side of the hill. For the leeward side, however, this assumption normally does not remain valid anymore. Even if we do not have a flow separation (with the strict definition of having negative velocities at certain locations), we usually have the so-called “*non-separated sheltering*” in the leeward of the hill (Belcher et al., 1993; Belcher and Hunt, 1998; Belcher, 1999). It is also already known that linearized perturbation models (without turbines) do not result in sufficiently accurate predictions on the leeward side of the hills (even with moderate slopes) due to this non-separated sheltering effect (e.g. Britter et al., 1981). For the leeward side of the hill, a special treatment will be used, which will be presented in Section 7.4.

Herein, we use a linearized perturbation approach, which is inspired by the work of Hunt et al. (1988). In the present paper, we build on that model so that we can account for

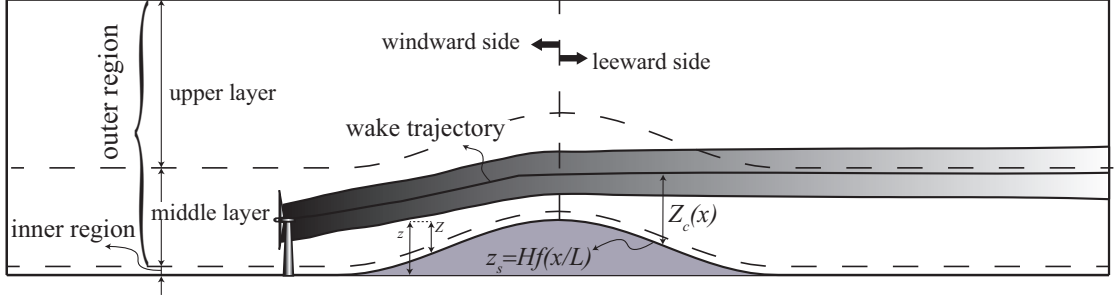


Figure 7.2 – Schematic of the second step of the model.

the evolution of the wind turbine wakes over hills. The hill considered here has a surface equation of  $z_s = Hf(x/L)$ , where  $H$  is the height at the hilltop,  $L$  is the half-length of the hill,  $f(x/L) \leq 1$  and  $f(0) = 1$ . In this analysis, we assume  $H/L$  is sufficiently small.

### Governing equations and coordinate systems

$\bar{u}$ ,  $\bar{v}$  and  $\bar{w}$  are the mean streamwise, spanwise and vertical velocities in the case of the wake flow over a hill. This velocity field can be expressed in terms of the velocity field over a flat terrain (i.e., the base flow) and some perturbation velocities (see Figure 7.1). The way that the perturbed velocities are linked to the base flow field depends on the coordinate system in which we express the flow. In general, there are two types of coordinates that can be envisaged for this purpose: Cartesian coordinates  $(x, y, z)$  and terrain-following coordinates  $(X, Y, Z)$ . The choice between these two types of coordinates in different regions of the flow should be based on the nature of the flow. The common practice is that as we move closer to the ground the terrain-following coordinates become more suitable, and in higher distances from the ground, Cartesian coordinates are preferred. In this section, we define the terrain-following coordinates as:  $X = x$ ,  $Y = y$ ,  $Z = z - Hf(x/L)$ . The perturbation velocities are defined in Cartesian and terrain-following coordinates by Equations (7.8) and (7.9), respectively:

$$\bar{u}(x, y, z) = U(x, y, z) + \Delta u(x, y, z), \quad (7.8a)$$

$$\bar{v}(x, y, z) = \Delta v(x, y, z), \quad (7.8b)$$

$$\bar{w}(x, y, z) = \Delta w(x, y, z), \quad (7.8c)$$

$$\bar{p}(x, y, z) = P(x, y, z) + \Delta p(x, y, z), \quad (7.8d)$$

$$\bar{u}_t(x, y, Z) = U(x, y, Z) + \Delta u_t(x, y, Z), \quad (7.9a)$$

$$\bar{v}_t(x, y, Z) = \Delta v_t(x, y, Z), \quad (7.9b)$$

$$\bar{w}_t(x, y, Z) = U \frac{H}{L} f'\left(\frac{x}{L}\right) + \Delta w_t(x, y, Z), \quad (7.9c)$$

$$\bar{p}_t(x, y, Z) = P(x, y, Z) + \Delta p_t(x, y, Z) \quad (7.9d)$$

where  $U$  is the mean streamwise velocity field over a flat terrain (i.e., the base flow), and the subscript  $t$  indicates a quantity expressed in the terrain-following coordinates. The momentum and continuity equations for the flow are written as:

$$\bar{u} \frac{\partial \bar{u}}{\partial x} + \bar{v} \frac{\partial \bar{u}}{\partial y} + \bar{w} \frac{\partial \bar{u}}{\partial z} = -\frac{1}{\rho} \frac{\partial \bar{p}}{\partial x} + \frac{1}{\rho} \frac{\partial \tau_{1j}}{\partial x_j}, \quad (7.10a)$$

$$\bar{u} \frac{\partial \bar{v}}{\partial x} + \bar{v} \frac{\partial \bar{v}}{\partial y} + \bar{w} \frac{\partial \bar{v}}{\partial z} = -\frac{1}{\rho} \frac{\partial \bar{p}}{\partial y} + \frac{1}{\rho} \frac{\partial \tau_{2j}}{\partial x_j}, \quad (7.10b)$$

$$\bar{u} \frac{\partial \bar{w}}{\partial x} + \bar{v} \frac{\partial \bar{w}}{\partial y} + \bar{w} \frac{\partial \bar{w}}{\partial z} = -\frac{1}{\rho} \frac{\partial \bar{p}}{\partial z} + \frac{1}{\rho} \frac{\partial \tau_{3j}}{\partial x_j}, \quad (7.10c)$$

$$\frac{\partial \bar{u}}{\partial x} + \frac{\partial \bar{v}}{\partial y} + \frac{\partial \bar{w}}{\partial z} = 0, \quad (7.10d)$$

where  $\tau$  is the turbulent stress tensor.

As shown in Figure 7.2, flow over hills is commonly divided into two regions: (1) the inner region which is a relatively thin layer close to the ground, and (2) the outer region which is located just above the inner region. The gradients of the perturbation turbulent stresses are considerable only in the inner region, and in the outer region they can be neglected (Jackson and Hunt, 1975). The turbine wake flows are essentially located in the outer region (for example see section 4.6 of Emeis, 2013). It is also noteworthy that the inner region in a turbulent flow (unlike a laminar flow) has little effect on the outer region (Hunt et al., 1988). That is why, in our analysis, we focus on the outer region. The thickness of the inner region  $l$  can be determined from solving the equation  $l \ln(l/z_o) = 2\kappa^2 L$ , where  $\kappa$  is the von Kármán constant and  $z_o$  is the surface roughness length (Jackson and Hunt, 1975). Alternatively, one can use the following approximate explicit relation:  $l = (1/8)z_o(L/z_o)^{0.9}$ . For example, for a hill of 100 m height and  $H/L = 0.5$  in a farmland ( $z_o = 0.1$  m), the height of the inner region would be about  $l = 11$  m.

The outer region, in turn, is further divided into two layers: (1) the middle layer, and (2) the upper layer. The main difference between these two layers, in this analysis, is in the type of the coordinate systems by which the perturbation velocities are related to the base flow. In the middle layer, the flow has a terrain-following nature (hence, we use the terrain-following coordinates 7.9), and in the upper layer, the Cartesian coordinates is

proved to better capture the physics of the flow (Hunt et al., 1988). We continue this section by studying the flow in these two layers.

### Upper layer

First, we consider the upper layer. Here, for the case of a 2D hill, we can neglect the spanwise velocity  $\bar{v}$ , and after linearization of the Equations (7.10), we obtain the following equations for the perturbation velocities:

$$U(x, y, z) \frac{\partial \Delta u}{\partial x} + \Delta w \frac{\partial U(x, y, z)}{\partial z} = -\frac{1}{\rho} \frac{\partial \Delta p}{\partial x}, \quad (7.11a)$$

$$U(x, y, z) \frac{\partial \Delta w}{\partial x} = -\frac{1}{\rho} \frac{\partial \Delta p}{\partial z}, \quad (7.11b)$$

$$\frac{\partial \Delta u}{\partial x} + \frac{\partial \Delta w}{\partial z} = 0. \quad (7.11c)$$

It should be noted that in Equation (7.11a) we have neglected the term  $\Delta u \partial U / \partial x$  compared with the term  $U \partial \Delta u / \partial x$ , as the streamwise recovery of the wake is relatively small.

In the upper layer, where  $\partial U / \partial z$  is small, the above equations reduce to a Laplace equation for  $\Delta w$ . This equation can be solved, and from continuity the solution for  $\Delta u$  is obtained:

$$\Delta u^U = \left( \frac{H}{L} \right) \left( \frac{1}{\pi} \right) \int_{-\infty}^{\infty} \frac{(\partial f / \partial x)(\xi / L) \cdot (x - \xi) d\xi}{(x - \xi)^2 + z^2}, \quad (7.12)$$

where  $\xi$  is a dummy variable for integration, and the superscript  $U$  indicates a quantity in the upper layer. Furthermore, we can now express the total  $\bar{u}$  velocity for both the wake and no-wake case:

$$\left. \begin{array}{l} \text{no wake: } \bar{u}_{nw}^U = U_{nw}(z) + \Delta u^U, \\ \text{wake: } \bar{u}_w^U = U_w(x, y, z) + \Delta u^U, \end{array} \right\} \quad (7.13)$$

where the subscripts  $w$  and  $nw$  indicate wake (i.e. when the turbine is present) and no-wake (i.e. the case without turbine) cases, respectively.

### Middle layer

The height of the middle layer  $h_m$  is considered to be  $h_m = L$  for long hills ( $L > H$ ) which is the case in the current study (Hunt et al., 1988). In the middle layer, the pressure is taken to be varying only in the horizontal directions (i.e.,  $\partial \Delta p_t / \partial Z = 0$ ). We then obtain the following equation for the streamwise and vertical velocities:

$$\bar{u}_t \frac{\partial^2 \bar{w}_t}{\partial Z^2} - \bar{w}_t \frac{\partial^2 \bar{u}_t}{\partial Z^2} = 2 \frac{\partial}{\partial Z} \left[ \bar{v}_t \frac{\partial \bar{u}_t}{\partial y} \right], \quad (7.14)$$

In the case of a base flow which is only a function of  $z$  (e.g. in the no-wake case), the right-hand side of Equation (7.14) is equal to zero (because  $\partial U / \partial y = 0$ ). However, in the case of a wake flow, not only  $\partial U / \partial y \neq 0$ , but also it is not negligible; in fact, it has the same order of magnitude as  $\partial U / \partial z$ . Nevertheless, for a 2D hill, it is a good assumption to consider  $\bar{v}_t$  as negligible. Therefore, in this case we can still neglect this term, and the equation becomes:

$$\bar{u}_t \frac{\partial^2 \bar{w}_t}{\partial Z^2} - \bar{w}_t \frac{\partial^2 \bar{u}_t}{\partial Z^2} = 0 \quad (7.15)$$

After considering  $\bar{u}_t \approx U$  the above equation becomes an ODE, which can be solved for  $\bar{w}_t$ . Next, by continuity,  $\Delta u_t$  can be obtained (the details can be found in Hunt et al., 1988):

$$\left. \begin{aligned} \Delta u_t &= -[A(x) - Hf] \frac{\partial U(x, y, Z)}{\partial Z} - \frac{B(x, y) J(x, y, Z)}{U(x, y, Z)}, \\ \text{where: } J(x, y, Z) &= 1 + U(x, y, Z) \frac{\partial U(x, y, Z)}{\partial Z} \int_{Z_l}^Z \frac{d\zeta}{U^2(x, y, \zeta)}. \end{aligned} \right\} \quad (7.16)$$

where  $Z_l = \sqrt{lz_o}$ ,  $l$  is the thickness of the inner region (see above for determining the value of  $l$ ), and  $\zeta$  is a dummy variable for the integration. The functions  $A(x)$  and  $B(x, y)$  shall be found from the matching of the middle layer to the inner region and upper layer, respectively. Matching  $\bar{w}$  between the middle layer and inner region results in  $A(x) = Hf(x/L)$  (Hunt et al., 1988). Now we match  $\bar{u}$  between the middle and upper layers in a direct manner which is different from the approximate matching of Hunt et al. (1988). For this purpose, we equate  $\bar{u}$  at  $z = h_m + Hf(x/L)$  and  $\bar{u}_t$  at  $Z = h_m$ , and after some manipulations, we obtain the following relation for  $B(x, y)$ :

$$B(x, y) = \frac{[U(x, y, Z = h_m) - \bar{u}^U(x, y, z = h_m + Hf(x/L))] U(x, y, Z = h_m)}{J(x, y, Z = h_m)}, \quad (7.17)$$

Now, the only remaining part of the model that needs to be determined is the mean velocity distribution  $U(x, y, z)$  of the base flow. For the case of the flow without the

## 7.2. An analytical modelling framework for wake flows over hills

turbine, we consider a logarithmic profile, and for the case of wake flow behind a wind turbine, we consider a velocity deficit function calculated in Section 7.2.2.

$$\left. \begin{array}{l} \text{no wake: } U(x, y, z) = U_{nw}(z) = \frac{u_*}{\kappa} \ln(z/z_o), \\ \text{wake: } U(x, y, z) = U_w(x, y, z) = U_{nw}(z) \{1 - C(x) e^{-\frac{r^2}{2\delta^2}}\}, \end{array} \right\} \quad (7.18)$$

where,  $C(x)$  and  $\delta(x)$  are already determined in Section 7.2.2.

By using the above relations for the base flow in Equations (7.16), we are able to obtain  $\Delta u_t$  in the middle layer for both the wake and no-wake cases. Next, by using Equation (7.9), we can get the total perturbed streamwise velocity  $u_t$ :

$$\left. \begin{array}{l} \text{no wake: } \bar{u}_{nw}^M = U_{nw}(z) + \Delta u_t^M, \\ \text{wake: } \bar{u}_w^M = U_w(x, y, z) + \Delta u_t^M, \end{array} \right\} \quad (7.19)$$

where the superscript  $M$  indicates a quantity in the middle layer. The velocity deficit is then obtained as:

$$\bar{u}_{\text{def}}(x, y, Z) = \bar{u}_{nw}^M - \bar{u}_w^M. \quad (7.20)$$

For the no-wake case (i.e. flow over a hill without turbine), normally the upper layer solution is used (i.e.  $\bar{u}_{nw}^U$  in (7.13)). This is an industry standard choice and normally results in more accurate results than the middle layer solution for the no-wake case (for example in the orographic model used in the Wind Atlas Analysis and Application Program (WAsP) [Bowen and Mortensen, 2004](#)). In this case, in order to be consistent between the wake and the no-wake cases, we can define  $\bar{u}_w^{UM}$  in terms of the upper layer solution for the no-wake case and the velocity deficit of (7.20):

$$\bar{u}_w^{UM}(x, y, Z) = \bar{u}_{nw}^U(x, y, Z + Hf(x/L)) - \bar{u}_{\text{def}}(x, y, Z). \quad (7.21)$$

Finally, the trajectory of the wake center is defined as:

$$Z_c(x) = \underset{Z}{\operatorname{argmax}} (\bar{u}_{\text{def}}(x, y_h, Z)), \quad (7.22)$$

where  $y_h$  is the  $y$ -position of the turbine hub.

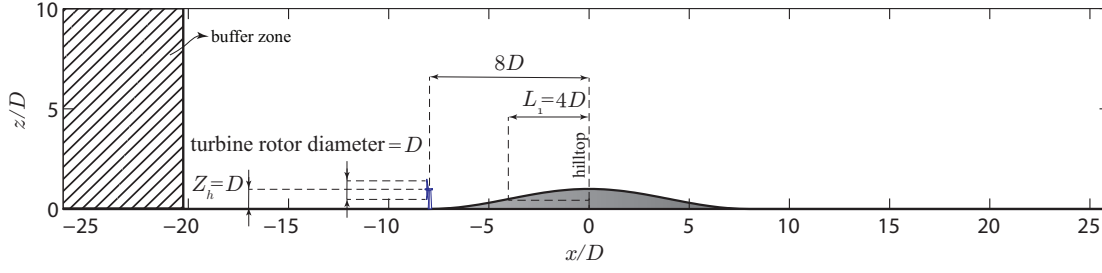


Figure 7.3 – Domain of the simulations.

### 7.3 Numerical experiments

For the purpose of acquiring new and more detailed insight about the problem at hand and also for testing the above-described modeling framework, we perform some numerical experiments using LES. In this section, the LES set-up and some key qualitative results are presented.

#### 7.3.1 LES set-up

In our numerical experiments, we simulate the flow through a turbine which is sited upstream of a 2D hill. The hub-height and the diameter of the turbine are chosen to be equal, as these two values are close together also in real wind turbines. Regarding the dimensions of the hill, our aim is to have a hill of significant height with respect to the turbine dimensions. For this purpose, we have taken the hill height to be just equal to hub-height of the turbine.

The simulation domain is shown in Figure 7.3. The terrain profile is given by the following equation:

$$z_s(x) = \begin{cases} \frac{1}{2}H \left[ 1 + \cos \left[ \frac{\pi}{2L_1}(x) \right] \right], & -2L_1 \leq x < 0 \\ \frac{1}{2}H \left[ 1 + \cos \left[ \frac{\pi}{2L_2}(x) \right] \right], & 0 \leq x < 2L_2 \\ 0, & \text{otherwise,} \end{cases} \quad (7.23)$$

where  $z_s$  is the height of the terrain, the origin of  $x$  (as shown in Figure 7.3) is the position of the hilltop,  $H$  is the hill height which has the values of  $H = D$ , and  $L_1$  and  $L_2$  are the half-lengths of the hill for the windward and leeward sections, respectively. Regarding the values of  $L_1$  and  $L_2$ , we should keep in mind that the hill is required not to be too steep for application of the framework of Section 7.2. Accordingly, a value of  $4D$  is chosen for  $L_1$ . For the basic symmetrical hill, which is the basic case in this paper, we have  $L_2 = L_1$ ; however, we will investigate different values of  $L_2$  in Section 7.4.

In our LES, the filtered incompressible Navier–Stokes equations (for a neutrally-stratified



ABL) are solved, which can be written in rotational form as:

$$\frac{\partial \tilde{u}_i}{\partial x_i} = 0, \quad (7.24)$$

$$\frac{\partial \tilde{u}_i}{\partial t} + \tilde{u}_j \left( \frac{\partial \tilde{u}_i}{\partial x_j} - \frac{\partial \tilde{u}_j}{\partial x_i} \right) = -\frac{\partial \tilde{p}^*}{\partial x_i} - \frac{\partial \tau_{ij}}{\partial x_j} - \frac{f_i}{\rho} + F_p \delta_{i1}, \quad (7.25)$$

where the tilde represents a three-dimensional spatial filtering operation,  $\tilde{u}_i$  is the filtered velocity in the  $i$ -direction (with  $i = 1, 2, 3$  corresponding to the streamwise ( $x$ ), spanwise ( $y$ ) and vertical ( $z$ ) directions, respectively),  $\tilde{p}^* = \tilde{p}/\rho + \frac{1}{2}\tilde{u}_i\tilde{u}_i$  is the modified kinematic pressure where  $\tilde{p}$  is the filtered pressure,  $\tau_{ij} = \widetilde{u_i u_j} - \tilde{u}_i \tilde{u}_j$  is the kinematic SGS stress,  $f_i$  is a body force (per unit volume) used to model the effects of the turbine on the flow,  $F_p$  acts as the driving force of the flow (in the streamwise-periodic case), and  $\rho$  is the constant fluid density. In this paper,  $u$ ,  $v$  and  $w$  notations are also used for the  $u_1$ ,  $u_2$  and  $u_3$  velocity components, respectively. Regarding the parametrization of the SGS stresses, the Lagrangian scale-dependent dynamic model (Stoll and Porté-Agel, 2006b) is used.

The turbine forces acting on the flow are modelled using the standard actuator disk model (Wu and Porté-Agel, 2011). The hilly terrain at the bottom of the domain is dealt with by using a terrain-following coordinate system, whose details are described in Shamsoddin and Porté-Agel (2017b). The horizontal boundary conditions are mathematically periodic. For the upper boundary, an impermeable free-stress boundary condition is assigned, and for the lower boundary, the instantaneous surface shear stress is calculated using the Monin-Obukhov similarity theory (which for the neutral case of this study simply reduces to the log law). To eliminate the periodicity of the flow in the streamwise direction, a buffer zone technique is employed, in which we feed an inflow field to our simulation. This inflow field is obtained from an offline precursory simulation over flat terrain (Tseng et al., 2006; Wan and Porté-Agel, 2011; Wu and Porté-Agel, 2011; Shamsoddin and Porté-Agel, 2014, 2016, 2017b). The details of the LES framework, its numerics and the SGS model are described, for instance, in Albertson and Parlange (1999), Porté-Agel et al. (2000), Stoll and Porté-Agel (2006b), Wan et al. (2007), Porté-Agel et al. (2011) and Shamsoddin and Porté-Agel (2017b).

The dimensions of the domain are  $52.5D$ ,  $8.75D$  and  $10D$  in the  $x$ -,  $y$ - and  $z$ -directions, respectively. The number of grid points in the  $x$ -,  $y$ - and  $z$ -directions are, respectively, 210, 60 and 122. Moreover, the ratio of the surface roughness length to the domain height (i.e.  $10D$ ) is set to  $10^{-4}$  which is a typical value for a farmland. The accuracy of this LES framework has been tested in several validations studies: the validation of the

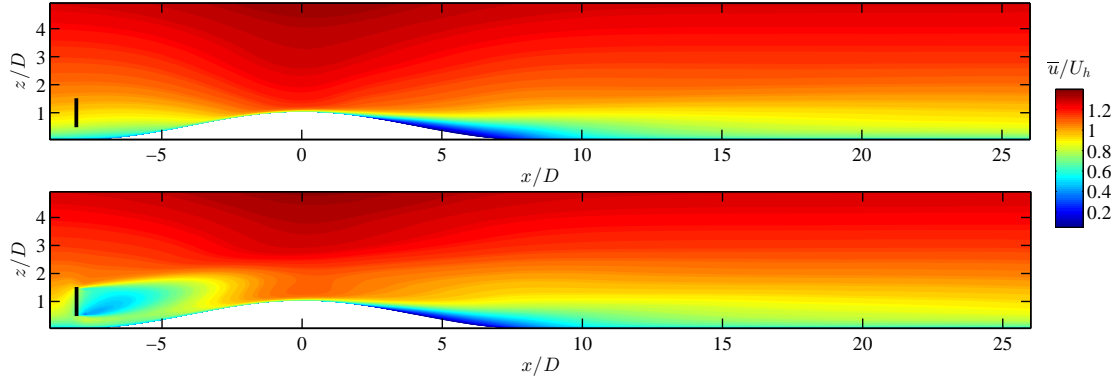


Figure 7.4 – Contours of the normalized mean streamwise velocity ( $\bar{u}/U_h$ ) in the  $xz$ -plane going through the center of the turbine. Top: no wake case. Down: turbine case.

actuator disk model was performed in [Wu and Porté-Agel \(2011\)](#) and [Porté-Agel et al. \(2011\)](#) and the validation of the coordinate transformation technique was carried out in [Wan et al. \(2007\)](#). On top of these, the combined application of the actuator disk and coordinate transformation methods was validated in [Shamsoddin and Porté-Agel \(2017b\)](#). The chosen resolution of the grid is well within the range that has been previously shown to result in grid-independent results for the cases of application of the coordinate transformation (see [Wan et al. \(2007\)](#), Sect. 3) and flow through actuator disks (see [Wu and Porté-Agel \(2011\)](#), Sect. 4, and [Wu and Porté-Agel \(2013\)](#), Sect. 4.1), and the case of the combined application of the the coordinate transformation and the actuator disks ([Shamsoddin and Porté-Agel, 2017b](#)).

### 7.3.2 Qualitative LES results

Figure 7.4 shows the contours of the normalized streamwise component of the mean velocity for both wake and no-wake cases. The velocities are normalized by the velocity at hub-height far upwind of the hill  $U_h$  (i.e. over flat terrain). To isolate the turbine wake, we define the velocity deficit as follows:

$$\bar{u}_{\text{def}}(x, y, z) = \bar{u}_{nw}(x, y, z) - \bar{u}_w(x, y, z), \quad (7.26)$$

where the subscripts  $w$  and  $nw$  indicate wake and no-wake cases, respectively. In other words, to obtain the velocity deficit at a given point, we subtract the velocity of that point in the wake case from the velocity of the same point in the no-wake case. Traditionally, in turbine wake flows over flat terrain, the velocity deficit is defined based on the incoming velocity profile; however, in our case here, the incoming flow is perturbed both by the hill and the turbine, therefore the traditional definition of velocity deficit is not able to isolate the effect of the turbine (i.e., the turbine wake). It is noteworthy to mention that the definition in Equation (7.26) is reduced to the traditional definition of velocity deficit in the case of turbine wake flow over a flat terrain.

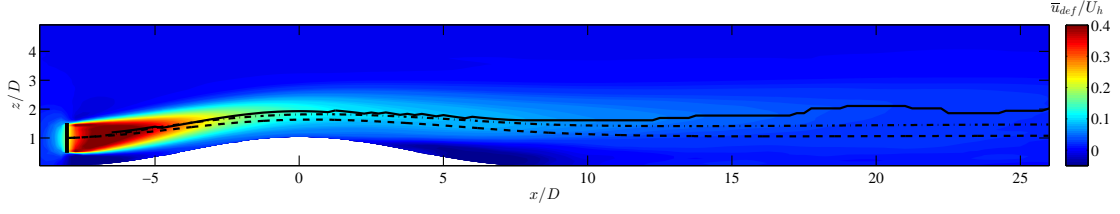


Figure 7.5 – Contours of the normalized mean streamwise velocity deficit ( $\bar{u}_{def}/U_h$ ) in the  $xz$ -plane going through the center of the turbine. Wake center trajectory (solid line) and streamlines going through the center of the rotor for the no-wake (dashed line) and wake (dash-dotted line) cases are also shown.

Figure 7.5 shows the normalized velocity deficit in the vertical midplane of the domain. The turbine wake and the wake center trajectory (black solid line) can be seen in this figure. The wake center trajectory is defined as:

$$z_c(x) = \operatorname{argmax}_z (\bar{u}_{def}(x, y_h, z)), \quad (7.27)$$

where  $z_c(x)$  is the  $z$ -coordinate of the wake center as a function of  $x$ , and  $y_h$  is the  $y$ -coordinate of the center of the turbine. Together with the wake center, the mean streamlines of the flow (going through the turbine hub position) in the wake (dash-dotted line) and no-wake (dashed line) cases are also depicted in the figure. The relative position of these three lines with respect to each other is worthy of attention. The wake streamline is located above the no-wake streamline; this is because the presence of the wake decelerates the flow causing the streamlines to expand (with respect to no-wake case) in the way that their distance to the ground increases. This figure also shows that the wake center trajectory is not coincident with the wake streamline; this is also observed in cross-flow jet flows (e.g. Gutmark et al., 2008).

In Figure 7.5, it can be seen that behind the hill a region of negative velocity deficit is formed (this can be observed more clearly in the velocity deficit profiles of Section 7.5). This region implies that the presence of the turbine mitigates the wind-sheltering effect of the hill. In other words, the turbine accelerates the flow in the leeward of the hill with respect to the no-wake case.

Figure 7.6 shows the velocity deficit in several stream-normal  $yz$  planes. The wake cross-section seems axisymmetric as no significant asymmetry is observed. Another interesting observation in Figure 7.6, is the behaviour of the *deficit streamline* vectors. These streamlines can be understood as the flow patterns for which the turbine is responsible, and are obtained based on the spanwise and vertical velocity deficits, i.e.  $\bar{v}_{def}$  and  $\bar{w}_{def}$ , respectively. These two quantities are defined similarly as  $\bar{u}_{def}$  in (7.26). We see a clear pair of counter-rotating vortices at each  $yz$  plane on the hill, whose sense of rotation is the same on the windward and leeward side. We now try to explain the formation of

these vortices. The key point here is that the turbine wake induces an upward vertical velocity in the flow over the hill (i.e.  $-\bar{w}_{\text{def}} > 0$ ); this is evident in Figure 7.6 and is consistent with the upward shift of the streamlines (in the wake case with respect to the no-wake case) in Figure 7.5. This positive induced vertical velocity ( $-\bar{w}_{\text{def}}$ ) vanishes far from the wake in the  $z$ -direction and is maximum somewhere in the wake region. Therefore, one can view this situation as an analogue to the cross-flow jet case, where we have a main jet (here  $\bar{u}_{\text{def}}$ ) and a cross-flow (here  $\bar{w}_{\text{def}}$ ), which is perpendicular to the jet and has a significant variation in the direction perpendicular to the jet (here  $z$ ). The formation of counter-rotating vortex pairs in cross-flow jets has been broadly observed and discussed (e.g. Kamotani and Greber, 1972; Fearn and Weston, 1974; Kelso et al., 1996; Cortelezzi and Karagozian, 2001) and the same flow structure was also observed and explained in the work of Bastankhah and Porté-Agel (2016), who studied wakes of turbines in yawed conditions. The main difference here is that in our case these counter-rotating vortex pairs are observed in the velocity deficit field, whereas in the cross flow jets and yawed-turbine case, these vortex pairs are noticeable in the wake flow field itself.

### 7.4 The wake in the leeward side of the hill

As it was discussed in section 7.2.3, in the leeward side of the hill, we have either a separated flow or a non-separated sheltering effect of the hill which causes strong asymmetries between leeward and windward regions of the flow. The non-separated sheltering effect is easily noticeable in Figure 7.4(top), where there is a clear asymmetry between the mean velocity distribution up- and downwind of the hilltop. This suggests that the linearized models can no longer well predict the flow downwind of the hilltop. The flow behaviour in this region is so complex that there is a scarcity of reliable simple analytical prediction models for this region in the literature even for the case of boundary-layer flows without any wake. Herein, it is attempted to analyse the wake behaviour on the leeward side, mainly based on our observations of our LES results.

The flow on the windward side up until the hilltop, which is more influenced by the windward profile of the hill, is relatively more predictable than on the leeward side. Here, we want to see how the wake trajectory in the leeward side is affected by the leeward hill profile. In other words, we would like to see how significantly the wake responds to different leeward hill profiles. For this purpose, for the same windward hill profile, we systematically change the leeward hill profile to see how the wake trajectory responds to this change. As can be seen in Figure 7.7, we have changed the half-length of the leeward side of the hill ( $L_2$  in Equation (7.23)) from  $1.36D$  to infinity. The extreme case of  $L_2 \rightarrow \infty$ , in fact, corresponds to an escarpment of the same height as the other hills. Some interesting conclusions can be made from this figure. First, we see that the leeward hill profile has almost no effect on the windward trajectory of the wake. Second and maybe more interestingly, it can be seen that, even though the leeward hill

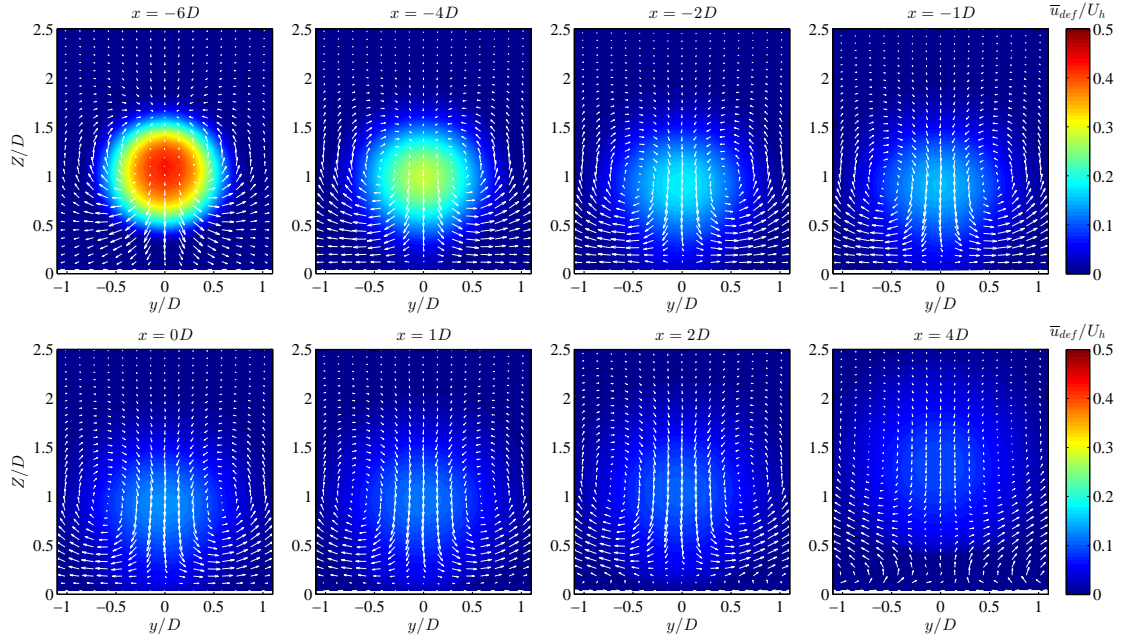


Figure 7.6 – Contours of the normalized mean streamwise velocity deficit ( $\bar{u}_{def}/U_h$ ) in several  $yz$  planes at different streamwise positions

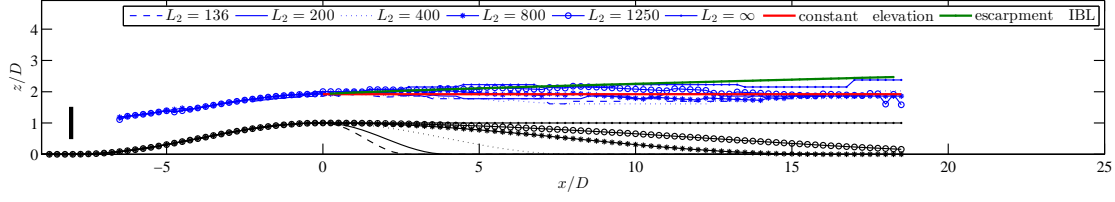


Figure 7.7 – Trajectory of the turbine wake over 6 hills of different leeward shapes. The blue lines show the wake center trajectory for hills of different leeward profile. Each black line shows a leeward hill profile corresponding to a blue line with the same line marker. The half-length of the leeward hill profile ( $L_2$ ) for each case (or line marker) is specified in the legend.

profile has gone through significant changes, the wake trajectory above it has not changed significantly. In other words, the leeward wake trajectory is found to be only a weak function of the leeward hill profile. Especially for the hills (not for the extreme case of the escarpment), we also see that the elevation of the wake trajectory does not change considerably downwind of the hilltop.

#### 7.4.1 Hills

Figure 7.7, besides different wake center trajectories, also shows a red line which is a straight horizontal line whose elevation is equal to the elevation of the wake center at the hilltop  $z_c^{ht}(=z_c(0))$ . It can be seen that this line is a good approximation for the wake center trajectory in the leeward side of the hill. This approximation proves to be useful because we can calculate the trajectory of the wake center until the hilltop using the methods of Section 7.2 and afterwards we can assume the trajectory to be a horizontal line as an approximation. Moreover, to reflect this trajectory modification in the velocity profiles on the leeward side, we can simply center the calculated velocity deficit (i.e. 7.20) around this trajectory.

#### 7.4.2 Escarpments

In the limiting case of the constant-elevation leeward hill profile ( $L_2 \rightarrow \infty$ ), it can be seen that the wake center ascends. This is because of the development of an internal boundary layer (IBL) on the plateau surface. Even though the flow upstream of the hill is a fully-developed boundary-layer flow, it is well-known that the velocity profile at the hilltop is close to be uniform (e.g. Britter et al., 1981; Ishihara et al., 1999; Tian et al., 2013; Hyvärinen and Segalini, 2017a). Therefore, after the hilltop and on the plateau the boundary layer again starts to develop on the new ground. Such an approach to flow over escarpments has already been adopted, for example in Emeis et al. (1995) (or section 4.3 of Emeis, 2013). The evolution of the IBL, which involves deceleration of the flow

near the ground, requires that the streamlines diverge upwards, and as a consequence the locus of the wake center moves upward. To predict this upward motion, we benefit from the findings in previous studies of IBLs (for a review see section 4.5.3 of Garratt, 1994). In order to model the growth of the IBL, it is common to use an analogy between the IBL growth and diffusion of a smoke plume (Miyake, 1965; Pasquill, 1972; Jackson, 1976; Garratt, 1990). Employing this analogy the following equation for the upward displacement of passive particles diffusing in space from the ground can be used. The original equation was first derived by Miyake (1965) and we use its modified version by Pasquill (1972):

$$\frac{\Delta Z_p}{z_o} \left[ \ln \left( \frac{\Delta Z_p}{z_o} \right) - 1 \right] + 1 = \frac{A(x - x_{ht})}{z_o}, \quad (7.28)$$

where  $\Delta Z_p$  is the upward displacement of the passive particles,  $x_{ht}$  is the  $x$ -position of the hilltop (or the surface roughness transition), and  $A \approx \kappa^2$  is a constant (Pasquill, 1972; Garratt, 1990). The above non-linear equation can be solved to obtain  $\Delta Z_p$  as a function of  $x$ . The height of the IBL,  $h_b$ , can then be obtained as  $h_b = 3\Delta Z_p$  (Garratt, 1994).

If we treat the wake flow at the hilltop as a passive scalar plume and assume that its vertical displacement is close to that of a ground-level source, then we can use (7.28) as a first approximation for the upward displacement of the wake center. For this purpose,  $\Delta Z_p$  is replaced by  $\Delta Z_c$  in (7.28), where  $\Delta Z_c$  is the upward displacement of the wake center with respect to  $z_c^{ht}$ . This approximation is justifiable especially for long hills, because the velocity deficit at the hilltop becomes relatively small. In Figure 7.7, the green line shows  $\Delta Z_c + z_c^{ht}$ , where  $\Delta Z_c$  is the solution of the Equation (7.28). It can be seen that this method results in a good approximation for the wake trajectory on the plateau part of an escarpment.

## 7.5 Validation of the analytical model

In this section, we intend to compare the results of the analytical model presented in Section 7.2 to those of LES for the symmetrical hill of Section 7.3.2. As mentioned in Section 7.2.2, the model needs the velocity at the hub-height level for the flow over the hill without the wind turbines (i.e.  $U_{nw}^h(x)$ ) as an input (i.e.  $U_b(x)$ ). There, we pointed out that to obtain  $U_{nw}^h(x)$ , one can use the model developed by Jackson and Hunt (1975), i.e. equation (7.13) for the no-wake case. This is carried out for this hill and  $U_{nw}^h(x)$  is shown in Figure 7.8(right). The ZPG wake width  $\delta_0(x)$  which is the wake width over the flat terrain in our case is another input which is obtained by LES and shown in Figure 7.8(left).

With these inputs available, we can use the model and assess its results. In Figure 7.9, the recovery of the wake center velocity for the flat terrain and hill cases can be seen. The effect of pressure gradient can be seen and the model shows good capability

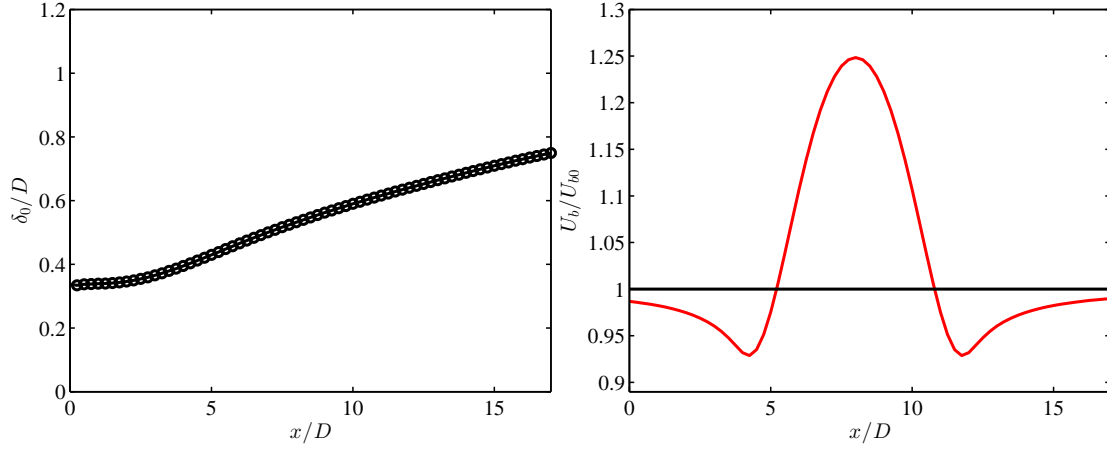


Figure 7.8 – The inputs of the model. Left: the wake width over flat terrain. Right:  $U_b(x)$  as obtained from equation (7.13) (i.e.  $U_b(x) = \bar{u}_{nw}^U$ ) for the hill (red line) and flat terrain (black line)

of capturing it. Moreover, Figures 7.10 and 7.11 show the velocity deficit and velocity profiles of the wake flow over the hill at different streamwise positions. It can be seen that the agreement between the analytical model and the LES results is good. We have also reproduced the streamwise velocity field in the vertical midplane of the domain in Figure 7.12. This contour plot should be compared with the one in Figure 7.5.

The wake center trajectory can also be elicited from the already-presented framework. Up until the hilltop, equation (7.22) is used, and for the leeward side, as explained in Section 7.4.1, a horizontal constant elevation line is considered as an approximation for the wake center trajectory. This is shown in Figure 7.13. The wake center trajectory for an escarpment (based on equation (7.28)) is also plotted in this figure. The agreement between the trajectories obtained from LES and the predicted trajectories is good.

## 7.6 A closer look into the effect of pressure gradient on the wake recovery over hills

In this section, we aim to illustrate the effect of pressure gradient on wake recovery over hills more clearly, as we believe this effect is an important factor that differentiates wake flows over topography from the ones over flat terrain. To do this, we place the turbine in different upwind locations with respect to the hill and compare its recovery with the flat terrain case. We change the position of the turbine from far upstream of the hill to the hilltop, as shown in Figure 7.14. Figure 7.15 shows the recovery of the wake center velocity for all the cases together with the flat terrain wake. In this figure,  $\bar{u}_{\text{def}}$  is normalized in two ways; in the left panel, a constant value of  $U_h$  is used, and in the right panel, the deficit at each point is normalized by the no-wake velocity of exactly the



## 7.6. A closer look into the effect of pressure gradient on the wake recovery over hills

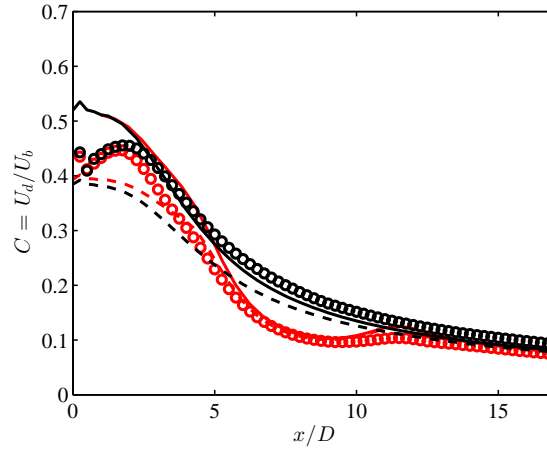


Figure 7.9 – Normalized maximum velocity deficit as a function of the streamwise distance over flat terrain (black) and over the hill (red). The circles indicate LES results, the solid lines are the solution obtained from equation (7.2), and the dashed lines are the asymptotic solution of equation (7.7).

same point. Both ways are useful. The first way is easy to interpret and use, as all of the curves are normalized with a constant value. The second way is insightful, because it takes into account the magnitude of the velocity at the position of the turbine in the no-wake case. For example, the mere fact that the velocity at the hilltop is larger than the one at the foot of the hill, leads to a higher magnitude of velocity deficit for a turbine (with the same thrust coefficient) placed at the hilltop. Thus, to remove this effect from our comparison we can normalize the deficit by the local velocity in the no-wake case.

As it can be seen, by moving the turbine position, the changes in the wake recovery are significant. The important observation is that, when the turbine keeps approaching the hilltop from far upstream, the recovery rate keeps increasing up until a certain point with a certain distance to the hilltop (region I in Figure 7.14). After this point, if we move the turbine further closer to the hilltop, the recovery rate keeps decreasing (region II). This is especially clear, when the turbine is placed at the hilltop, where the wake recovers significantly slower due to the adverse pressure gradient on the leeward of the hill (this is in agreement with what Politis et al., 2012, have observed). This trend is also illustrated schematically in Figure 7.14. The above-described trend in the wake recovery rate can have implications on the turbine placement in a wind farm, i.e., depending on the position with respect to the hill, the streamwise spacing between two turbines should/can be more (e.g. in region II) or less (e.g. in region I) than the spacing between the same turbines on the flat terrain.

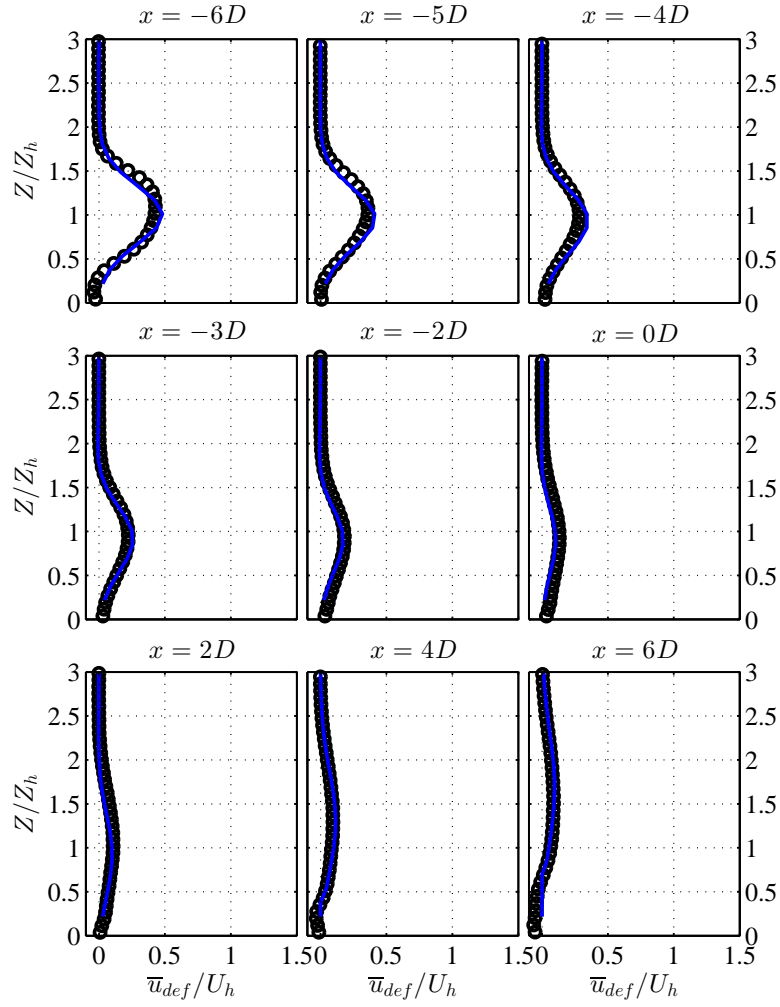


Figure 7.10 – Normalized velocity deficit profiles at different streamwise positions obtained from LES (black circles) and the analytical model (blue line)

## 7.6. A closer look into the effect of pressure gradient on the wake recovery over hills

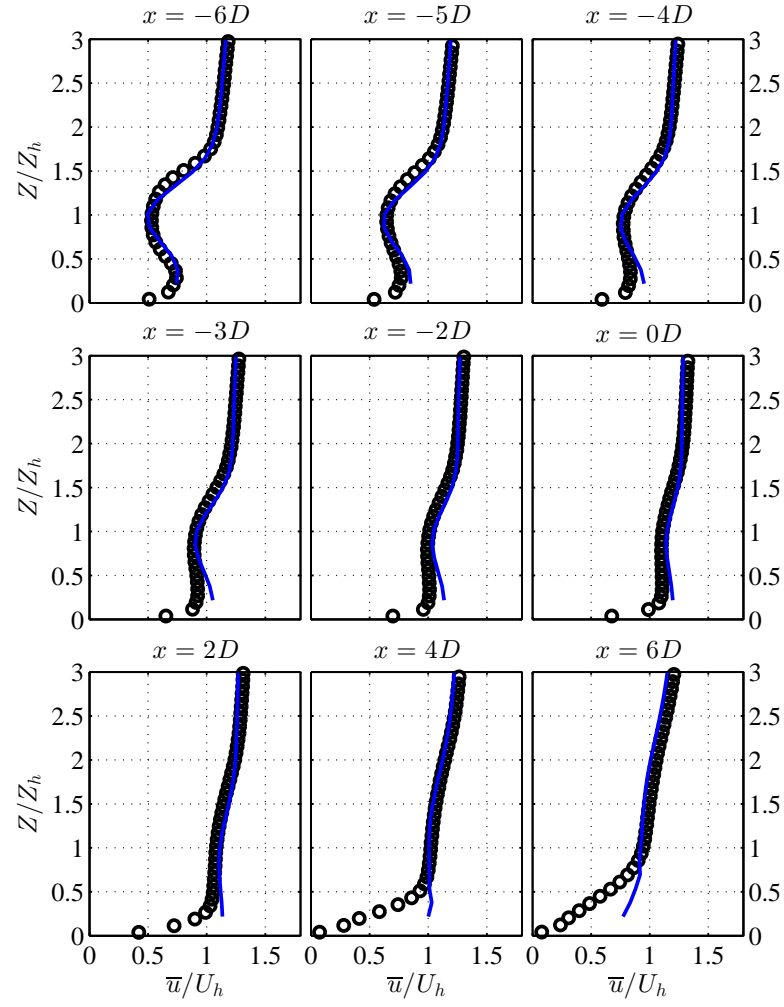


Figure 7.11 – Normalized mean streamwise velocity profiles at different streamwise positions obtained from LES (black circles) and the analytical model (blue line)

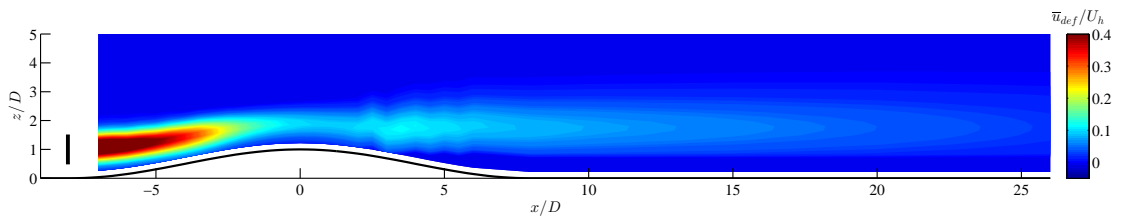


Figure 7.12 – Contours of velocity deficit in the  $xz$  plane predicted by the model

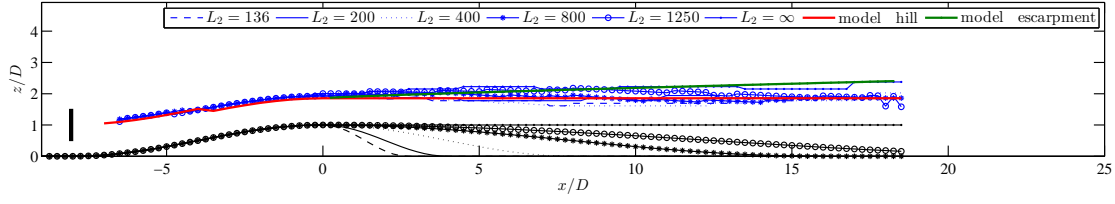


Figure 7.13 – Trajectory of the wake obtained from LES (blue lines) and the analytical model (red lines)

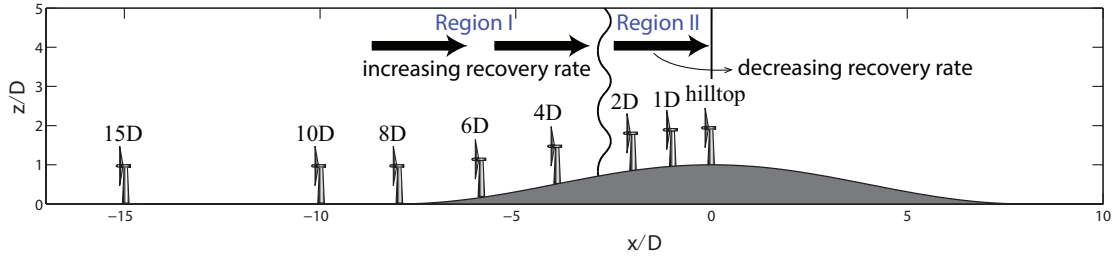


Figure 7.14 – Schematic of different turbine placements with respect to the hill. The distance of the turbine to the hilltop is shown on top of the turbine for each placement case.

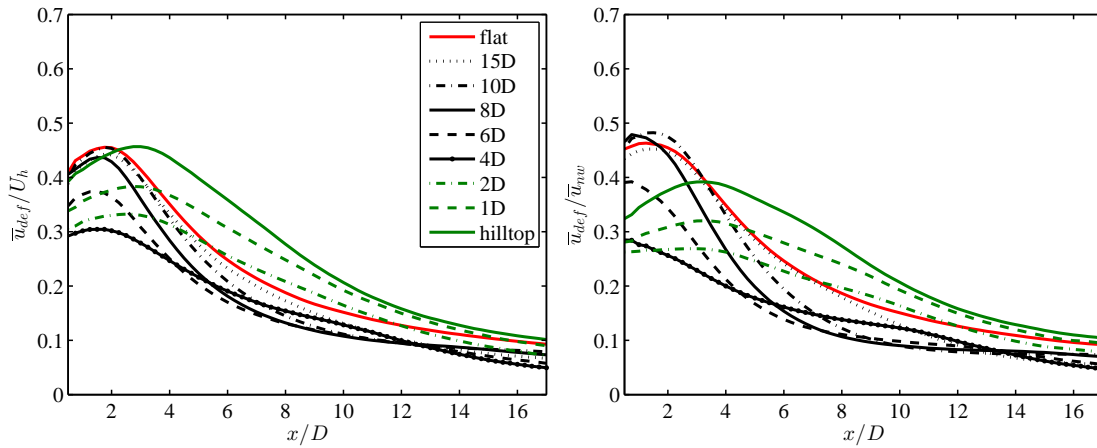


Figure 7.15 – Wake center velocity recovery for different turbine positions with respect to the hill. The legend is related to Figure 7.14.

## 7.7 Conclusion

We have developed an analytical framework to model the behaviour of wind turbine wakes over two-dimensional hills. The model comprises two steps: first, the response of the wake evolution to the pressure gradient caused by the hill is calculated; second, the response of the wake to the streamline distortion caused by the hill is modeled. The first step was achieved by using a recently developed model by [Shamsoddin and Porté-Agel \(2018\)](#), and the second step was accomplished by performing a linearized perturbation analysis. Furthermore, we benefit from LES to obtain more detailed knowledge about the wake flow over hills. In particular, we use LES data to compare the results of the analytical model with, and also to better understand the behaviour of the wake on the leeward side of the hill. We also performed numerical experiments to better clarify the effect of the hill-induced pressure gradient on the wake recovery, by changing the position of the turbine with respect to the hill.

It was shown that the wake recovers faster on the windward side of the hill than its leeward, due to the mainly favourable pressure gradient on the windward side and the adverse one on the leeward side. The trajectory of the wake was found to closely follow the terrain on the windward side of a hill with the same height as the turbine hub-height and moderate slope. However, on the leeward side, the trajectory showed little dependence on the hill profile and mainly maintained a constant elevation. The trajectory of the wake on the leeward side was also studied for a limiting case of an escarpment, and it was shown that an IBL forms on the plateau which leads to an upward displacement of the wake center. This displacement was also quantified by using available models in the literature.

There is much room for more investigations on this topic. First of all, systematic parametric studies of the turbine-hill systems are needed. In fact, several key geometrical features are involved in this problem (e.g. hill height to hub-height ratio, hill slope, position of the turbine with respect to the hill), whose effects should be systematically studied. The present analysis can be extended to three-dimensional hills. Such hills are likely to have special effects on the wake behaviour which differentiate them from 2D hills. Finally, there is a shortage of high-resolution wind-tunnel measurements of wakes over hills, which makes new experimental research on this subject highly valuable.



## 8 Conclusion

### Overall summary

Here, we summarize the research performed for the two main topics addressed in this thesis: (1) vertical-axis wind turbines, (2) wind turbines on topography.

### Vertical-axis wind turbines

In this part, first (in Chapter 2) we adapted and implemented two actuator-type VAWT parameterization models for use in numerical flow simulations. The purpose of the models is to facilitate flow simulations which have the goal of studying the wake of VAWTs and their performance in the ABL and eventually predicting sizable wind farms. One model was the actuator-swept surface model (ASSM), in which the time-averaged turbine-induced forces are distributed on a surface swept by the turbine blades. The other model was the actuator line model (ALM), in which the instantaneous blade forces are only spatially distributed on lines representing the blades. We applied both models in a numerical experiment (using LES) which was a reproduction of a water-channel experiment. The agreement between the simulation results and the measurements was promising. Having the turbine models validated, we moved to the next target (Chapter 3) and studied the wake structure and energetic performance of a megawatt-VAWT placed in the ABL. We characterized, in particular, the energetic performance of such a turbine by calculating the power coefficient of the turbine for more than 100 different combinations of tip-speed ratios and blade chord lengths (i.e. different solidities). The optimum combination of solidity (defined as  $Nc/R$ , where  $N$  is the number of blades,  $c$  is the chord length and  $R$  is the rotor radius) and tip-speed ratio was found to be 0.18

and 4.5, respectively. This combination resulted in a power coefficient of 0.47.

### Wind turbines on topography

To shed more light on the problem of turbine wakes on topography, we have first created the necessary building blocks (i.e. Chapters 4, 5 and 6) one by one and finally have taken advantage of these building blocks in our last study (i.e. Chapter 7). Nevertheless, it should be noted that each of those building blocks are also *independently* insightful and useful.

First (in Chapter 4), we made sure that we have a functional LES framework that can deal with both turbines and topography. In doing so, we implemented the combined actuator disk model (to parameterize the effect of turbines) and the coordinate transformation method (to resolve the topography) in our LES framework. Subsequently, we reproduced a wind-tunnel experiment in which five turbines were sited on a single hill. The agreement between the LES results and the measurements was good, and it paved the way for later utilizations of the framework.

In our quest for modeling and better understanding of wakes over hills, we realized that the hill-induced pressure gradient has a significant effect on the wake evolution. Therefore, we decided to systematically and closely analyze the effect of pressure gradient on turbulent wakes, and especially to analytically model it. To do so, we first considered a planar wake (in Chapter 5). We developed an analytical model to predict the evolution of a turbulent planar wake under an arbitrary pressure gradient condition. The model is based on the cross-stream integration of the streamwise momentum equation and used the self-similarity of the mean flow. We have also made an experimentally-supported assumption that the ratio of the maximum velocity deficit to the wake width is independent of the imposed pressure gradient. The model then was applied to an experimental case, and the agreement between the model results and measurements was remarkable. However, since turbine wakes are axisymmetric, the model should be extended to axisymmetric wakes. We carried out this task in our next step (Chapter 6). To test the developed model, we designed and developed an appropriate numerical experiment using our LES framework. The analytical model was successfully validated with the LES dataset. One important value of this analysis was that it isolated the effect of the pressure gradient, as it considered a wake whose centreline is straight (with no streamline curvature). In other words, we have decoupled the effect of pressure gradient from that of streamline curvature. For both planar and axisymmetric wakes, it was observed that in favourable pressure gradients the wake recovers faster and widens slower with respect to the zero pressure gradient case. The reverse is true for wakes in adverse pressure gradients.

In the final chapter of this part (Chapter 7), we aimed to analyze what happens to a turbine wake when it meets a 2D hill. In particular, we were interested in identifying the



---

most important features of such an interaction (i.e. wake-hill interaction) and also in being able to predict the wake evolution over a hill. We have developed an analytical framework to model the behaviour of wind turbine wakes over two-dimensional hills. The model comprises two steps: first, we calculate the response of the wake evolution to the pressure gradient caused by the hill; second, we model the response of the wake to the streamline distortion caused by the hill. The first step was achieved by using the model developed in Chapter 6, and the second step was accomplished by performing a linearized perturbation analysis. Furthermore, we benefited from LES to obtain more detailed knowledge about the wake flow over hills. In particular, we used LES data to compare the results of the analytical model with, and also to better understand the behaviour of the wake in the leeward side of the hill. We also performed some numerical experiments to better clarify the effect of the hill-induced pressure gradient on the wake recovery, by changing the position of the turbine with respect to the hill. It was shown that the wake recovers faster on the windward side of the hill than its leeward, due to the mainly favourable pressure gradient on the windward side and the adverse one on the leeward side. The trajectory of the wake was found to closely follow the terrain on the windward side of a hill with the same height as the turbine hub-height and moderate slope. However, on the leeward side, the trajectory showed little dependence on the hill profile and mainly maintained a constant elevation. The trajectory of the wake on the leeward side was also studied for a limiting case of an escarpment, and it was shown that an IBL forms on the plateau, which leads to an upward displacement of the wake center. This displacement was also quantified by using models available in the literature.

## Future research perspectives

Both parts of this thesis (i.e. VAWTs and wind turbines on topography) definitely have still much room for future research. The key point in this regard is the selection of the topic for this future research, in a way that it guides us to solve challenging, meaningful and substantial problems. Examples of what could/should be done within the subject of both parts of this thesis are the following.

### Vertical-axis wind turbines

For VAWTs, the research should focus on the intrinsic features of VAWT wakes which clearly *differentiate* them from HAWTs.

- One intrinsic feature of VAWT wakes is the geometry of the wake generating object. For the simplest case of a straight-bladed VAWT, the shape of the frontal area of the rotor is a rectangle, which, in theory, can have any aspect ratio. This is in contrast to the frontal area of HAWTs, which is always a circle whose aspect ratio cannot be changed by definition (circles are self-similar). This feature of

VAWTs immediately brings up the question of how the aspect ratio (or in general the shape) of a VAWT-rotor affects the wake recovery. Or the question of whether an optimum aspect ratio exists or not.

- Another intrinsic feature of VAWTs is their sense of rotation with respect to each other when they are placed in an array. For example, two side-by-side VAWTs can be arranged in three different configurations with respect to the incoming wind based on their sense of rotation. There have been claims in the literature that counter-rotating VAWTs can dramatically enhance the power output of a VAWT-pair, but the validity of these claims has never been examined.
- Another feature which is again related to the sense of rotation of the blades is the wake rotation and tip vortices. It is known that HAWTs generate tip and root vortices and also that there is a wake rotation phenomenon. The sense of rotation of the VAWT blades make these phenomena completely different in VAWTs compared with HAWTs. How can these dynamic differences change the wake behaviour? For example, how can these differences change (if at all) the wake recovery or wake meandering of a VAWT?
- Considering the above points, a systematic study of VAWT *farms* is the logical next step. Do VAWT farms have some special characteristics which have not been seen in HAWT farms?

### Wind turbines on topography

- Systematic parametric studies of the turbine-hill systems are needed. In fact, several key geometrical features are involved in this problem (e.g. hill height to hub-height ratio, hill slope, position of the turbine with respect to the hill), whose effects should be systematically studied.
- In this thesis, we have considered only 2D hills. The combination of a turbine and a three-dimensional hill has yet to be analyzed systematically. Such hills are likely to have special effects on the wake behaviour which differentiate them from 2D hills. For example, the effects that may arise due to the spanwise placement of the turbine with respect to the hill.
- Apart from single and isolated hills, multi-scale terrain and its effect on performance of wind turbines and wind farms should be studied. For this purpose, the data of real wind farms on complex terrain proves to be very useful.
- There is a shortage of high-resolution wind-tunnel and field measurements of wakes over hills, which makes new experimental research on this subject even more valuable.

# Bibliography

- Abkar, M. and Porté-Agel, F. A new boundary condition for large-eddy simulation of boundary-layer flow over surface roughness transitions. *J Turbul*, 13(23):1–18, 2012.
- Albertson, J. D. and Parlange, M. B. Surfaces length scales and shear stress: implications for land-atmosphere interactions over complex terrain. *Water Resour Res*, 35:2121–2132, 1999.
- Ansorge, T., Fallen, M., Günther, P., Ruh, C., and Wolfanger, T. Numerical simulation of wake-effects in complex terrain and application of a reynolds-stress turbulence model. In Tsipouridis, J., editor, *Proc. EWECC*, volume 94, pages 448–453, Thessaloniki, Greece, 1994.
- Araya, D. B. and Dabiri, J. O. A comparison of wake measurements in motor-driven and flow-driven turbine experiments. *Experiments in Fluids*, 56(7):1–15, 2015. ISSN 1432-1114. doi: 10.1007/s00348-015-2022-7. URL <http://dx.doi.org/10.1007/s00348-015-2022-7>.
- Arya, S. P. S. and Shipman, M. S. An experimental investigation of flow and diffusion in the disturbed boundary-layer flow over a ridge - I. mean flow and turbulence structure. *Atmos Environ*, 15:1173–1184, 1981.
- Bachant, P. and Wosnik, M. Characterising the near-wake of a cross-flow turbine. *Journal of Turbulence*, 16(4):392–410, 2015. doi: 10.1080/14685248.2014.1001852.
- Bagchi, P. and Balachandar, S. Steady planar straining flow past a rigid sphere at moderate reynolds number. *Journal of Fluid Mechanics*, 466:365–407, 2002. doi: 10.1017/S0022112002001490.
- Baskaran, V., Smits, A. J., and Joubert, P. N. A turbulent flow over a curved hill. part 2. effects of streamline curvature and streamwise pressure gradient. *Journal of Fluid Mechanics*, 232:377–402, 1991. doi: 10.1017/S0022112091003737.
- Bastankhah, M. and Porté-Agel, F. A new analytical model for wind-turbine wakes. *Renewable Energy*, 70:116 – 123, 2014. ISSN 0960-1481. doi: <https://doi.org/10.1016/j.renene.2014.01.002>. URL <http://www.sciencedirect.com/science/article/pii/S0960148114000022>.

## Bibliography

---

- [S0960148114000317](#). Special issue on aerodynamics of offshore wind energy systems and wakes.
- Bastankhah, M. and Porté-Agel, F. Experimental and theoretical study of wind turbine wakes in yawed conditions. *Journal of Fluid Mechanics*, 806:506–541, 2016. doi: 10.1017/jfm.2016.595.
- Battisti, L., Zanne, L., Dell’Anna, S., Dossena, V., Persico, G., and Paradiso, B. Aerodynamic measurements on a vertical axis wind turbine in a large scale wind tunnel. *Journal of Energy Resources Technology*, 133(3):031201–031201–9, 2011.
- Bechmann, A., Sørensen, N. N., Berg, J., Mann, J., and Réthoré, P.-E. The bolund experiment, part II: blind comparison of microscale flow models. *Boundary-Layer Meteorol*, 141(2):245–271, 2011. ISSN 0006-8314. doi: 10.1007/s10546-011-9637-x.
- Belcher, S. Wave growth by non-separated sheltering. *European Journal of Mechanics - B/Fluids*, 18(3):447 – 462, 1999. ISSN 0997-7546. doi: [https://doi.org/10.1016/S0997-7546\(99\)80041-7](https://doi.org/10.1016/S0997-7546(99)80041-7). URL <http://www.sciencedirect.com/science/article/pii/S0997754699800417>. Three-Dimensional Aspects of Air-Sea Interaction.
- Belcher, S. E. and Hunt, J. C. R. Turbulent flow over hills and waves. *Annual Review of Fluid Mechanics*, 30(1):507–538, 1998. doi: 10.1146/annurev.fluid.30.1.507. URL <https://doi.org/10.1146/annurev.fluid.30.1.507>.
- Belcher, S. E., Newley, T. M. J., and Hunt, J. C. R. The drag on an undulating surface induced by the flow of a turbulent boundary layer. *Journal of Fluid Mechanics*, 249: 557–596, 1993. doi: 10.1017/S0022112093001296.
- Berg, J., Mann, J., A., B., Courtney, M., and Jørgensen, H. The bolund experiment, part I: flow over a steep, three-dimensional hill. *Boundary-Layer Meteorol*, 141:219–243, 2011.
- Berg, J., Troldborg, N., Sørensen, N., Patton, E. G., and Sullivan, P. P. Large-eddy simulation of turbine wake in complex terrain. *Journal of Physics: Conference Series*, 854(1):012003, 2017. URL <http://stacks.iop.org/1742-6596/854/i=1/a=012003>.
- Bergeles, G., Michos, A., and Athanassiadis, N. Velocity vector and turbulence in the symmetry plane of a darrieus wind generator. *J Wind Eng Ind Aerodyn*, 37:87–101, 1991.
- Blackwell, B. F., Sheldahl, R. E., and Feltz, L. V. Wind tunnel performance data for the darrieus wind turbine with naca 0012 blades. Technical report, Sandia National Laboratories, 1976.
- Bowen, A. J. and Mortensen, N. G. Wasp prediction errors due to site orography. Technical Report Risø-R-995(EN), Risø National Laboratory, Roskilde, Denmark, 2004.

- Bradley, E. An experimental study of the profiles of wind speed, shearing stress and turbulence at the crest of a large hill. *Q J R Meteorol Soc*, 106:101–123, 1980.
- Bradley, E. F. The influence of thermal stability and angle of incidence on the acceleration of wind up a slope. *J Wind Eng Ind Aerodyn*, 15:231–242, 1983.
- Britter, R. E., Hunt, J. C. R., and Richards, K. J. Air flow over a two-dimensional hill: studies of velocity speed-up, roughness effects and turbulence. *Q J R Meteorol Soc*, 107:91–110, 1981.
- Brochier, G., Fraunie, P., Beguier, C., and Paraschivoiu, I. Water channel experiments of dynamic stall on darrieus wind turbine blades. *AIAA Journal of Propulsion and Power*, 2:445–49, 1986.
- Castellani, F., Astolfi, D., Burlando, M., and Terzi, L. Numerical modelling for wind farm operational assessment in complex terrain. *Journal of Wind Engineering and Industrial Aerodynamics*, 147(Supplement C):320 – 329, 2015. ISSN 0167-6105. doi: <https://doi.org/10.1016/j.jweia.2015.07.016>. URL <http://www.sciencedirect.com/science/article/pii/S0167610515001981>.
- Castellani, F., Astolfi, D., Mana, M., Piccioni, E., Becchetti, M., and Terzi, L. Investigation of terrain and wake effects on the performance of wind farms in complex terrain using numerical and experimental data. *Wind Energy*, 20(7):1277–1289, 2017. ISSN 1099-1824. doi: 10.1002/we.2094. URL <http://dx.doi.org/10.1002/we.2094>. we.2094.
- Castelli, M. R., Englaro, A., and Benini, E. The darrieus wind turbine: Proposal for a new performance prediction model based on CFD. *Energy*, 36(8):4919–4934, 2011. ISSN 0360-5442. PRES 2010.
- Chaviaropoulos, P. and Douvikas, D. Mean wind field prediction over complex terrain in the presence of wind turbine (s). In Petersen, E. L., Jensen, P., Rave, K., Helm, P., and Ehmann, H., editors, *EWEC-CONFERENCE-*, pages 1208–1211, Nice, France, 1999.
- Chen, T. and Liou, L. Blockage corrections in wind tunnel tests of small horizontal-axis wind turbines. *Experimental Thermal and Fluid Science*, 35(3):565–569, 2011. ISSN 0894-1777. doi: <http://dx.doi.org/10.1016/j.expthermflusci.2010.12.005>. URL <http://www.sciencedirect.com/science/article/pii/S0894177710002438>.
- Cheng, W.-C. and Porté-Agel, F. Evaluation of subgrid-scale models in large-eddy simulation of flow past a two-dimensional block. *International Journal of Heat and Fluid Flow*, 44:301–311, December 2013.
- Clark, T. L. A small-scale dynamic model using a terrain-following transformation. *J Comput Phys*, 24:186–215, 1977.

## Bibliography

---

- Corby, G. A. The airflow over mountains – a review of the state of current knowledge. *Q J R Meteorol Soc*, 80:491–521, 1954.
- Cortelezzi, L. and Karagozian, A. R. On the formation of the counter-rotating vortex pair in transverse jets. *Journal of Fluid Mechanics*, 446:347–373, 2001.
- Crespo, A. and Hernandez, J. A numerical model of wind turbine wakes and wind farms. In Palz, W. and Sesto, E., editors, *European Wind Energy Conference EWEK*, volume 2, pages 111–115, Rome, Italy, 1986.
- Crespo, A., Manuel, F., Grau, J., and Hernandez, J. Modelization of wind farms in complex terrain. application to the Monteahumada wind farm. In Garrad, A., Palz, W., and Scheller, S., editors, *Proceedings of the 1993 European Community Wind Energy Conference*, pages 436–439, Travemünde, Germany, 1993.
- Dabiri, J. O. Potential order-of-magnitude enhancement of wind farm power density via counter-rotating vertical-axis wind turbine arrays. *Journal of Renewable and Sustainable Energy*, 3:043104, 2011.
- Deaves, D. M. Wind over hills: a numerical approach. *Q J R Meteorol Soc*, 1:371–391, 1976.
- Deaves, D. M. Computations of wind flow over two-dimensional hills and embankments. *J Wind Eng Ind Aerodyn*, 6:89–111, 1980.
- Diebold, M., Higgins, C., Fang, J., Bechmann, A., and Parlange, M. B. Flow over hills: A large-eddy simulation of the bolund case. *Boundary-Layer Meteorol*, 148(1):177–194, 2013. ISSN 0006-8314. doi: 10.1007/s10546-013-9807-0.
- Dörnbrack, A. and Schumann, U. Numerical simulation of turbulent convective flow over wavy terrain. *Boundary-Layer Meteorol*, 65:323–355, 1993.
- Emeis, S. *Wind energy meteorology: atmospheric physics for wind power generation*. Springer-Verlag Berlin Heidelberg, 2013. ISBN 978-3-642-30522-1. doi: <https://doi.org/10.1007/978-3-642-30523-8>.
- Emeis, S., Frank, H. P., and Fiedler, F. Modification of air flow over an escarpment — results from the hjarde mál experiment. *Boundary-Layer Meteorology*, 74(1):131–161, Apr 1995. ISSN 1573-1472. doi: 10.1007/BF00715714. URL <https://doi.org/10.1007/BF00715714>.
- EWEA. Wind energy scenarios for 2030, 2015. URL <https://www.ewea.org/fileadmin/files/library/publications/reports/EWEA-Wind-energy-scenarios-2030.pdf>.
- Fearn, R. and Weston, R. Vorticity associated with a jet in a cross flow. *AIAA Journal*, 12(12):1666–1671, Dec. 1974. ISSN 0001-1452. doi: 10.2514/3.49576. URL <https://doi.org/10.2514/3.49576>.

- Ferziger, J. H. and Perć, M. *computational methods for fluid dynamics*. Springer-Verlag, New York, 1996.
- Finnigan, J. J., Raupach, M. R., Bradley, E. F., and Aldiss, G. K. A wind tunnel study of turbulent flow over a two-dimensional ridge. *Boundary-Layer Meteorol*, 50:277–317, 1990.
- Fischer, G., Van Velthuisen, H., Shah, M., and Nachtergaele, F. O. Global agro-ecological assessment for agriculture in the 21st century: methodology and results, 2002. URL <http://pure.iiasa.ac.at/6667/>.
- Fortunato, B., Dadone, A., and Trifoni, V. A two-dimensional methodology to predict vertical axis wind turbine performance. *Journal of Solar Energy Engineering*, 117(3): 187–193, 1995.
- Fujisawa, N. and Shibuya, S. Observations of dynamic stall on darrieus wind turbine blades. *J Wind Eng Ind Aerodyn*, 89(2):201–214, 2001.
- Garratt, J. *The atmospheric boundary layer*. Cambridge University Press, 1994. ISBN 9780521467452.
- Garratt, J. R. The internal boundary layer — a review. *Boundary-Layer Meteorology*, 50(1):171–203, Mar 1990. ISSN 1573-1472. doi: 10.1007/BF00120524. URL <https://doi.org/10.1007/BF00120524>.
- Gong, W., Taylor, P., and Dörnbrack, A. Turbulent boundary-layer flow over fixed aerodynamically rough two-dimensional sinusoidal waves. *J Fluid Mech*, 312:1–37, 1996.
- Günther, P., Fallen, M., and Wolfanger, T. Numerical wake simulation of a hawt considering topography and using a mesoscale turbulence model. In Garrad, A. D., Palz, W., and Scheller, S., editors, *Proc. 1993 European Community Wind Energy Conf*, pages 448–450, Travemünde, Germany, 1993.
- Gutmark, E. J., Ibrahim, I. M., and Murugappan, S. Circular and noncircular subsonic jets in cross flow. *Physics of Fluids*, 20(7):075110, 2008. doi: 10.1063/1.2946444. URL <https://doi.org/10.1063/1.2946444>.
- GWEC. Global wind report, annual marker update, 2016. URL <http://gwec.net/global-figures/graphs/>.
- Ham, N. D. Aerodynamic loading on a two-dimensional airfoil during dynamic stall. *AIAA Journal*, 6(10):1927–1934, 1968.
- Hansen, K. S., Barthelmie, R. J., Jensen, L. E., and Sommer, A. The impact of turbulence intensity and atmospheric stability on power deficits due to wind turbine wakes at Horns Rev wind farm. *Wind Energy*, 15(1):183–196, 2012. ISSN 1099-1824.

## Bibliography

---

- Hara, Y., Suzuki, T., Ochiai, Y., and Hayashi, T. Velocity field measurements in wake of a straight-bladed vertical axis wind turbine. In *ASME-JSME-KSME 2011 Joint Fluids Engineering Conference*, volume 1, pages 1839–1849, Hamamatsu, Japan, July 2011.
- Helmis, C., Papadopoulos, K., Asimakopoulos, D., Papageorgas, P., and Soilemes, A. An experimental study of the near wake structure of a wind turbine operating over complex terrain. *Solar Energy*, 54(6):413–428, 1995.
- Hemon, A., Huberson, S., and Zervos, A. Numerical study of wind turbine operation in complex terrain. In Quarton, D. C. and Fenton, V. C., editors, *Proceedings of the 13th British Wind Energy Association (BWEA) Conference, Wind Energy Conversion*, pages 343–349, Swansea, UK, 10-12 April 1991.
- Hibbs, B. D. HAWT performance with dynamic stall. Technical Report SERI/STR 217-2732, AeroVironment, Inc., Monrovia, California, February 1986.
- Hofemann, C., Simao Ferreira, C. J., Van Bussel, G. J. W., Van Kuik, G. A. M., Scarano, F., and Dixon, K. R. 3D stereo PIV study of tip vortex evolution on a VAWT. In *Proceedings of EWEC*, 2008.
- Holinka, S. Offshore use of vertical-axis wind turbines gets closer look, 2012. URL <http://www.renewableenergyworld.com/articles/2012/08/offshore-use-of-vertical-axis-wind-turbines-gets-closer-look.html>.
- Hunt, J. C. R. and Eames, I. The disappearance of laminar and turbulent wakes in complex flows. *Journal of Fluid Mechanics*, 457:111–132, 2002. doi: 10.1017/S0022112001007236.
- Hunt, J. C. R., Leibovich, S., and Richards, K. J. Turbulent shear flow over low hills. *Q J R Meteorol Soc*, 114:1435–1470, 1988.
- Hyvärinen, A. and Segalini, A. Effects from complex terrain on wind-turbine performance. *Journal of Energy Resources Technology*, 139(5):051205–051205–10, Mar. 2017a. ISSN 0195-0738. doi: 10.1115/1.4036048. URL <http://dx.doi.org/10.1115/1.4036048>.
- Hyvärinen, A. and Segalini, A. Qualitative analysis of wind-turbine wakes over hilly terrain. *Journal of Physics: Conference Series*, 854(1):012023, 2017b. URL <http://stacks.iop.org/1742-6596/854/i=1/a=012023>.
- Iizuka, S. and Kondo, H. Performance of various sub-grid scale models in large-eddy simulation of turbulent flow over complex terrain. *Atmos Environ*, 38:7083–7091, 2004.
- Ishihara, T., Hibi, K., and Oikawa, S. A wind tunnel study of turbulent flow over a three-dimensional steep hill. *J Wind Eng Ind Aerodyn*, 83:95–107, 1999.
- Ivanell, S., Sørensen, J., Mikkelsen, R., and Henningson, D. Analysis of numerically generated wake structures. *Wind Energy*, 12(1):63–80, January 2009.



- Ivanova, L. A. and Nadyozhina, E. D. Numerical simulation of wind farm influence on wind flow. *Wind Engineering*, 24(4):257–269, 2000. doi: 10.1260/0309524001495620. URL <https://doi.org/10.1260/0309524001495620>.
- Jackson, N. A. The propagation of modified flow downstream of a change in roughness. *Quarterly Journal of the Royal Meteorological Society*, 102(434):924–933, 1976. ISSN 1477-870X. doi: 10.1002/qj.49710243420. URL <http://dx.doi.org/10.1002/qj.49710243420>.
- Jackson, P. S. and Hunt, J. C. R. Turbulent wind flow over a low hill. *Q J R Meteorol Soc*, 101:929–955, 1975.
- Jenkins, G. J., Mason, P. J., Moores, W. H., and Sykes, R. I. Measurements of the flow structure around ailsa craig, a steep, three-dimensional, isolated hill. *Q J R Meteorol Soc*, 107:833–851, 1981.
- Jensen, N. O. A note on wind generator interaction. Technical Report Risø-M-2411, Risø National Laboratory, Roskilde, 1983.
- Johnston, S. J. Proceedings of the vertical-axis wind turbine (vawt) design technology seminar for industry, april 1-3, 1980. Technical report, Sandia National Laboratories, 1980.
- Kamotani, Y. and Greber, I. Experiments on a turbulent jet in a cross flow. *AIAA Journal*, 10(11):1425–1429, Nov. 1972. ISSN 0001-1452. doi: 10.2514/3.50386. URL <https://doi.org/10.2514/3.50386>.
- Kelso, R. M., Lim, T. T., and Perry, A. E. An experimental study of round jets in cross-flow. *Journal of Fluid Mechanics*, 306:111–144, 1996. doi: 10.1017/S0022112096001255.
- Kim, W.-W. and Menon, S. A new dynamic one-equation subgrid-scale model for large eddy simulations. *AIAA Paper No. 95-0356*, January 1995.
- Krettenauer, K. and Schumann, U. Numerical simulation of turbulent convection over wavy terrain. *J Fluid Mech*, 237:261–299, 1992.
- Kumar, V., Paraschivoiu, M., and Paraschivoiu, I. Low reynolds number vertical axis wind turbine for mars. *Wind Engineering*, 34(4):461–476, 2010.
- Lindenberg, S., Smith, B., O’Dell, K., et al. 20% wind energy by 2030, 2008.
- Liu, X., Thomas, F. O., and Nelson, R. C. An experimental investigation of the planar turbulent wake in constant pressure gradient. *Physics of Fluids*, 14(8):2817–2838, 2002. doi: 10.1063/1.1490349. URL <http://dx.doi.org/10.1063/1.1490349>.
- Lu, H. and Porté-Agel, F. A modulated gradient model for large-eddy simulation: application to a neutral atmospheric boundary layer. *Physics of Fluids*, 22:015109, 2010. doi: 10.1063/1.3291073.

## Bibliography

---

- Lu, H. and Porté-Agel, F. Large-eddy simulation of a very large wind farm in a stable atmospheric boundary layer. *Physics of Fluids*, 23:065101, 2011.
- Lu, H. and Porté-Agel, F. A modulated gradient model for scalar transport in large-eddy simulation of the atmospheric boundary layer. *Physics of Fluids*, 25(1):015110, 2013.
- Lu, H. and Porté-Agel, F. On the development of a dynamic nonlinear closure for large-eddy simulation of the atmospheric boundary layer. *Boundary-Layer Meteorology* (in press), 2014.
- Magnaudet, J., Rivero, M., and Fabre, J. Accelerated flows past a rigid sphere or a spherical bubble. part 1. steady straining flow. *Journal of Fluid Mechanics*, 284:97–135, 1995. doi: 10.1017/S0022112095000280.
- Mason, P. J. Flow over the summit of an isolated hill. *Boundary-Layer Meteorol*, 37:385–405, 1986.
- Mason, P. J. Large-eddy simulation: a critical review of the technique. *Q J R Meteorol Soc*, 120:1–26, 1994.
- Mason, P. J. and King, J. C. Measurements and predictions of flow and turbulence over an isolated hill of moderate slope. *Q J R Meteorol Soc*, 111:617–640, 1985.
- Mason, P. J. and Sykes, R. I. Flow over an isolated hill of moderate slope. *Q J R Meteorol Soc*, 105:383–395, 1979.
- Mason, P. J. and Thomson, D. J. Stochastic backscatter in large-eddy simulations of boundary layers. *J Fluid Mech*, 242:51–78, 1992.
- McNerney, G. M. Accelerometer measurements of aerodynamic torque on doe/sandia 17-m vertical-axis wind turbine. Technical report, Sandia National Laboratories, 1981.
- Migoya, E., Crespo, A., García, J., Moreno, F., Manuel, F., Ángel Jiménez, and Costa, A. Comparative study of the behavior of wind-turbines in a wind farm. *Energy*, 32(10):1871 – 1885, 2007. ISSN 0360-5442. doi: <https://doi.org/10.1016/j.energy.2007.03.012>. URL <http://www.sciencedirect.com/science/article/pii/S0360544207000588>.
- Miyake, M. Transformation of the atmospheric boundary layer over inhomogeneous surfaces. Technical Report Sci. Rep. 5R-6, Univ. of Washington, 1965.
- Moeng, C. A large-eddy simulation model for the study of planetary boundary-layer turbulence. *J Atmos Sci*, 46:2311–2330, 1984.
- Monin, A. and Obukhov, M. Basic laws of turbulent mixing in the ground layer of the atmosphere. *Tr. Akad. Nauk SSSR Geophys. Inst.*, 24:163–187, 1954.
- Muraca, R. J. and Guillotte, R. J. Wind tunnel investigation of a 14 ft vertical-axis windmill. Technical report, NASA TMX-72663, (National Aeronautics and Space Administration, Langley), 1976.

- Nakayama, A. Curvature and pressure-gradient effects on a small-defect wake. *Journal of Fluid Mechanics*, 175:215–246, 1987. doi: 10.1017/S0022112087000375.
- Nguyen, V. D., Vittecoq, P., Bourassa, P., and Mercadier, Y. Étude en soufflerie d’un rotor de type Darrieus. Technical Report Rept. MEC-81-2, Mechanical Engineering Department, University of Sherbrooke, August 1981.
- Noll, R. B. and Ham, N. D. Dynamic stall of small wind systems. Technical report, Aerospace Systems Inc., Burlington, MA, February 1983.
- Orszag, S. and Pao, Y.-H. Numerical computation of turbulent shear flows. *Advances in Geophysics*, 18A:225–236, 1975.
- Paraschivoiu, I. *Wind Turbine Design—With Emphasis on Darrieus Concept*. Polytechnic International Press, Montreal, 2002.
- Pasquill, F. Some aspects of boundary layer description. *Quarterly Journal of the Royal Meteorological Society*, 98(417):469–494, 1972. ISSN 1477-870X. doi: 10.1002/qj.49709841702. URL <http://dx.doi.org/10.1002/qj.49709841702>.
- Pearse, J. R., Lindley, D., and Stevenson, D. C. Wind flow over ridges in simulated atmospheric boundary layers. *Boundary-Layer Meteorol*, 21:77–92, 1981.
- Penna, P. J. and Kuzina, J. C. Magdalen islands vawt summary and index of experimental data; 1980-1982. Technical report, National Research Council of Canada, Ottawa, Ontario, October 1984.
- Peskin, C. S. Flow patterns around heart valves—numerical method. *J Comput Phys*, 10(2):252–271, 1972.
- Pierce, B., Moin, P., and Dabiri, J. O. Evaluation of point-forcing models with application to vertical axis wind turbine farms. Annual research briefs, Center for Turbulence Research, Stanford University, Stanford, CA, 2013.
- Politis, E. S., Prospathopoulos, J., Cabezon, D., Hansen, K. S., Chaviaropoulos, P. K., and Barthelmie, R. J. Modeling wake effects in large wind farms in complex terrain: the problem, the methods and the issues. *Wind Energy*, 15:161–182, 2012.
- Pope, S. B. *Turbulent Flows*. Cambridge University Press, 2000.
- Porté-Agel, F., Meneveau, C., and Parlange, M. B. A scale-dependent dynamic model for large-eddy simulation: application to a neutral atmospheric boundary layer. *J Fluid Mech*, 415:261–284, 2000.
- Porté-Agel, F., Wu, Y. T., Lu, H., and Conzemius, R. J. Large-eddy simulation of atmospheric boundary layer flow through wind turbines and wind farms. *J Wind Eng Ind Aerodyn*, 99(4):154–168, 2011.

## Bibliography

---

- Porté-Agel, F., Wu, Y.-T., and Chen, C.-H. A numerical study of the effects of wind direction on turbine wakes and power losses in a large wind farm. *Energies*, 6(10): 5297–5313, 2013. ISSN 1996-1073. doi: 10.3390/en6105297. URL <http://www.mdpi.com/1996-1073/6/10/5297>.
- Raithby, G. D., Stubley, G. D., and Taylor, P. A. The askervein hill project: a finite control volume prediction of three-dimensional flows over the hills. *Boundary-Layer Meteorol*, 39:247–267, 1987.
- Rajagopalan, R. G. and Fanucci, J. B. Finite difference model for vertical-axis wind turbines. *AIAA Journal of Propulsion and Power*, 1(2):432–436, November-December 1985.
- Rajagopalan, R. G., Berg, D. E., and Klimas, P. C. Development of a three-dimensional model for the Darrieus rotor and its wake. *AIAA Journal of Propulsion and Power*, 11(2):185–195, 1995.
- Richards, B. Initial operation of Project Eole 4MW vertical-axis wind turbine generator. In *Windpower '87*, San Francisco, October 1987. Annual Conference of Americal Wind Energy Association.
- Rogers, M. M. The evolution of strained turbulent plane wakes. *Journal of Fluid Mechanics*, 463:53–120, 2002. doi: 10.1017/S0022112002008686.
- Rolin, V. F. C. and Porté-Agel, F. Wind-tunnel study of the wake behind a vertical axis wind turbine in a boundary layer flow using stereoscopic particle image velocimetry. *Journal of Physics: Conference Series*, 625(1):012012, 2015.
- Rumsey, C. L. and Ying, S. X. Prediction of high lift: review of present CFD capability. *Progress in Aerospace Sciences*, 38(2):145 – 180, 2002. ISSN 0376-0421. doi: [http://dx.doi.org/10.1016/S0376-0421\(02\)00003-9](http://dx.doi.org/10.1016/S0376-0421(02)00003-9). URL <http://www.sciencedirect.com/science/article/pii/S0376042102000039>.
- Ryan, K. J., Coletti, F., Elkins, C. J., Dabiri, J. O., and Eaton, J. K. Three-dimensional flow field around and downstream of a subscale model rotating vertical axis wind turbine. *Experiments in Fluids*, 57(3):1–15, 2016. ISSN 1432-1114. doi: 10.1007/s00348-016-2122-z. URL <http://dx.doi.org/10.1007/s00348-016-2122-z>.
- Scheurich, F. and Brown, R. Effect of dynamic stall on the aerodynamics of vertical-axis wind turbines. *AIAA Journal*, 49(11):2511–2521, November 2011.
- Schienenbein, L. A. Developement, installation and testing of a wind turbine Diesel Hybrid – final report. Technical report, DAF Indal Ltd, January 1979.
- Schulz, C., Klein, L., Weihing, P., Lutz, T., and Krämer, E. Cfd studies on wind turbines in complex terrain under atmospheric inflow conditions. *Journal of Physics: Conference Series*, 524(1):012134, 2014. URL <http://stacks.iop.org/1742-6596/524/i=1/a=012134>.

- Segalini, A. Linearized simulation of flow over wind farms and complex terrains. *Philosophical Transactions of the Royal Society of London A: Mathematical, Physical and Engineering Sciences*, 375(2091), 2017. ISSN 1364-503X. doi: 10.1098/rsta.2016.0099. URL <http://rsta.royalsocietypublishing.org/content/375/2091/20160099>.
- Segalini, A. and Inghels, P. Confinement effects in wind-turbine and propeller measurements. *Journal of Fluid Mechanics*, 756:110–129, 2014. doi: 10.1017/jfm.2014.440.
- Shamsoddin, S. and Porté-Agel, F. Large eddy simulation of vertical axis wind turbine wakes. *Energies*, 7(2):890–912, 2014.
- Shamsoddin, S. and Porté-Agel, F. A large-eddy simulation study of vertical axis wind turbine wakes in the atmospheric boundary layer. *Energies*, 9(5), 2016. ISSN 1996-1073.
- Shamsoddin, S. and Porté-Agel, F. Turbulent planar wakes under pressure gradient conditions. *Journal of Fluid Mechanics*, 830:R4, 2017a. doi: 10.1017/jfm.2017.649.
- Shamsoddin, S. and Porté-Agel, F. Large-eddy simulation of atmospheric boundary-layer flow through a wind farm sited on topography. *Boundary-Layer Meteorology*, 163(1):1–17, Apr 2017b. ISSN 1573-1472. doi: 10.1007/s10546-016-0216-z. URL <https://doi.org/10.1007/s10546-016-0216-z>.
- Shamsoddin, S. and Porté-Agel, F. A model for the effect of pressure gradient on turbulent axisymmetric wakes. *Journal of Fluid Mechanics*, 837:R3, 2018. doi: 10.1017/jfm.2017.864.
- Sheldahl, R. E. and Blackwell, B. F. Free-air performance tests of a 5 meter diameter Darrieus turbine. Technical Report SAND77-1063, Sandia National Laboratories, December 1977.
- Sheldahl, R. E. and Klimas, P. C. Aerodynamic characteristics of seven airfoil sections through 180 degrees angle of attack for use in aerodynamic analysis of vertical axis wind turbines. Technical Report SAND80-2114, Sandia National Laboratories, 1981.
- Sheldahl, R. E., Klimas, P. C., and Feltz, L. V. Aerodynamic performance of a 5-meter-diameter Darrieus turbine. *AIAA Journal of Energy*, 4(5):227–232, September 1980.
- Shen, W. and Sørensen, J. Numerical modeling of wind turbine wakes. *Journal of Fluids Engineering*, 124:393–399, June 2002.
- Shen, W., Zhang, J., and Sørensen, J. The actuator surface model: a new Navier–Stokes based model for rotor computations. *Journal of Solar Energy Engineering*, 131(1): 011002–011002–9, 2009.
- Simao Ferreira, C. J., van Kuik, G., and van Bussel, G. J. Wind tunnel hotwire measurements, flow visualization and thrust measurement of a VAWT in skew. In *Proceedings of the AIAA/ASME Wind Energy Symposium*, 2006.

## Bibliography

---

- Simao Ferreira, C. J., van Bussel, G. J. W., Scarano, F., and van Kuik, G. 2D PIV visualization of dynamic stall on a vertical axis wind turbine. In *Proceedings of the AIAA/ASME Wind Energy Symposium*, 2007.
- Smagorinsky, J. General circulation experiments with the primitive equations. *Monthly Weather Review*, 91(3):99–164, 1963.
- Smith, A. M. O. High-lift aerodynamics. *Journal of Aircraft*, 12(6):501–530, June 1975. ISSN 0021-8669. doi: 10.2514/3.59830. URL <https://doi.org/10.2514/3.59830>.
- Snyder, W. H., Khurshudyan, L. H., Nekrasov, I. V., Lawson, R. E., and Thompson, R. S. Flow and dispersion of pollutants within two-dimensional valleys. *Atmos Environ*, 25A: 1347–1375, 1991.
- South, P. and Rangi, R. S. An experimental investigation of a 12 Ft. diameter high speed vertical-axis wind turbine. Technical Report TR-LA-166, National Research Council of Canada, Ottawa, Ontario, April 1975.
- Stefanatos, N. C., Voutsinas, S., Rados, K., and Zervos, A. A combined experimental and numerical investigation of wake effects in complex terrain. In *Proceedings of EWECC*, volume 94, pages 484–90, 1994.
- Stefanatos, N. C., Morfiadakis, E., and Glinou, G. Wake measurements in complex terrain. In *Proceedings of the 1996 European Union Wind Energy Conference, Göteborg, Sweden*, pages 773–7, 1996.
- Stoll, R. and Porté-Agel, F. Effect of roughness on surface boundary conditions for large-eddy simulation. *Boundary-Layer Meteorol*, 118:169–187, 2006a.
- Stoll, R. and Porté-Agel, F. Dynamic subgrid-scale models for momentum and scalar fluxes in large-eddy simulation of neutrally stratified atmospheric boundary layers over heterogeneous terrain. *Water Resour Res*, 42:W01409, 2006b. doi: 10.1029/2005WR003989.
- Strickland, J. H., Smith, T., and K., S. A vortex model of the Darrieus turbine: an analytical and experimental study. Technical Report SAND-81-7017, Sandia National Laboratories, Albuquerque, NM, June 1981.
- Sykes, R. I. An asymptotic theory of incompressible turbulent boundary-layer flow over a small hump. *J Fluid Mech*, 101:647–670, 1980.
- Takahashi, T., Kato, S., Murakami, S., Ooka, R., Yassin, M., and Kono, R. Wind tunnel tests of effects of atmospheric stability on turbulent flow over a three-dimensional hill. *J Wind Eng Ind Aerodyn*, 93(2):155–169, 2005. ISSN 0167-6105.
- Taylor, G. J. and Smith, D. Wake measurements over complex terrain. In Quarton, D. C. and Fenton, V. C., editors, *Proceedings of the 13th British Wind Energy Association*

- (BWEA) Conference, *Wind Energy Conversion*, pages 335–342, Swansea, UK, 10–12 April 1991.
- Taylor, P. and Gent, P. R. A model of atmospheric boundary-layer flow above an isolated two-dimensional 'hill'; an example of flow above "gentle topography". *Boundary-Layer Meteorol*, 7:349–362, 1974.
- Taylor, P. and Teunissen, H. The askervein hill project: overview and background data. *Boundary-Layer Meteorol*, 39:15–39, 1987.
- Taylor, P. A. Numerical studies of neutrally stratified planetary boundary-layer flow above gentle topography. I: two-dimensional cases. *Boundary-Layer Meteorol*, 12:37–60, 1977.
- Taylor, P. A., Walmsley, J. L., and Salmon, J. R. A simple model of neutrally stratified boundary-layer flow over real terrain incorporating wavenumber-dependent scaling. *Boundary-Layer Meteorol*, 26:169–189, 1983.
- Templin, R. J. and Rangi, R. S. Vertical-axis wind turbine development in canada. *IEE Proceedings A - Physical Science, Measurement and Instrumentation, Management and Education - Reviews*, 130(9):555–561, December 1983. ISSN 0143-702X. doi: 10.1049/ip-a-1.1983.0085.
- Tennekes, H. and Lumley, J. L. *A first course in turbulence*. MIT press, 1972.
- Tescione, G., Ragni, D., He, C., Simao Ferreira, C. J., and van Bussel, G. J. Experimental and numerical aerodynamic analysis of vertical axis wind turbine wake. In *International Conference on Aerodynamics of Offshore Wind Energy Systems and Wakes*, Lyngby, Denmark, 2013.
- Teunissen, H., Shokr, M., Bowen, A., Wood, C., and Green, D. The askervein hill project: wind tunnel simulations at three length scales. *Boundary-Layer Meteorol*, 40:1–29, 1987.
- Thomas, F. O. and Liu, X. An experimental investigation of symmetric and asymmetric turbulent wake development in pressure gradient. *Physics of Fluids*, 16(5):1725–1745, 2004. doi: 10.1063/1.1687410. URL <http://dx.doi.org/10.1063/1.1687410>.
- Tian, W., Ozbay, A., Yuan, W., Sarkar, P., and Hu, H. An experimental study on the performances of wind turbines over complex terrains. In *51st Am Inst Aeronaut Astronaut Aerospace Sci. Mtg*, Grapevine, Texas, USA, 07–10 January 2013.
- Troldborg, N., Sørensen, J., and Mikkelsen, R. Actuator line simulation of wake of wind turbine operating in turbulent inflow. *J. Phys.: Conf. Ser.*, 75:012063, 2007.
- Tseng, Y.-H., Meneveau, C., and Parlange, M. B. Modeling flow around bluff bodies and predicting urban dispersion using large eddy simulation. *Environ Sci Technol*, 40: 2653–2662, 2006.



## Bibliography

---

- Uchida, T. and Ohya, Y. Numerical simulation of atmospheric flow over complex terrain. *J Wind Eng Ind Aerodyn*, 81(1-3):283–293, 1999. ISSN 0167-6105. doi: [http://dx.doi.org/10.1016/S0167-6105\(99\)00024-0](http://dx.doi.org/10.1016/S0167-6105(99)00024-0).
- Vermeulen, P., Builtjes, P., Dekker, J., and Bueren, G. An experimental study of the wake behind a full-scale vertical-axis wind turbine. Technical Report 79-06118, TNO report, 1979.
- Vittecoq, P. and Laneville, A. Étude en soufflerie d’un rotor de type Darrieus. Technical Report Rept. MEC-82-2, Mechanical Engineering Department, University of Sherbrooke, Canada, August 1982.
- Voutsinas, S. G., Rados, K. G., and Zervos, A. The effect of the non-uniformity of the wind velocity field in the optimal design of wind parks. In Palz, W., editor, *Proceedings of the 1990 European Community Wind Energy Conference*, pages 181–185, Madrid, Spain, 10-14 September 1990.
- Wan, F. and Porté-Agel, F. Large-eddy simulation of stably-stratified flow over a steep hill. *Boundary-Layer Meteorol*, 138(3):367–384, 2011.
- Wan, F., Porté-Agel, F., and Stoll, R. Evaluation of dynamic subgrid-scale models in large-eddy simulations of neutral turbulent flow over a two-dimensional sinusoidal hill. *Atmos Environ*, 41(13):2719–2728, April 2007.
- Wilson, R. E. and Walker, S. N. Fixed-wake analysis of the darrieus rotor. Technical Report SAND81-7026, Sandia National Laboratories, July 1981.
- Wood, N. Wind flowover complex terrain: a historical perspective and the prospect for large-eddy modelling. *Boundary-Layer Meteorol*, 96:11–32, 2000.
- Worstell, M. H. Aerodynamic performance of the DOE/Sandia 17-m-diameter vertical-axis wind turbine. *AIAA Journal of Energy*, 5(1):39–42, January 1981.
- Wu, Y. T. and Porté-Agel, F. Large-eddy simulation of wind-turbine wakes: evaluation of turbine parametrisations. *Boundary-Layer Meteorol*, 138(3):345–366, 2011.
- Wu, Y. T. and Porté-Agel, F. Atmospheric turbulence effects on wind-turbine wakes: an LES study. *Energies*, 5(12):5340–5362, December 2012.
- Wu, Y. T. and Porté-Agel, F. Simulation of turbulent flow inside and above wind farms: model validation and layout effects. *Boundary-Layer Meteorol*, 146(2):181–205, 2013.
- Wurtele, M. G., Sharman, R. D., and Datta, A. Atmospheric lee waves. *Annual Review of Fluid Mechanics*, 28:429–476, 1996.
- Wynnanski, I., Champagne, F., and Marasli, B. On the large-scale structures in two-dimensional, small-deficit, turbulent wakes. *Journal of Fluid Mechanics*, 168:31–71, 1986. doi: 10.1017/S0022112086000289.



- Xu, D. and Taylor, P. A. A non-linear extension of the mixed spectral finite difference model for neutrally stratified turbulent flow over topography. *Boundary-Layer Meteorol*, 59:177–186, 1992.
- Xu, D., Ayotte, K. W., and Taylor, P. A. Development of a non-linear mixed spectral finite difference model for turbulent boundary layer flow over topography. *Boundary-Layer Meteorol*, 70:341–367, 1994.
- Yang, X., Sotiropoulos, F., Conzemius, R. J., Wachtler, J. N., and Strong, M. B. Large-eddy simulation of turbulent flow past wind turbines/farms: the virtual wind simulator (VWiS). *Wind Energy*, 18:2025–2045, 2014. doi: 10.1002/we.1802.
- Yang, X., Howard, K. B., Guala, M., and Sotiropoulos, F. Effects of a three-dimensional hill on the wake characteristics of a model wind turbine. *Physics of Fluids*, 27(2): 025103, 2015. doi: 10.1063/1.4907685. URL <https://doi.org/10.1063/1.4907685>.
- Yoshizawa, A. and Horiuti, K. A statistically-derived subgrid-scale kinetic energy model for the large-eddy simulation of turbulent flows. *J. Phys. Soc. Jpn.*, 54:2834–2839, 1985.
- Zeman, O. and Jensen, N. O. Modification of turbulence characteristics in flow over hills. *Q J R Meteorol Soc*, 113:55–80, 1987.
- Zheng, K., Tian, W., Qin, J., and Hu, H. Investigation of wind turbine wakes over complex terrain based on actuator disk method. AIAA AVIATION Forum. American Institute of Aeronautics and Astronautics, June 2017. doi: 10.2514/6.2017-4073. URL <https://doi.org/10.2514/6.2017-4073>.



# Sina Shamsoddin

## Curriculum Vitae

### Education

- 2013–2018 **Ph.D.**, *EPFL*, Lausanne, Switzerland.  
Mechanical Engineering
- 2011–2013 **M.Sc.**, *EPFL*, Lausanne, Switzerland, *overall GPA: 5.68/6.0*.  
Energy Management and Sustainability
- 2006–2010 **B.Sc.**, *Amirkabir University of Technology (Tehran Polytechnic)*, Tehran, Iran,  
*overall GPA: 18.33/20.0*.  
Mechanical Engineering

### Research interests

- Fluid Mechanics
- Wind Energy
- Turbulence
- Wakes
- Large Eddy Simulation
- Flow over Topography

### Honors and awards

- 2017 **First prize in ACCES Visualization Contest – dynamic category**, *EPFL*, Lausanne, Switzerland.
- 2013 **Student Excellence first (1st) prize for the best results in the M.Sc. program among students of class of 2011-2013**, *EPFL*, Lausanne, Switzerland.
- 2010 **Ranked first (1st) for the best results in the B.Sc. program among 120 students of class of 2006-2010**, *Amirkabir University of Technology (Tehran Polytechnic)*, Tehran, Iran.
- 2010 **Being exempted from M.Sc. program entrance exam as an “Exceptionally Talented student”**, *Amirkabir University of Technology (Tehran Polytechnic)*, Tehran, Iran.
- 2006 **Ranked 75th in the Iranian undergraduate nationwide entrance exam**, Tehran, Iran.

---

## Languages

Kurdish mother tongue  
Persian mother tongue  
English fluent  
French level C1  
German level C1

---

## References

◦ **Prof. Fernando Porté-Agel**, EPFL, Lausanne ([fernando.porte-agel@epfl.ch](mailto:fernando.porte-agel@epfl.ch))

---

## Publications and Presentations

### Journal Publications

- [1] **S. Shamsoddin** and F. Porté-Agel. Large eddy simulation of vertical axis wind turbine wakes. *Energies*, 7(2):890–912, 2014.
- [2] **S. Shamsoddin** and F. Porté-Agel. A large-eddy simulation study of vertical axis wind turbine wakes in the atmospheric boundary layer. *Energies*, 9(5), 2016.
- [3] **S. Shamsoddin** and F. Porté-Agel. Large-eddy simulation of atmospheric boundary-layer flow through a wind farm sited on topography. *Boundary-Layer Meteorology*, 163(1):1–17, Apr 2017.
- [4] **S. Shamsoddin** and F. Porté-Agel. Turbulent planar wakes under pressure gradient conditions. *Journal of Fluid Mechanics*, 830, 2017.
- [5] **S. Shamsoddin** and F. Porté-Agel. A model for the effect of pressure gradient on turbulent axisymmetric wakes. *Journal of Fluid Mechanics*, 830, 2018.
- [6] **S. Shamsoddin** and F. Porté-Agel. Wind turbine wakes over hills wakes. under review in *Journal of Fluid Mechanics* 2018.

### Conference Presentations

- [7] S. Shamsoddin and F. Porté-Agel. Large eddy simulation of vertical axis wind turbine wakes. In *EGU, General Assembly*, Vienna, Austria, April 27 - May 02 2014.
- [8] S. Shamsoddin and F. Porté-Agel. Large eddy simulation of vertical axis wind turbine wakes. In *21st AMS Symposium on Boundary Layers and Turbulence*, Leeds, United Kingdom, June 9-13 2014.
- [9] S. Shamsoddin and F. Porté-Agel. Large-eddy simulation of atmospheric boundary-layer flow through a wind farm sited on complex terrain. In *EGU General Assembly*, Vienna, Austria, April 12-17 2015.
- [10] S. Shamsoddin and F. Porté-Agel. Large-eddy simulation of atmospheric boundary-layer flow through a wind farm sited on complex terrain. In *Wind-*

*chemin en forel, 1 – 1072 Forel (Lavaux) – Switzerland*

☎ +41 78 841 63 88 • 📞 +41 21 693 08 45

✉ [sina.shamsoddin@epfl.ch](mailto:sina.shamsoddin@epfl.ch)

🌐 <https://people.epfl.ch/sina.shamsoddin?lang=en>

*Farms 2015: Large wind-power plants: interaction, control and integration*,  
Leuven, Belgium, July 8-10 2015.

- [11] Sina Shamsoddin and F. Porté-Agel. A large-eddy simulation study of vertical axis wind turbine wakes in the atmospheric boundary layer. In *EGU General Assembly*, Vienna, Austria, April 17-22 2016.
- [12] Sina Shamsoddin and F. Porté-Agel. A large-eddy simulation study of vertical axis wind turbine wakes in the atmospheric boundary layer. In *EGU General Assembly*, Vienna, Austria, April 23-28 2017.